ADVANCED MATERIAL CHARACTERIZATION AND MODELING THE FOREIGN BODY IMPACT DAMAGE INITIATION AND PROGRESSION OF A LAMINATED CARBON COMPOSITE

A Thesis Submitted to
The Graduate School of Engineering and Sciences of
İzmir Institute of Technology
in Partial Fulfillment of the Requirements for the Degree of

DOCTOR OF PHILOSOPHY

in Mechanical Engineering

by
Mesut BAYHAN

July 2023

İZMİR

We approve the thesis of **Mesut BAYHAN**

Examining Committee Members:

Prof. Dr. Alper TAŞDEMİRCİ
Department of Mechanical Engineering, İzmir Institute of Technology

Prof. Dr. Hatice Seçil ARTEM
Department of Mechanical Engineering, İzmir Institute of Technology

Prof. Dr. Evren Meltem TOYGAR
Department of Mechanical Engineering, Dokuz Eylül University

Prof. Dr. B. Burak ÖZHAN
Department of Mechanical Engineering, Manisa Celal Bayar University

Assist. Prof. Dr. Selçuk SAATCI
Department of Civil Engineering, İzmir Institute of Technology

4 July 2023

Prof. Dr. Alper TAŞDEMİRCİ
Supervisor, Department of
Mechanical Engineering
İzmir Institute of Technology

Prof. Dr. Mustafa GÜDEN
Co-Supervisor, Department of
Mechanical Engineering
İzmir Institute of Technology

Prof. Dr. M. İ. Can DEDE
Head of the Department of
Mechanical Engineering

Prof. Dr. Mehtap EANES
Dean of the Graduate School of
Engineering and Sciences

ACKNOWLEDGMENTS

First of all, I would like to state my thankfulness to TUBITAK (Scientific and Technological Council of Turkey) and TUSAS (Turkish Aerospace Industries) for the financial support to project number 118C086.

I would like to express my gratitude to my supervisor Prof. Dr Alper TAŞDEMİRCİ and my co-advisor Prof. Dr. Mustafa GÜDEN for their constant encouragement and invaluable guidance. Their contribution to the achievements of this work is significant.

I certainly would like to extend my gratitude to Çağdaş KAMBUR and Remzi Ecmel ECE for their kindness, friendly support, and their invaluable suggestions for this research. Also, I would like to thank to the project manager Dr. Sinan YILMAZ for his support and care.

Special appreciation also goes to my thesis progress committee members, Prof. Dr. Evren Meltem TOYGAR and Prof. Dr. Hatice Seçil ARTEM for their academic support and encouragement through my Ph.D. program.

I sincerely thanks to all my friends especially Çetin BAKICI, Samed ENSER, Seçkin MARTİN, Semih Berk SEVEN, and others for helping me in many ways during my study. Thanks for the friendship and memories.

Finally, I would like to thank my family and dedicate this work to them because I would not have been able to accomplish all this without their presence.

ABSTRACT

ADVANCED MATERIAL CHARACTERIZATION AND MODELING THE FOREIGN BODY IMPACT DAMAGE INITIATION AND PROGRESSION OF A LAMINATED CARBON COMPOSITE

The coupon level composite sample tests and the accompanying numerical models were carried out to predict the response of woven carbon fiber composite structures against impact. The numerical models of the coupon-level tests were implemented in LSDYNA software using the MAT_162 and MAT_58 composite material models. The results obtained by both quasi-static and dynamic tests were used to determine their constants. In addition to the tests that were used for the determination and calibration of the material model parameters, separate tests and their models were performed for the validation, including punch shear tests and low-velocity impact tests. It could be said that the material models examined were considered comprehensive and precise as the experimental results were well predicted by the numerical models. Also, the rate sensitivity of the woven carbon composite in the in-plane and thickness directions was investigated experimentally and numerically. In the tests, the DIC method was employed in the determination of the displacement and strain of the specimen. Based on the results obtained, it was concluded that the in-plane tensile properties are rate insensitive. Besides, the simulations of the component level tests, such as bird strike and drone impact, were established to investigate the damage initiation and propagation within the composite. It was found that the drone impact results in more severe damage compared to the bird impact. It is worth noting that the development of such precise composite material models to simulate dynamic loadings will definitely shorten the time between the beginning of designing and the component testing.

ÖZET

KATMANLI KARBON KOMPOZİTİN İLERİ MALZEME KARAKTERİZASYONU VE YABANCI CİSİM ÇARPMA HASAR BAŞLANGICININ VE İLERLEYİŞİNİN MODELLENMESİ

Örgülü karbon fiber kompozit yapıların darbeye karşı tepkisini belirlemek amacıyla kupon seviyesi kompozit numune testleri ve beraberinde nümerik modeller gerçekleştirilmiştir. Kupon seviyesindeki testlerin nümerik modelleri, MAT_162 ve MAT_58 kompozit malzeme modelleri kullanılarak LSDYNA programında gerçekleştirildi. Hem yarı statik hem de dinamik testlerden elde edilen sonuçlar malzeme sabitlerini belirlemek amacıyla kullanıldı. Malzeme modeli parametrelerinin belirlenmesi ve kalibrasyonu için kullanılan testlere ek olarak, doğrulama için zımba kesme testlerinin ve düşük hızlı çarpma testlerinin de bulunduğu ayrı testler ve bu testlerin nümerik modelleri yapılmıştır. Deneysel sonuçların nümerik modeller tarafından doğru bir şekilde tahmin edilmiş olmasından dolayı incelenen malzeme modellerinin kapsamlı ve doğru olduğu söylenebilmektedir. Ayrıca, örgülü karbon kompozitin düzlem-içi ve kalınlık yönlerindeki gerinim hızı hassasiyeti deneysel ve nümerik olarak incelenmiştir. Testlerde, numunenin yer değiştirmesinin ve geriniminin hesaplanmasında Dijital Görüntü Korelasyonu (DGK) yöntemi kullanılmıştır. Elde edilen sonuçlara dayanarak, düzlem-içi malzeme özelliklerin gerinim hızı hassasiyetinin olmadığı sonucuna varılmıştır. Bunlara ek olarak, kuş çarpması ve drone çarpması gibi komponent seviyesi testlerin simülasyonları, kompozit içindeki hasarın başlangıcını ve ilerleyişini gözlemlemek amacıyla oluşturulmuştur. Drone çarpmasının kuş çarpmasına göre daha ağır hasarla sonuçlandığı sonucuna ulaşılmıştır. Dinamik yüklemeleri modellemek amacıyla bu tür hassas kompozit malzeme modellerinin geliştirilmesinin, tasarımın başlangıcı ile komponent testi arasındaki süreyi kısaltacağına dikkat edilmelidir.

TABLE OF CONTENTS

LIST OF FIGURES

Figure **Page**

Figure **Page**

Figure **Page**

Figure **Page**

Figure **Page**

LIST OF TABLES

Table **Page**

CHAPTER 1

INTRODUCTION

The components of aircraft must be tested in accordance with regulations written by Federal Aviation Administration (FAA) and European Aviation Safety Agency (EASA), and the airworthiness of aircraft must be approved before aircraft begin to operate in the sky. Thus, the component level tests are essential in demonstrating the airworthiness of aircraft, but they are costly to implement as the components to be tested have to be transported to testing facility location and conducted by using large, heavy equipment and tools. For the purpose of validation through modeling, component tests are also requiring too many real-time measurements taken on the component tested by means of strain gages, load cells, etc.

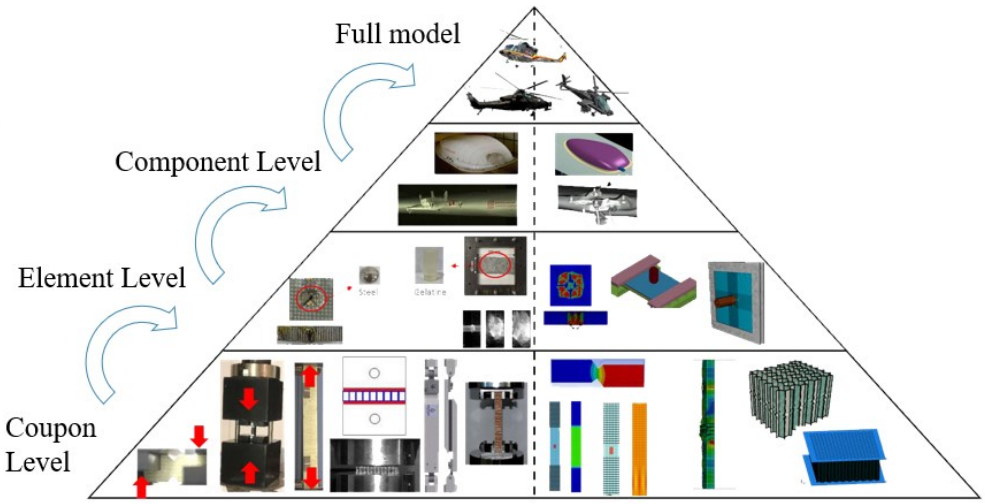

Figure 1.1. Extending Building Block Approach

Extending Building Block Approach in Figure 1.1 is widely used in the design of composite structures in the aerospace industry. It includes coupon level tests, element level tests, component level tests and full model tests. According to this approach, the component level tests are in the third level while the coupon level tests are in the first level. Therefore, it is essential to carry out coupon level tests extensively since an accurately simulated model may reduce the cost of the component level tests or may eliminate this type of tests.

The mechanical properties of composites are investigated via a set of standard and non-standard experimental tests. The former includes tensile tests, compression tests, shear tests, flexural tests, open-hole tests and low-velocity impact tests while the latter is the tests performed to determine material constants required for modeling composite material in finite element solver such as elastic constant measurement tests, laterally constrained compression tests, off-axis compression tests and punch shear tests. The studies investigating the mechanical properties of woven carbon epoxy composites through the standard and non-standard test methods will be mentioned here.

In the determination of the in-plane and through-thickness properties of composite materials, tensile tests are performed in the in-plane directions (warp and weft directions) and through-thickness direction, respectively. The studies investigating these properties in accordance with the related standard and non-standard test methods will be explained in the next.

Naik et al.[1] investigated the notched and unnotched tensile strength of plain weave carbon composites with single layer and six-layer according to ASTM 3039[2]. The failure stress and strain of the six-layer carbon composite were found to be about 500 MPa and 0.02 mm/mm for the warp direction and 400 MPa and 0.018 mm/mm for the weft direction, respectively. The reason why a lower strength in the weft direction was obtained compared to the warp direction was explained by the use of the unbalanced plain weave composite. It was reported that the strength value for the single layer composite was lower compared to that of the composite laminate.

Hou and Ruiz[3] determined the tensile properties of woven carbon composite, which had a commercial code of T300/914. The specimen having a non-standard geometry were tested at low ($1.2x10^{-4}$ s^{-1}), intermediate (4 s^{-1}) and high strain rates (600 s^{-1}). At quasi-static strain rates the tensile strength and modulus in the warp direction were calculated as 539.5 MPa and 73.5 GPa while they were calculated as 550 MPa and 63 GPa in the weft direction. The reason that the warp modulus was higher than the weft modulus was explained by the more fibers introduced in the warp direction compared to the weft one. Besides, Poisson's ratio was calculated as 0.055. It was reported that as the strain rate increased the in-plane properties such as tensile strength and modulus remained unchanged.

The tensile strength and modulus in the warp and weft direction of five-harness satin weave carbon composite were investigated by Kumagai et al.[4] in accordance with ASTM 3039[2]. The tensile strengths were found to be 844 MPa and 790 MPa while the

elastic moduli were measured as 72.8 GPa and 76 GPa for the warp and weft (fill) direction. Poisson's ratio (ϑ_{wf}) was also determined as 0.074 from the axial and transverse strains measured by the strain gages attached to the specimen.

Tensile properties of the different composites reinforced with plain weave (PW) and 8-harness satin weave (8HS) were investigated by Paiva et al.[5] according to ASTM D3039[2]. Two epoxy types were used as matrix material in the fabrication of the composite, namely diglycidil-ether of bisphenol-A epoxy (F155^{TM}) and modified epoxy (F584^{TM}). The tensile strength was calculated as 950.05 MPa, 810 MPa, 1185.4 MPa and 985.9 MPa for F155/PW, F155/8HS, F584/PW and F584/8HS composites while the elastic modulus was found to be 57.8 GPa, 67.8 GPa, 65.6 GPa and 71.5 GPa, respectively. It was specified that the F584 matrix type showed better mechanical properties compared to F155 one, and the tensile strength of plain weave composite was higher than those of satin weave composite while the elastic modulus of satin weave was found to be higher compared to those of plain weave composite.

The unnotched tensile properties of carbon fiber reinforced thermoplastic and thermoset composites were examined by Vieille and Taleb[6] in accordance with EN 6035. The five-harness satin weave was selected as reinforcement fabric while polyphenylene sulfide (PPS) and epoxy were employed as thermoplastic and thermoset resin, respectively. The tensile strength and modulus of the thermoset composite in the in-plane direction were calculated as 690 MPa and 63.3 GPa, and the Poisson's ratio was determined as 0.04.

Tensile properties of the carbon fiber composite, AGP370-5H/3501-62, in the warp and weft direction[7] were examined in accordance with ASTM D3039. The density and fiber volume fraction of the composite investigated was 1600 kgm^{-3} and 60%, respectively. The strain gages attached to the test coupon were employed to measure strain in the axial and transverse directions. The warp and weft elastic moduli were determined to be 77 GPa and 75 GPa while 963 MPa and 838 MPa were calculated as the tensile strength in these directions. Besides, the strain at failure and the Poisson's ratio were found to be 0.013 and 0.07 in both directions.

According to ASTM 3039, a uniaxial tensile load was applied to five-harness and eight-harness carbon fiber composite to measure in-plane properties at quasi-static strain rate[8]. It was explored that damage occurred in the weft yarns at the interlacing points as matrix cracking and multiple cracks were observed before failure. It was reported that at the failure an extensive delamination was not observed, and fiber fracture occurred

instantly. The picture taken by scanning electron microscopy (SEM) through the axial section of the sample can be seen in Figure 1.2 in which multiple cracks in the weft yarn were observed after the fracture. In addition, in-plane tensile strength, elastic modulus and failure strain were calculated as 835 MPa, 69.8 GPa and 0.017, respectively.

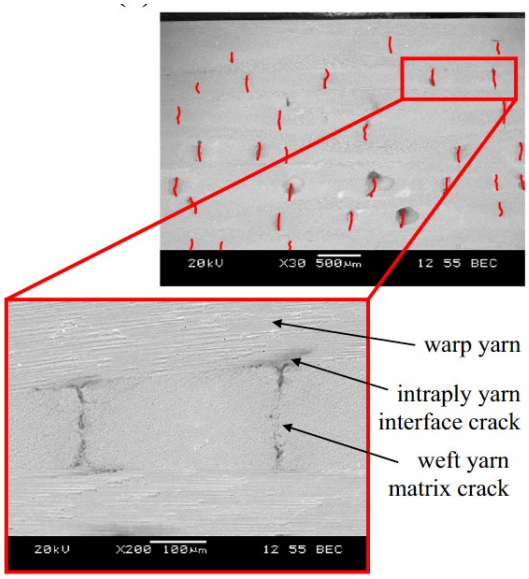

Figure 1.2. SEM photograph of axial section of 8-harness satin composite (Source: Montesano et al.[8])

Lu et al.[9] performed a study on plain weave carbon composite to characterize the in-plane properties at quasi-static and dynamic strain rates. The in-plane tensile strength, modulus and failure strain at the quasi-static rate were determined as 588.73 MPa, 49.14 GPa and 0.0133, respectively. It was reported that the in-plane tensile properties increased with increasing strain rates, showing strain rate dependence.

Tensile properties and open-hole tensile properties of a five-harness carbon fiber composite were investigated in accordance with ASTM D3039 and ASTM D5766, respectively[10]. It was concluded that the failure in tensile specimens without the hole occurred around the middle section of the test coupon. 739.8 MPa, 62.9 GPa and 0.059 were calculated to be the tensile strength, tensile modulus and the Poisson ratio of the carbon composite tested. The open-hole tensile strength was calculated as 508.8 MPa, corresponding to a reduction of 31% in material tensile strength.

Zhou et al.[11] conducted an experimental study on woven carbon composites including plain and twill weave to investigate their mechanical behavior under in-plane tensile loading. The tensile strength and modulus were determined as 723 MPa and 61.4

GPa in the warp direction while they were calculated to be 462 MPa and 52.1 GPa for the weft direction. For twill-660 and twill-400 composites, the warp strength (and modulus) were 805 MPa (and 62.8 GPa) and 978 MPa (and 64.6 GPa) while the weft ones were 559 MPa (and 59.5 GPa) and 898 MPa (and 65.2 GPa), respectively. It was reported that the crimp ratio had an enormous influence on the determination of mechanical properties. With increasing the crip ratio, smaller strength and modulus values were obtained, and the stress versus strain curve showed bi-linear behavior.

In addition to the in-plane standard tests, the investigation of strain rate sensitivity of the carbon composite in the in-plane directions is of notable importance. So far, many efforts have been made to investigate whether the unidirectional and/or woven carbon composites are strain-rate sensitive[12–35] or strain-rate insensitive[3,36–49]. However, a certain answer for that question is not found. Different mechanisms that are considered to be effective on strain rate effect have been proposed. In woven composites, the weave type of the composite is thought to be a reason for the strain rate sensitivity since when the composite is subjected to the tensile load, the matrix resists the straightening of the fiber material during the course of the deformation, meaning that the matrix carries a significant portion of the applied load [35,50]. On the other hand, this mechanism is not effective in unidirectional composites because of the limited deformation of the matrix material. Besides, the bond between the resin and the reinforcement material is considered to be effective in the strain rate behavior of the composite before the loss of integrity occurs between the constituents[50].

On the methods used in the determination of the through-thickness tensile properties of composite (Figure 1.3), a comprehensive research was performed by Lodeiro et al[51]. It was reported that the parallel-sided, circular wasted, and RARDE short block geometries could be used in the calculation determination of the out-of-plane tensile properties while C-shaped composite was not recommended due to the complex failure modes (tensile and shear failure mode) occurred during the course of the loading.

To determine out-of-plane tensile properties of tape, woven and braided carbon fiber epoxy composites, Jackson and Ifju performed four-point bending tests on L- shaped composite [52]. Each L-shaped tape, woven and braided composites were also tested using a hinged loading mechanism for comparison of the results obtained from the four point point bending test method. It was reported that the composite was subjected to different stress fields. In case the composite was tested using a four-point bending fixture, the stress field occurred due to stress related to the bending moment. While, in the hinged loading

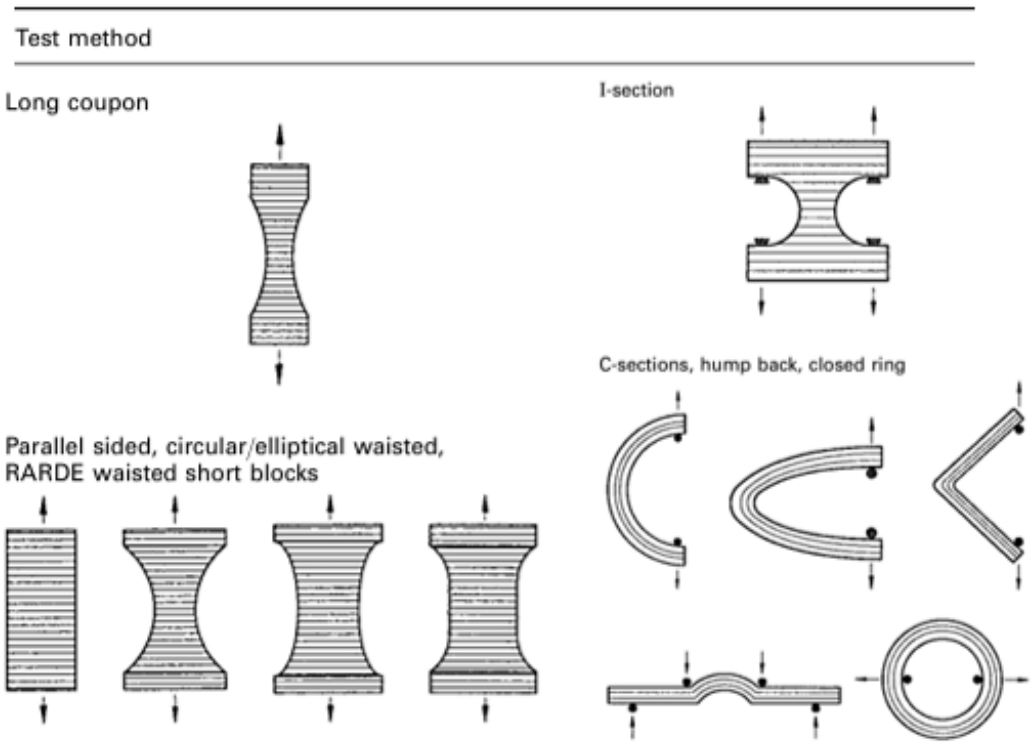

Figure 1.3. Through-thickness tensile test methods

(Source: Lodeiro et al.[51])

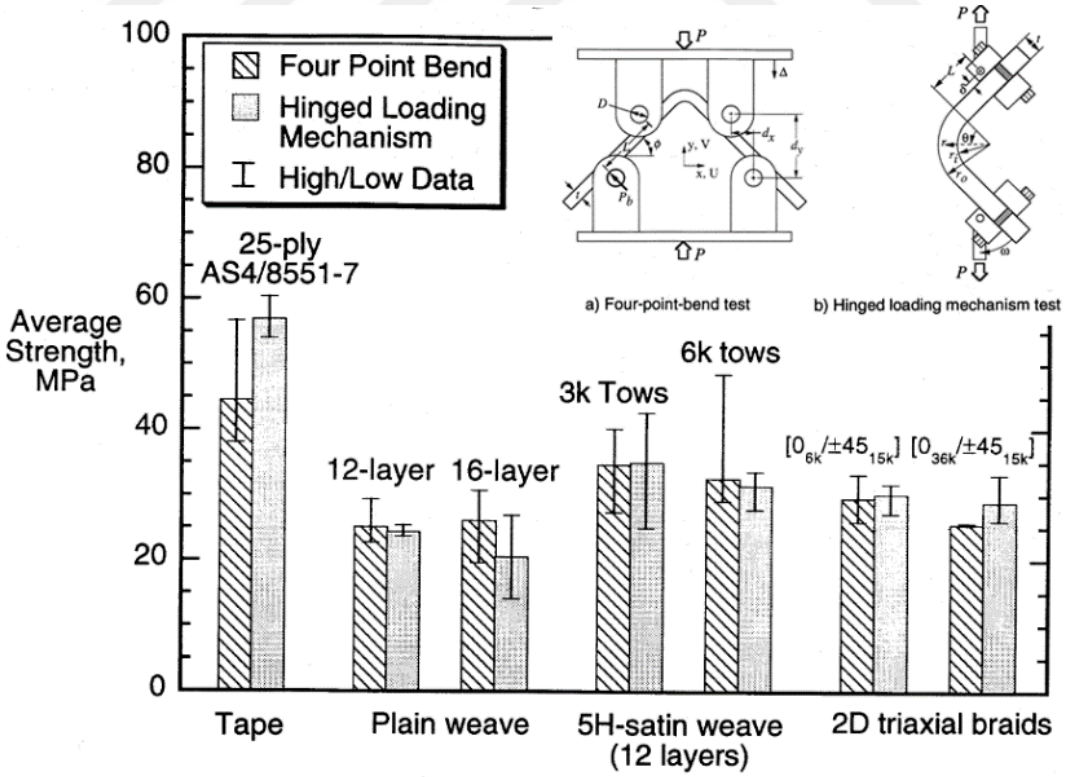

Figure 1.4. Through-thickness tensile properties of different composites

(Source: Jackson et al.[52])

mechanism a stress field having two components due to the moment and end force arose around the angle. It was concluded that the strength determined by both test methods was found to be similar (Figure 1.4), and the through-thickness tensile strength of plain weave was lower compared to that of unidirectional composite. Also, the average through-thickness tensile strength of the five-harness satin weave composite was calculated as 34 MPa.

A numerical and experimental study on investigation of the through-thickness tensile properties of a carbon composite reinforced with twill weave was carried out by Chen et al.[53]. The density and fiber volume fraction of the carbon composite was 1.42 g/cm^3 and about 60%, respectively. A specimen of the thin-waist section (Figure 1.5) was employed to measure strength, modulus and failure strain at quasi-static and high strain rates. The through-thickness tensile strength, modulus and failure strain were calculated at quasi-static loading rate as 2.82 MPa, 1.25 GPa and 0.0022 mm/mm, respectively. It was reported that the tensile strength and modulus in the out-of-plane direction increased as the loading rate increased.

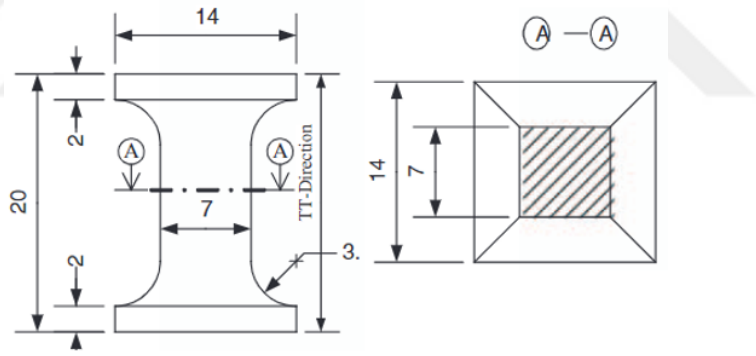

Figure 1.5. Dimensions of the through-thickness specimen
(Source: Chen et al.[53])

Abot and Daniel[54] carried out a study to examine the through-thickness properties of a woven carbon composite having a commercial code of AGP370-5H/3501-6S. A flatwise tensile specimen adhered to aluminum shanks (Figure 1.6) was subjected to tensile load to determine the through-thickness tensile properties. It was concluded that the out-of-plane tensile stress increased linearly up to fracture, and the failure of the specimen took place in the specimen's middle section. The out-of-plane strength and modulus were calculated as 59.8 MPa and 12.8 GPa, respectively while strain at failure was found to be 0.005. Besides, it was emphasized that the elastic properties obtained

from the through-thickness tensile specimen were similar to those of the unidirectional and fabric composites.

Nakai et al.[55] conducted an experimental study in which waisted composite specimens reinforced with unidirectional and cross-ply carbon fabrics were tested to analyze the influence of reinforcement type on the tensile properties. The tensile strength and strain were determined sequentially as 16.2 MPa and 0.003 mm/mm for the cross-ply composite at quasi-static strain rate. It was reported that as the strain rate increased the tensile strength increased while the tensile strain at facture decreased. Besides, the tensile properties of the unidirectional composite were found to be higher than those of the cross-ply composite.

The compressive properties of carbon composite are determined through compression tests in the in-plane directions (warp and weft directions) and out-plane direction. The studies investigating these properties according to the standard (ASTM D6641[56]) and non-standard test methods will be explained in the next.

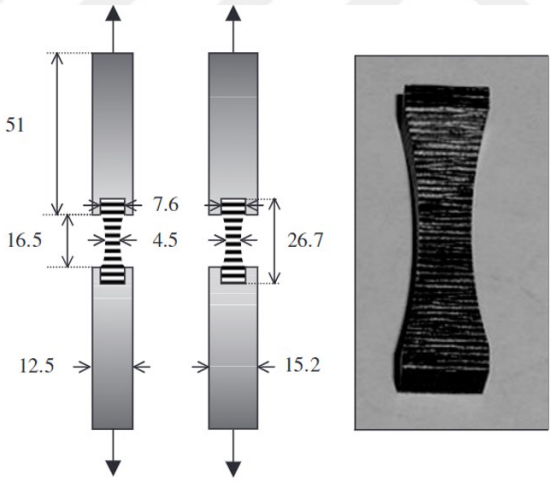

Figure 1.6. Flatwise tensile test specimen
(Source: Abot et al.[54])

The in-plane compressive properties of woven carbon composite were determined using a non-standard specimen at low, intermediate and high strain rates by Hou and Ruiz[3]. The compressive strength, modulus and failure strain in the weft direction were calculated as 550 MPa, 60 GPa and 0.0093, respectively. The compressive strength was found to increase with increasing strain rate.

A modified IITRI test fixture by which the compressive load was applied through the end compression was employed to determine the compressive properties of the carbon

composite in the warp and weft direction[7]. The compressive strength and compressive modulus were found to be nearly similar for both in-plane directions, 870 MPa and 69 GPa, while the failure strain in the warp and weft direction was determined as 0.016 and 0.013, respectively.

Liu et al.[57] performed an experimental study on a five-harness carbon composite to determine its mechanical properties. The weft and warp compressive properties were determined according to GB-3352-82 (Chinese test standard) that are similar to ASTM D3410. Besides, the effect of the resin content on the compressive properties was investigated. It was reported that for the resin content of 40 % the compressive strength and modulus were calculated as 353.1 MPa and 40.3 GPa in the warp direction and 635.5 MPa and 54 GPa in the weft direction. The compressive strength was reported to increase with increasing resin content up to 40 % while the compressive modulus decreased. Beyond that amount of resin content, the strength and modulus values decreased with increasing resin content. This was explained by the fact that as the resin content increased, the interfacial strength increased.

A study on a plain weave carbon composite was performed to characterize the carbon composite at quasi-static and dynamic strain rates[58]. In the study, the in-plane compressive properties of the composite were performed in accordance with ASTM D3410[59]. The average compressive strength, modulus and failure strain were calculated as 438.5 MPa, 51.82 GPa and 0.00775 mm/mm, respectively.

The in-plane shear properties of the composite can be determined from the tensile test results of $[\pm 45]_{ns}$ composite specimen according to ASTM D3518[60] while the out-of-plane shear properties are calculated from the notched composite specimens in accordance with ASTM D5379[61]. The studies investigating these properties will be explained in the next.

A series of tests were carried out at different strain rates to measure the in-plane shear properties of T300/914 carbon composite material [3]. The shear strength, modulus and strain were determined as 128 MPa, 4.8 GPa and 0.14 mm/mm, respectively. The shear properties were found to be dependent on the strain rate since these properties were dominated by the matrix.

The in-plane shear properties of five-harness satin woven carbon composite[4], which was named commercially as T800H/3633, were determined according to ASTM D3518[60]. The in-plane strength and modulus were found to be 74 MPa and 4.69 GPa while 0.0327 mm/mm was calculated as the shear strain at failure. It was stated that the

in-plane shear behavior of the composite depended on the matrix properties due to the contribution of the matrix to the load carried by the composite.

Abot et al.[7] carried out a study on the investigation of the in-plane properties of a woven carbon composite. To measure in-plane shear properties, a test coupon with a ply orientation of $[\pm 45]_{ns}$ was tested in accordance with ASTM D3518. Also, two strain gages in the axial and transverse directions bonded on the test specimen to calculate shear strain. In-plane shear strength, shear modulus and shear strain were reported to be 70 MPa, 6.5 GPa and 0.034 mm/mm, respectively. It was specified that the shear stress increased linearly with shear strain up to a shear strain of 0.004, and a stress softening occurred. Thereafter, shear stress remained unchanged with increasing shear strain up to the facture.

An experimental study on the determination of the in-plane properties of a cross-ply carbon composite at quasi-static and high strain rates was performed by Lu et al[9]. A tensile load was applied to a $[\pm 45]_6$ carbon specimen via Shimadzu testing machine at quasi-static strain rates and split Hopkinson tensile bar at high strain rates. The quasi-static shear strength, shear modulus and shear strain at failure were calculated as 153.43 MPa, 10.84 GPa and 0.14 mm/mm, respectively. It was stated that due to the scissoring effect (rotation of the fibers through the load axis) the strain at failure in shear tests was found to be higher than that in tensile tests of $[0/90]_6$ specimen. Besides, it was reported that the in-plane shear properties improved with increasing strain rates.

To examine the out-of-plane share properties on 3-1 and 3-2 planes a V-notched test specimen was tested via a modified Iosipescu test fixture[54]. It was reported that the shear stress increased linearly and then showed a stress-softening behavior. Thereafter, the shear stress remained unchanged until the fracture. The properties on the 3-1 plane were calculated to be 74.8 MPa, 5.1 GPa and 0.08 mm/mm for the shear strength, shear modulus and shear strain while they were determined on the 3-2 plane as 65.4 MPa, 4.1 GPa and 0.08 mm/mm, respectively.

In addition to the standard tests mentioned above, there are other tests to determine the material constants of composite materials. These parameters are required to model composite materials using solid material models in LSDYNA, especially material model 162. These non-standard tests include Punch Shear Tests, Out-of-Plane Off-axis Compression Tests and Low-velocity Impact Tests. The studies in which the non-standard test types were performed were reviewed and explained in the next.

In 2014, high-velocity impact and perforation simulations of a plain weave carbon composite were established by Tehrani et al.[62]. A series of non-standard tests as well as

standard tests were performed. To calculate fiber crush strength and fiber shear strength, a quasi-static punch shear test was performed. The results were also employed in the calibration and verification of damage parameters (m1, m2, m3 and m4) of material model 162. After the calibration, the fiber crush strength and fiber shear strength were found to be 900 MPa and 120 MPa, respectively.

In 2021, an extensive study on quasi-static and dynamic characterization of plain weave carbon composite was performed by Shi et al.[58]. In the study, non-standard test methods like double-shear-test and Brazilian tests were performed to determine fiber shear strength (497 MPa) and through-thickness tensile strength (45 MPa) of composite, respectively. Strain rate parameters (C_{raten}) and damage parameters (AM_n) were calculated by comparing the numerical results and high strain rate compression test results. Besides, the modulus reduction parameter (OMGMX) was determined as 0.999 via the Low Velocity Impact Test carried out in the Drop Tower testing device.

In addition to coupon level tests mentioned, component level tests are required in the certification of an aircraft. One of them is the foreign object impact test, especially the bird strike test. Foreign objects, which is defined as any object that does not belong to the aircraft or its system, are the serious threat that an aircraft may encounter during take-off, climb, cruise, descent and landing phase. The damage from these objects to the aircraft may result in the aircraft crash, malfunctioning the aircraft's sub-systems or equipment, or may cause crew injury and/or dead. The definition of Foreign Object Damage given by the Federal Aviation Administration is that "Any damage attributed to a foreign object that can be expressed in physical or economic terms which may or may not downgrade the product's safety or performance characteristics"[63].

The foreign object types can be seen in Figure 1.7. It consists of inanimate objects such as hail and animate objects like birds. In recent years, drones have been begun appearing in the sky due to advancements in unmanned aerial vehicle (UAV) technology and their use in different operations and/or activities (search operation, photography, filming, etc.). Their significantly increased use results in collision events between aircraft and drones. For instance, in 2017 a UH-60M Blackhawk helicopter was impacted by a DJI Phantom 4 quadcopter[64]. That's why, the drone has been classified as an inanimate foreign object. While many studies have been performed to investigate bird strike and hail impact until now, a few attempts have been made to characterize the mechanical behavior of the materials that make up drones and to observe the damage induced by

drones on aircraft components. In some, the aircraft components impacted by equally weighted drones and birds were examined.

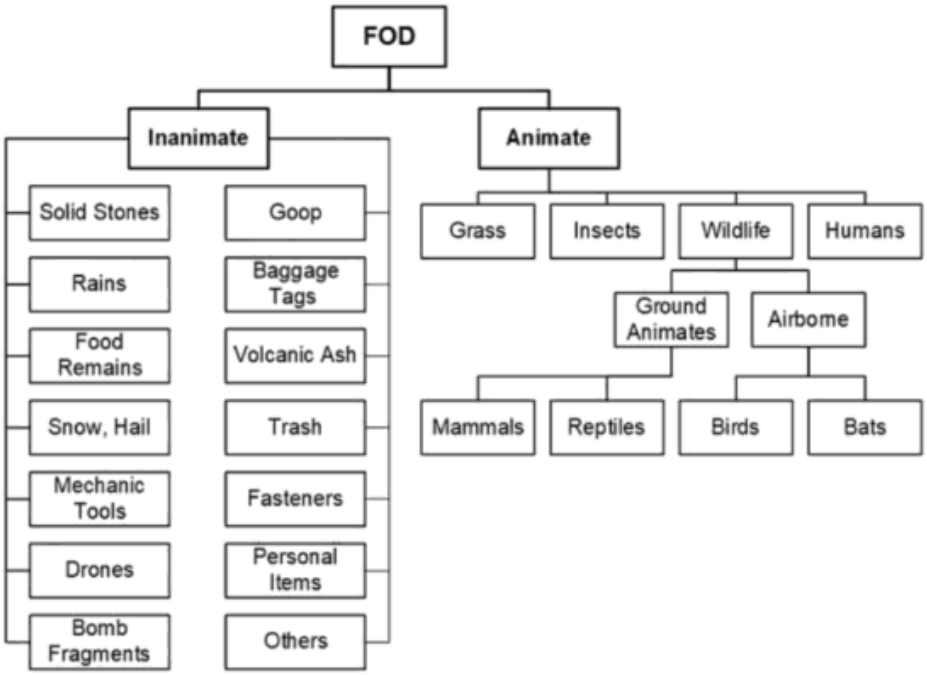

Figure 1.7. Classification of foreign objects
(Source: Civil Aviation Safety Authority[65])

In 2013, a pioneering study on damage potential of drones was performed by Civil Aviation Safety Authority[65]. Through damage assessment in the collision events between the densest and heaviest parts of a UAV and the engine, airframe, and windscreen of a manned aircraft it was concluded that catastrophic damage might not be observed in case of drone ingestion by engine. The collision between the drone and airframe at a velocity of above 200 kts may result in airframe penetration. It was also reported that a drone impact on the windshield of a commercial aircraft in landing and/or cruise phase may cause the penetration of the windscreen.

In 2017, a turbojet engine was numerically impacted by drones and birds to observe the damage on the engine fan blades and to compare the extent of the damage caused by both the drone and bird[66]. The mass of the drone and bird was selected as 2.5 kg in accordance with the regulations followed in bird strike certification tests. It was stated that due to the fact that the drone is made up of different rigid materials like battery, motor and payload (gimbal and camera), a different procedure is followed in the modeling of the drone compared to the bird as shown in Figure 1.8. It was found out that the drone

impact caused more severe damage to fan blades compared to bird impact because of the rigid components (battery, motor and payload) of the drone. In a later study[67], the carbon fiber and titanium fan blades were impacted by drones different in size and mass (hobby and professional drones) to classify the risk levels presented by these drones. It was reported that titanium and composite blades are not significantly damaged in the hobby drone ingestion event while the professional drone ingestion results in extensive damage of both fan blade types investigated.

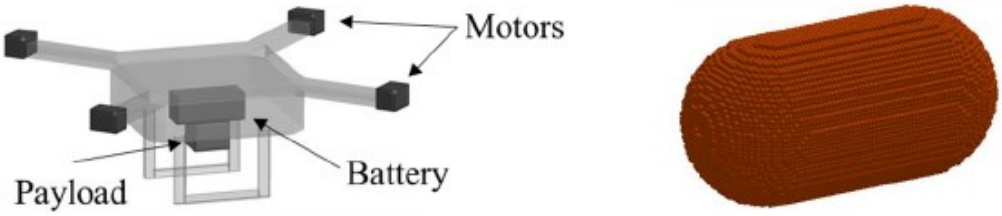

Figure 1.8. Drone and bird model
(Source: Song et al.[66])

In the same year, the Federal Aviation Administration (FAA) performed a study on the collision between an aircraft and a UAV and between an aircraft and a bird[68]. Three-dimensional CAD models of a DJI Phantom 3-quadcopter were first obtained through reverse engineering and the finite element model of the quadcopter (Figure 1.10) was formed in LSDYNA finite element software. Then, to use in the validation and verification of numerical model of UAV, a single component-level and full-scale tests on UAV were carried out. The calibrated UAV model was employed to model the collision event between the UAV and the horizontal stabilizer, vertical stabilizer, windshield and wing of an aircraft. It was reported that the tail took severe damage after the drone collision while less damage was observed on the windshield compared to the components examined. Also, a vertical stabilizer subjected to bird impact was simulated, the bird impact damage was then compared to that obtained from the drone of equivalent mass. It was seen that compared to the bird strike, the simulated part of the aircraft took more severe damage in the drone collision event. Due to the hard parts of the drone (camera, gimbal and battery), penetration occurred. In another study, the damage severity of a col lision between a UAV and the engine of an aircraft was investigated[69]. It was concluded that the engine of the aircraft in the take-off phase took severe damage from the drone impact due to the fact that the maximum rotational speed of the fan was reached.

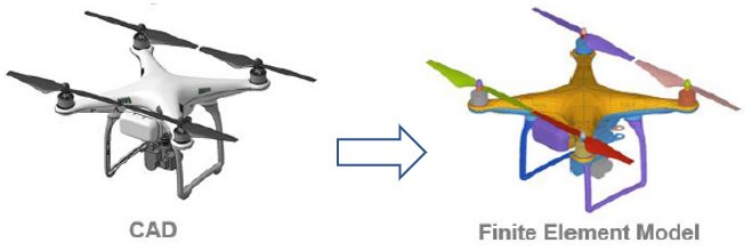

Figure 1.9. CAD and Finite Element Model of UAV
(Source: Olivares et al.[68])

In 2019, experimental and numerical studies on the horizontal stabilizer subjected to drone impact were performed by Meng et al.[70]. Also, a bird impact simulation of the horizontal stabilizer was formed to assess the severity of the damage in the collision between the drone and the aircraft structure investigated. The mass of the drone (Figure 1.11) and the bird were 3.4 kg and 3.6 kg, respectively. It was found that the horizontal stabilizer took more severe damage in the drone impact scenario compared to the bird striker. Also, the hard part of the drone, especially the battery, penetrated the structure.

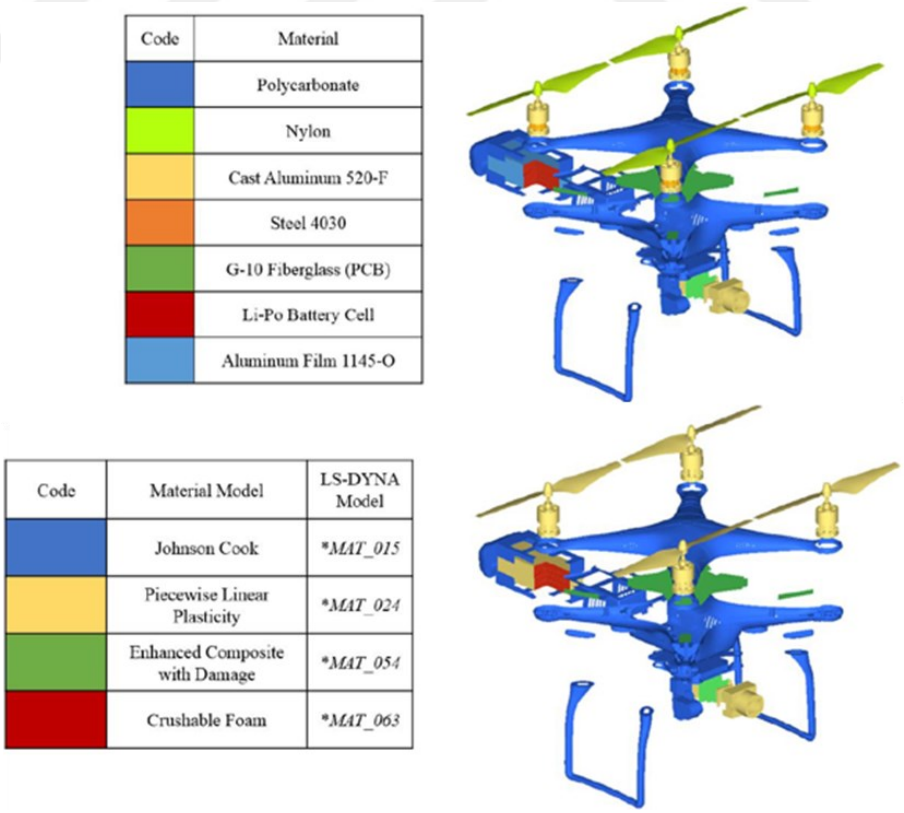

Figure 1.10. UAV materials and corresponding material models
(Source: Olivares et al.[68])

In that year, a numerical study was performed on the wing fixed leading edge of an aircraft to improve its strength against UAV impacts by using a triangular reinforcement structure[71]. A drone with a mass of 1.2 kg and an impact velocity of 127 m/s was employed in the impact study. It was concluded that the reinforcement type investigated reduced the severity of the damage and the penetration of the battery into the airframe as well as the fuel tank were prevented.

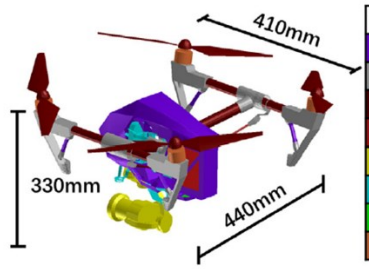

Code	Material
	Polycarbonate
	Polyamide 6
	Carbon Fiber Reinforced Polymer
	battery
	camera
	6061-T6 aluminum alloy
	electronic boards
	motor

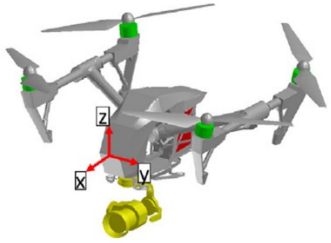

Component	Mass/kg	Center of gravity/mm
Total UAS	3.428	(-197, 0, 5)
motors	0.462	(-214, 0, 12)
battery	0.57	(-271, 0, 4)
camera	0.64	(-125, 0, -161)

Figure 1.11. The mass and material of the drone components
(Source: Meng et al.[70])

In 2020, a numerical study was performed on drone-engine collision[72]. The number of damaged fan blades as well as damage size were investigated at different impact positions and drone postures with the aid of the finite element method. The forward speed of the drone and the rotational speed of the engine were selected as 92.6 m/s and 523.6 rad/s to correspond to the aircraft take-off velocity and the maximum thrust level of the engine. It was reported that both drone position and posture have a significant influence on the number of fan blades damaged. Especially, more damage on fan blades was observed as the drone posture was getting complex.

In the same year, a report on damage assessment after the collision between a drone and a windshield and between a drone and the leading edge of a wing was published by Dadouche et al[73]. In the experiments, the drone hold in the barrel via sabot was fired on the windshield and leading edge fixed on the test fixture. It was concluded that after the drone impact at a velocity of 128.6 m/s, all the glass layers were severely damaged

and were broken into fragments propagating through the cabin (Figure 1.12 (a)) while skin fracture and penetration occurred on the leading edge of the wing (Figure 1.12 (b)).

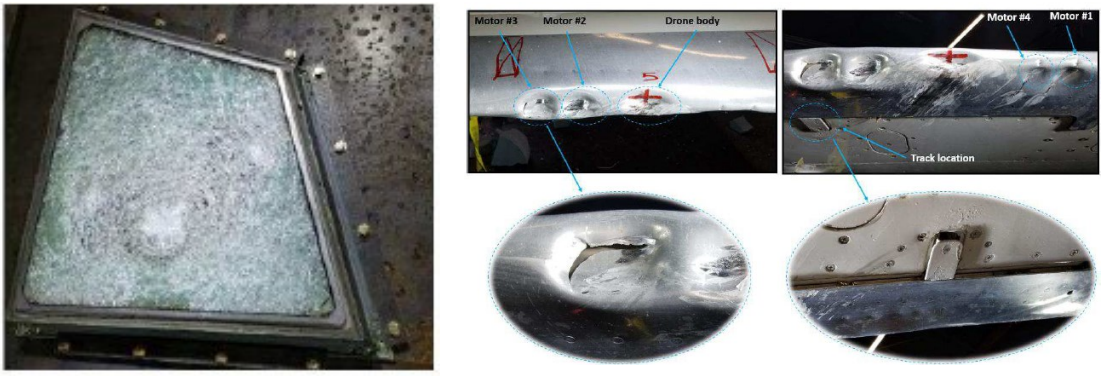

(a) (b)

Figure 1.12. (a) The damage occurred on (a) windshield and (b) wing after the drone collision (Source: Dadouche et al.[73])

In 2020, a study on the windshield of a helicopter subjected to both bird and drone impact was numerically carried out[74]. The impact velocity of the drone, DJI Phantom III, and bird, which had a mass of 1 kg, was selected to be 80 m/s that is the maximum speed for the helicopter in the cruise phase. It was found out that in both cases the windshield sustained severe damage (Figure 1.13), but in the drone impact event, the load concentrated where the component of the drone made contact with the windshield, and penetration then occurred. While, the bird impact caused the damage of the top parts of the windshield to which a clamped boundary condition was applied. After that the bird flowed over the surface of the windshield and released into the cockpit.

In 2020, the windshield of an aircraft was impacted by a different type of light drone to assess whether the existing regulations for the bird impact are valid for the drone impact or not[75]. To verification and modification of the numerical models, full-scale drone impact tests were also performed. Besides, numerical models for the bird strike scenario and the drone impact were established to observe the damage difference between them. To make a comparison of damages caused by the drone and the bird, special care was taken to ensure that their kinetic energies were the same. The mass of the drone and bird was 1.36 kg and 1.8 kg while their impact velocities were 152. m/s and 132.73 m/s, respectively. It was concluded that compared to the bird strike, more damage was induced to the windshield by the drone strike (Figure 1.14) and the maximum force value obtained

during the course of the impact was found to be more in the drone strike due to denser and harder components of the drone.

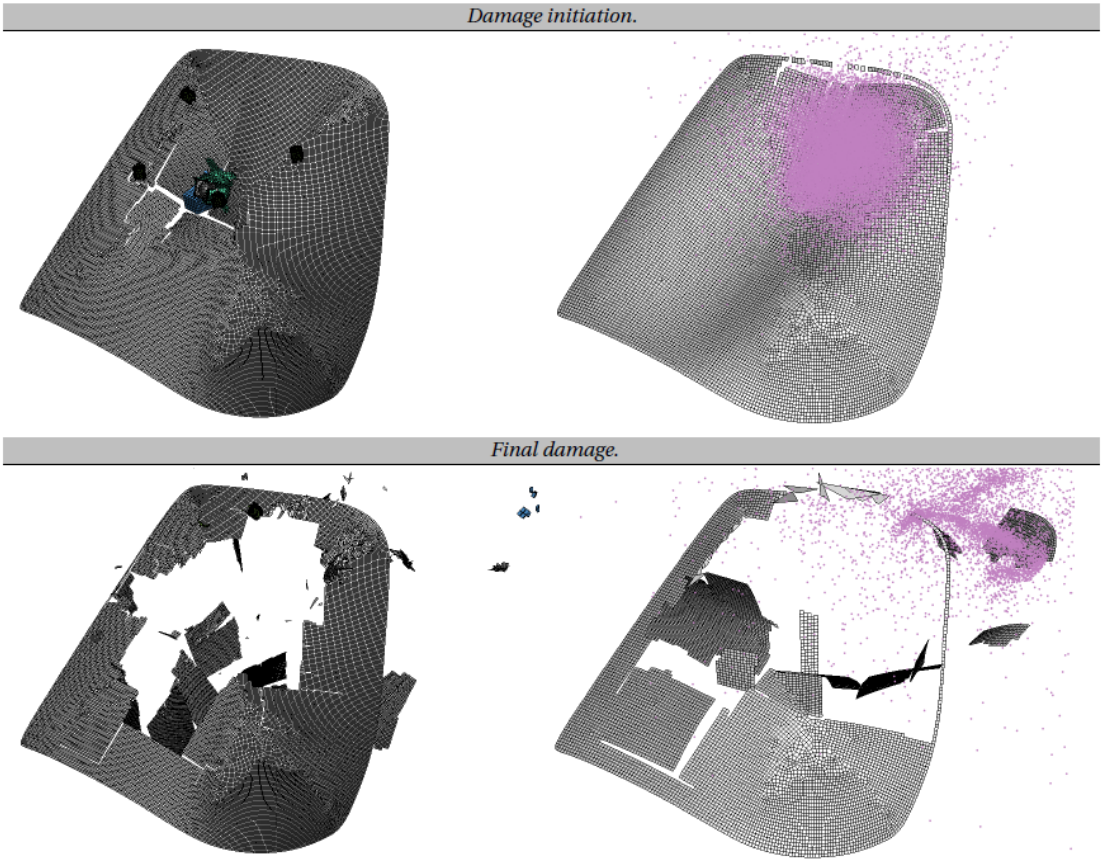

(a) (b)

Figure 1.13. Damage initiation and final damage results of the windshield obtained from (a) drone impact and (b) bird impact (Source: Jonkheijm[74])

In 2021, an experimental and numerical study on the collision between a 1.36 kg drone, Phantom 4, and an aircraft nose was performed by Lu et al.[76]. The structure also collided with a bird with a mass of 1.8 kg under the same condition to make comparison damages caused by both foreign object types. It was concluded that the structure sustained severe damage as impacted by the drone due to the hard components of the drone (motor, camera and battery) while the bird caused only the deformation of the structure and skimmed over the test component. Unlike the bird strike, the impact of the hard parts of the drone caused the structure to tear at the contact points and they penetrated through the structure (Figure 1.15).

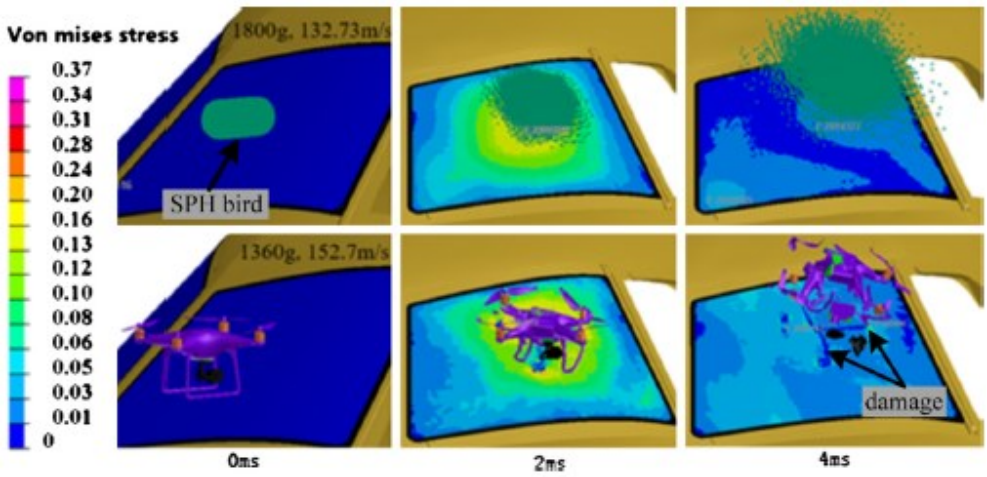

Figure 1.14. Damage caused by drone impact and bird strike

(Source: Lu et al.[75])

In 2021, a collision simulation between a drone categorized as harmless, which have a mass of 250 g, and an aircraft engine having titanium fan blades was established to assess whether the drone impact had an influence on the operation of the engine or not[77]. In addition to the impact of the harmless drone, the engine impacted by a drone with a mass of 0.75 kg was also examined to make a damage comparison. It was concluded that no damage was observed on the fan blades in the harmless drone impact simulations. While, the impact of the heavier drone resulted in the damage of the fan blades. Another numerical study on titanium fan blades impacted by drones of 0.5 kg, 1kg and 2 kg mass was performed by Sivakumar et al.[78]. Damage severity was investigated for different phases of the flight by selecting an appropriate impact speed and engine rotational speed i.e., rotational speed was varied from 3000 RPM to 5000 RPM while 145 knots, 200 knots and 250 knots were selected as the impact velocity. It was found out that as contact force exerted by the drone increased with increasing the rotational speed and impact velocity. In the critical case in which the engine with a rotational speed of 5000 rpm collided with a 2 kg drone at an impact velocity of 145 knots, it was observed that some fan blades were fractured and displaced. Another numerical study on the engine subjected to drone impact was performed to investigate the thrust loss after collision[79]. To assess damage severity, the effect of different factors such as collision configuration, position and flight phases was considered. The damage and thrust loss were found to be more as the drone collision occurred near the root of the fan blades of the engine. The collision was found to be more severe when the aircraft was impacted during the take-off phase.

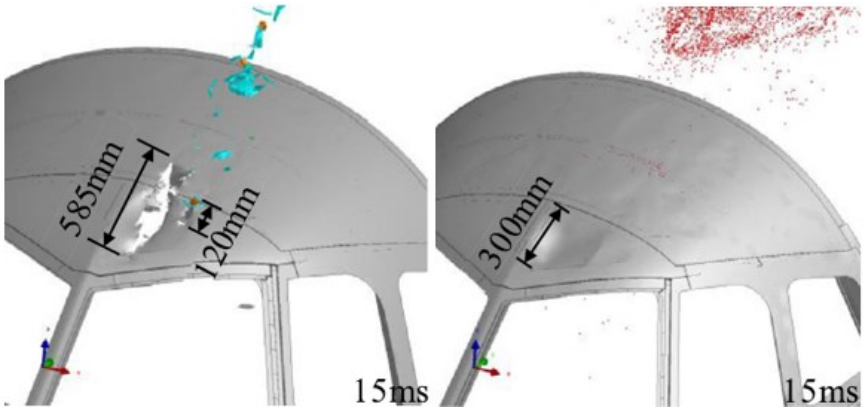

(a) (b)

Figure 1.15. Damaged structure after the collision (a) drone and (b) bird (Source: Lu et al.[76])

In 2021, a simulation of the windshield of a helicopter, which was impacted by two types of foreign objects, a drone and bird, was performed to observe and compare the damage caused by them[80]. The effect of the different parameters (the thickness and material type of the windshield and the impact velocity) on the damage performance of the windshield was also examined. It was found that as in the bird impact cases, the thinner and thicker polycarbonate windshields were not penetrated by both types of the drone at impact velocities considered. However, the increase in the thickness of the acrylic windshield did not improve its fracture performance since the drones and the birds penetrated through thinner and thicker acrylic windshields at all the impact velocities investigated.

In 2021, a report on the simulation of a wing leading edge subjected to single and multiple hits of drones with different weights as well as bird strikes was published[81]. It was reported that as the weight of the drone increased, the leading edge was penetrated, which caused the deformation of the spar. The damage in the leading edge was found to be more in the multiple impact case compared to the single impact case. Also, unlike in the bird strike, skin failure and penetration were observed in the impact event of the drone with the same weight.

In 2022, a radome made of quartz fibers and honeycomb core was impacted by a drone known as DJI Mavic 2 Zoom to investigate its damage resistance to drone collision[82]. It was concluded that the radome was penetrated when impacted by the drone

at lower velocities compared to the bird strike. However, at that impact velocity the bird flowed over the radome and no penetration occurred.

In 2022, a numerical study on the titanium fan blades of an aircraft engine was carried out to assess the damage severity of drones and birds [83]. The effect of the impact energy on the damage of the engine was examined by using drone (and bird) types in different weights. It was concluded that the severity of the damage increased with increasing rotation speed of the engine under the same impact velocity. Compared to the bird strike, the fan blades of the engine sustained severe damage. Also, the engine was damaged severely as impacted by the drone having a mass of greater than 1500 g. The position of the drone at the impact instant was found to be important since the collision position of 75% was reported to cause the highest damage severity among the impact positions examined.

In 2022, the collision severity of the wing leading edges and the windscreen of a helicopter under a drone impact was investigated through a numerical study[84]. The limit impact velocity for the perforation of the wing and windscreen was found to be about 80 m/s and 90m/s, respectively. A collision between the drone and wing at a velocity of 150 m/s resulted in the perforation of the wing spar. The skin sustained severe damage as impacted at the velocities between the limit velocity and 150 m/s. The boundary condition was found to play an essential role in the assessment of the damage severity since the clamped boundary condition caused the damage to concentrate along boundaries while the use of the real boundary condition resulted in center damage.

1.1. Aim and Scope of the Study

Although woven carbon fiber composites are used in many fields such as defense and aviation, literature review shows that few studies have been focused on the detailed mechanical characterization of the woven carbon composite. Thus, there needs to be fully validated and calibrated material models used in modeling carbon fiber composite using the shell element and solid element in finite element software, especially in LSDYNA, in the existing literature. Therefore, the first aim of the study is to accurately characterize the quasi-static and dynamic behavior of carbon fiber composite material through a series of quasi-static and high strain rate tests and to obtain the validated and calibrated material model parameters for the shell element and solid element. Also, from the previous studies

investigating the strain rate sensitivity of carbon composites, it has been found that there is strong debate on the rate sensitivity of the composite material, whether it is rate sensitive or not. Thus, the study aims to answer that question by performing quasi-static and high-strain rate tensile tests by means of the strain gages and DIC system.

The second aim is to numerically predict damage initiation and progression on the carbon composite structure subjected to foreign body impact, especially drone impact since the literature review shows that drone collision causes more severe damage to the components of an aircraft. In addition to that, according to the literature survey, there are many studies on metallic and glass components of the aircraft. Therefore, it is aimed to fill a gap in the literature by investigating the damage behavior of carbon composites subjected to drone impacts and bird strikes.

CHAPTER 2

EXPERIMENTAL METHODOLOGY

In this chapter, test methodologies, equipment and conditions were introduced. The required calculations to find the mechanical properties of carbon composite are also presented such as tensile, compressive and shear strength. Besides, to explore the effect of strain rate on the mechanical properties of carbon composite quasi-static and dynamic tests to be performed are presented. Test methodologies employed to examine the influence of foreign object damage such as ice impact and low-velocity impact on the behavior of the composite plate are explained.

2.1. Material

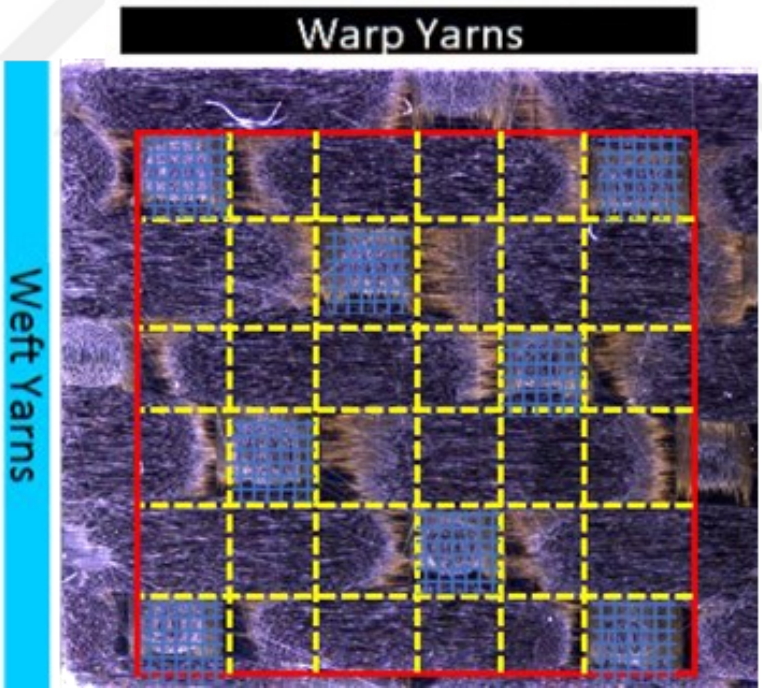

Figure 2.1. Top view of the five-harness satin weave carbon composite

In this study, a five-harness satin weave composite consisting of AS4-3K carbon fiber and epoxy resin was used. The woven architecture can be seen in Figure 2.1. There are two directions, which are the weft and warp directions. The weft direction represents 0-degree while the warp one is 90-degree. In the satin type, the weft fiber floats over four

warp yarns and under one. In the warp face, the warp fiber floats over the weft fibers while in the weft face the weft fibers floats over the warp fibers (Figure 2.2(a) and (b)).

The composite plates with different thicknesses were cured in an autoclave at a pressure of 7 bar and at a temperature of 180°C, and the process took 8 hours. The test coupons and/or specimens to be used in mechanical characterization and impact tests were further cut via a water jet and CNC router.

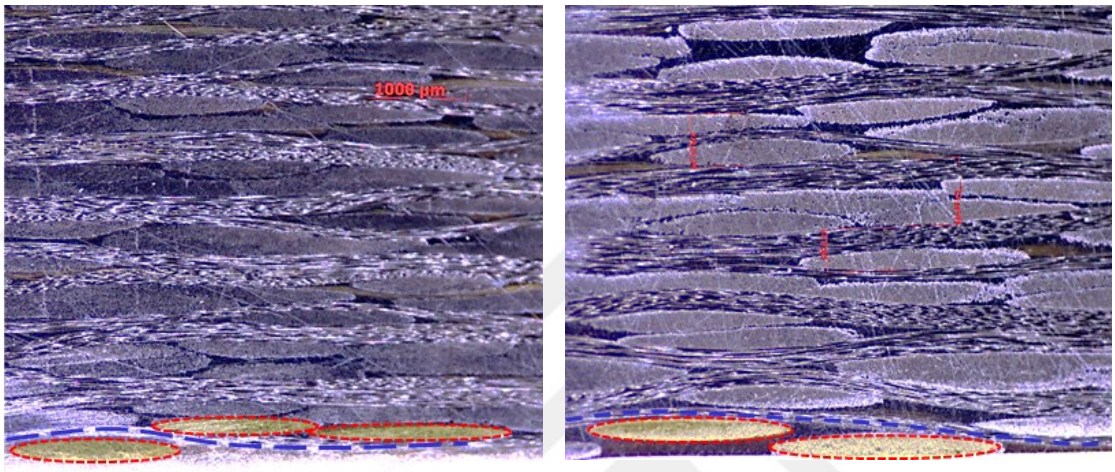

(a) (b)

Figure 2.2. (a) Warp face and (b) Weft face of the carbon composite

Figure 2.3 shows the optical image results. The average fiber diameter was calculated as 7.19 μm (Figure 2.3 (a)) and cured ply thickness was determined as 0.28 mm (Figure 2.3 (b)). In addition, the neat resin properties can be seen in Table 2.1.

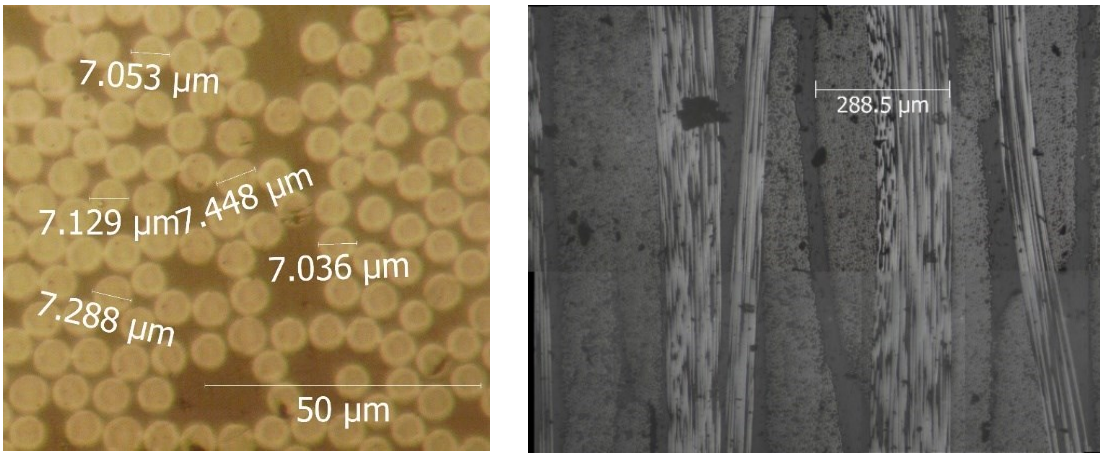

(a) (b)

Figure 2.3. (a) Average fiber diameter and (b) cured ply thickness

Table 2.1. The typical neat resin properties

(Source: HexPly [85])

Colour	Yellow
Density	1.301 g/cc
Glass Transition Temperature, T_g dry	200°C
Glass Transistion Temperature, T_g wet	154°C
Tensile Strength	121 MPa
Tensile Modulus	4670 MPa

2.2. Digital Image Correlation (DIC)

Ncorr[86], which is open-source digital image correlation MATLAB software, is used to determine displacement and strain fields within a region of interest (ROI) for a deformed material sample. It employs image processing techniques for this purpose. Basically, the reference picture (initial undeformed image) is divided into small subsections, referred to as subsets, and their respective locations in the current (subsequent deformed image) configurations are then calculated. Displacement and strain values are determined for each subset via the transformation employed to fit the subset's location in the current configuration. Finally, the grid including displacement and strain values relative to the reference configuration is obtained.

Equipment used in specimen preparation for DIC can be seen in Figure 2.4. The first step followed in the preparation of test samples for DIC is that the surface of the specimen is sanded using sandpaper with fine grit, and the sanded area is then cleaned by an industrial tissue or cloth. Thereafter, the surface is sprayed with white spray paint to obtain a white background on the sample. Random black speckle patterns are sprayed onto the white surface of the specimen by airbrush.

Figure 2.4. Equipment used in specimen preparation for DIC

2.3. Density and Volume Fraction Calculations

The Density and volume fraction of the composite were investigated in accordance with ASTM Test Methods. These test methods were explained in detail in the following sections.

2.3.1. Density Calculation

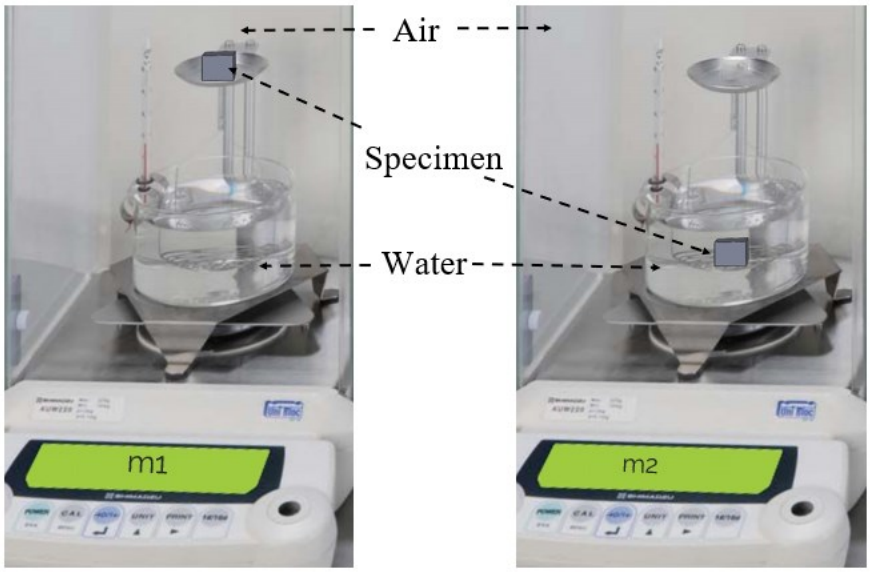

Figure 2.5. Density measurement system

ASTM D792-20[87] Standard Test Method was employed to determine the density of carbon composite. The measurement system used in density calculation can be seen in Figure 2.5. It consists of a mass measurement system, a glass crucible, suspension wire and fluid (water). Archimedes' principle is employed in this system. It is stated that when an object is immersed in water, the buoyant force on the object is equal to the weight of water displaced. The volume of water displaced by the object is therefore equal to the volume of the object. It is then employed to calculate the density of the object. Formulas used in the calculation are shown in Equation (2-1). All measurements were performed at room temperature. Three cubic samples with dimensions of 12.7x12.7x12.7 mm were weighted in air, and all samples were then immerged into water by means of a suspension wire. Following recording the mass of the samples, they were dried. Their masses were measured and re-recorded. The density of the composite was determined based on the recorded volumes and weights.

$$\rho_c = \left(\frac{m_1}{m_3 - m_2}\right)\rho_w \tag{2-1}$$

ρ_c = the density of the composite (g/cm^3)

m_1 = apparent mass of specimen, without wire or sinker, in air

m_2 = apparent mass of specimen (and of sinker, if used) completely immersed and of the wire partially immersed in liquid

m_3 = dried mass of the specimen after immersion

ρ_w = density of water, (1 g/cm^3)

2.3.2. Volume Fraction Calculation

The volume fraction of carbon composite laminates was determined by the acid digestion method according to ASTM D3171-15 (PROCEDURE-A)[88]. Cubic composite samples were cut 12.7x12.7x127 mm in size by waterjet, and three samples were prepared for volume fraction calculation. In this method, each sample was weighed and recorded, then they were placed into a separate glass crucible containing nitric acid. They were heated by a hot plate heater for at least 4 hours. After the matrix was fully digested, all samples were washed with distilled water to remove nitric acid, samples were then dried in an oven. Subsequent to being weighted and recorded all samples, percentage weight and volume fractions of the reinforcement material, which is carbon fiber, were calculated using the following formulas.

$$W_r(\%) = \frac{m_{initial}}{m_{fiber}}100 \tag{2-2}$$

$m_{initial}$ = initial mass of the sample

m_{fiber} = final mass of the sample after digestion

$$V_r\ (\%) = W_r(\%)\frac{\rho_c}{\rho_r} \tag{2-3}$$

ρ_r = density of the reinforcement, (1.79 g/cm^3) [89]

ρ_c = density of the specimen, g/cm^3

2.3.3. Tensile Tests

The in-plane and out-of-plane tensile properties of the composite were investigated according to ASTM standards. Also, the strain rate effect was examined by performing tensile tests at quasi-static and dynamic strain rates.

2.3.3.1. Standard Tensile Tests

Tensile tests were performed in accordance with ASTM 3039[2]. A Shimadzu machine equipped with a 300 kN load cell was used in these tests. Five composite samples were tested for each in-plane direction, namely warp and weft directions. End-tabs were not used, but emery cloth was placed on the interface between tensile specimens and the test grip instead. Furthermore, the crosshead velocity was set to 2 mm/min, and the gage length was selected as 50 mm. Extensometer markers were placed on tensile samples by considering the selected gage length. Strain gages were also attached in the middle of the samples to determine Poisson's ratio (ϑ_{12} or ϑ_{12}). Moreover, Young's modulus was calculated from the elastic region in the stress-strain curves drawn for those samples with extensometer markers and strain gages. Tensile strength for both warp and weft directions were calculated using the following equation.

$$F^{tu} = P^{max}/A \tag{2-4}$$

F^{tu} = ultimate tensile strength, MPa

P^{max} = maximum force before failure, N

A = average cross-sectional area, mm^2

In addition to the in-plane tensile test mentioned above, the through-thickness tensile test was conducted to determine the tensile properties of the composite in the through-thickness direction in accordance with ASTM D7291[90]. The dimension of the

tensile test specimen and the specimen to be tested can be seen in Figure 2.6. The specimen was adhered to aluminum shanks using epoxy adhesive, and a strain gage bonded on the test specimen to measure strain. The measured strain was further employed to determine the elastic modulus of the composite in the thickness direction. According to the test standard, the specimen was tested with a cross-head velocity of 0.1 mm/min. More information on the test procedure and calculations can be found in the related test standard.

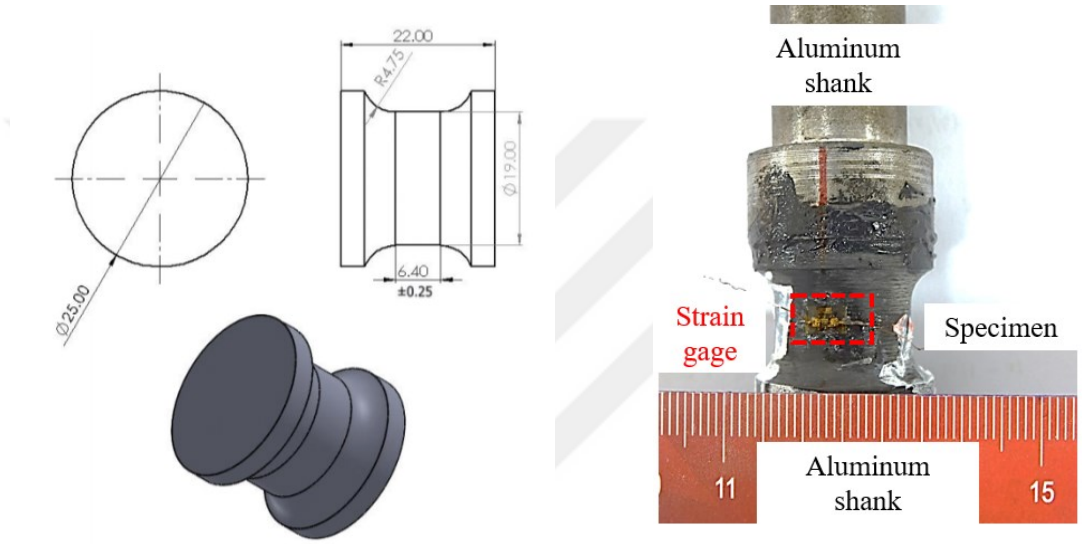

(a) (b)

Figure 2.6. (a) Dimensions of the through-thickness tensile test specimen and (b) the specimen prepared for test

2.3.3.2. Quasi-static Strain Rate Tests

Quasi-static behavior of carbon composite was investigated using Shimadzu testing device (Figure 2.7). In quasi-static tests, the composite specimen (Figure 2.8) was adhered to the steel fixtures by epoxy metal adhesive, it then fixed to the fixtures by bolts. During tensile tests, deformation of the composite was recorded to observe the damage within it during the loading and to calculate the strain distribution by Digital Image Correlation (DIC) method.

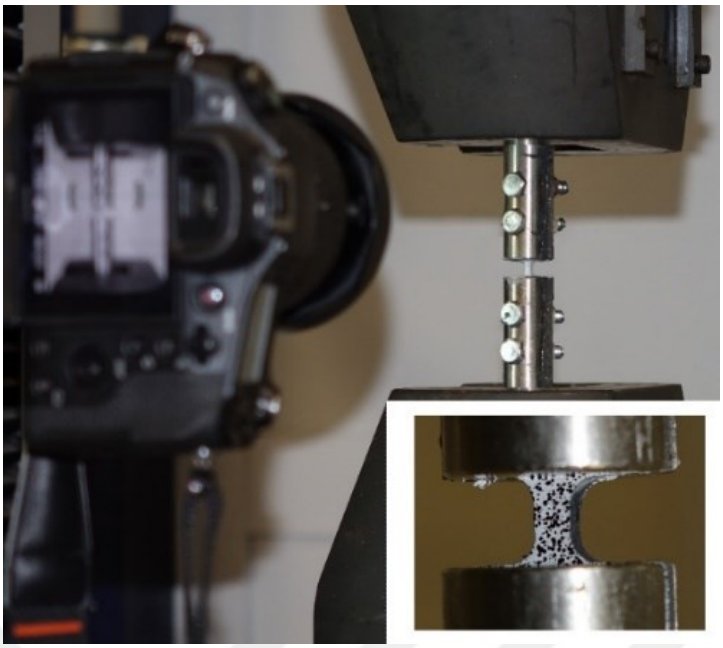

Figure 2.7. Quasi-static tensile testing system

The quasi-static tensile tests were performed at two different strain rates, namely 10^{-5} and 10^{-4} s^{-1}. The cross-head velocity of the machine corresponding strain rate was determined using Equation (2-5) ($\dot{\varepsilon}$ strain rate, V cross-head velocity and l_0 gage length). Displacement was measured by using a synchronized video extensometer and the machine stroke. It was also calculated from video record by using DIC method. The video extensometer markers were placed on the steel fixtures. The displacements calculated from the ways were then compared to each other.

$$\dot{\varepsilon} = \frac{V}{l_0} \tag{2-5}$$

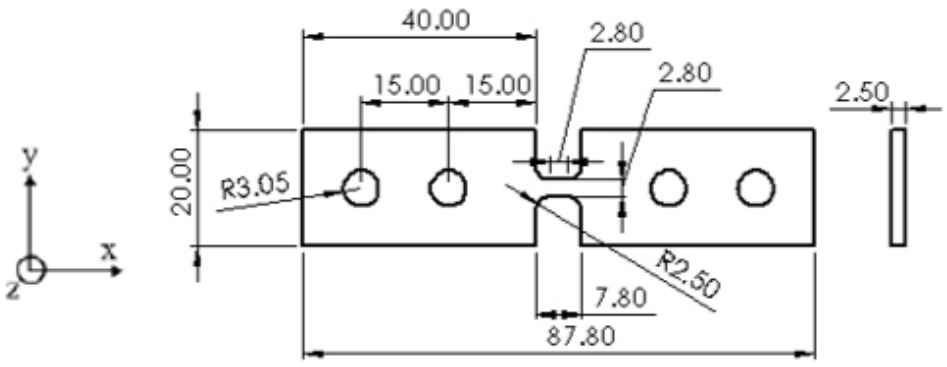

Figure 2.8. Quasi-static and dynamic tensile test specimen

2.3.3.3. High Strain Rate Tests

Split Hopkinson tensile bar (SHTB) is employed to load composite specimens at high strain rates. Figure 2.9 shows a picture of the bar system and test equipment. A high-speed video camera with a light source was used to record the deformation of tensile and shear test samples. Frames taken from the recorded videos were also employed to calculate the displacement and strain of samples by the DIC method.

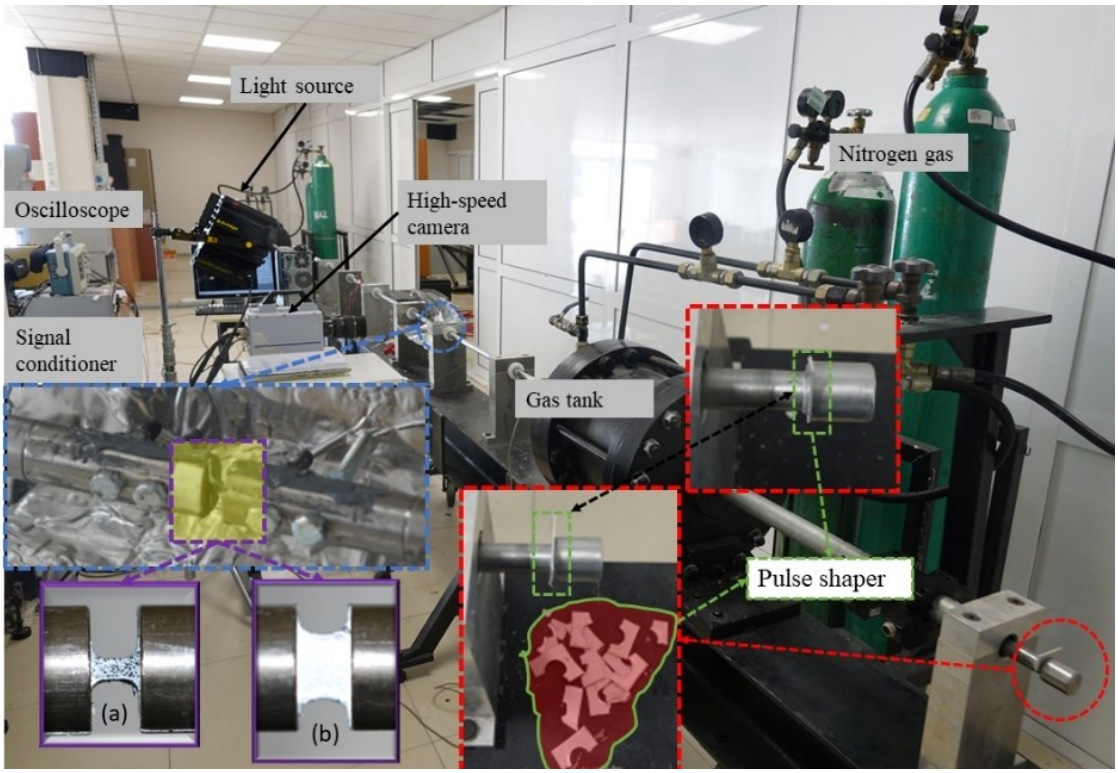

Figure 2.9. Tensile test of composite samples having (a) [0/90]n ply orientation and (b) [±45]n ply orientation

A schematic representation of the bar can be seen in Figure 2.10. The SHTB test system involves a striker tube, an incident bar, a transmitter bar, and a test specimen that is fixed to the incident and transmitter bars by using an epoxy adhesive and bolts. The bar material is 316 L whose density and elastic modulus are 7990 kgm^{-3} and 193 GPa, respectively.

The striker bar is propelled by the release of pressurized gas. A single elastic wave of tension is generated when the striker tube hits the anvil. It then propagates along the incident bar towards the specimen-incident bar interface. When the pulse reaches the

interface, some part of it reflects back through the incident bar as a compressive pulse, and the rest propagates along the transmitter bar. Using Equation (2-6), the stress and strain of a tensile specimen tested can be calculated.

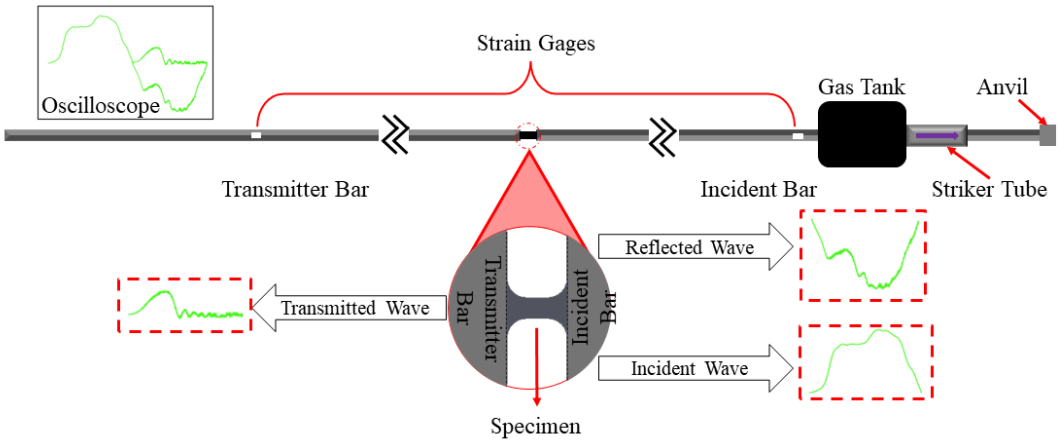

Figure 2.10. Schematic representation of split Hopkinson tension bar

$$\sigma_s = \frac{A_b E_b}{A_s}\varepsilon_t$$
$$\varepsilon_s = 2\frac{c_b}{l_0}\int_0^t \varepsilon_r dt \qquad (2\text{-}6)$$

where

σ_s , tensile stress of the composite sample,

A_b , cross-sectional area of the bar,

E_b , elastic modulus of the bar,

A_s , cross-sectional area of the specimen,

ε_t , transmitter strain, mm/mm

ε_s , tensile strain of the sample, mm/mm

c_b , wave-velocity of the bar,

l_0 , initial length (gage length) of the specimen,

ε_r , reflected strain, mm/mm

$[0/90]_n$ carbon specimen s were tested in two different in-plane directions, the weft and the warp directions, at two different strain rates. By the results obtained the strain rate

sensitivity of the carbon composite was investigated as well as deformation. Besides, pulse shapers with a thickness of 2 mm were employed so that the carbon test coupons were deformed at a nearly constant strain rate and in stress equilibrium. They were placed between the striker tube and the incident bar. By doing so, the pulse shaper was first crushed by the striker tube and then hit the anvil. Aluminum was selected as pulse shaping material, and dynamic tensile tests were performed at two strain rates by using one quarter and one-half pulse shapers. Pulse shapers used in tests and their position on the incident bar can be seen in Figure 2.9 (a).

2.3.4. Compression Tests

The in-plane compressive properties of the composite were investigated according to the ASTM standard. Also, the strain rate effect was examined by performing compression tests at quasi-static and dynamic strain rates.

2.3.4.1. Standard Compression Tests

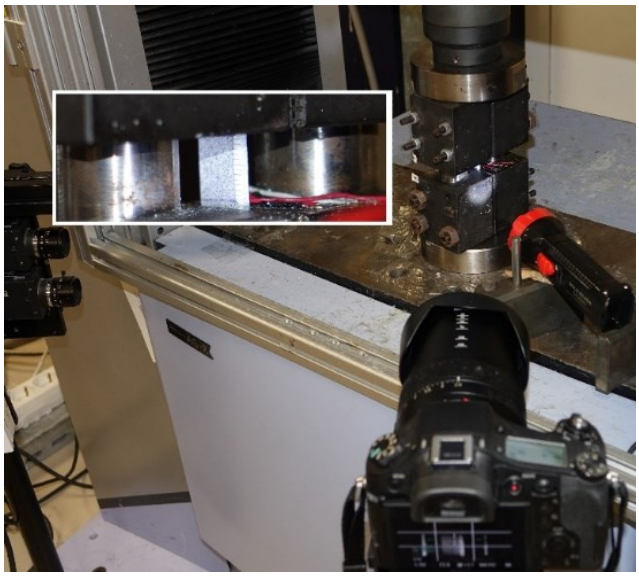

Figure 2.11. Compression Test

Standard compression tests (Figure 2.11) on samples in warp and weft directions were carried out according to ASTM 6641[56]. Five compression test coupons without end-tabs were tested for each direction. Strain gages were placed on the coupons to determine

Poisson's ratio while the elastic modulus was calculated from the stress strain curves generated using both strain gages and the Digital Image Correlation (DIC) system because of position of the video camera; the video camera was placed in an angled position rather than perpendicular to the coupon surface.

$$F^{cu} = \frac{P_f}{wh} \tag{2-7}$$

F^{cu} = laminate compressive strength, MPa

P_f = maximum load to failure, N

w = specimen gage width, mm

h = specimen gage thickness, mm

The crosshead displacement rate of 1.3 mm/min was utilized to fail the coupons under compressive loading. This load was transferred to the coupons in shear and end loading. That's why, this method is called as a combined loading testing method. Moreover, the failure mode, area and location of tested coupons were determined based on the three-part code defined by ASTM (Figure A.2). Compressive strength Equation (2-7) and modulus, Poisson's ratio, and strain-at-failure were determined by performing this standard test method.

2.3.4.2. Quasi-static Strain Rate Tests

The effect of quasi-static strain rates on carbon composites was investigated using cubic samples with dimensions of 10x10x10 mm at crosshead displacement rates of 10^{-3} mm/sec, 10^{-2} mm/sec and 10^{-1} mm/sec. Cubic samples were compressed in the warp, weft, and thickness directions. Besides, end-caps made of Inconel inserts were employed in compression tests to prevent the ends of samples in both warp and weft directions from splitting axially. Cubic specimens were inserted into these end-caps together with and without Bison epoxy metal adhesive. In this way, the effect of confinement on the splitting mechanism and compressive response of in-plane cubic samples was investigated. By this test, compressive strength and modulus of carbon composite were calculated at different quasi-static strain rates.

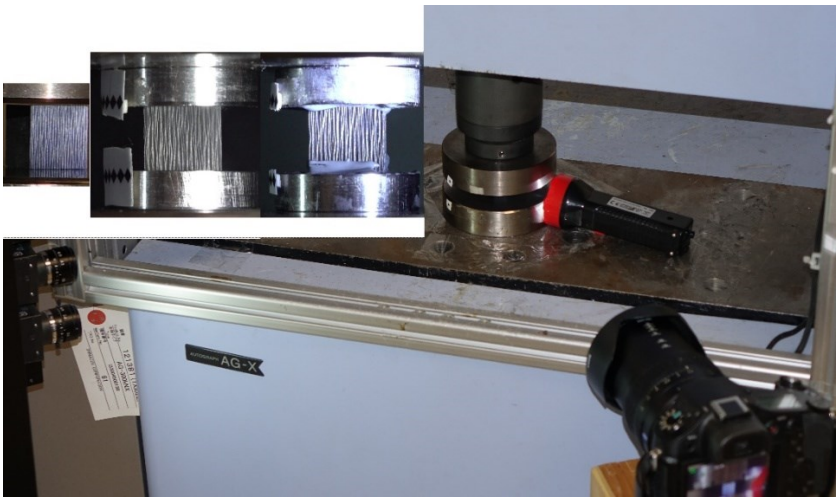

Figure 2.12. Quasi-static compression tests on cubic samples

2.3.4.3. Dynamic Compression Tests

Figure 2.13 show a schematic representation of the split Hopkinson pressure bar (SHPB). This testing method involves a gas gun, a striker bar that sits in the barrel, an incident bar and a transmitter bar. All the bars are of a diameter of 19.4 mm and made of Inconel having a density of 8394 kgm^{-3} and an elastic modulus of 204 GPa.

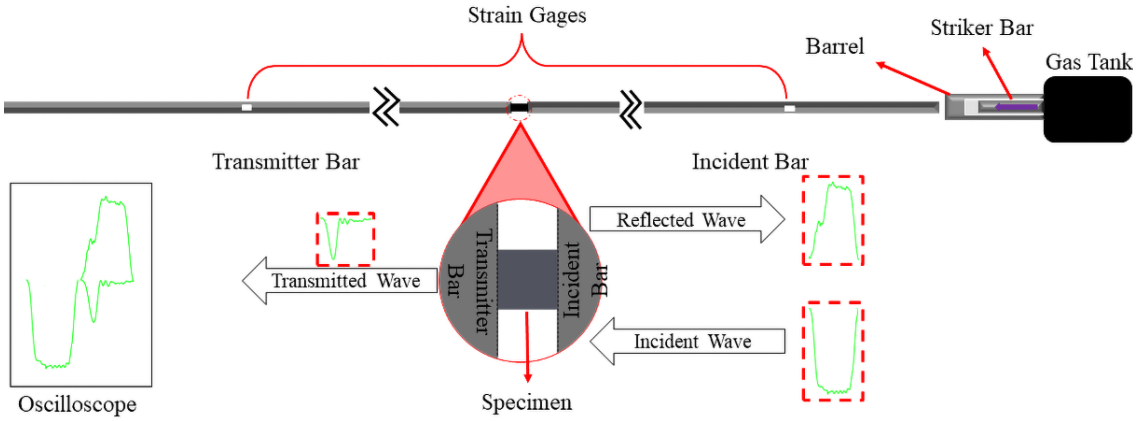

Figure 2.13. Schematic representation of split Hopkinson pressure bar

As shown in the figure above, the composite sample to be tested is placed and sandwiched between the incident and transmitter bar. After releasing the pressurized gas, the striker bar moves in the barrel towards the incident bar. When the striker bar hits the incident bar, a compressive elastic pulse, the incident pulse, occurs, and it propagates

throughout the incident bar. On reaching the interface between the specimen and the incident bar, some part of it reflects back along the incident bar, which is called as the reflected wave and the rest goes through the transmitter bar, which is called as the transmitted wave. By using strain gages attached to the incident and transmitter bars, elastic straining of the bars is obtained. The stress versus strain curve of the specimen is then determined by using the following equations.

$$\sigma_s = \frac{A_b E_b}{A_s}\varepsilon_t$$
$$\varepsilon_s = 2\frac{c_b}{l_0}\int_0^t \varepsilon_r dt \tag{2-8}$$

where

σ_s , compressive stress of the composite sample,

A_b , cross-sectional area of the bar,

E_b , elastic modulus of the bar,

A_s , cross-sectional area of the specimen,

ε_t , transmitter strain, mm/mm

ε_s , tensile strain of the sample, mm/mm

c_b , wave-velocity of the bar,

l_0 , initial length (gage length) of the specimen,

ε_r , reflected strain, mm/mm

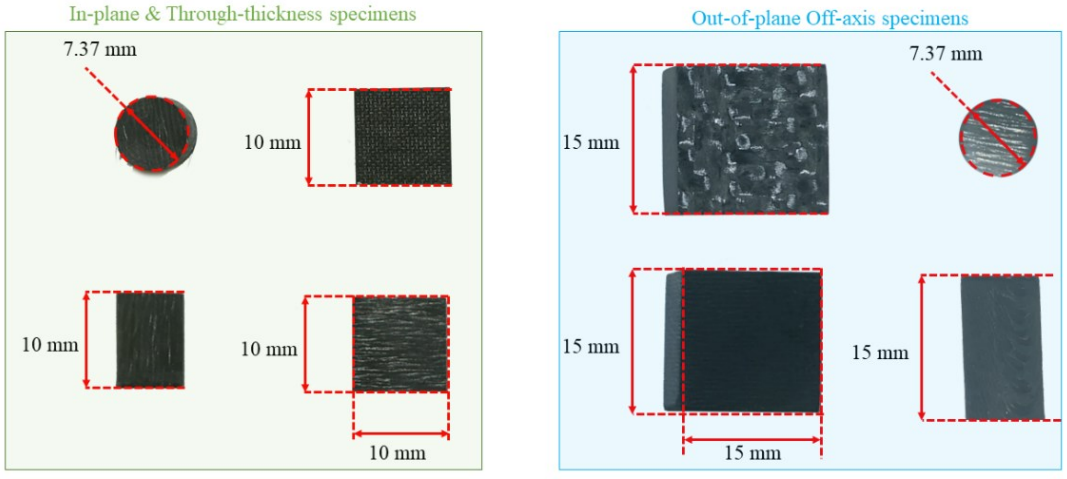

Figure 2.14. Cubic and cylindrical specimen dimensions

Cubic and cylindrical in-plane, through-thickness and out-of-plane off-axis composite specimens were tested at dynamic strain rates to investigate the influence of strain rate. In the testing of cubic composite specimens, the incident pulse was shaped by copper with a thickness of 1 mm and a square cross-sectional area of 25 mm^2. While, cylindrical composites were tested without using pulse shapers. The dimensions of cubic and cylindrical specimens can be seen in Figure 2.14.

2.3.5. Shear Tests

The in-plane shear properties of the composite were investigated according to the ASTM standard. In addition, the strain rate effect was examined. The related test methods were explained in the following sections.

2.3.5.1. Tensile Tests of ±45° Carbon Fiber Composite

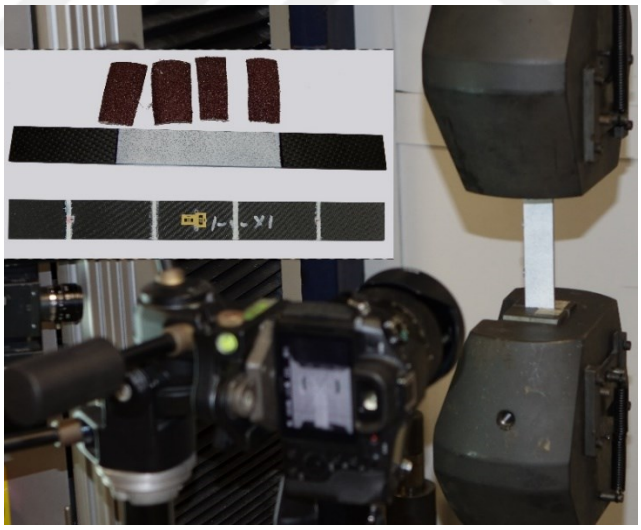

Figure 2.15. Tensile test of ±45° Carbon Fiber Composite

The in-plane shear properties were investigated using a standard test method covered by ASTM D3518[60]. Tensile test coupons of carbon composites with a fiber orientation of ±45-degree were tested at a displacement rate of 2 mm/min. The dimensions of the coupon were the same as those used in tensile tests. Longitudinal and transverse strains were monitored using strain gages to calculate shear strain. Strain gages

attached on a test coupon, extensometer system, video camera as well as loading system are shown in Figure 2.15. Besides, the deformations of test coupons were recorded to determine shear strain by digital image correlation (DIC), and shear strains calculated from DIC were verified by those obtained from strain gages. Briefly, in this testing method, a uniaxial tensile load is applied to the composite test specimen, shear stress and strains at failure are then calculated using the following equations based on Mohr-Coulomb theory or by Mohr's circle.

$$\tau_{12} = \frac{P}{2A} \quad , \quad \sigma_a = \frac{P}{A} \tag{2-9}$$

P = maximum load, N

A = cross-sectional area , mm^2

σ_a = axial stress, MPa

$$\gamma_{12} = \varepsilon_x - \varepsilon_y \qquad \varepsilon_{12} = \frac{\gamma_{12}}{2} \tag{2-10}$$

γ_{12} = engineering shear strain, mm/mm

ε_x = longitudinal normal strain, mm/mm

ε_y = lateral normal strain, mm/mm

ε_{12} = engineering strain, mm/mm

2.3.5.2. Quasi-static Strain Rate Tests

The shear strength of the carbon composite was investigated at different quasi-static strain rates by non-standard testing method. Compared to the test coupon specified in ASTM D3518 the coupons in this test were smaller in size and had two notches, one at each side. BISON epoxy adhesive was employed to adhere test coupons to the testing fixture, it was then connected to the grips. The fixed fixture together with a test coupon and video camera are depicted in the following figure while, the test fixture, composite sample and BISON epoxy metal adhesive for bonding can be seen in the inset figure. The tensile load was applied to coupons at crosshead velocities of 0.112 mm/min and 1.12

mm/min corresponding to 10^{-5} s^{-1} and 10^{-4} s^{-1} strain rates. From this test, shear strength and shear strain were calculated at different quasi-static strain rates. DIC was also used to calculate shear strain and to monitor the deformation of composite test specimens.

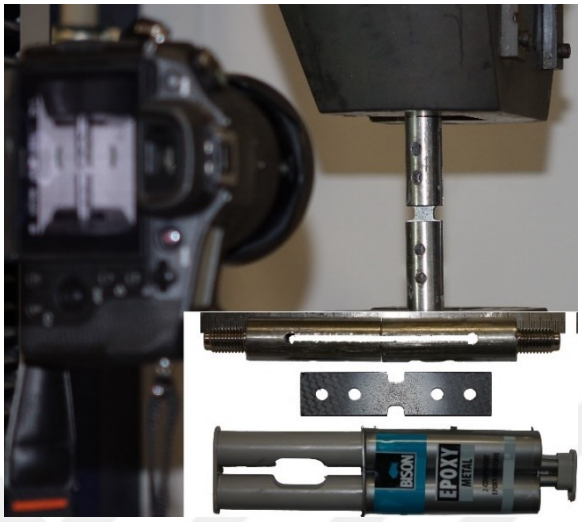

Figure 2.16. Quasi-static shear test equipment and specimen

2.3.5.3. High Strain Rate Tests

The shear properties of the carbon composite at high strain rates were investigated by applying tensile loads to $[\pm 45]_n$ carbon specimens in the split Hopkinson tension bar (Figure 2.9 (b)). Unlike tensile tests of $[0/90]_n$ composites, the incident pulse was not shaped in $[\pm 45]_n$ carbon specimen tensile tests, and tests were performed at just one dynamic strain rate. Shear stresses were calculated according to the following equation while shear strain and shear modulus were calculated by the DIC method.

$$\sigma_s = \frac{A_b E_b}{2A_s} \varepsilon_t \tag{2-11}$$

where

σ_s , in-plane shear stress of the composite sample,

A_b , cross-sectional area of the bar,

E_b , elastic modulus of the bar,

A_s , cross-sectional area of the specimen,

ε_t , transmitter strain, mm/mm

2.3.5.4. V-Notched Beam Test Method

The interlaminar shear strength of the carbon composite was determined by the v-notched beam method in accordance with ASTM 5379[91]. Test equipment and v-notched beam composite coupon can be shown in Figure 2.17. There are two identical parts of the test fixture which are fixed and moving. The former limits the translational and rotational movement of a composite beam while the latter moves along the bearing post. The compressive load is transferred from the moving halve to the composite beam as the shear load.

By the application of compression force to the moving part, pure shear stress is obtained in the region between the notch roots of a composite beam. The moment is, therefore, zero at that region. This can be shown in the diagram of shear force and bending moment diagram. These diagrams are depicted in Figure A.3. According to the test standard, crosshead velocity was set to 2 mm/min. Two strain gages in an orientation of ±45° were placed between the notch roots of the composite beam to calculate shear strain and shear modulus. The DIC measurement system was also employed in these calculations. Failure of composite beams was identified according to failure codes defined by the ASTM standard. These failure codes can be found in Figure A.4.

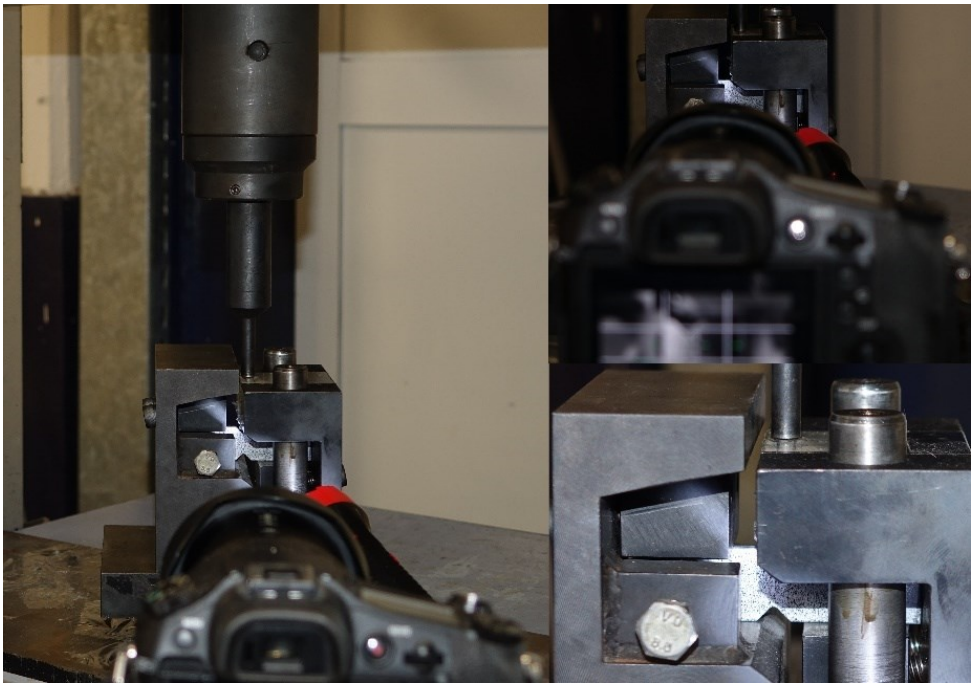

Figure 2.17. V-notched shear test fixture and specimen

Shear stresses ($\tau_{13}\ and\ \tau_{23}$) and shear strains ($\gamma_{13}\ and\ \gamma_{23}$) were calculated using the following equations. Shear moduli ($G_{13}\ and\ G_{23}$) were determined from these shear stress strain curves generated.

$$\tau = \frac{P}{A} \quad , \quad A = bw \tag{2-12}$$

τ = shear strength, MPa

P = maximum load, N

A = cross-sectional area, mm^2

w =coupon width (between notch roots), mm

h =coupon thickness, mm

$$\gamma = |\varepsilon_{+45}| + |\varepsilon_{-45}| \tag{2-13}$$

γ = engineering shear strain, mm/mm

ε_{+45} = + 45° normal strain, mm/mm

ε_{-45} = −45° normal strain, mm/mm

2.3.6. Elastic Constant Determination Test

To calculate Poisson's ratios ($\vartheta_{31}\ and\ \vartheta_{32}$) and Elastic modulus ($E_3$) as well as failure strain elastic constant determination tests, which is a non-standard test method, were performed. Cubic samples with the size of 12.7x12.7x12x7 mm were subjected to compressive loading at different displacement rates (0.0127 mm/sec, 0.127 mm/sec and 1.27 mm/sec) to investigate strain rate effects. Three strain gages were attached on the cubic samples loaded along the thickness direction to record strains in loading direction and transverse directions (strains in warp and weft directions). Besides, in some tests, DIC speckle patterns were painted on samples instead of strain gages to monitor their deformation and to determine Poisson's ratio. The tests were recorded by two video cameras simultaneously.

Test equipment can be seen in Figure 2.18. Stress, transverse strain, and axial strain curves were generated from these recorded data. Using transverse strain versus

axial strain curves a region was selected between 0.01 and 0.06 axial strain, that region was then fitted linearly. After that, Poisson's ratio was calculated from the intercept value of obtained linear fit equation. In the same way, the elastic modulus was also determined from the stress versus axial strain curves generated.

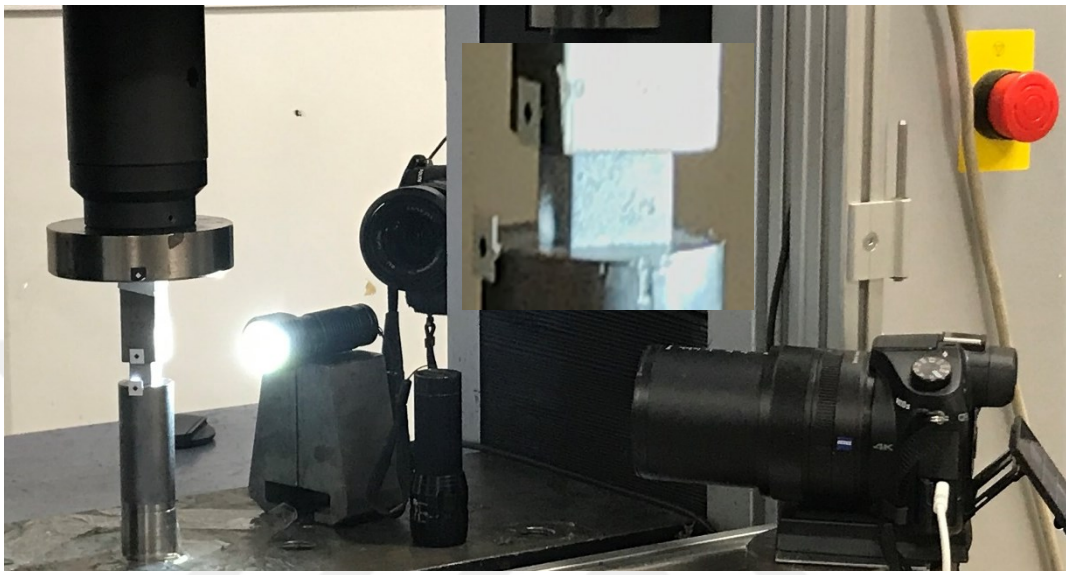

Figure 2.18. Elastic constant determination test equipment

2.3.7. Laterally Constrained Compression Tests

Fiber crush strength, fiber shear strength and frictional coefficient were determined by laterally constrained compression test on cubic composite samples with 12.7x127.7x12.7 mm in dimension. This method is a non-standard testing method, and more detailed information can be found in the study performed by Parkow et al[92]. The test fixture consists of two parts, namely a fixed hardened steel jig that constrains cubic samples laterally during compressive loading and a hardened steel pillar that transfers the applied force from the load cell of the device to samples. Test equipment and test fixture can be seen in Figure 2.19.

Tests were performed at different crosshead velocities, namely 0.00127 mm/sec, 0.0127 mm and 0.127 mm/ sec to determine the effect of strain rate on the aforementioned material properties. Through-thickness cubic samples placed within the test fixture were compressed until failure. Due to lateral confinement of samples during loading, failure occurred a shear plane through the material. The normal and shear stress components on that shear plane as well as fiber crush strength were calculated as follows,

$$S_{FC} = F_{max}/A \tag{2-14}$$

S_{FC} = Fiber crush strength, MPa

A = cross-sectional area, mm

F_{max} = the peak force, N

$$S_N = S_{FC}\cos^2\theta \ , \ S_{NFS} = \frac{1}{2}S_{FC}\sin 2\theta \tag{2-15}$$

S_N , S_{NFS} = the normal and shear stress component

θ = failure plane angle, degree

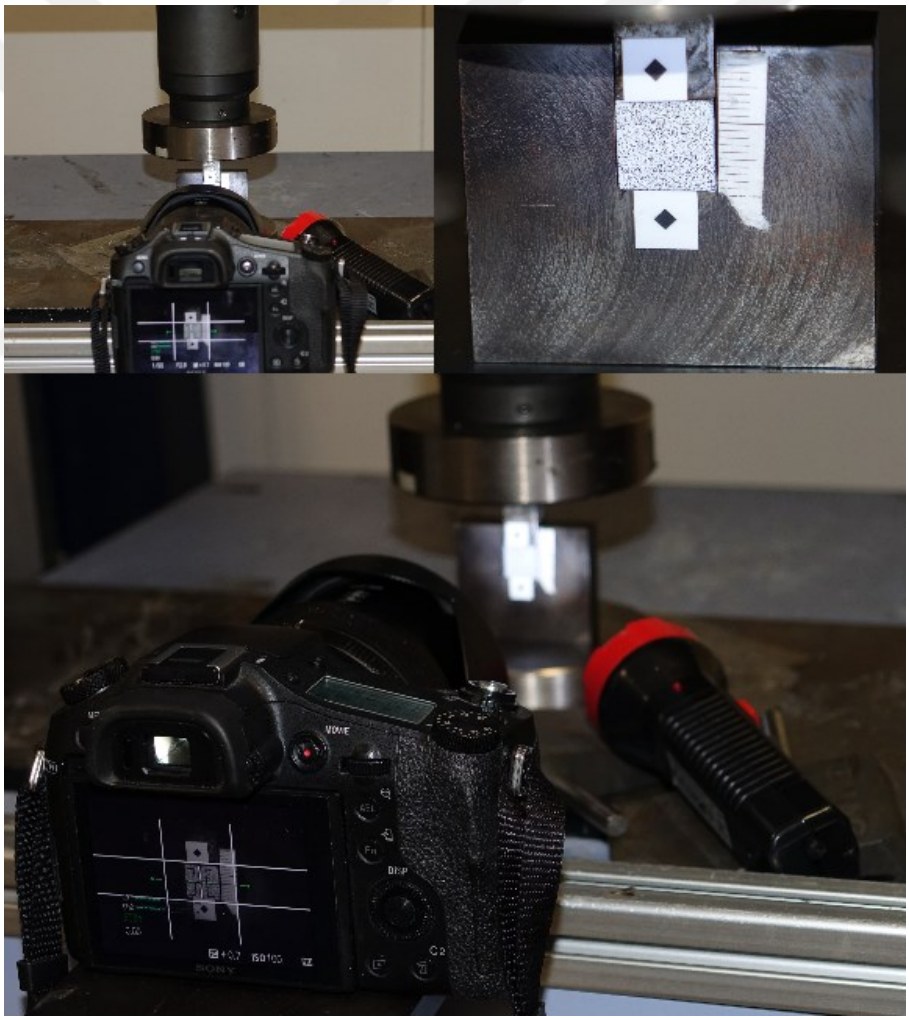

Figure 2.19. Laterally constrained compression test equipment and specimen

The relation between these stress components and fiber shear strength can be seen in the following figure.

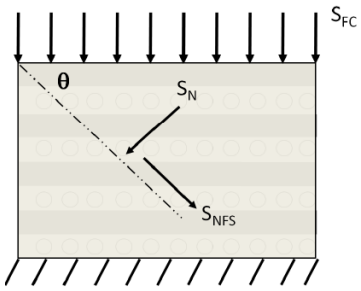

Figure 2.20. Shear failure planes (Source: Pankow and Yen[92])

Fiber shear strength was calculated from Mohr's circle transformation by considering the fact that one of the principal stresses is S_{FC} while the other is 0 and the following equations.

$$S_{FS} = S_{NFS} + \mu S_N$$
$$\mu = tan(\emptyset) \quad (2\text{-}16)$$
$$\emptyset = 90 - 2\theta$$

μ = friction coefficient

$\emptyset$ = friction angle, degree

2.3.8. Out-of-plane Off-Axis Compression Tests

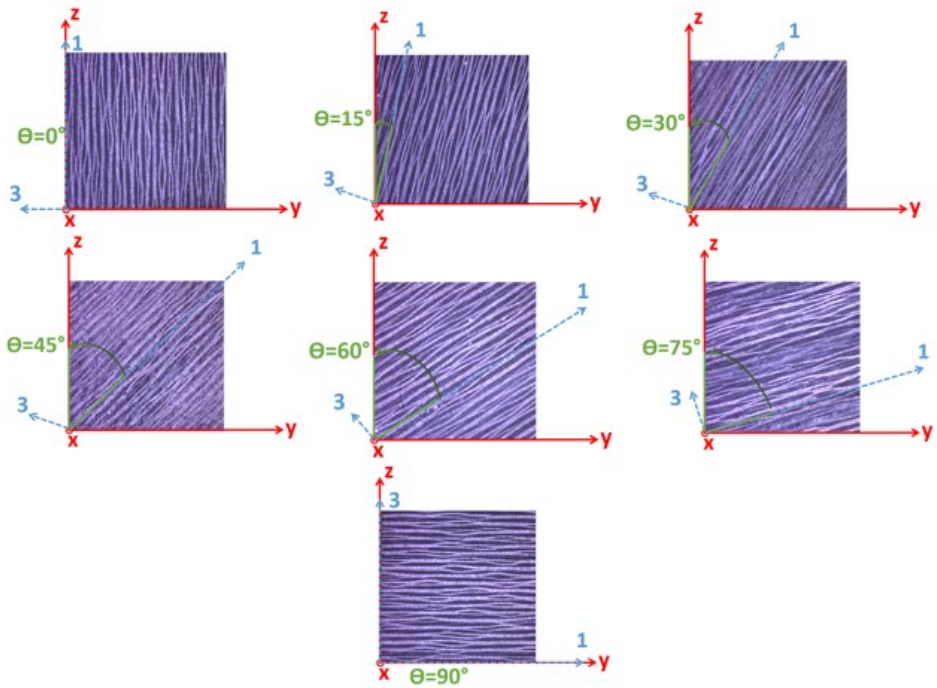

Figure 2.21. Cubic samples to be tested in different out-of-plane direction

Another non-standard testing method is the out-of-plane off-axis compression test. The tests were performed to determine the interlaminar shear strength and Coulomb friction factor of composite laminate. By using this testing method, Gillispie et al.[93] investigated the interlaminar shear strength and Coulomb friction factor of S2-glass composite material. More detailed information about the methodology can be found in that study.

To determine interlaminar shear strength in the 1-3 plane, composite samples were rotated around the y-axis. Figure 2.21 depicts cubic samples to be tested in the out-of-plane directions of 0°,15°, 30°, 45°, 60°,75° and 90°. These samples with dimensions of 15x15x15 mm were first sandwiched between two hardened steel pillars, compression loads with crosshead velocities of 0.0015 mm/sec, 0.015 mm/sec and 0.15 mm/sec were then applied to them by means of the top pillar.

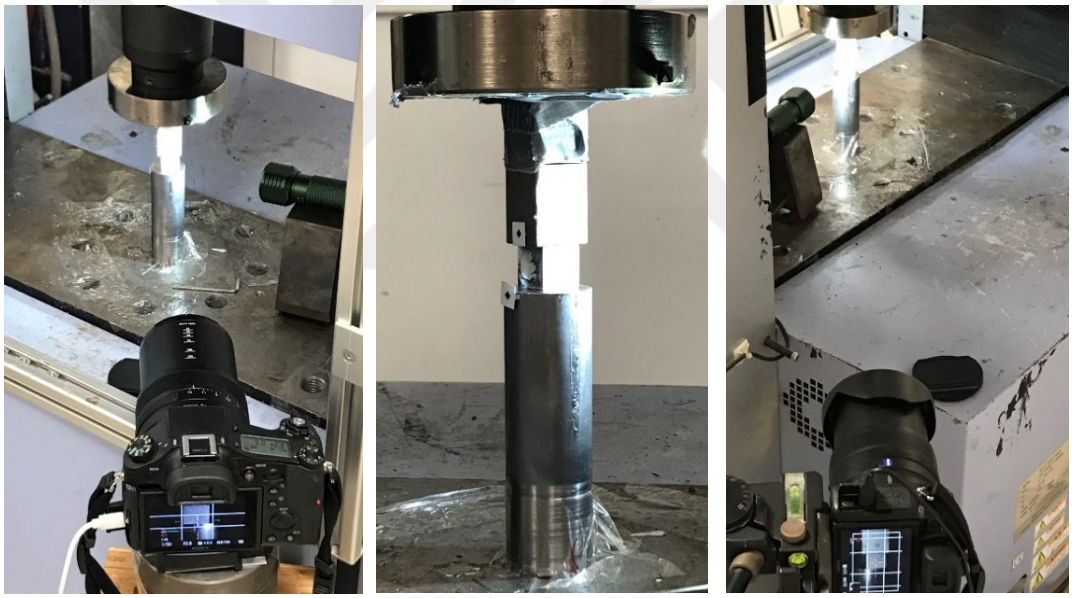

Figure 2.22. Out-of-plane off-axis compression test system (a) camera-1, (b) specimen, and (c) camera-2

Extensometer markers were placed on these pillars to measure the displacement of samples. By using two video cameras the deformation of test specimens was recorded during tests (Figure 2.22). These recorded videos were also used for DIC measurement to measure the displacements and strains on both faces of cubic composite, which are perpendicular to warp and weft directions. For each out-of-plane loading direction three samples were tested at each quasi-static strain rate. After all tests were performed, failure stress values were calculated for each strain rate and each loading direction. Stress values

in the corresponding plane were then calculated using stress transformation equations, as shown below.

$$\sigma_1 = \sigma_z \cos^2(\theta) \tag{2-17}$$

$$\sigma_3 = \sigma_z \sin^2(\theta) \tag{2-18}$$

$$\tau_{13} = \sigma_z sin(\theta) cos(\theta) \tag{2-19}$$

σ_z = maximum stress, MPa

The calculated interlaminar shear stress values (τ_{13}) and transverse stress values (σ_3) were fitted with a linear equation Then interlaminar shear strength and Coulomb friction factor were calculated by equating the following equation to the obtained linear fit equation.

$$\tau_{13} = S_{130} + \sigma_3 tan(\varphi) \tag{2-20}$$

φ = The Coulomb's friction angle

S_{130} = reference interlaminar shear strength, MPa

2.3.9. Quasi-static Punch Shear Tests

Quasi-static punch shear test method was found by the University of Delaware Center for composite materials to calculate the fiber shear strength of composites[94]. The parts of test fixture can be seen in Figure 2.23. They are the top and bottom support rings, punch, bottom support and cover plate. Two different bottom support rings are available to obtain different support span-to-punch ratios (SPR), such as SPR=1.1 and SPR=2.0. SPR is defined as the ratio of the support span diameter to punch diameter. To achieve SPR=1.1, a bottom support ring with a central circular hole of 8.36 mm and a punch with a diameter of 7.6 mm while the same punch and a bottom support ring with a circular hole of 15.2 mm are used for SPR=2.0. Quasi-static punch shear strength was calculated from SPR=1.1 at quasi-static strain rates of 10^{-4} s^{-1}, 10^{-3} s^{-1} and 10^{-2} s^{-1} while it was determined

for SPR=2.0 at only one strain rate of 10^{-3} s^{-1}. The equation used in calculation of fiber punch shear strength (FPS) is as follows.

$$\text{FPS} = {}^{F_{PEAK}}/_{A_{PLUG}} \text{ , } A_{PLUG} = \pi D h_{plug} \tag{2-21}$$

F_{PEAK} = the peak load, N

D = punch diameter, mm

h_{plug} = Plug thickness, mm (h_{plug}=h_{sp}-h_{lip})

h_{sp} = Specimen thickness

h_{lip} = lip thickness

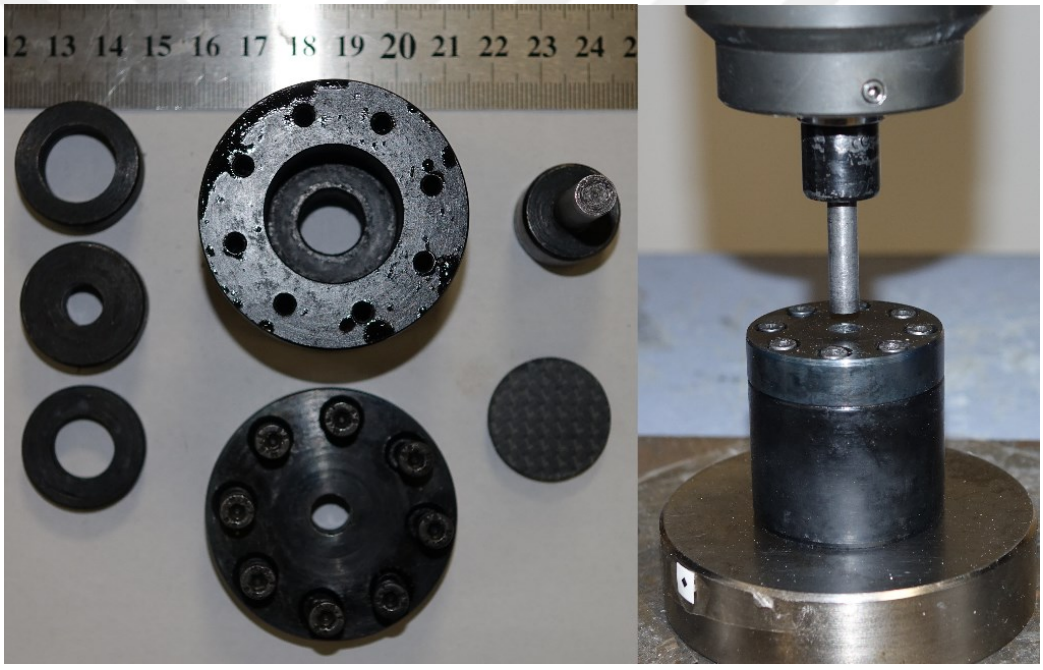

Figure 2.23. Quasi-static Punch Shear test fixture

2.3.10. Flexural Tests

The flexural strength of the carbon composite was determined from the three-point bending test in accordance with ASTM D790[95]. Carbon composites were tested until fracture occurred in the outer surface subjected to tensile loading. In Figure 2.24 a failed test coupon can be seen. The dimension of composite coupons is 127 mm in length, 12.7 mm in width and 3.2 mm in thickness. A support span-to-thickness of 16 was selected,

and the span distance was set to 50 mm. Crosshead velocity was calculated from Procedure A expressed in ASTM D790 standard test method. For a support span length of 50 mm, it was calculated as 1.3 mm/min. Bending stress and bending strain were determined using the following equations.

$$\sigma_f = \frac{3PL}{2bd^2} \tag{2-22}$$

σ = stress in the outer fibers at midpoint, MPa

P = load, N

L = support span, mm

b = width of beam tested, mm

d = depth of beam tested, mm

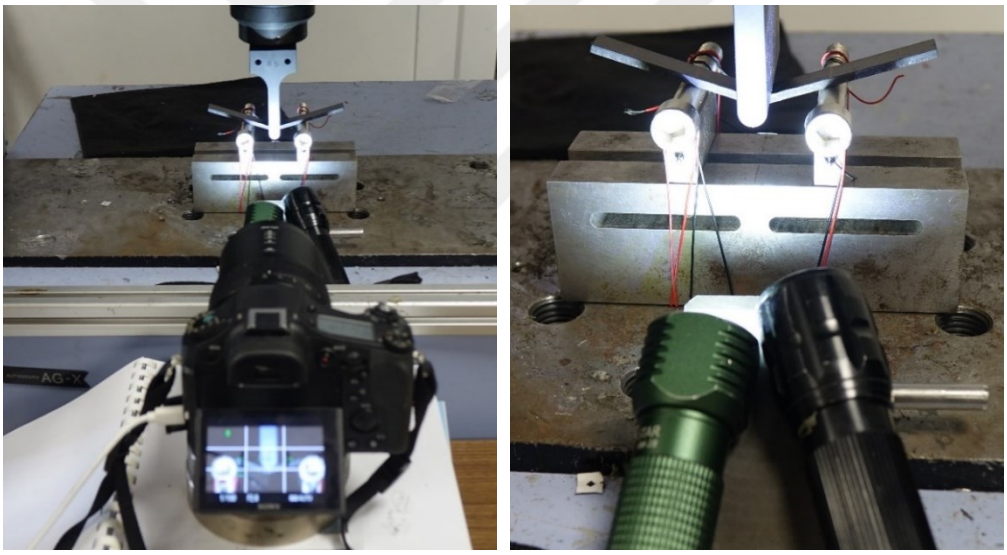

Figure 2.24. Flexural test fixture

$$\varepsilon_f = \frac{3Dd}{L^2} \tag{2-23}$$

ε = strain in the outer surface, mm/mm

P = maximum deflection of the center of the beam, mm

L = support span, mm

d = depth of beam tested, mm

2.3.11. Open-Hole Tests

Open-hole tensile (Figure 2.25) and compression (Figure 2.26) tests are performed to investigate the influence of a notch on the mechanical properties of carbon composite. It is also used to calculate one of the material constants of the Material Model 162 card in the LSDYNA finite element code, which is scale factor residual compressive strength.

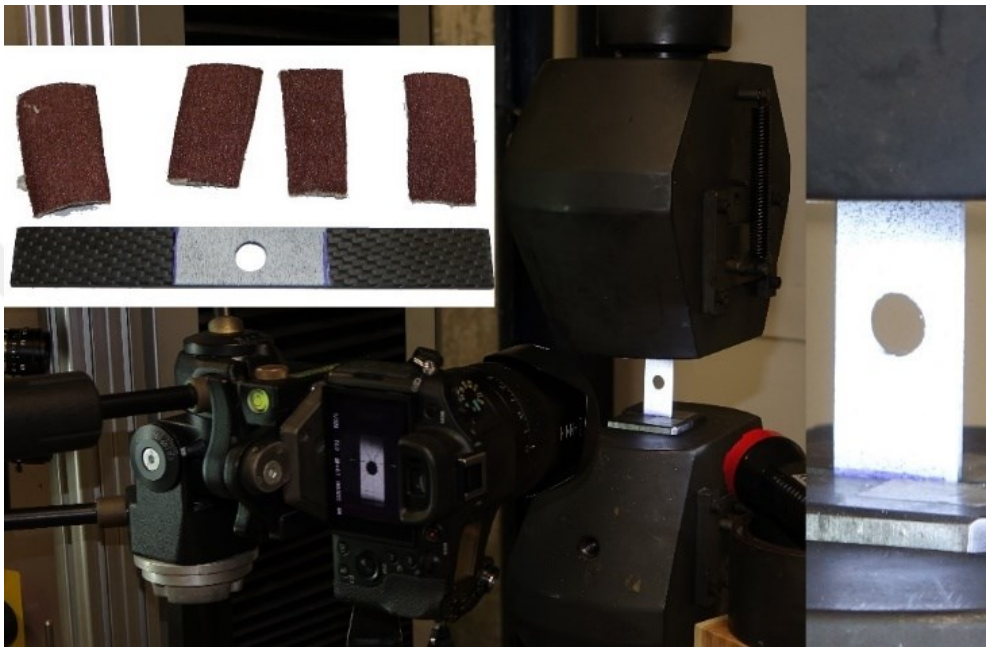

Figure 2.25. Open-Hole Tensile Tests

Both open-hole tensile and compression tests were performed at different crosshead velocities to examine the loading rate. In the former one, displacement rates of 0.5 mm/sec and 2 mm/min were employed while the latter one was carried out at crosshead velocities of 0.5 mm/sec and 1.3 mm/min. One of the crosshead velocities of open-hole tensile and compression tests was selected as the same that used in the standard tensile and compression tests, respectively. Strength reduction for both open-hole tests was calculated using the following equation.

$$SFR = \frac{\sigma_{notched}}{\sigma_{unnotched}} \tag{2-24}$$

SFR = strength reduction factor

$\sigma_{notched}$ = notched strength, MPa

$\sigma_{unnotched}$ = unnotched strength, MPa

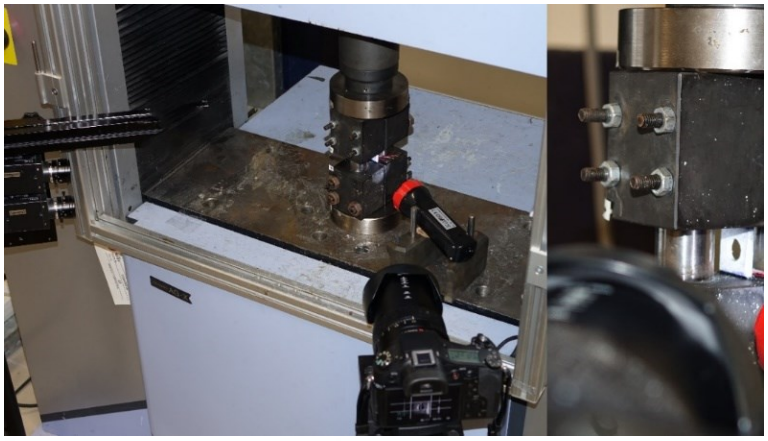

Figure 2.26. Open-Hole compression tests

2.3.12. Ice Impact Tests

The mechanical behavior of carbon composite subjected to single or multiple ice impacts was investigated by using a modified split Hopkinson pressure bar testing device.

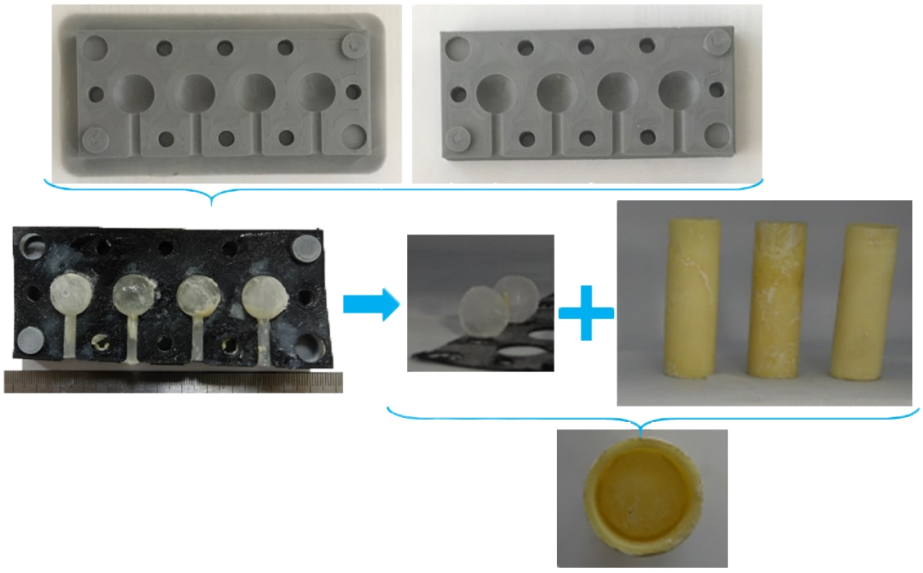

Figure 2.27. Manufacturing steps followed in the production of ice

In the production of the ice with a diameter of 16 mm, a polylactic acid (PLA) mold created by a 3D printer was employed. The mold and the pictures taken from the production steps of ice can be seen in Figure 2.27.

The mold consists of two parts. Each part has four cavities having the same diameter and eight holes to fix the parts of the mold each other by bolts. Also, each part has four small holes to fill water into cavities of the mold. A thermoplastic polyurethane (TPU) layer is employed between the two parts of the mold as a water leakage prevention layer.

The steps followed in the production of ice was listed as follows.

- applying Wax to the cavities into the mold for easy separation of ice from the mold,
- placing a TPU layer between the halves of the mold,
- fixing bolts,
- filling water into the cavities,
- holding the mold in the freezing of a refrigerator for an hour,
- removing of the ice from the mold,
- keeping the ice in the freezing for nearly twenty-four hours.

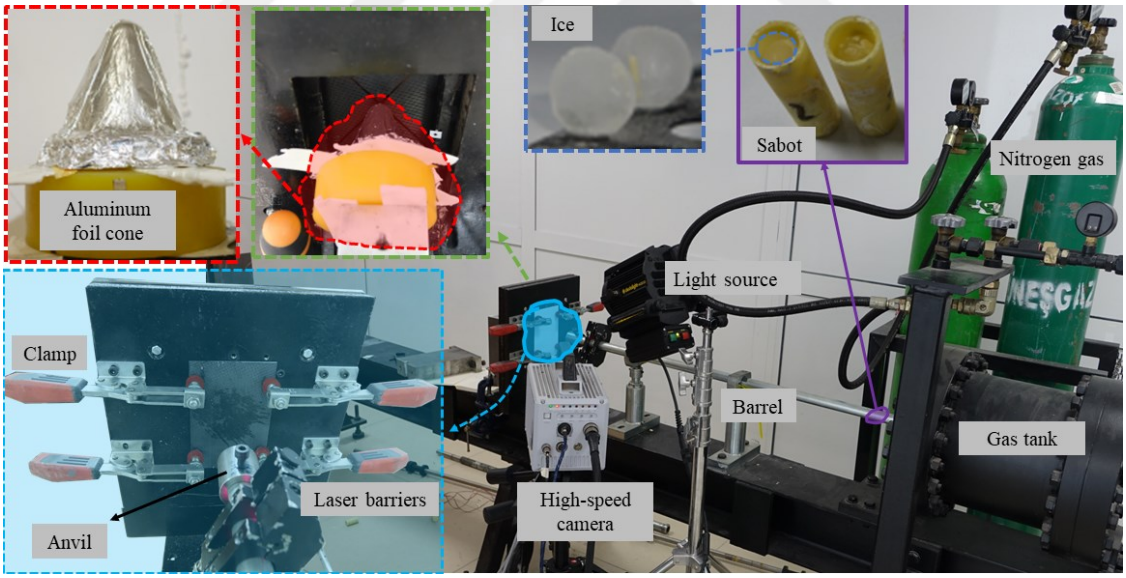

Figure 2.28. Ice impact test system and test equipment

Sabot, which was made of polyurethane by using a suitable steel mold, was employed to prevent ice from damaging into the barrel and to provide a central impact on composite plates. The sabot and ice to be used in tests were kept in the freezing until the impact tests, and at the time of testing sabot were weighed, then ice was placed into the cavity of the sabot. After the total mass had again weighed and noted to determine the mass of the ice, the impact test was performed. All the single and multiple ice impact tests

were performed on the composite specimens of 0.8 mm and 2 mm thickness at a velocity of 95 m/s. Sabot and ice prepared for one of the impact tests can be seen in Figure 2.27.

For ice impact tests the split Hopkinson pressure bar test system was modified. Figure 2.28 shows test system and equipment employed during ice tests. It consists of a gas tank to pressurize nitrogen gas, a barrel to propel ice towards composite plates, a pair of laser barriers to measure the velocity of the ice, a high-speed camera and light source to record impact events, a holder to clamp composite plates, an anvil to prevent sabots from impacting composite plates, and aluminum foil cone to determine the displacement of the rear face of the composite plate at the end of the impact. The position of the foil during the test can be also seen in Figure 2.28.

2.3.13. Low-Velocity Impact Tests

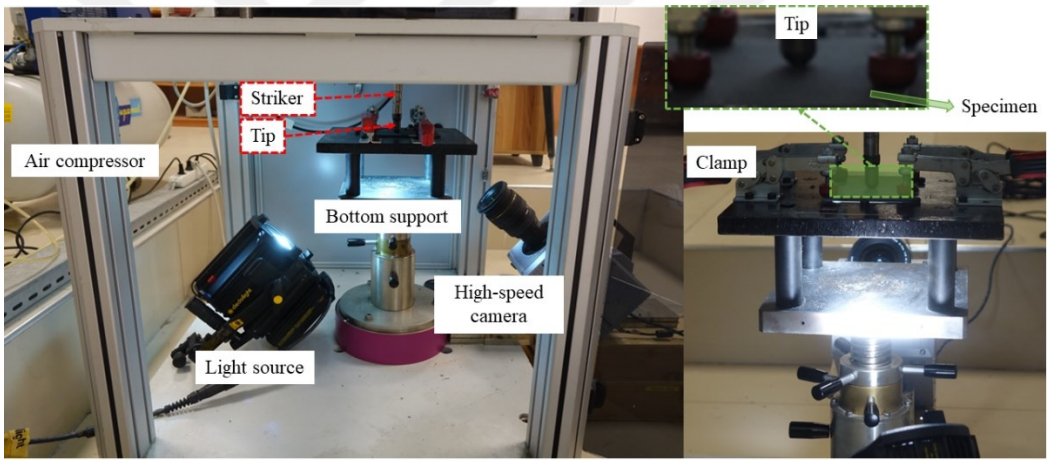

Figure 2.29. Low-velocity impact test set-up

Low-velocity impact tests were performed using the drop weight test system (Figure 2.29). The system involves a striker with a gage to carry out impact events and to measure the force applied to specimens, photocells to measure the impact velocity of the striker and the bottom support fixture to fix and clamp the specimen to be tested. In addition to that, a high-speed video camera and a light source was employed to record the impact events: the camera and the light source were positioned in a way that it records the damage occurring at the back surface of the specimen. The striker having the capability to measure the maximum force of 90 kN was selected for the impact tests. In the impact tests different impact energies were investigated by selecting the suitable additional mass or the striker velocity. For both penetration and perforation cases the

impact tests were carried out. In the perforation test, a composite specimen was impacted by the striker with an impact velocity of 7 m/s and a total mass of 2.8 kg, corresponding to an impact energy of 68.6 Joule. In the penetration case, composite laminates were subjected to single and multiple impacts to investigate the effect of single and multiple impacts on the mechanical behavior of the carbon composite. The specimen was impacted with an impact velocity of 3.5 m/s and a total mass of 2.8 kg, corresponding to an impact energy of 17.16 Joule. Besides, the total mass of the system was increased to from 2.8 kg to 5.8 kg by holding the impact velocity constant, and the composite was impacted with a corresponding impact energy of 35.525 Joule. In this case, the striker did not completely pass through the composite as well and rebounding of the striker took place.

CHAPTER 3

NUMERICAL METHODOLOGY

In this chapter, composite material models and their theories as well as numerical models of the tests are explained in detail.

3.1. Composite Material Models

Table 3.1. Composite material models available in LSDYNA material library[96,97]

Material ID	Architecture		Damage	Element Type			Rate sensitivity
	UD	Woven		Shell	Tshell	Solid	
MAT_22	✓	✗	✗	✓	✗	✓	✗
MAT_54	✓	✗	✓	✓	✗	✗	✗
MAT_55	✓	✗	✓	✓	✗	✗	✗
MAT_58	✓	✓	✓	✓	✓	✗	✗
MAT_59	✓	✓	✓	✓	✓	✓	✗
MAT_158	✓	✓	✓	✓	✓	✗	✓
MAT_161/162	✓	✓	✓	✗	✗	✓	✓
MAT_213			✓	✓	✗	✓	✓
MAT_219			✓	✓	✓	✗	✗
MAT_261			✓	✓	✓	✓	✗
MAT_262			✓	✓	✓	✓	✗

LSDYNA finite element software has a wide range of material libraries, so it enables many different materials to be modeled. Some of them are especially used to model composite materials. Commonly employed composite material models are summarized as shown in Table 3.1. From this table, it can be understood that MAT_162 material model has many advantages over other material models examined. One of these advantages is delamination. This material model has a stress-based delamination failure

model; therefore, there is no needed to strive to set additional failure criteria for delamination in comparison to the other composite material models studied. Another advantageous is that the strain rate effect is taken into account by a strain rate dependent function. However, for complex and huge composite structures the MAT_162 for solid elements can be insufficient due to the fact that it takes considerable time in the solution of problems. In this case, MAT_58 for unidirectional and woven composites or MAT_54 for unidirectional composites can be employed. The former is based on the continuum damage model while the latter is based on the progressive damage model. In addition to that, the former can predict pre- and post-softening of composites but the latter cannot. This is the advantage of MAT_58 over MAT_54&55.

As stated in detail before, in the numerical parts of the study the simulation of the solid elements was performed using MAT_162 material model while Mat_58 was employed to model shell elements.

3.1.1. MAT_58 Material Model

MAT_LAMINATED_COMPOSITE_FABRIC material model was implemented in LSDYNA finite element solver by Matzenmiller et al[98]. The material model is also called as MLT composite material model. As shown in Table 3.1, this material model is commonly employed to model unidirectional and fabric laminates by shell and thick shell elements. The failure modes and damage mechanics implemented is explained in the next sections.

3.1.1.1. Failure Criteria

Depending on the fiber architecture -unidirectional and fabric composites- to be modeled, it is possible to simulate the composite by using different failure surface types available in MAT_58. Failure criteria invoked by the failure surface types can be seen in Table 3.2. Compared to the other failure types, non-smooth failure surface type (faceted failure surface, FS = -1) is commonly used to simulate the fabric composites since all failure criteria invoked by this failure surface type are considered as independent of each other. The hardening behavior in a shear stress-shear strain curve can be easily predicted by the material model. The shear stress versus strain curves of the carbon fiber investigated in this study showed the non-linear behavior, so the non-smooth failure

surface type was selected in the modeling. In the table below stress components are expressed in terms of effective stresses since voids and microcracks is presented in the damaged regions of composites, and load is borne by the region that was not affected by damage.

Table 3.2. Failure surface types

FS = 0	***FS = 1***	***FS = -1***
Fiber Tensile/Compressive Failure		
$\left(\frac{\breve{\sigma}_{11}}{X_{T,C}}\right)^2 = 1$	$\left(\frac{\breve{\sigma}_{11}}{X_{T,C}}\right)^2 + \left(\frac{\breve{\sigma}_{12}}{X_S}\right)^2 = 1$	$\left(\frac{\breve{\sigma}_{11}}{X_{T,C}}\right)^2 = 1$
Matrix Tensile/Compressive Failure		
$\left(\frac{\breve{\sigma}_{22}}{Y_{T,C}}\right)^2 + \left(\frac{\breve{\sigma}_{12}}{S_C}\right)^2 = 1$	$\left(\frac{\breve{\sigma}_{22}}{Y_{T,C}}\right)^2 + \left(\frac{\breve{\sigma}_{12}}{S_C}\right)^2 = 1$	$\left(\frac{\breve{\sigma}_{22}}{Y_{T,C}}\right)^2 = 1$
Shear Failure		
✖	✖	$\left(\frac{\breve{\sigma}_{12}}{S_C}\right)^2 = 1$

- The subscripts of T, C and S represent Tensile, Compression, and Shear, respectively.
- $\breve{\sigma}$ represents effective stress

3.1.1.2. Damage Model

The components of effective stress tensor ($\breve{\sigma}$) in the Table 3.2 are expressed in terms of the nominal (true) stress (σ) and the damage operator as follows.

$$\begin{Bmatrix} \breve{\sigma}_{11} \\ \breve{\sigma}_{22} \\ \breve{\sigma}_{12} \end{Bmatrix} = \begin{bmatrix} \frac{1}{1-\omega_{11}} & 0 & 0 \\ 0 & \frac{1}{1-\omega_{22}} & 0 \\ 0 & 0 & \frac{1}{1-\omega_{12}} \end{bmatrix} \begin{Bmatrix} \sigma_{11} \\ \sigma_{22} \\ \sigma_{12} \end{Bmatrix} \tag{3-1}$$

$$\breve{\sigma} = \boldsymbol{M}\sigma$$

where ω_{11}, ω_{22} and ω_{12} are named as damage evolution variables, and corresponds to matrix, fiber and shear damage, respectively. The damage operator, **M**, is equivalent to

the identity matrix before any damage initiation or evolution, therefore $\breve{\sigma} = \sigma$. The damage variable is defined by the following equation.

$$\omega_{ij} = 1 - \exp\left[-\frac{1}{me}\left(\frac{\varepsilon}{\varepsilon_f}\right)^m\right] \tag{3-2}$$

where ε is the current strain, ε_f is the nominal failure strain and m expresses the strain-dependent evolution of tension, compression, and shear failure modes. The material response (σ=C(ω)*ε) is then determined by the following elastic matrix that considers damage. It is calculated from the inverse of the compliance tensor [98].

$$C(\omega) = \frac{1}{D}\begin{bmatrix} (1-\omega_{11})E_1 & (1-\omega_{11})(1-\omega_{22})E_1 & 0 \\ (1-\omega_{11})(1-\omega_{22})E_1 & (1-\omega_{22})E_2 & 0 \\ 0 & 0 & D(1-\omega_{12})G \end{bmatrix} \tag{3-3}$$

where $D = 1 - (1-\omega_{11})(1-\omega_{22})\vartheta_{12}\vartheta_{21}$. The components of effective stress tensor in the failure criteria of the non-smooth failure surface are then rearranged as follows.

Table 3.3. Non-smooth failure surface (FS = -1)

Longitudinal Tensile/Compressive Failure

$$f_{longitudinal} = \left(\frac{\sigma_{11}}{(1-w_{11,C,T})X_{T,C}}\right)^2 - r_{T,C}{}^{longitudinal} = 0$$

Transverse Tensile/Compressive Failure

$$f_{transverse} = \left(\frac{\sigma_{22}}{(1-w_{22,C,T})Y_{T,C}}\right)^2 - r_{T,C}{}^{longitudinal} = 0$$

Shear Failure

$$f_{shear} = \left(\frac{\tau_{12}}{(1-w_{12})S_C}\right)^2 - r^{shear} = 0$$

3.1.1.3. MAT_58 inputs

The required inputs for MAT_58 material model is summarized as shown in Table 3.4. The inputs in red color are elastic constants of the material, and they are directly

calculated from the results of mechanical characterization tests expect TAU1 and GAMMA1 (Figure 3.1 (a)). TAU1 and GAMMA1 parameters are not specified in LSDYNA user manual. Therefore, they were calculated by using LSOPT optimization software by comparing the experimental and numerical shear test results. Besides, the purple inputs are a stress values to which the stress drops after it reaches its maximum. The effect of these parameters on shear stress-strain curves and tensile/compression stress-strain curves can be seen in Figure 3.1. FS parameter, shown in green color in the Table 3.4, is employed to invoke the failure surface type explained in Section 3.1.1.1. Whilst, ERODS parameter, shown in orange in the table, is the maximum effective strain, and a layers of the element is utterly eroded or failed after its effective strain reaches the maximum effective strain defined in ERODS. It is determined by comparing the experimental and numerical results.

Table 3.4. Required material constants for MAT_58

	R0	EA	EB	(EC)	PRBA	TAU1	GAMMA1
GAB	GBC	GCA	SLIMT1	SLIMC1	SLIMT2	SLIMTC2	SLIMS
AOPT	TSIZE	ERODS	SOFT	FS	EPSF	EPSR	TMSD
XP	YP	ZP	A1	A2	A3	PRCA	PRCB
V1	V2	V3	D1	D2	D3	BETA	
E11C	E11T	E22C	E22T	GMS			
XC	XT	YC	YT	SC			

The inputs in red color are elastic constants of the material, and they are directly calculated from the results of mechanical characterization tests expect TAU1 and GAMMA1 (Figure 3.1 (a)). TAU1 and GAMMA1 parameters are not specified in LSDYNA user manual. Therefore, they were calculated by using LSOPT optimization software by comparing the experimental and numerical shear test results. Besides, the purple inputs are a stress values to which the stress drops after it reaches its maximum. The effect of these parameters on shear stress-strain curves and tensile/compression stress-strain curves can be seen in Figure 3.1. FS parameter, shown in green color in the Table 3.4, is employed to invoke the failure surface type explained in Section 3.1.1.1. Whilst, ERODS parameter, shown in orange in the table, is the maximum effective strain, and a layers of the element is utterly eroded or failed after its effective strain reaches the

maximum effective strain defined in ERODS. It is determined by comparing the experimental and numerical results.

3.1.2. MAT_162 Material Model

This material model has been developed by Materials Sciences Corporation (MSC). Fiber failure, matrix damage and delamination behavior can be successfully predicted by MAT_162. The effect of the strain rate on the progressive failure of composites is also taken into consideration by the strain rate dependent functions. Its progressive failure model is based on the Hashin failure criteria[99], and it also includes the damage model based on damage mechanics found by Matzenmiller et al.[98] to simulate the softening behavior of composites after damage initiation. Moreover, MAT_162 includes a stress-based delamination failure model; therefore, it enables to simulate the delamination damage within composites.

3.1.2.1. Failure Criteria

In the failure criteria, a, b and c directions corresponding X, Y and Z principal directions are designated as the in-plane fill, in-plane warp and out-of-plane directions for fabric composites, respectively. The failure criteria invoked in the simulation of composite materials by MAT_162 material model is as follows.

- The Fill and Warp Fiber Tensile/Shear Failure Modes, $\sigma_a, \sigma_b > 0$

$$f_6 - r_6^2 = \left(\frac{\langle \sigma_a \rangle}{S_{aT}}\right)^2 + \frac{(\tau_{ab}^2 + \tau_{ca}^2)}{S_{aFS}^2} - r_6^2 = 0 \tag{3-4}$$

$$f_7 - r_7^2 = \left(\frac{\langle \sigma_b \rangle}{S_{bT}}\right)^2 + \frac{(\tau_{ab}^2 + \tau_{bc}^2)}{S_{bFS}^2} - r_7^2 = 0 \tag{3-5}$$

$$S_{aFS} = SFS \text{ and } S_{bFS} = SFS * S_{bT}/S_{aT} \tag{3-6}$$

where SFS is the fiber mode shear strength, S_{aT} and S_{bT} are the axial tensile strengths, and S_{aFS} and S_{bFS} are the layer shear strengths due to fiber shear failure.

- Compressive Failure in The Fill and The Warp Directions, $\sigma_a, \sigma_b < 0$

$$f_8 - r_8^2 = \left(\frac{\langle \sigma_a' \rangle}{S_{aC}}\right)^2 - r_8^2 = 0\,, \qquad \sigma_a' = -\sigma_a + \langle -\sigma_c \rangle \tag{3-7}$$

$$f_9 - r_9^2 = \left(\frac{\langle \sigma_b' \rangle}{S_{bC}}\right)^2 - r_9^2 = 0\,, \qquad \sigma_b' = -\sigma_b + \langle -\sigma_c \rangle \tag{3-8}$$

$$f_{10} - r_{10}^2 = \left(\frac{\langle p \rangle}{S_{FC}}\right)^2 - r_{10}^2 = 0\,, \qquad p = \frac{\sigma_a + \sigma_b + \sigma_c}{3} \tag{3-9}$$

where S_{aC} and S_{bC} are the axial compressive strengths, p is the hydrostatic pressure, and S_{FC} is the layer strength related to the fiber crush failure.

- In-Plane Shear Stress Failure

$$f_{11} - r_{11}^2 = \left(\frac{\tau_{ab}}{S_{ab}}\right)^2 - r_{11}^2 = 0 \tag{3-10}$$

where S_{ab} is the layer shear strength

- Delamination Failure

$$f_{12} - r_{12}^2 = S^2 \left\{ \left(\frac{\langle \sigma_c \rangle}{S_{cT}}\right)^2 + \left(\frac{\tau_{bc}}{S_{bc}}\right)^2 + \left(\frac{\tau_{ca}}{S_{ca}}\right)^2 \right\} - r_{12}^2 = 0 \tag{3-11}$$

$$\left\{\frac{S_{ca}}{S_{bc}}\right\} = \left\{\frac{S_{ca}^{(0)}}{S_{bc}^{(0)}}\right\} + \tan(\varphi)\langle -\sigma_c \rangle \tag{3-12}$$

where S_{cT} is the through thickness tensile strength, S_{bc}, and S_{ca} are the shear strengths, σ_c is the compressive normal stress, and φ is the coulomb friction angle.

In fabric composites, the fill and warp fiber tensile/shear failure are defined by the quadratic interaction between axial and shear stresses as mentioned above. In case a layer fails in this failure mode, it cannot withstand any loads in the loading direction.

The maximum stress criterion is employed to determine the in-plane compressive failure in both fill and warp directions. As the failure within a layer is predicted by this failure mode, it is presumed that a residual axial compressive load ($S_{aRC} = SFFC * S_{aC}$ or $S_{bRC} = SFFC * S_{bC}$) is carried by the layer in the direction along which the damage propagates. Contrary to the failure behavior in the damaged direction, the load capacity in the direction that is the perpendicular to the damage direction (the transverse direction) is not affected by the damage ($\sigma_a = -S_{aCR}$ or $\sigma_b = -S_{bCR}$).

Besides, the failure model of a composite laminate subjected to compressive pressure (p) is predicted by the crush failure mode (Equation (3-9)). On the failure, it is presumed that the composite shows elastic behavior while it cannot withstand any tensile loads. The in-plane shear failure occurring without fiber breakage is determined by the failure mode which is the designated by f_{11} in Equation (3-10). As this failure mode occurs, the failed element can continue to carry loads in the axial direction while it cannot bear in-plane shear stress anymore. The matrix damage in through-thickness direction is calculated by the delamination failure mode. When a damage is predicted by this failure mode, the specimen behaves elastically in the in-plane directions, and the shear strengths in (ca) and (bc) are reduced to zero. For tensile mode, the specimen cannot bear any tensile load whilst in compressive mode it behaves elastically.

3.1.2.2. Damage Model

The softening behavior after the initiation of damage is simulated by the damage model based on the MLT damage mechanic approach. To calculate elastic response of the material, the stiffness matrix [C] is determined by inverting the compliance matrix [S] that includes the damage variable defined in Equation (3-13).

$$\bar{\omega}_i = 1 - \exp\left(\frac{1}{m_j}\left(1 - r_j^{m_j}\right)\right) \qquad r_j \geq 1 \tag{3-13}$$

where r_j and m_j are the damage threshold shown in Equation (3-4) - (3-12) and material damage parameter, respectively. The initial value of the damage threshold is equal to one, meaning that the damage variable ($\bar{\omega}_i$) initially equals to zero. It corresponds

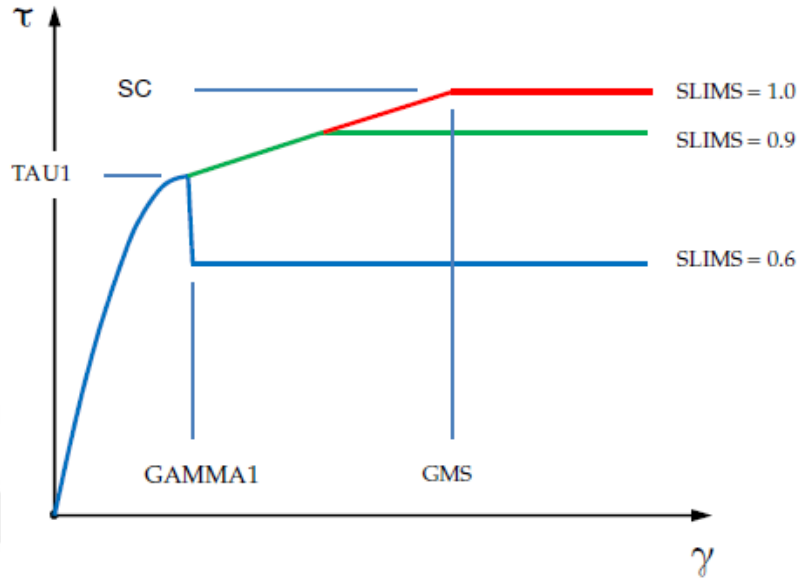

(a)

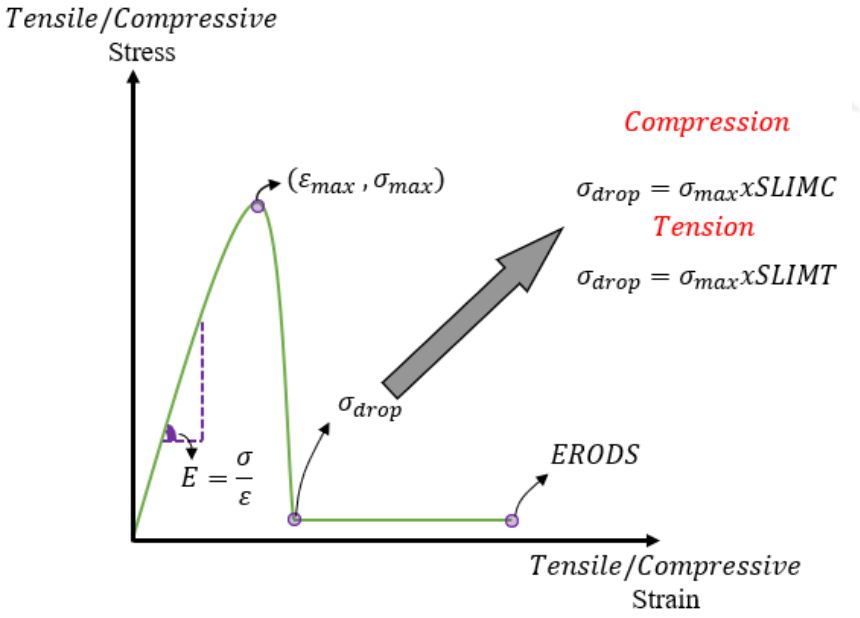

(b)

Figure 3.1. The effect of stress limit factor on (a) shear stress[96] and (b) tensile/compressive stress

a linear elastic behavior. As the damage occurs ($r_j \geq 1$), the linear elastic response of the material is calculated by the stiffness matrix including the damage variable (the inverse of the compliance matrix, $[S]^{-1}$).

$$[S] = \begin{bmatrix} \frac{1}{(1-\bar{\omega}_1)E_a} & \frac{-\vartheta_{ba}}{E_b} & \frac{-\vartheta_{ca}}{E_c} & 0 & 0 & 0 \\ \frac{-\vartheta_{ab}}{E_a} & \frac{1}{(1-\bar{\omega}_2)E_b} & \frac{-\vartheta_{cb}}{E_c} & 0 & 0 & 0 \\ \frac{-\vartheta_{ac}}{E_a} & \frac{-\vartheta_{bc}}{E_b} & \frac{1}{(1-\bar{\omega}_3)E_c} & 0 & 0 & 0 \\ 0 & 0 & 0 & \frac{1}{(1-\bar{\omega}_4)G_{ab}} & 0 & 0 \\ 0 & 0 & 0 & 0 & \frac{1}{(1-\bar{\omega}_5)G_{bc}} & 0 \\ 0 & 0 & 0 & 0 & 0 & \frac{1}{(1-\bar{\omega}_6)G_{ca}} \end{bmatrix} \quad (3\text{-}14)$$

Elastic modulus reduction in k[th] direction is expressed by the following equations.

$$E_k = (1-\bar{\omega}_k)E_{k0} = E_{k0}\exp\left(\frac{1}{m_k}\left(1-r_k^{m_k}\right)\right), r_k = \frac{\varepsilon_k}{\varepsilon_{ky}} \quad (3\text{-}15)$$

where E_k is the initial elastic modulus, r_k is the damage threshold, ε_k is the current strain, and ε_{ky} is the yield strain in that direction. For the damaged material, the stress-strain relationship can be considered as follows.

$$\sigma_k = E_k\varepsilon_k = E_{k0}\exp\left(\frac{1}{m_k}\left(1-\left(\frac{\varepsilon_k}{\varepsilon_{ky}}\right)^{m_k}\right)\right) \quad (3\text{-}16)$$

Equation (3-16) is updated by considering that $\sigma_{ky} = E_{k0}\varepsilon_{ky}$, then the following equation is obtained.

$$\frac{\sigma_k}{\sigma_{ky}} = \frac{\varepsilon_k}{\varepsilon_{ky}}\exp\left(\frac{1}{m_k}\left(1-\left(\frac{\varepsilon_k}{\varepsilon_{ky}}\right)^{m_k}\right)\right) \quad (3\text{-}17)$$

As considering the equation above, it can be said that when the damage threshold ($r_k = \varepsilon_k/\varepsilon_{ky}$) is bigger than one, the equation defines the post-yield damage softening part of the stress versus strain curve. Contrary to the above statement, when the damage threshold is lower than one, the equation describes the linear elastic part of the stress versus strain curve.

The strain effect in MAT_162 is taken into consideration for the strength and elastic moduli by the following equations.

$$\{S_{RT}\} = \{S_0\}\left(1 + C_{rate1} \ln \frac{\{\dot{\bar{\varepsilon}}\}}{\dot{\varepsilon}_0}\right) \tag{3-18}$$

$$\{E_{RT}\} = \{E_0\}\left(1 + C_{rate} \ln \frac{\{\dot{\bar{\varepsilon}}\}}{\dot{\varepsilon}_0}\right) \tag{3-19}$$

$$\{S_{RT}\} = \begin{Bmatrix} S_{aT} \\ S_{aC} \\ S_{bT} \\ S_{bC} \\ S_{FC} \\ S_{FS} \end{Bmatrix} \text{ and } \{\dot{\bar{\varepsilon}}\} = \begin{Bmatrix} |\dot{\varepsilon}_a| \\ |\dot{\varepsilon}_a| \\ |\dot{\varepsilon}_b| \\ |\dot{\varepsilon}_b| \\ |\dot{\varepsilon}_c| \\ (\dot{\varepsilon}_{ca}^2 + \dot{\varepsilon}_{bc}^2)^{1/2} \end{Bmatrix} \tag{3-20}$$

$$\{E_{RT}\} = \begin{Bmatrix} E_a \\ E_b \\ E_c \\ G_{ab} \\ G_{bc} \\ G_{ca} \end{Bmatrix}, \{\dot{\bar{\varepsilon}}\} = \begin{Bmatrix} |\dot{\varepsilon}_a| \\ |\dot{\varepsilon}_b| \\ |\dot{\varepsilon}_c| \\ |\dot{\varepsilon}_{ab}| \\ |\dot{\varepsilon}_{bc}| \\ |\dot{\varepsilon}_{ca}| \end{Bmatrix} \text{ and } \{C_{rate}\} = \begin{Bmatrix} C_{rate2} \\ C_{rate2} \\ C_{rate4} \\ C_{rate3} \\ C_{rate3} \\ C_{rate3} \end{Bmatrix} \tag{3-21}$$

3.1.2.3. MAT_162 inputs

MAT_162 material model involves thirty-four material model constants including elastic properties, erosion parameters, damage parameters and strain rate parameters. These parameters can be seen in Table 3.5.

Elastic properties in red color in the table above are directly calculated from the results of mechanical characterization tests. They include the tensile and compressive in

the principal directions, and shear strengths as well as the elastic moduli and shear moduli. The SFFC constant is named as scale factor for residual compressive strength, and the function or effect of that parameter is the same as SLIM parameters of the MAT_58 explained in Section 3.1.1.3. Its effect on a stress-strain curve is illustrated in Figure 3.2.

Table 3.5. MAT_162 inputs

	R0	EA	EB	EC	PRBA	PRCA	PRCB
GAB	GBC	GCA	AOPT	MACF			
XP	YP	ZP	A1	A2	A3		
V1	V2	V3	D1	D2	D3	BETA	
SAT	SAC	SBT	SBC	SCT	SFC	SFS	SAB
SBC	SCA	SFFC	AMODEL	PHIC	E_LIMT	S_DELM	
OMGMX	ECRSH	EEXPN	CREATE1	AM1			
AM2	AM3	AM4	CRATE2	CRATE3	CRATE4		

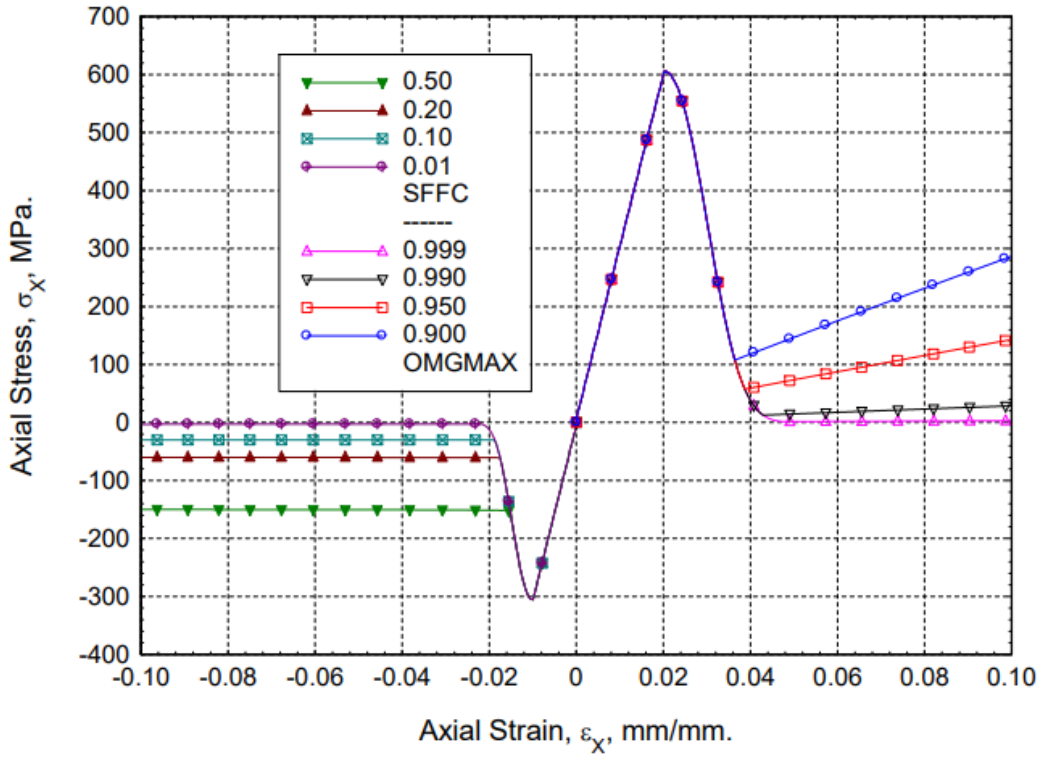

Figure 3.2. The effect of OMGMX and SFFC parameters on a stress-strain curve (Source: Gama et al.[103])

The erosion parameters in purple color are employed to erode an element by considering the tensile strain (E_LIMT), compressive relative volume (ECRSH) and

expansive relative volume (EEXPN). The parameters related to the strain rate can be seen in blue color in Table 3.5. The effect of each rate parameter on strength or elastic/shear modulus can be found in Equations (3-18) and (3-20). Other parameters such as OMGMX, S_DELM and BETA are employed to limit the damage variable for the reduction in elastic moduli (Figure 3.2), to obtain the delamination damage close to the damage observed in experiments and to define fiber orientation angle, respectively. The green parameters are invoked to simulate the post-softening behavior of composite as explained in detail in Section 3.1.2.2. They are calculated from the experimental and numerical results of the punch-shear tests. The procedure to find the damage parameters are explained in detail in other studies[101,102].

3.2. Modeling of Delamination

In LSDYNA the decohesion between the layers of composites, delamination failure, is modeled by either material model itself, using cohesive zone modeling or using tiebreak contact types between the layers. The material model including delamination failure is the one that is explained in detail in Section 3.1.2.1 while in cohesive zone modeling cohesive elements are defined between the layers of a composite Besides, automatic tie-break contact types together with the MAT_162 material model were employed to model delamination in LSDYNA in few studies [104–106]. Either automatic surface to surface tiebreak or automatic one-way surface to surface tie-break contacts can be selected. For both contacts, the coincide nodes of the layers of a composite plate is tied until a failure criterion is reached. After the criteria is met, the tied contact fails. With the scope of this study the former one, automatic surface to surface tiebreak, was selected in the simulation of the cohesion between the plies of the composite. This contact type is employed with an option, and the commonly used ones are 7,9 and 11 for solid elements. The tie-break contact with these options uses a bilinear constitutive law. The bilinear constative law valid in tensile loading (double cantilever beam test) and shear loading (end notched flexure test) is illustrated in Figure 3.3. The tensile loading corresponds Mode-I while shear loading corresponds Mode II and Mode III, depending on the relative displacement between the nodes with respect to the crack orientation.

The relative displacements of δ_1^0 and $\delta_{2,3}^0$ correspond the onset of damage. When the material subjected to the load before these relative displacements, it behaves

elastically, there is no permanent damage on the cohesion. Beyond these displacement values (the maximum normal or shear forces are exceeded), damage occurs, it then propagates. The damage propagation lasts until it reaches the relative displacement values of δ_1^f and $\delta_{2,3}^f$. Once these displacements are reached, the debonding between the layers takes place, meaning that the permanent damage occurs. The area under the curve obtained in the tensile loading corresponds to the fracture energy of Mode I. While, it corresponds to the facture energy of Mode II and Mode III in the shear loading. In Mode II, the layers slide relative to each other in the 2 direction (in-plane shear) while in Mode III they slide relative to each other in the 3 direction (out-of-plane shear). It is worth noting that the Mode I fracture toughness is lower than Mode II and III fracture toughness. Since Mode II components exists in Mode III tests, Mode III fracture toughness values is not calculated correctly. Therefore, in the delamination analysis Mode III fracture toughness is assumed to be equal Mode II fracture toughness.

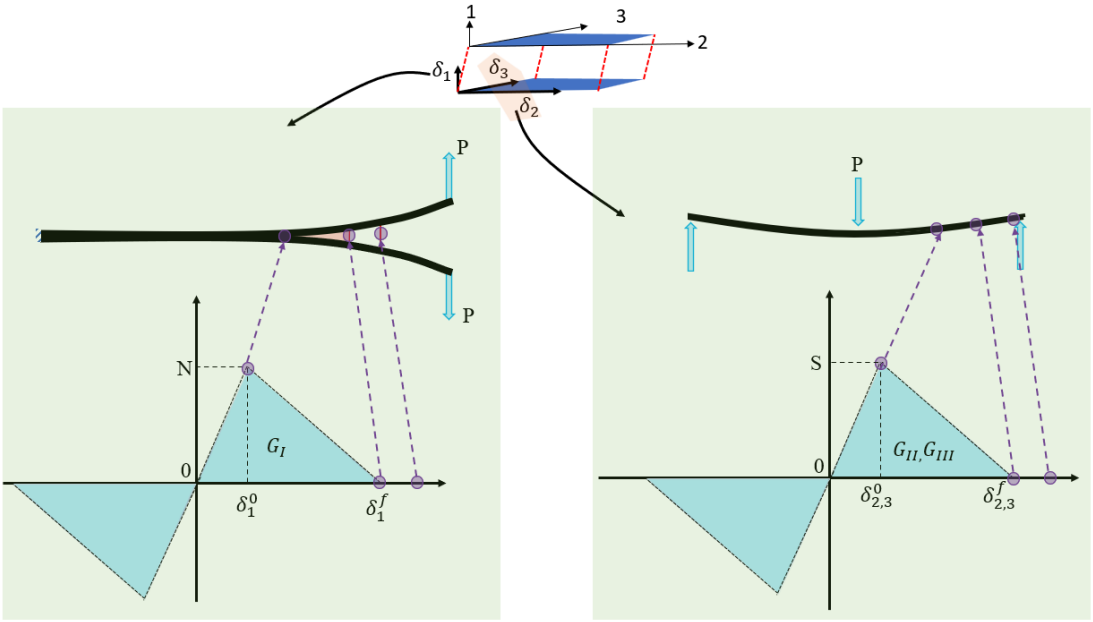

Figure 3.3. The bilinear constitutive law in Mode I and Mode II and III

For the combined loading including the tensile and shear loading a mixed-mode interaction occurs. The mixed-mode behavior is illustrated for the bilinear constitutive law in Figure 3.4. In this case, the propagation of the damage can take place the damage onset value that described in the previous section. The relative displacement attained in the shear loading is calculated from the two relative displacement values in 2 and 3

directions shown in Figure 3.3. The equation for the total shear relative displacement value is as follows.

$$\delta_{Shear} = \sqrt{(\delta_2)^2 + (\delta_3)^2} \tag{3-22}$$

Then the total mixed mode relative displacement is defined as

$$\delta_m = \sqrt{(\delta_1)^2 + (\delta_{Shear})^2} \tag{3-23}$$

The contribution of the different modes is expressed as

$$\beta = \frac{\delta_{Shear}}{\delta_1} \tag{3-24}$$

The damage onset criterion and the damage propagation criterion in the mixed mode is summarized in the following table. In the damage onset criterion, a quadratic delamination criterion is used.

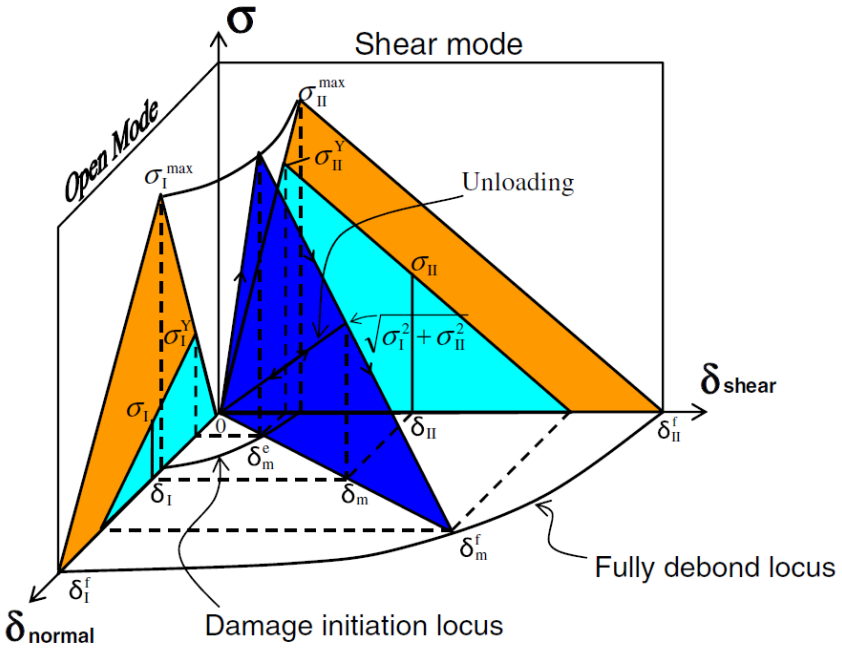

Figure 3.4. The bilinear constitutive law in mixed-mode loading

(Source: Jiang et al.[107])

Table 3.6. Damage onset and propagation criterion in mixed mode

Damage initiation		$\left(\frac{t_1}{N}\right)^2 + \left(\frac{t_{shear}}{S}\right)^2 = 1$ $\delta_m^0 = \begin{cases} \delta_S^0 \delta_N^0 \sqrt{\frac{1+\beta^2}{(\delta_S^0)^2 + (\beta\delta_N^0)^2}} & \leftarrow \delta_1 > 0 \\ 1 & \leftarrow \delta_1 \leq 0 \end{cases}$
Damage propagation	Power law criterion	$\left(\frac{G_I}{G_{Ic}}\right)^\alpha + \left(\frac{G_{shear}}{G_{Sc}}\right)^\alpha = 1$ $\delta_m^f = \begin{cases} \frac{2(1+\beta^2)}{k\delta_m^0}\left(\left(\frac{1}{G_{Ic}}\right)^\alpha + \left(\frac{\beta^2}{G_{Sc}}\right)^\alpha\right)^{-1/\alpha} & \leftarrow \delta_1 > 0 \\ \delta_s^f & \leftarrow \delta_1 \leq 0 \end{cases}$
	Benzeggah and Karnane' s criterion	$G_{Ic} + (G_{Sc} - G_{Ic})\left(\frac{G_{shear}}{G_{Ic} + G_{shear}}\right)^\eta = G_I + G_{shear}$ $\delta_m^f = \begin{cases} \frac{2}{k\delta_m^0}\left(G_{Ic} + (G_{Sc} - G_{Ic})\left(\frac{\beta^2}{1+\beta^2}\right)^\eta\right) & \leftarrow \delta_1 > 0 \\ \delta_s^f & \leftarrow \delta_1 \leq 0 \end{cases}$

Table 3.7. Interface properties

Interface Strength	
Normal Strength (MPa)	40
Shear Strength (MPa)	78
Fracture Toughness	
Mode I fracture toughness (N/m) [108]	375
Mode II and III fracture toughness (N/m) [108]	1467
Other parameters	
The B-K criterion constant, η [108]	2.25
Penalty stiffness (MPa) [108]	10^8

For the damage propagation prediction there are two criteria in LSDYNA, namely the power law criterion and Benzeggah and Karnane's criterion. The B-K criterion is used to appropriately represent for the variation of fracture toughness as a function of mode mixity ratio $\left({G_{shear}}/{G_{Ic} + G_{shear}}\right)$. The B-K criterion fitting parameter,η, is determined by a curve fit to the fracture toughness values. These toughness values are calculated experimentally using mixed mode bending tests at different mode mixity ratios, the double cantilever beam tests for pure mode I $\left({G_{shear}}/{G_{Ic} + G_{shear}} = 0\right)$ and the end-notched flexure tests for pure mode II $\left({G_{shear}}/{G_{Ic} + G_{shear}} = 1\right)$. Depending on the mode mixity ratio investigated, the mixed-mode response, blue shaded area in Figure 3.4, might be closer to mode-I or mode-II responses.

In this study, the B-K criterion was used to model delamination failure by the automatic surface to surface contact type with an option 9. The required parameters for this cohesion contact type were directly taken from a study[108] in literature except the ones that are interface strengths, namely normal strength and shear strength. These strength values were calculated from mechanical characterization tests. These parameters can be found in Table 3.7.

3.3. Simulation of Tensile Tests

The modeling of tensile test involves the modeling of the standard tensile test coupons at quasi-static strain rates and the numerical model of the dynamic tensile

specimen at quasi-static and high strain rates. These models are explained in detail in the next sections.

3.3.1. Standard Tensile Test Model

Numerical model of the standard tensile test coupon can be seen in Figure 3.5 (a). The model includes only test coupon that has nine layers through the thickness. Orientations of these layers are illustrated in Figure 3.5 (b). For each layer the fiber orientation angle was defined as 0 or 90-degree using BETA property of MAT_162 material model. The same boundary conditions as the experiment were applied to the tensile model by using BOUNDARY_SPC_SET card. Nodes fixed by grips of test fixture were defined in SET_NODE card as moving and fixed side. The translational and rotational motion of nodes in the fixed side were constrained.

While, those in the moving side was allowed to only move along x-axis. A section plane was specified in the middle section of the coupon by DATABASE_CROSS_SECTION_PLANE card to calculate the stress in the composite coupon. For strain calculation, two nodes having a distance of 0.1 meter along x axis were defined in DATABASE_HISTORY_NODE card. A constant velocity was applied to the nodes in the moving side by using BOUNDARY_PRESCRIBED_MOTION_SET card.

Settings used in quasi-static tensile models simulated using shell elements were the same as that employed in solid elements. Different from the solid element models, in the shell models the effect of element size on the response of composite were investigated by using different mesh sizes, 0.5x0.5 mm, 1x1 mm, 1.5x1.5 mm, 2x2 mm and 2.5x2.5 mm. Besides, the layers of composite were modeled as a single layer, and the fiber orientation and the number of the layers were defined in PART_COMPOSITE card.

3.3.2. Quasi-static Tensile Test Model

A numerical tensile test model was also formed by using a dynamic tensile test specimen (Figure 3.6). The model consists of steel fixtures defined as RIGID material and the dynamic tension test coupon. Coinciding nodes of fixtures and the bottom and the top layers of composite were merged to transfer the applied load to one side of the spec-

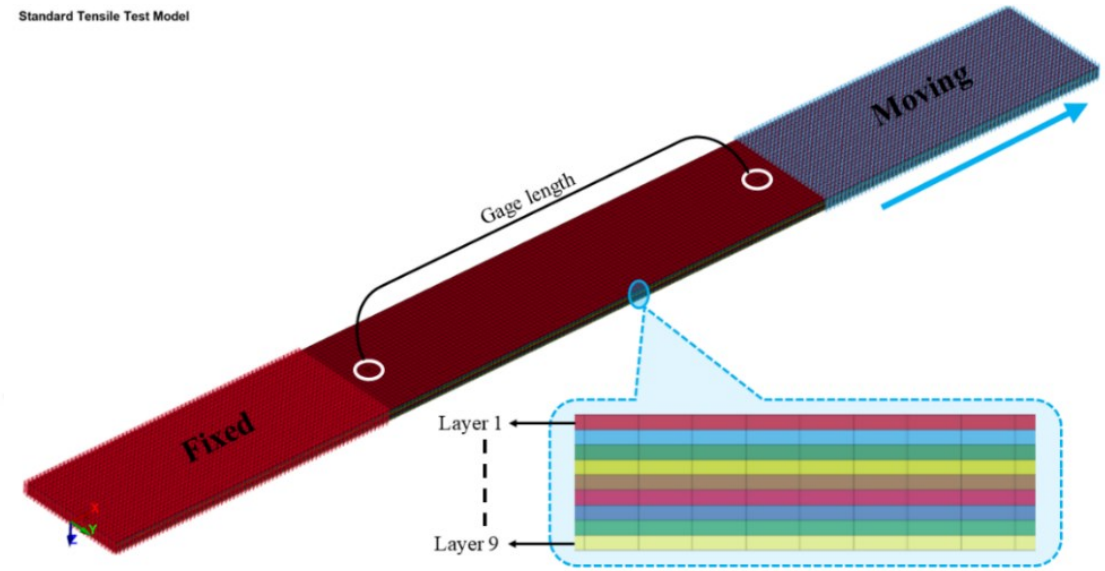

(a)

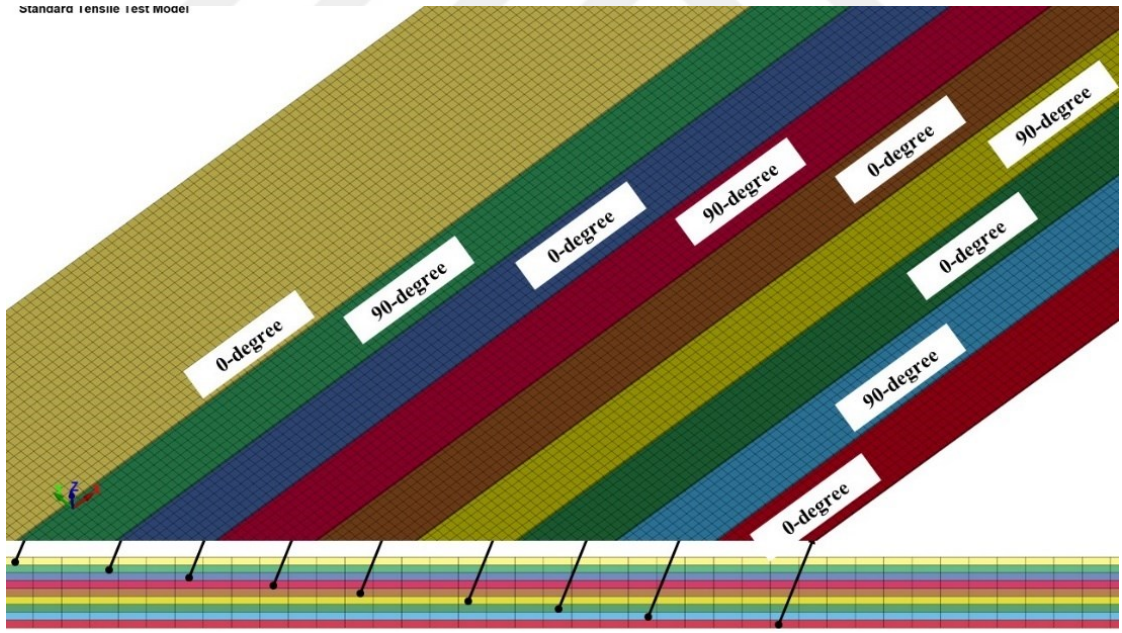

(b)

Figure 3.5. (a) Standard tensile test model and (b) its ply orientation

imen and to fix the other side. The fixed and moving motions of the top and the bottom rigid parts were specified in BOUNDARY_PRESCRIBED_MOTION_RIGID card. A finer quad-mesh with a size of 0.28x0.28 mm was preferred in the gage section of the specimen while the part of the specimen that placed in fixtures and the fixtures itself were meshed with a coarser quad-mesh with a size of 1x1 mm. Two nodes in the gage section (DATABASE_HISTORY_NODE) and section plane in the middle section of the composite specimen (DATABASE_CROSS_SECTION_PLANE) were defined for strain and stress calculations of the composite, respectively. Because of erosion of solid elements during loading, ERODING_SINGLE_SURFACE between composite layers were defined. It is also employed to provide interaction between the layers of composite after delamination.

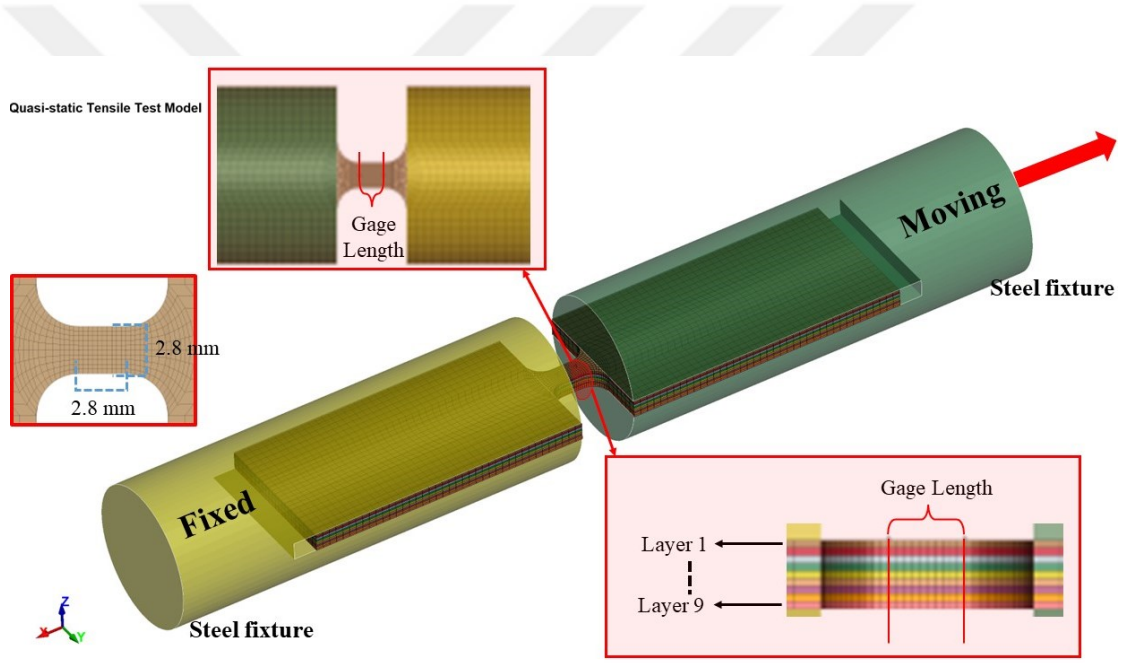

Figure 3.6. Quasi-static tensile test model

3.3.3. Dynamic Tensile Test Model

The numerical model of dynamic tensile tests can be found in Figure 3.7. The model involves an incident bar, a transmitter bar and a composite specimen. The dimensions of the specimen are the same as those used in the quasi-static tensile model. The model was constructed without a striker bar. Instead, the incident pulse obtained from the test was defined in DEFINE_CURVE card and the segments on the front surface (the

farthest surface from the composite-incident bar interface) of the incident bar were specified in SET_SEGMENT card. The load defined was then applied to the segments by using LOAD_SEGMENT_SET card. Tensile strain and stress of the composite were calculated from the nodes in DATABASE_HISTORY_NODE and the section specified in DATABASE_CROSS_SECTION_PLANE card, respectively. Besides, two solid elements found in the strain gage points were defined in DATABASE_HISTORY_ELEMENT to monitor and record the bar response occurring the incident and transmitter bar after loading.

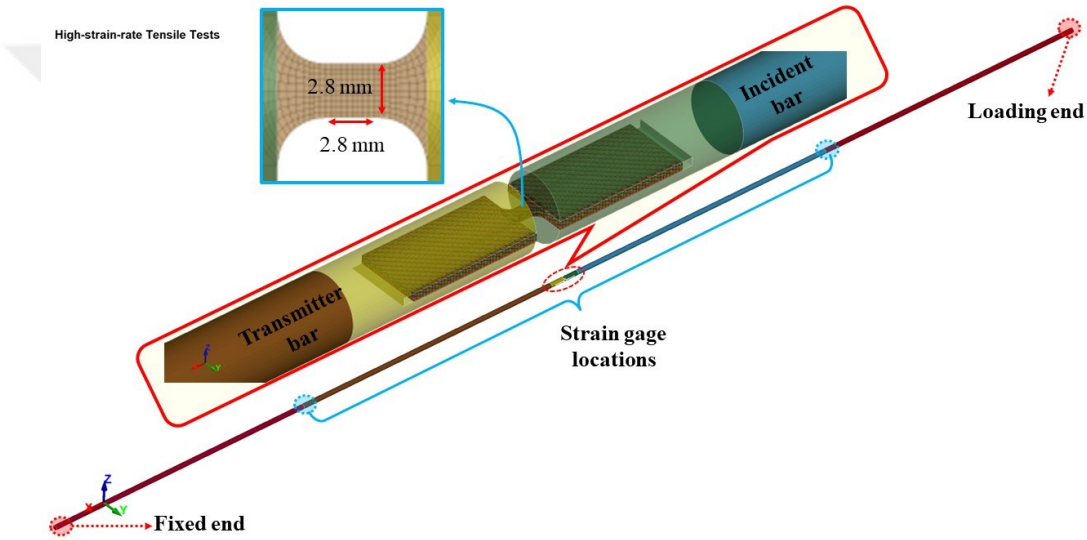

Figure 3.7. High-strain rate tensile test model

3.4. Simulation of Compression Tests

The numerical model of compression tests performed according to the ASTM test standard can be seen in Figure 3.8. Here, the composite sample was modeled using solid elements. The compression test model was simulated similar to that of the tensile test. Like standard tensile test model, numerical model of the compression test includes only the composite test coupon. The fiber orientation was also the same as the numerical model of the tensile specimen and can be seen in Figure 3.5 (b). Contrary to the tensile model, the load was applied along negative x-axis in the compression models. In addition, a finer quad mesh with size of 0.28x0.28 mm was employed in the gage section.

The numerical compression test model using shell elements was the same as the numerical tensile test model except for the loading direction. Also, it was meshed with different mesh sizes such as 1.3x1.3 mm and 2.5x2.5 mm to investigate the effect of element size.

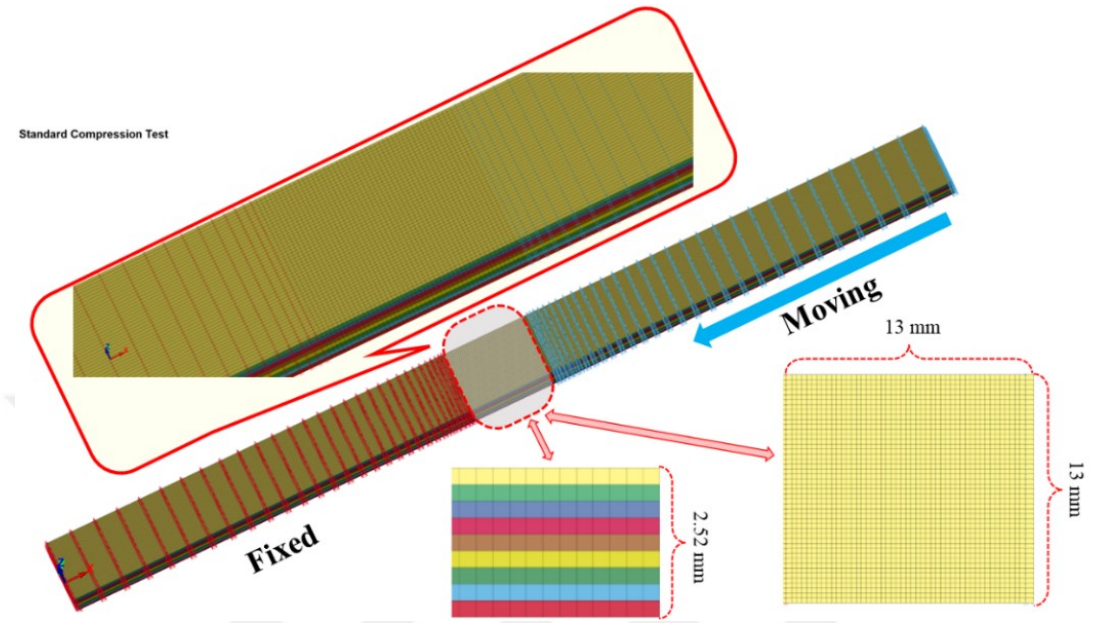

Figure 3.8. Standard compression test model

3.5. Simulation of In-plane Shear Tests

Numerical models of the standard shear test, quasi-static and dynamic tests were explained in the following sections.

3.5.1. Standard In-plane Shear Test Model

Figure 3.9 (a) shows the numerical model of shear tests. It was similar to the numerical model of the tensile test which was explained in detail in 3.3.1. Unlike the tensile model, in the shear model fiber orientation was defined as +45-degree or -45-degree using BETA option of MAT_162 instead of 0-degree or 90-degree. It is illustrated in Figure 3.9 (b). For the calculation of shear strain four nodes (two node pairs) were specified in DATABASE_HISTORY_NODE. These node pairs can be also seen in Figure 3.9 (b). As shown in the figure, the longitudinal strain is calculated from the nodes

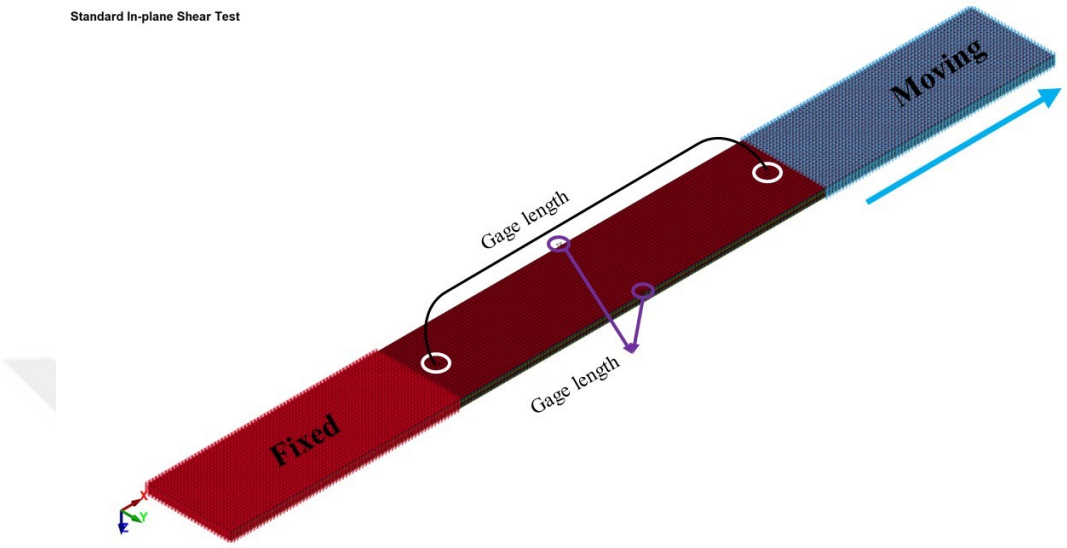

(a)

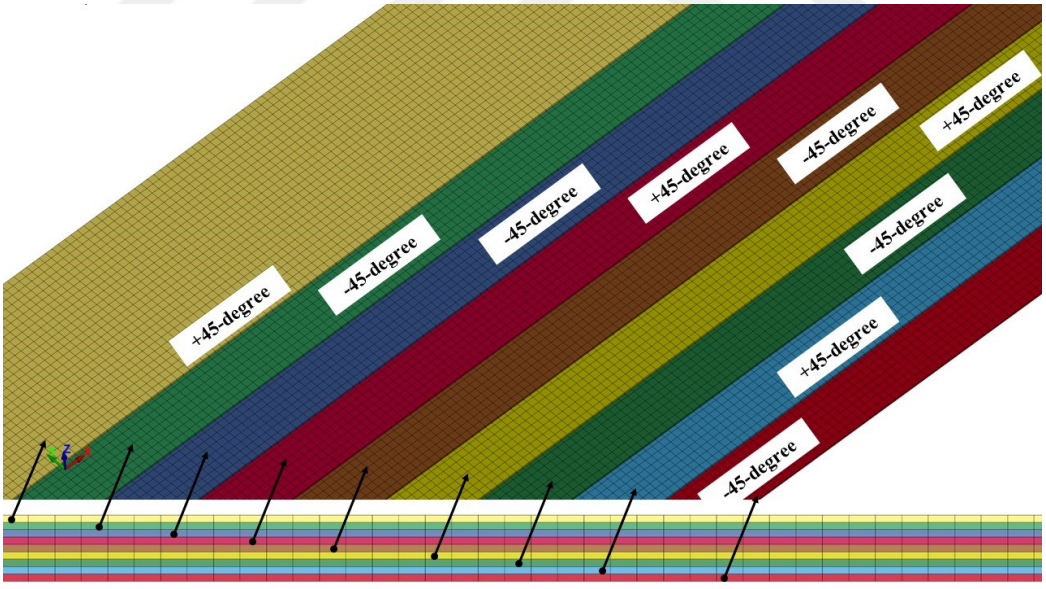

(b)

Figure 3.9. (a) Standard shear test model and (b) its ply orientation

specified by the white circles while the transverse strain is determined from the nodes marked by the purple circles. By summing of the longitudinal and transverse strain the shear strain was calculated. DATABASE_CROSS_SECTION_PLANE card was specified in the middle section of the composite sample to read and record the force history in the x direction, which was the loading direction. For the shear stress calculation, the force history was divided by two times the cross-sectional area.

MAT_58 used in the shell model of the shear test involves has many material constants. Two of them are directly determined from the results of the numerical model of the shear test, namely TAU (stress limit of the nonlinear part of the shear stress versus strain curve) and GAMMA (strain limit of the nonlinear part of the shear stress versus strain curve). These material constants were determined by using LSOPT optimization software since how calculate these values are not expressed in the user manual of the LSDYNA. In many studies these parameters were determined by comparing the results obtained from experiment and numerical models. As in the solid model, in the shell model two node pair was defined for the calculation of the shear strain while a section in the middle of the specimen was specified for the calculation of the shear stress.

3.5.2. Quasi-static In-plane Shear Test Model

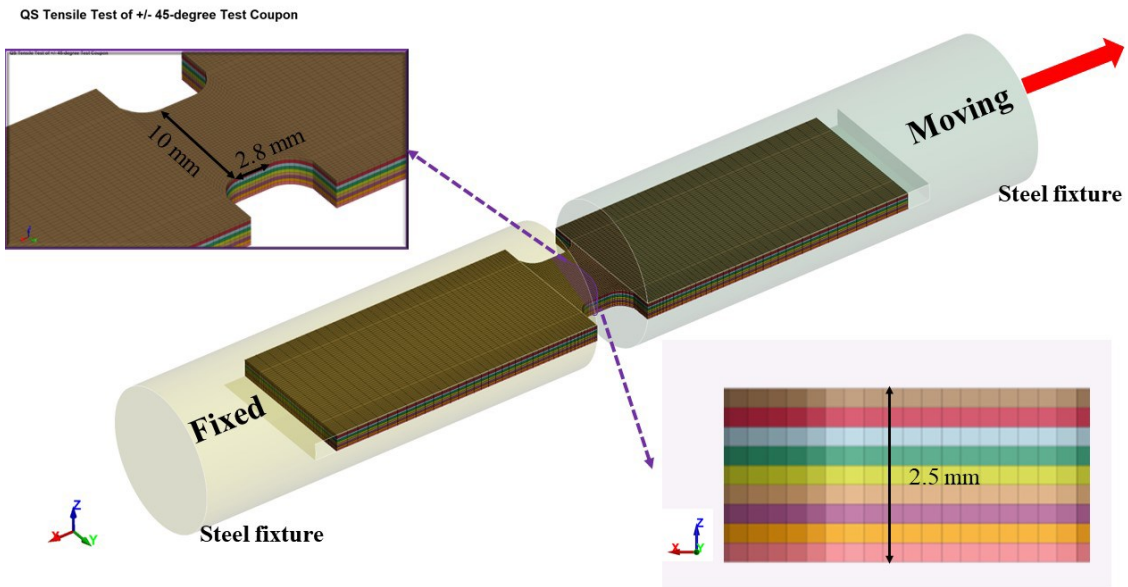

Figure 3.10. Quasi-static tensile test model of ±45-degree composite coupon

Quasi-static in-plane shear test model can be seen in Figure 3.10. The steps followed to model the quasi-static in-plane shear test was the same as those in the quasi-static tensile tests. It was expressed in detail in 0. Contrary to the cross-sectional area of the quasi-static tensile specimen in the gage section, a bigger cross-sectional area was preferred in the in-plane shear specimen. Shear strain and shear stress were calculated according to the steps explained in 3.5.1.

3.5.3. Dynamic In-plane Shear Test Model

A split Hopkinson tensile model of a $[\pm 45]_n$ composite specimen can be seen in Figure 3.11. Like the dynamic tensile model, the dynamic shear model consists of the incident bar, transmitter bar and the composite specimen. The model was formed without a striker bar. How the tensile load was applied to the incident bar, and the shear stress and strain calculations were explained in 3.3.3.

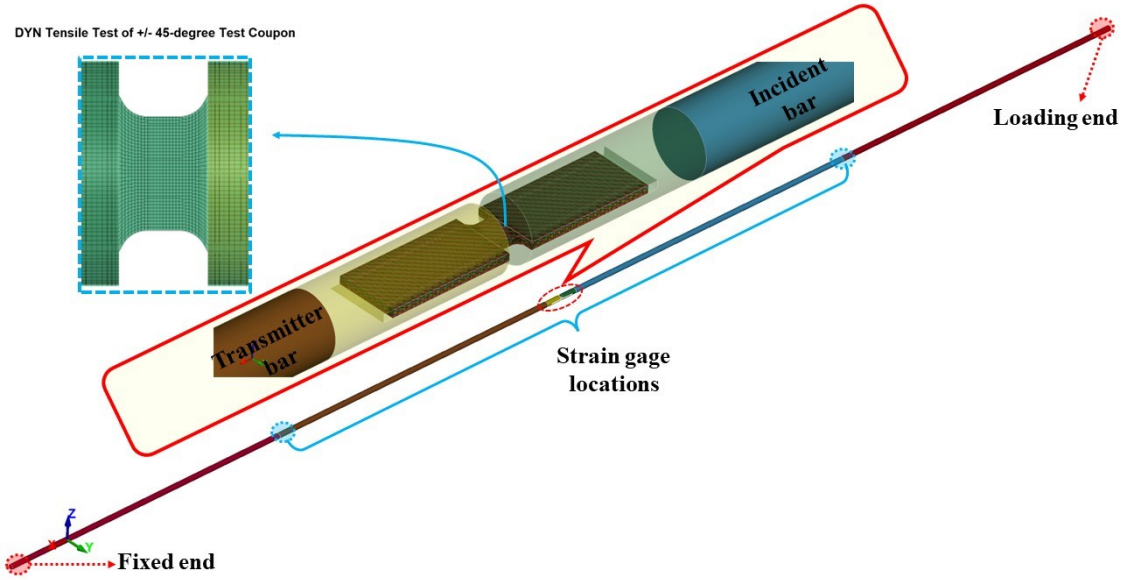

Figure 3.11. Dynamic tensile test model of ±45-degree composite coupon

3.6. Simulation of Out-of-plane Off-axis Compression Tests

Numerical model of quasi-static and dynamic off-axis tests were summarized in the next sections.

3.6.1. Simulation of Quasi-static Compression Tests of Out-of-plane Off-axis Samples

Figure 3.12 shows numerical quasi-static compression model of out-of-plane off-axis samples, namely 0°,15°,30°,45°,60°,75° and 90°. The compression model of each off-axis direction includes two steel platens and an off-axis sample. The top platen was free to move along the z-direction while the translational and rotational motion of the bottom one was constrained in all directions by using SPC_SET card.

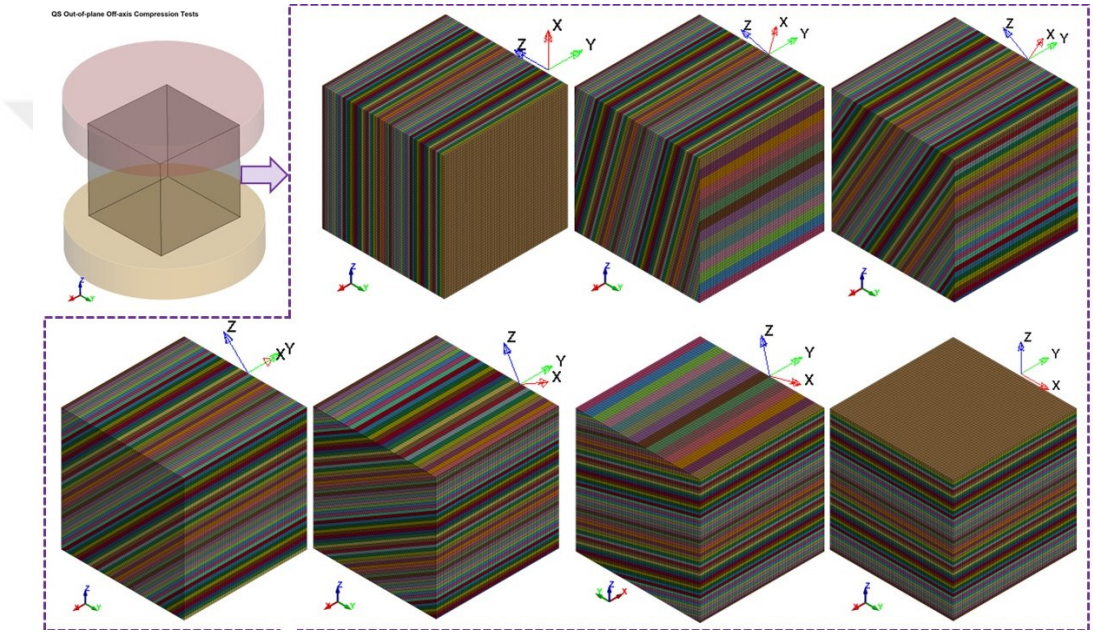

Figure 3.12. Numerical quasi-static compression tests of out-of-plane off-axis samples

The material of the platens was assigned as MAT_ELASTIC. The velocity curve was defined to the top one by using BOUNDARY_PRESCRIBED_MOTION_SET. ERODING_SINGLE_SURFACE contact was applied between the layers of the composite sample by creating a part set while AUTOMATIC_NODES_TO_SURFACE contact was applied between the composite and the top platen, and the between the composite and the bottom platen. The compressive stress was calculated from the contact history. While, the compressive strain was determined from the node defined in DATABASE_HISTORY_NODE. In the 0-degree model, the composite was of fifty-three layers, and the material coordinate system was specified by using AOPT 2 option of MAT_162 material model. For this in-plane compression model A and D vectors used in the definition of the material coordinate system were defined as (0,0,1) and (1,0,0),

respectively. For the through-thickness direction, these vectors were specified as (1,0,0) and (0,1,0), respectively. The material coordinates of the other out-of-plane off-axis samples (15°,30°,45°,60° and 75°) were specified by using DEFINE_COORDINATE _NODES.

3.6.2. Simulation of Dynamic Compression Tests of Out-of-plane Off-axis Specimens

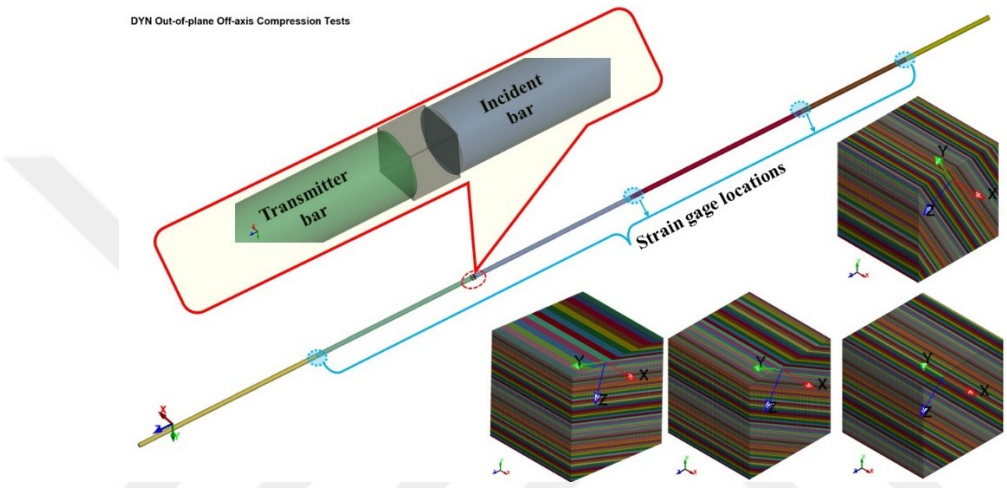

Figure 3.13. Simulation of dynamic compression tests of out-of-plane off-axis samples

Split Hopkinson pressure models of out-of-plane off-axis specimens can be seen in Figure 3.13. The model involves an incident bar, a transmitter bar and out-of-plane off-axis specimens. Numerical models of four off-axis tests (15°,30°,45° and 60°) were prepared to verify the material model constants calculated from experiments. While simulations were only performed for cubic ones, cylindrical off-axis specimens were not modeled because such geometries are difficult to mesh. For contact between the incident bar-the specimen and the transmitter bar-specimen AUTOMATIC_NODES_TO_ SURFACE was employed while ERODING_SINGLE_SURFACE contact was used between the layers of the composite specimen. By using DATABASE_HISTORY_ SOLID card, the elements placed in the strain gage locations were defined to obtain the stress occurring in the bars, and to compare the experimental and numerical bar stresses. By using the displacements of the two nodes in the loading direction compressive strain was calculated. These nodes were defined in DATABASE_HISTORY_NODE, and taken

from the face, close to specimen-bar interface, of the incident and the transmitter bar. The loading was applied to the incident bar as explained in 3.3.3.

3.7. Simulation of Quasi-static Punch Shear Tests

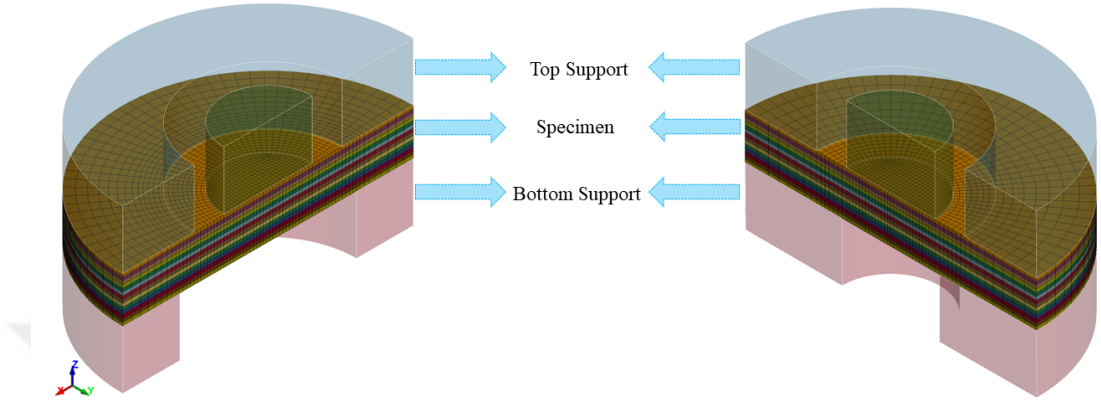

Figure 3.14. Quasi-static punch shear test models

Numerical model of the quasi-static punch shear tests can be seen in Figure 3.14 for the support to span ratio (SPR) of 1.1 and 2.0. For both numerical models the same settings were used. Both models consist of a bottom support, a top support and a composite specimen. The top support, the bottom support and the punch was model by using MAT_RIGID material model. The dimensions of the top supports, punch and the specimen were the same, but the inner diameters of the bottom part were different to obtain two different SPR ratios, namely 1.1 and 2. A pre-load of 5 kN was applied to the top parts by using BOUNDARY_PRESCRIBED_MOTION_RIGID card since in the experiments the top part was fixed to the bottom part by bolts. Because of the modeling of the half of the tests a symmetry plane was defined by using BOUNDARY_SLIDING _PLANE. CONTACT_AUTOMATIC_SURFACE_TO_SURFACE contact was used between the top support-the specimen and the bottom support-the specimen. While, ERODING_SURFACE_TO_SURFACE was selected to model contact between the layers of the composite and the punch. A node on the front surface - close to the specimen-punch contact interface-of the punch was specified to measure displacement, and force was determined by using the contact history in the loading direction.

3.8. Simulation of Flexural Test Models

Figure 3.15 shows the numerical model of a three-point bending test. The model includes two supporting pins, one loading pin and a flexural test specimen. Two different element number through the thickness were investigated, namely, one element per layer and three elements per layer. The support and loading pins were created by using RIGIDWALL_GEOMETRIC_CYLINDER_DISPLAY and RIGIDWALL_GEOMETRIC_CYLINDER_MOTION_DISPLAY, respectively. ERODING_SINGLE_SURFACE contact was only defined between the layers of the composite. The force and displacements histories were obtained from the rigid-wall histories in the loading direction.

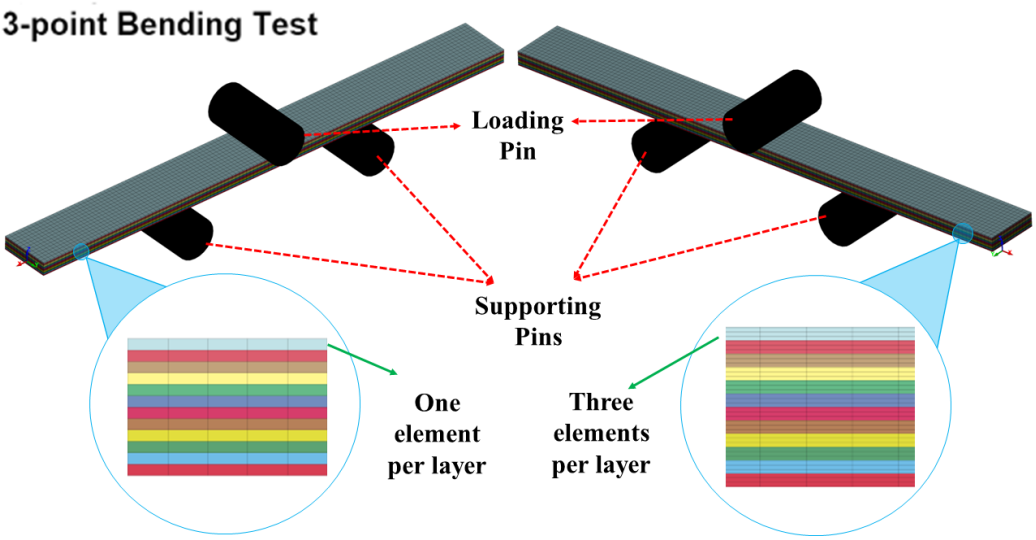

Figure 3.15. 3-point bending test models using solid elements

3-point bending simulation using the shell element can be seen in Figure 3.16. As in the solid element model, in the shell element models there are a loading pin, supporting pins and a flexure test specimen. The specimen was meshed with sizes of 1x1 mm and 2.5x2.5 mm to investigate the mesh size effect. MAT_RIGID material model was selected for the supporting and loading pins. The translational and rotational movement of the supporting pins were constrained by using BOUNDARY_SPC_SET card. The velocity of the loading pin was defined by BOUNDARY_PRESCRIBED_MOTION_RIGID card. For the contact between the loading pin and the specimen, and the supporting pins and

the specimen CONTACT_AUTOMATIC_SURFACE_TO_SURFACE contact was defined.

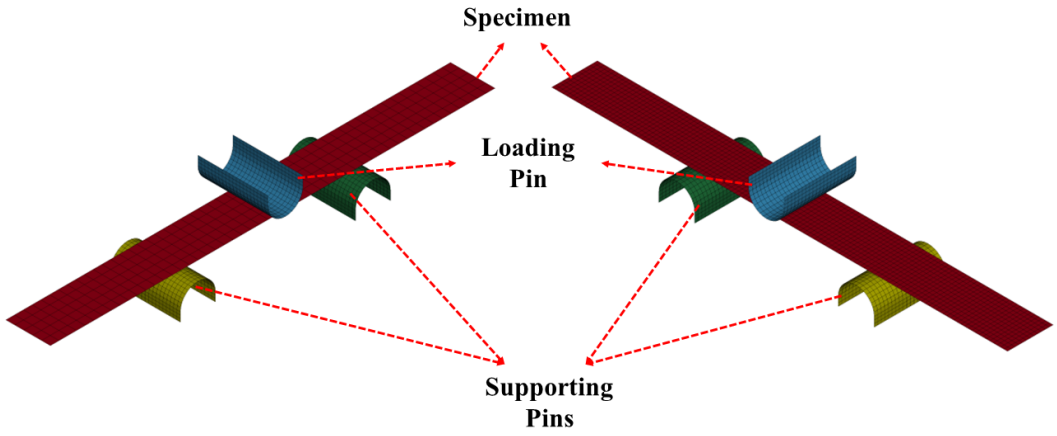

Figure 3.16. 3-point bending test models using shell elements

3.9. Simulation of Ice Impact Tests

Numerical model of ice impact tests (Figure 3.17) was established for the composites with thicknesses of 0.8 mm and 2 mm subjected to single and multiple impacts. Both numerical models consisted of a composite test specimen, an ice sphere and a steel fixture. The diameter and mass of the ice sphere were 2 g and 16 mm, respectively. The specimen was fixed from its four points in which the clamps were positioned. In the single impact case, a composite with a thickness of 0.8 mm was impacted by an ice sphere while ice spheres hit a 2 mm composite specimen in multiple impact cases. In both simulation the composite specimens were impacted at an impact velocity of 95 m/s, which was the same as the one used in the experiment. Unlike the single impact model, the multiple impact model involved three ice spheres having the same mass. A distance of 0.475 m between the ice spheres was determined by multiplying the impact velocity (95 m/s) by a specific time of 0.005 s. The time at which the oscillation of the composite was completed after impact was calculated from the single impact models. AUTOMATIC_NODES_TO_SURFACE contact was employed between the composite specimen and steel fixture while ERODING_NODES_TO_SURFACE was selected between the ice sphere(s) and the composite. Ice spheres with a mass of 2g and a diameter of 16 mm were created by using SPH_GENERATION tool of LSPREPOST. The total number of SPH element was 2176. MAT_PLASTICITY_COMPRESSION

_TENSION_EOS and TABULATED_COMPACTION was used for the material model and equation of state definition of the ice sphere. The material model constants and EOS parameters were directly taken from the literature[109].

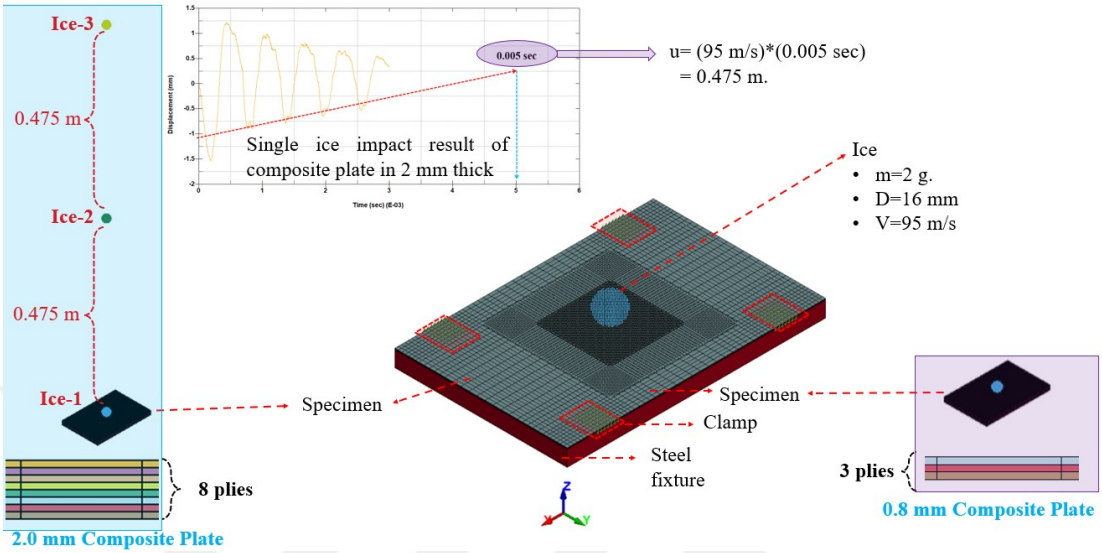

Figure 3.17. Single and Multiple Ice Impact Models

3.10. Simulation of Low-velocity Impact Tests

Numerical model of low-velocity impact test can be seen in Figure 3.18. The model consists of a striker, a steel fixture with a square cutout and the specimen. The impact simulations were performed at different striker velocities f– 3.5 m/s and 7 m/s- and at different impact energies – 35.525 Joule and 68.6 Joule- for penetration and perforation cases. In the perforation case, the same impact velocity (3.5 m/s) and a total mass of 2.8 kg as the experiment were employed, corresponding an impact energy of 17.16 Joule while for the penetration case an impact velocity of 3.5 m/s and a total mass of 5.8 kg were used to impact the composite specimen. The corresponding impact energy was of 35.525 Joule.

In the solid element models, the steel frame and the striker were modeled as a RIGID material. The striker velocity was set by using INITIAL_VELOCITY_RIGID_BODY card while the mass was added to the striker by using ELEMENT_MASS card. For this purpose, a node of the striker was selected, the mass required to obtain the same amount of total mass as that in experiments was added by considering the mass of striker itself. While AUTOMATIC_NODES_TO_SURFACE

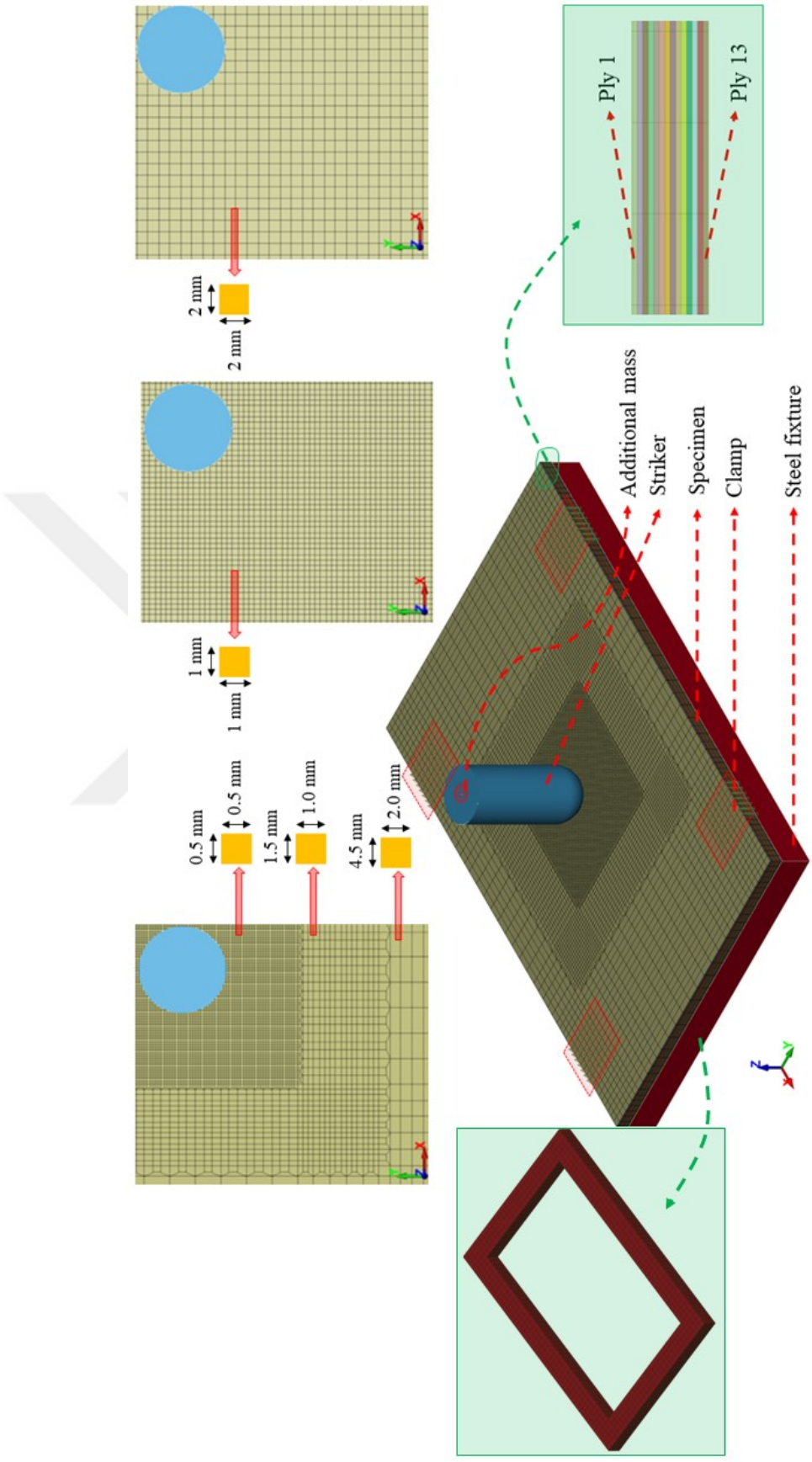

Figure 3.18. Numerical solid element model of low-velocity impact tests

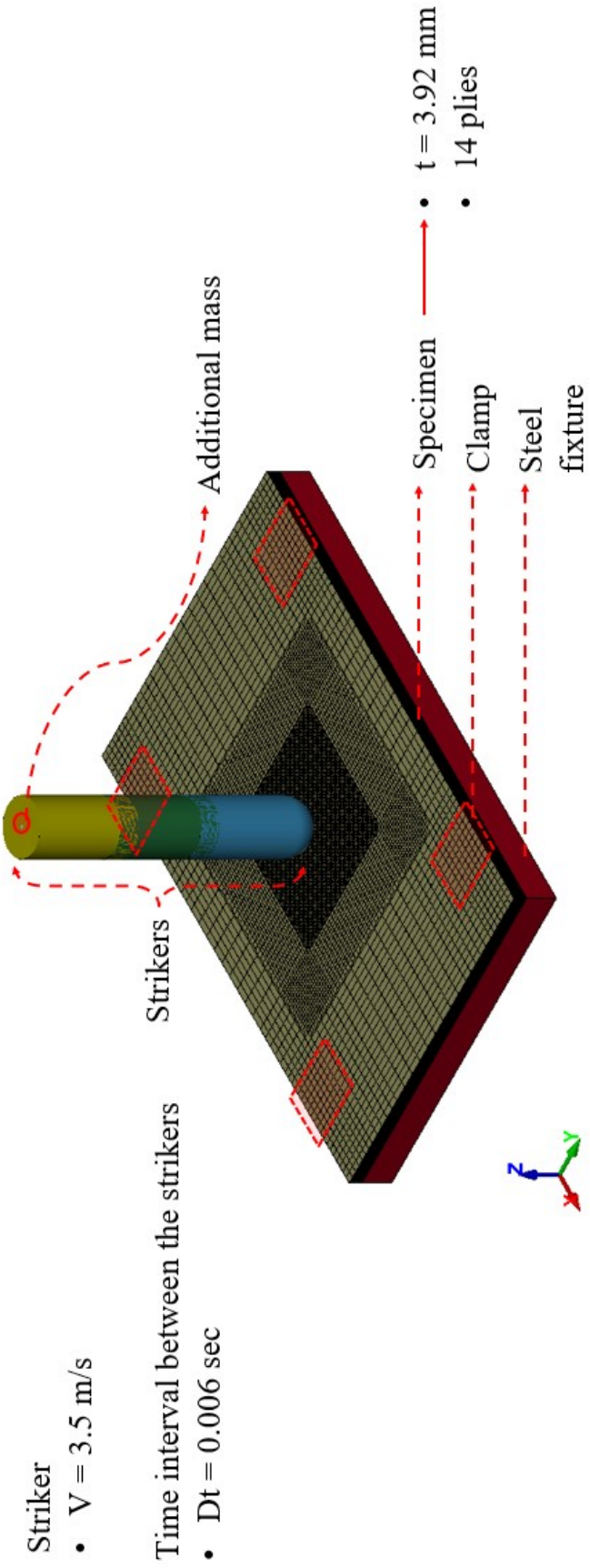

Figure 3.19. Numerical solid element model of low-velocity multi-hit impact tests

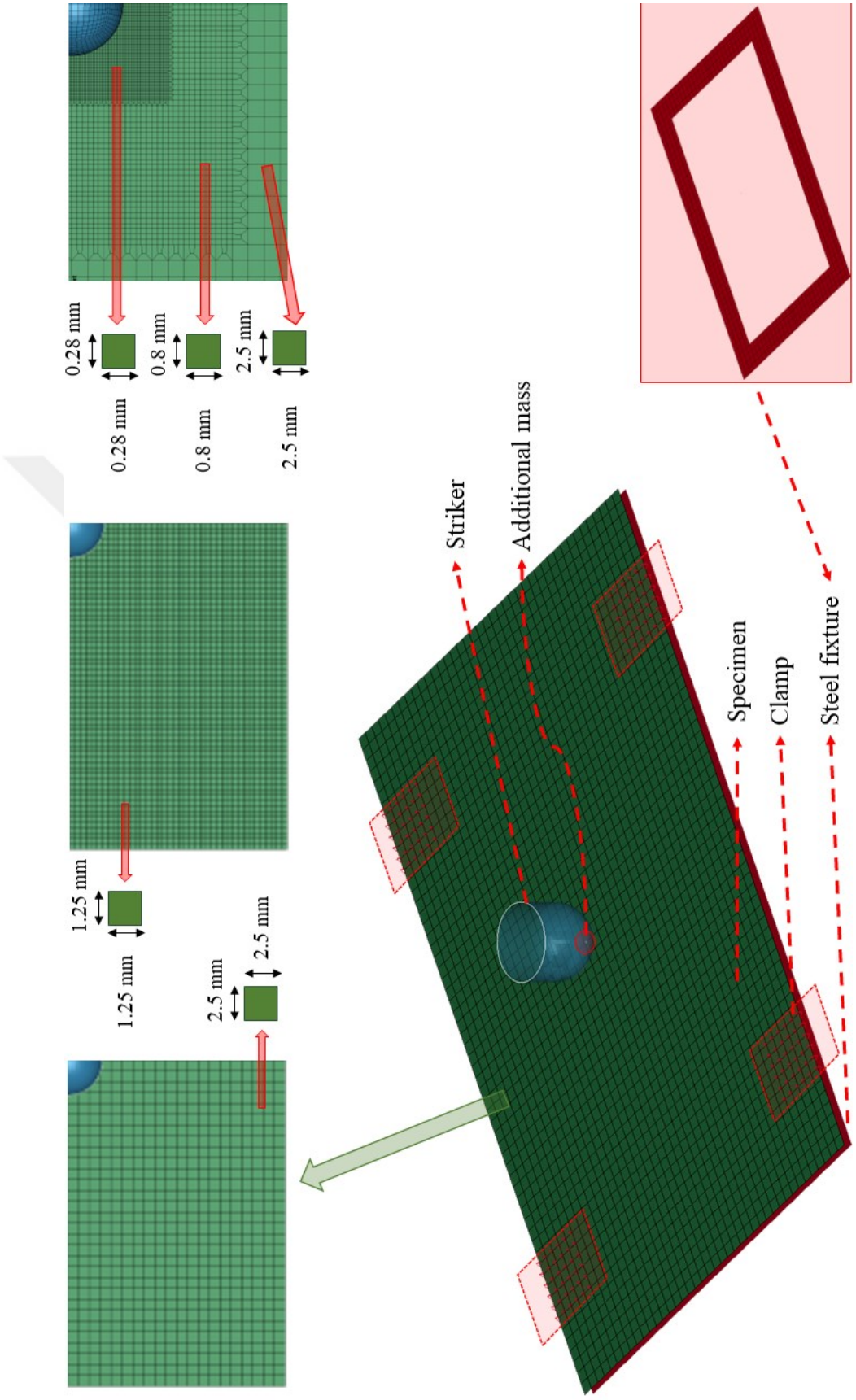

Figure 3.20. Numerical shell element model of low-velocity impact tests

contact was employed between the composite and steel fixture, ERODING_NODES_TO_SURFACE contact was set between the striker and the composite. In addition, the nodes the clamp positions in experiments were set as NODE_SET, the translational and rotational movements of this node set was then constrained by using BOUNDARY_SPC_SET card. To investigate the effect of the element size, the composite plate was meshed with quad selected, the mass required to obtain the same amount of total mass as that in experiments was added by considering the mass of striker itself. While AUTOMATIC_NODES_TO_SURFACE contact was employed between the composite and steel fixture, ERODING_NODES_TO_SURFACE contact was set between the striker and the composite. In addition, the nodes the clamp positions in experiments were set as NODE_SET, the translational and rotational movements of this node set was then constrained by using BOUNDARY_SPC_SET card. To investigate the effect of the element size, the composite plate was meshed with quad elements of sizes of 1x1 mm and 2x2 mm as well as a quad element of minimum sizes of 0.5x0x5 mm with transition mesh. Besides, the low-velocity multi-hit simulations (Figure 3.19) was also established in a similar way to the experiment mentioned in Section 2.3.13. A finer mesh was preferred around the impact zone as noted above (single impact case). The multi-hit numerical model consisted of three impactors, specimens and steel fixture, similar to the single impact case. The only difference between these simulations was that a time interval of 0.006 sec between the strikers with a velocity of 3.5 m/s was employed to simulate multiple impacts.

Shell element models includes a striker, a bottom support and a composite specimen (Figure 3.20). The specimen was meshed with 1.25x1.25 mm and 2.5x2.5 mm quad elements. The mesh of the specimen at the impact zone was refined by using the mesh transition in a such way that the element size at the impact zone was 0.28 mm while it was of 2.5 mm near the free edges of the composite laminate. As in the solid element model, the striker and the bottom support were modeled as a rigid material, and MAT_RIGID material model was defined for these parts, and the nodes the clamp positions were constrained by using BOUNDARY_SPC_SET card. AUTOMATIC_SURFACE_TO_SURFACE contact was employed between the composite and striker, the composite and the bottom support. INITIAL_VELOCITY_RIGID_BODY card was used to set the striker velocity. To add additional mass of the striker ELEMENT_MASS card was specified.

3.11. Foreign Body Impact Simulations

In the foreign body impact simulations two cases were considered. They were a bird impact model and a drone impact model. These models in which a component of the helicopter, forward cowling, were impact by bird and drone can be seen in Figure 3.21. The geometry of forward cowling was taken from the grabcad[110], and then meshed with Hypermesh. Woven carbon fiber composite with 10 plies investigated in this study was assigned for the material of the forward cowling. The shell element composite material model, MAT_LAMINATED_COMPOSITE_FABRIC, was employed in modeling of the cowling and the ply orientation of the composite was defined using PART_COMPOSITE card. The material constants were determined from the results obtained in the experimental part of the study. In the simulations, the transitional and rotational motion of the nodes located on the boundary of the cowling structure was constrained using BOUNDARY_SPC_SET card in LSPREPOST.

In the drone impact model, the drawing of the drone was taken from the grapcad[111] and its finite element mesh was generated using Hypermesh. The material models in use of the modeling of the drone in finite element as well as their constants were taken from the study performed by FAA[68]. More information on material models as well as their calibration and validation can be found in the study[68]. The contact between the drone and the cowling was defined using ERODING_NODES_TO_SURFACE contact card in LSPREPOST. The mass and the impact velocity of the drone were 1.2 kg and 150 m/s, respectively.

In the bird strike model, the bird[112] with a diameter of 0.0934 m and a mass of 1 kg was created by SPH_GENERATION tool in LSPREPSOT and modeled with MAT_NULL material model with EOS_GRUNEISEN equation of state. The constants for the material model and equation of state of the bird was taken from the open literature[113]. ERODING_NODES_TO_SURFACE contact was defined between the cowling and the bird. The impact velocity of the bird was 150 m/s, and it was defined using INITIAL_VELOCITY_NODE card.

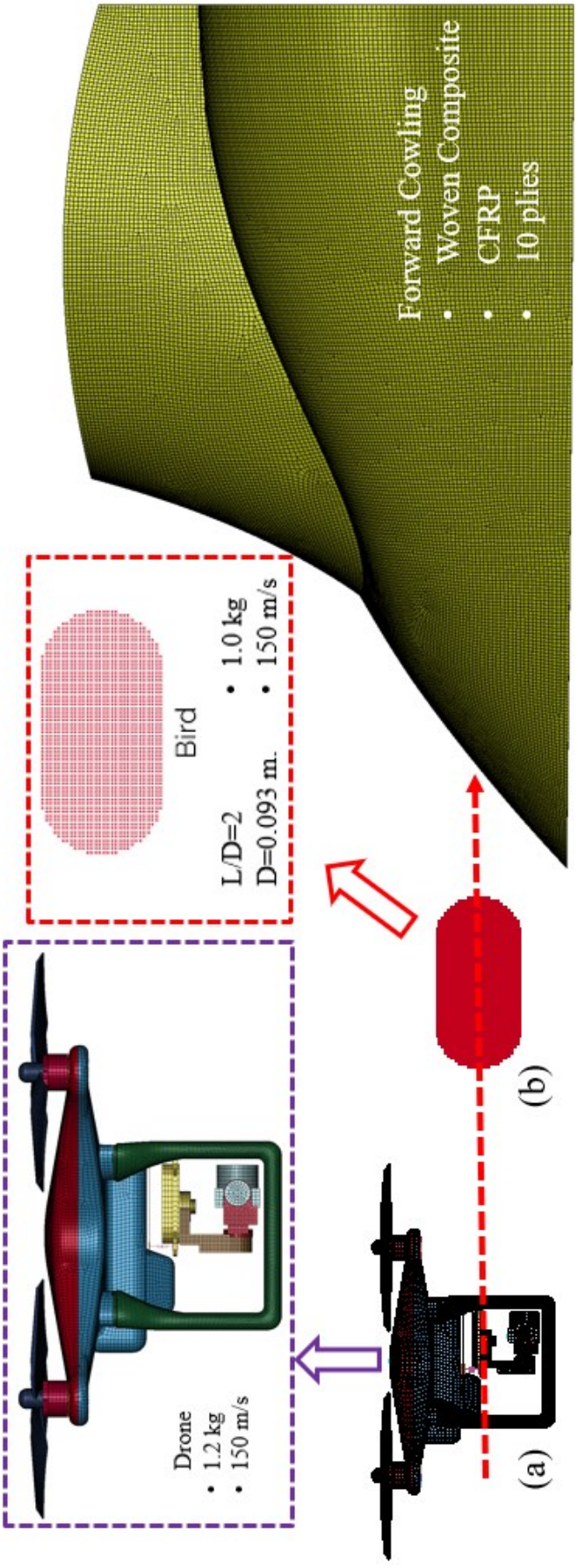

Figure 3.21. (a) Drone impact model and (b) Bird strike model

CHAPTER 4

EXPERIMENTAL RESULTS

In this section results obtained from tests mentioned a previous section were presented and expressed sequentially.

4.1. Density and Volume Fraction Calculation Results

Density and volume fraction test results were presented in the following sections.

4.1.1. Density Test Results

Table 4.1. Density calculation results

	m_1 (g)	m_2 (g)	m_3 (g)	ρ_c (g/cm^3)	Avg. ρ_c (g/cm^3)
Sample-1	3.3081	1.205	3.3117	1.57028	1.57051
Sample-2	3.365	1.225	3.3673	1.57074	

ρ_c (g/cm^3) : density of the specimen
m_1 : apparent mass of specimen, without wire or sinker, in air
m_2 : apparent mass of specimen (and of sinker, if used) completely immersed and of the wire partially immersed in liquid
m_3 : dried mass of the specimen after immersion
ρ_w (g/cm^3) : density of water **(1 g/cm^3)**

Table 4.2. Datasheet of carbon fiber epoxy composite (Source: HexPly[85])

	Units	AGP 280-5H
Fibre Type	–	AS4 3K
Fibre density	g/cm³ (lb/in³)	1.77 (0.065)
Weave	–	5HS
Mass	g/m² (oz/yd²)	286 (8.44)
Weight Ratio, Warp : Fill		50 :50
Nominal cured ply thickness @ 37% resin content	mm (inch)	0.289 (0.0114)
Nominal Fibre Volume	%	55.29
Nominal Laminate Density	g/cm³ (lb/in³)	1.57 (0.057)

In addition to the initial, wet and dried mass of carbon fiber composite samples, the average calculated density is presented in Table 4.1. The manufacturer datasheet can

also be seen in Table 4.2. From samples examined, the average density of carbon fiber composite was determined as 1.570 g/cm^3. The determined density value is ascertained to be the same as the value shown in the datasheet.

4.1.2. Volume Fraction Calculation Results

Table 4.3. Weight and volume fraction determination results

Group Name	$m_{initial}$	m_{fiber}	W_r (%)	Avg. W_r (%)	Vol (%)	Avg. Vol (%)
16	3.3565	2.2441	66.9		58.6	
17	3.4163	2.1112	61.8	65.4	54.2	57.4
18	3.3286	2.2527	67.7		59.4	

$m_{initial}$: initial mass of the specimen
m_{fiber} : final mass of the specimen after digestion or combustion
W_r (%) : weight percentage of reinforcement
Vol (%) : volume percentage of reinforcement

Table 4.3 shows the weight percentage and volume percentage results of the carbon fiber composite tested as well as the initial mass and the calculated mass after digestion of epoxy resin. The average weight and volume percentage were calculated as 65.4 % and 57.4 %, respectively. The calculated volume percentage was found to be similar to the value provided by the manufacturer. It is depicted in Table 4.2.

4.2. Tensile Test Results

The standard and strain rate test results performed in the in-plane and through-thickness directions were explained in the next sections.

4.2.1. Standard Tensile Test Results

Elastic modulus, tensile strength, longitudinal and transverse failure strains, and Poisson's ratio are depicted in Table 4.4 for carbon composite tested in the weft direction. Elastic modulus was calculated by using strains measured by both strain gages and extensometer. The average elastic modulus was determined from extensometer strain and strain gage as 67.99±1.51 GPa and 71.12±1.83 GPa, respectively. Besides, the average Poisson's ratio was found to be 0.057±0.0018 while 829.5±9.8 MPa was ascertained for

the peak stress. Lastly, the average failure extensometer strain in the longitudinal direction was determined as 0.0123 ± 10^{-4} and the average longitudinal strain of $0.01175\pm6.874x10^{-4}$ was found out from strain gages.

Elastic modulus, tensile strength, longitudinal and transverse failure strains, and Poisson's ratio are depicted in Table 4.4 for carbon composite tested in the weft direction. Elastic modulus was calculated by using strains measured by both strain gages and extensometer. The average elastic modulus was determined from extensometer strain and strain gage as 67.99±1.51 GPa and 71.12±1.83 GPa, respectively. Besides, the average Poisson's ratio was found to be 0.057±0.0018 while 829.5±9.8 MPa was ascertained for the peak stress. Lastly, the average failure extensometer strain in the longitudinal direction was determined as 0.0123 ± 10^{-4} and the average longitudinal strain of $0.01175\pm6.874x10^{-4}$ was found out from strain gages.

Table 4.4. Tensile test results of the coupons in the weft direction

E_{WE}=67.99 GPa υ_{WE} = 0.057	Elastic Modulus (GPa)		Failure Strain (mm/mm)			Poisson's Ratio	Peak Stress (MPa)
				Strain Gage			
	EXT	SG	EXT	Long.	Transv.		
TEN-WE-SD-Test_1	67.98	71.61	0.0124	0.0118	1.371E-4	0.0132	835.6
TEN-WE-SD-Test_2	69.23	69.23	0.0123	0.0117	3.368E-4	0.0287	834.3
TEN-WE-SD-Test_3	69.47	70.20	0.0124	0.0126	5.194E-4	0.0558	838.1
TEN-WE-SD-Test_4	67.58	73.44	0.0122	0.0109	6.196E-4	0.0584	814.4
TEN-WE-SD-Test_5	65.71	N.A.	0.0122	N.A.	N.A.	N.A.	825.0
Mean	67.99	71.12	0.0123	0.01175	4.03232E-4	0.0571	829.5
Std Dev	1.51	1.83	0.0001	6.87459E-4	2.12573E-4	0.0018	9.8
COV (%)	2.22	2.57	0.94	5.85	52.72	3.20	1.18

Table 4.5 shows elastic modulus, tensile strength, longitudinal and transverse failure strains, and Poisson's ratio of the warp direction of carbon laminate. Elastic modulus was calculated by performing the same steps as that used in the weft direction. The average elastic modulus was ascertained 61.92±1.15 GPa and 71.57±5.02 GPa from extensometer and strain gage strains, respectively. In addition, the average Poisson's ratio was determined as 0.0522±0.0116 while 732.0±42.9 MPa was ascertained for the peak stress. Lastly, the average failure extensometer and strain gage strains in the longitudinal direction were determined as 0.012±0.0008 and 0.01037±0.00131, respectively.

Stress versus strain curves for both the warp and weft direction can be seen in Figure 4.1 and Figure 4.2. In these figures it is seen that carbon fiber composite in these directions shows a linear stress strain behavior, and a brittle failure mode is also observed

Table 4.5. Tensile test results of the coupons in the warp direction

E_{WA}=61.92 GPa υ_{WA} = 0.052	Elastic Modulus (GPa)		Failure Strain (mm/mm)			Poisson's Ratio	Peak Stress (MPa)
	EXT	SG	EXT	Strain Gage Long.	Strain Gage Transv.		
TEN-WA-SD-Test_1	60.74	76.79	0.0111	0.0086	7.453E-4	0.0620	666.5
TEN-WA-SD-Test_2	61.12	74.59	0.0128	0.0103	1.698E-4	0.0233	772.2
TEN-WA-SD-Test_3	76.76	73.49	0.0109	0.0064 *	3.695E-4 *	0.0553	744.4
TEN-WA-SD-Test_4	62.98	68.65	0.0122	0.0116	1.526E-4	0.1675	763.3
TEN-WA-SD-Test_5	62.82	64.33	0.0117	0.0110	4.335E-4	0.0394	713.5
Mean	61.92	71.57	0.0117	0.01037	4.49532E-4	0.0522	732.0
Std Dev	1.15	5.02	0.0008	0.00131	2.88047E-4	0.0116	42.9
COV (%)	1.86	7.02	6.61	12.61	64.08	22.20	5.87

for these composites since stress values become zero after they reach the peak values. From failed test coupons in Figure B.1 (a) and Figure B.1 (b), it is discovered that there is no effect of shear on failure behavior because the cross-section in which failure occurs is flat, meaning that fracture takes place along a straight line, which is perpendicular to the loading direction.

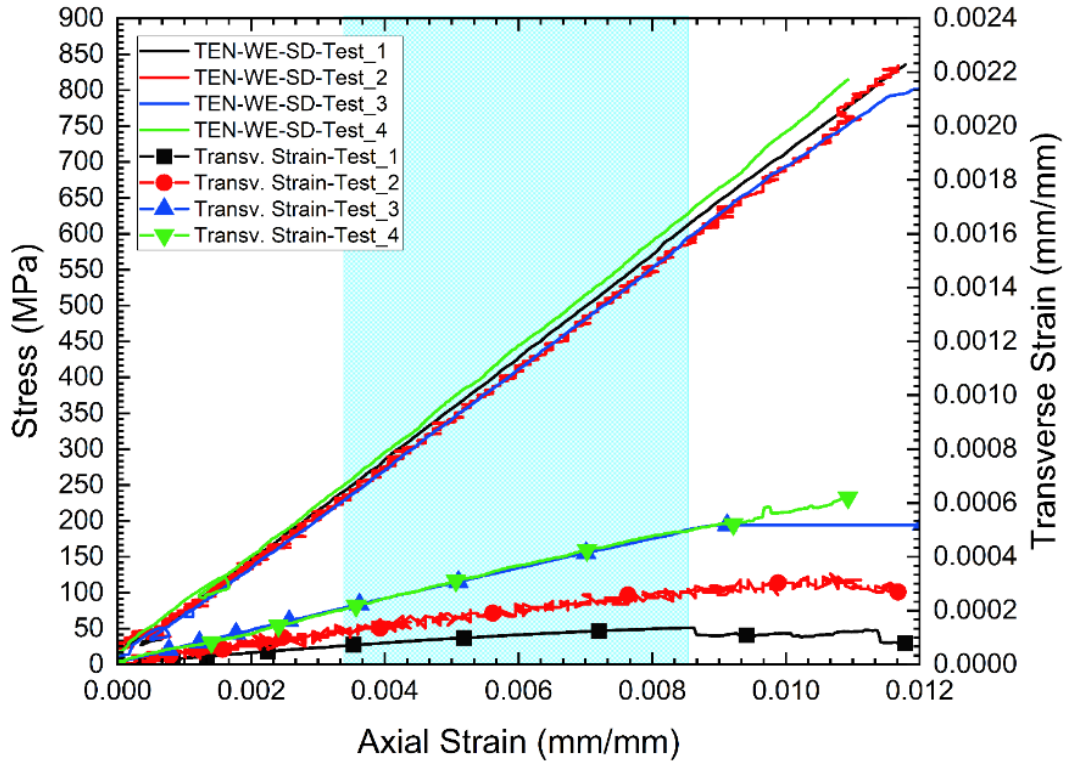

Figure 4.1. Tensile stress versus strain curves of composite in the weft direction

In the determination of the tensile properties in the through thickness direction, five flatwise tensile test specimens are tested according to the related test standard. One of the five tests performed is found to be valid. In the other four tests, the failure occurs in the adhesive layer bonding the flatwise tensile specimen to aluminum shank as shown in Figure 4.3 (a) and (b). Stress-displacement result of one of the invalid tests can be seen in Figure 4.3 (c). The stress at failure is calculated as 15 MPa. Since adhesive failure occurs, the expected strength is not obtained.

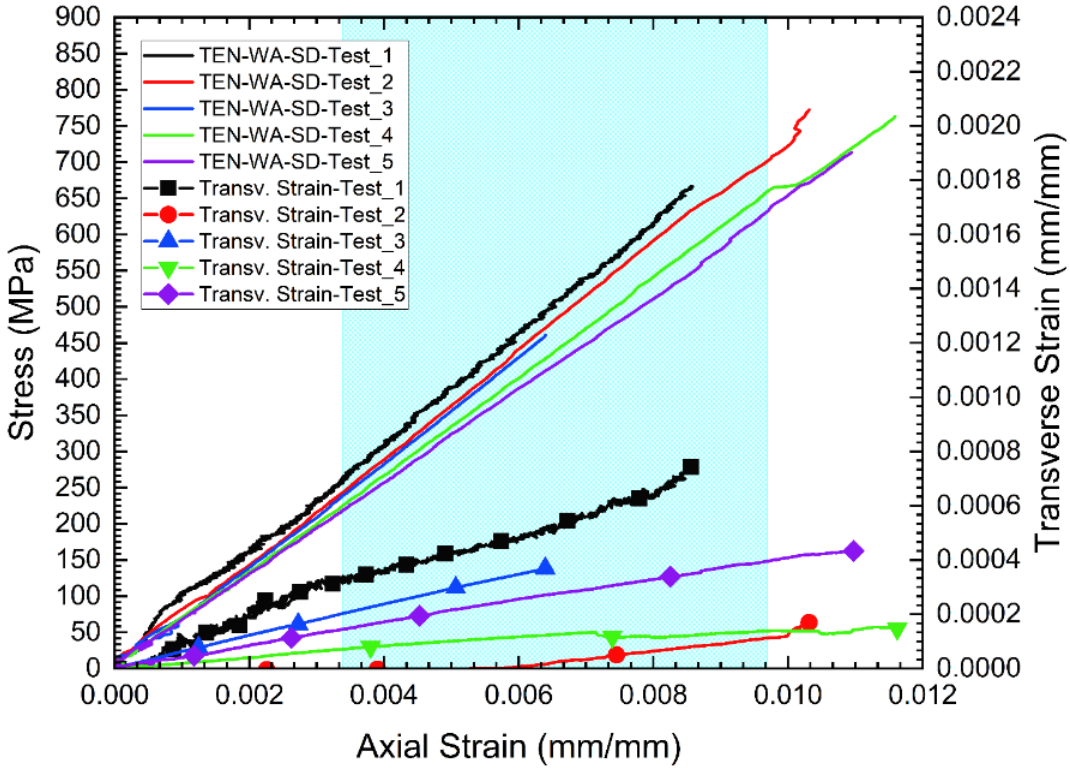

Figure 4.2. Tensile stress versus strain curves of composite in the warp direction

Due to the fact that the invalid number of the test is more, tensile strength is also investigated by Brazilian method[58]. The results obtained from both the standard tests and Brazilian test can be seen in Figure 4.3. As can be seen in the figure, the tensile strength determined by both methods is almost the same with each other. The average tensile strength is calculated as 38 MPa. Based on the standard tensile test results, the through-thickness elastic modulus and the failure strain are determined to be 7 GPa and 0.0046 mm/mm, respectively.

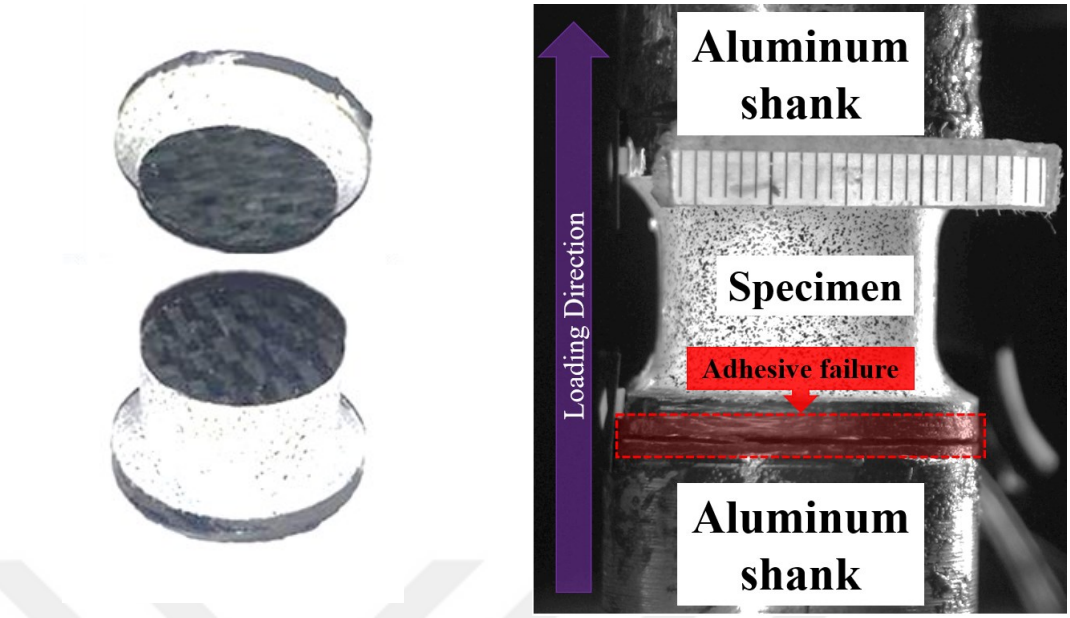

(a) (b)

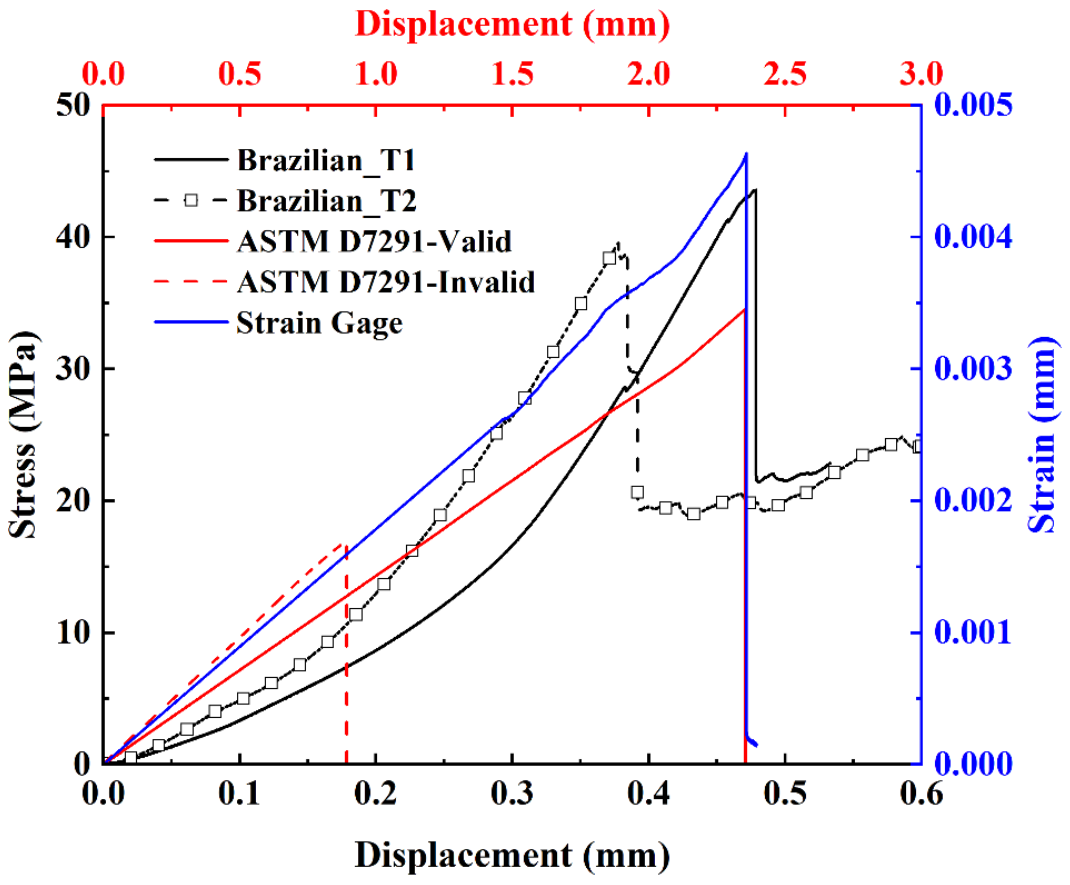

(c)

Figure 4.3. Specimen pictures taken from (a) the valid test and (b) the invalid test, and (c) Tensile stress-tensile strain versus displacement curve

4.2.2. Quasi-static Strain Rate Test Results

The results of the tensile test performed at quasi-static strain rates were explained in detail in Section 5.1.

4.2.3. High Strain Rate Test Results

The results of the tensile test performed at high strain rates were explained in detail in Section 5.1.

4.3. Compression Test Results

The results obtained from the standard compression tests and strain rate tests were presented in the next sections.

4.3.1. Standard Compression Test Results

Table 4.6. Compression test results of the coupons in the weft direction

E_{WE}= 58.55 GPa υ_{WE} = 0.0577	Axial Failure Strain (mm/mm)		Transv. Failure Strain (mm/mm)	Comp. Modulus (GPa)		Comp. Strength (MPa)	Poisson's Ratio
	DIC	SG	SG	DIC	SG		
COMP-WE-SD-Test_1	0.011	0.013	7.01008E-4	56.55	59.34	747.2	0.0577
COMP-WE-SD-Test_2	0.011	N.A.	N.A.	55.72	N.A.	642.6	N.A.
COMP-WE-SD-Test_3	0.014	N.A.	N.A.	58.75	N.A.	693.4	N.A.
COMP-WE-SD-Test_4	0.012	N.A.	N.A.	54.92	N.A.	639.3	N.A.
COMP-WE-SD-Test_5	0.014	0.011	4.36542E-4	57.90	57.748	704.1	0.0452
Mean	**0.012**	**0.012**	**5.68775E-4**	**56.77**	**58.55**	**685.3**	**0.0577**
Std Dev.	**0.001**	**0.001**	**1.87006E-4**	**1.56**	**1.13**	**45.3**	--
COV (%)	**11.864**	**6.442**	**32.87868**	**2.75**	**1.93**	**6.6**	--

Table 4.6 shows axial and transverse failure strain, compressive strength and modulus as well as Poisson's ratio for the composite tested in the weft direction. Stress strain curves and failed specimens are shown in Figure 4.5 - Figure 4.5 and Figure B.2 (a), respectively. Stress strain curves showed a linear behavior the same as that of tensile tests. All the specimens tested in that direction were found to be fail under a shear failure

mode because the failure plane was observed to be 45° to the loading direction. According to ASTM failure identification (Figure A.2), failure of all samples was coded as M(HT) (Multi-mode (through-thickness, transverse shear))-G(gage)-M(Middle). Moreover, the average compression strength and modulus for the weft direction were calculated as 685.3±45.3 MPa and 56.77±1.56 GPa, respectively. In addition to that, while the average axial failure strain was determined as 0.012 ± 10^{-3}, and Poisson's ratio was found to be 0.0577, respectively. Failure strain and Poisson's ratio ascertained in the compression test for the weft direction was found out to be similar to those obtained in tensile tests.

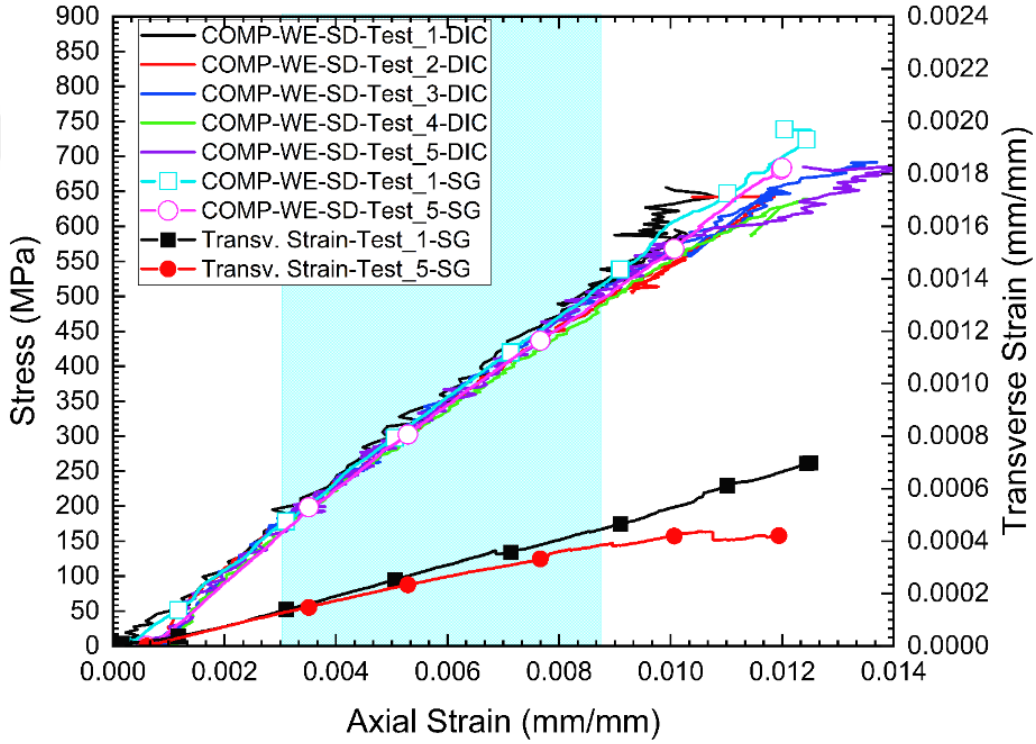

Figure 4.4. Compressive stress versus strain curves of composite in the weft direction

The calculated elastic properties of carbon fiber composite in the warp direction can be seen in Table 4.7. Stress versus strain plots of coupons in that direction as well as the deformed test coupons are listed in Figure 4.5 (b) and Figure B.2 (b), respectively. In addition to the failure identification code, the main deformation or failure modes were found to be the same as those observed in the weft direction — the main failure mode was shear while the failure identification code was M(HT) (Multi-mode (through-thickness, transverse shear))-G(gage)-M(Middle). As opposed to the weft coupons, no strain gages were employed. All the expressions or values related to displacement and

strain were calculated from DIC measurements. Average compressive strength, modulus and axial failure strain were therefore calculated as 564.3±20 MPa, 53.35±1.38 GPa and 0.01, respectively.

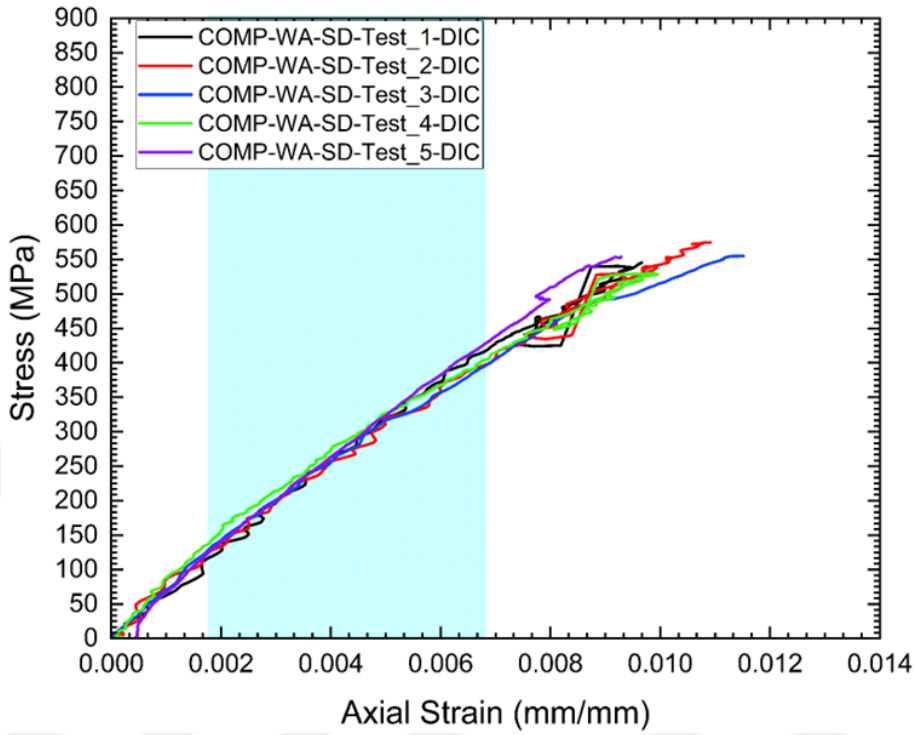

Figure 4.5. Compressive stress versus strain curves of composite in the warp direction

Compared to the weft directions, lower average strength and modulus values were obtained in the warp direction while a similar average failure strain value was observed for in-plane directions as with the weft and warp results of tensile test — tensile strength and modulus in the warp direction was lower than those in the weft direction. The reason to obtain lower mechanical properties in the warp direction than that in the weft direction could be the wearing of the warp fibers during the weaving process.

4.3.2. Quasi-static Strain Rate Test Results

Table 4.8 illustrates the compressive test results of weft samples at different quasi-static strain rates. The peak stress, elastic modulus and failure strain were calculated for each cubic sample at each strain rate. The values with red color indicate that they were

Table 4.7. Compression test results of the coupons in the warp direction

E_{WA}= 53.35 GPa υ_{WA} = 0.053 (calc.)	Axial Failure Strain (mm/mm)		Transv. Failure Strain (mm/mm)	Comp. Modulus (GPa)		Comp. Strength (MPa)	Poisson's Ratio
	DIC	SG	SG	DIC	SG		
COMP-WA-SD-Test_1	0.010	N.A.	N.A.	60.84	N.A.	550.0	N.A.
COMP-WA-SD-Test_2	0.011	N.A.	N.A.	54.92	N.A.	574.7	N.A.
COMP-WA-SD-Test_3	0.012	N.A.	N.A.	52.81	N.A.	555.0	N.A.
COMP-WA-SD-Test_4	0.010	N.A.	N.A.	52.31	N.A.	546.8	N.A.
COMP-WA-SD-Test_5	0.009	N.A.	N.A.	60.58	N.A.	595.0	N.A.
Mean	**0.010**	--	--	**53.35**	--	**564.3**	--
Std Dev.	**0.001**	--	--	**1.38**	--	**20.3**	--
COV (%)	**8.696**	--	--	**2.59**	--	**3.6**	--

excluded from the mean and standard deviation calculations since cubic samples failed at a lower value than expected. It was found out that as the strain rate was increased from 10^{-4} to 10^{-2} s^{-1}, failure strain, modulus and peak stress were not affected much. Weft properties were found to be independent of strain rate at the examined quasi-static strain rate range although all calculated properties at the strain rate of 10^{-2} s^{-1} were excluded. The average peak stress was found to be similar to that calculated by the standard test method while elastic modulus and failure strain were ascertained to be different. The reason could be the size of the cubic samples tested.

Table 4.8. Compression test results of the cubic samples in the weft direction at different quasi-static rates

	Failure Strain (mm/mm)	Elastic Modulus (GPa)	Peak Stress (MPa)
WE_10^{-4}_Test-1	0.0191	32.78	568.7
WE_10^{-4}_Test-2	0.0290	17.32	366.0
WE_10^{-4}_Test-3	0.0222	33.27	602.9
WE_10^{-3}_Test-1	0.0275	25.01	529.6
WE_10^{-3}_Test-2	0.0213	21.54	397.8
WE_10^{-3}_Test-3	0.0248	16.32	339.8
WE_10^{-2}_Test-1	0.0227	25.26	458.8
WE_10^{-2}_Test-2	0.0207	35.22	641.6
WE_10^{-2}_Test-3	0.0247	35.73	662.6
Mean	0.0217	34.25	618.9
Std Dev	0.0024	1.44	41.6
COV (%)	11.09	4.22	6.73

Stress strain curves generated from these tests are illustrated in Figure 4.6. In addition to the displacement and stress values at a specific time, the deformations of cubic samples over time are shown in Figure B.3 (a). In these results it can be seen that a crack occurs at the end of the sample near the loading platen when stress reaches the peak stress, it then propagates rapidly and causes samples to split axially followed by brooming. After axial splitting, shearing and brooming are also identified for all cubic samples. All failed samples tested in the weft direction at quasi-static strain rates can be found in Figure B.3 (b).

Compressive strength, elastic moduli and failure strains of the carbon fiber composite in the warp direction are depicted in Table 4.9 while stress strain curves at all quasi-static strain rates examined, the deformation of cubic samples over time and their broken parts can be seen in Figure 4.7, Figure B.4 (a) and (b), respectively. Material properties in the warp direction were found out to be independent of strain rates as with those in the weft direction. The average peak stress, modulus and failure strain were determined as 586.9±38 MPa, 34.92±2.92 GPa and 0.0194, respectively.

Table 4.9. Compression test results of the cubic samples in the weft direction at different quasi-static rates

	Failure Strain (mm/mm)	**Elastic Modulus (GPa)**	**Peak Stress (MPa)**
WA_10^{-4}_Test-1	0.0182	35.04	543.6
WA_10^{-4}_Test-2	0.0183	36.31	599.2
WA_10^{-4}_Test-3	0.0172	38.04	590.3
WA_10^{-3}_Test-1	0.0217	29.12	526.5
WA_10^{-3}_Test-2	0.0189	35.40	598.6
WA_10^{-3}_Test-3	0.0206	35.12	566.1
WA_10^{-2}_Test-1	0.0187	38.06	621.6
WA_10^{-2}_Test-2	0.0195	31.46	585.1
WA_10^{-2}_Test-3	0.0213	35.77	650.7
Mean	0.0194	34.92	586.9
Std Dev	0.0015	2.92	38.0
COV (%)	7.89	8.36	6.47

Besides, the failure mechanisms for samples in both the weft and warp directions were found to be the same, namely crack formation and propagation, and axial splitting, then shearing of fibers.

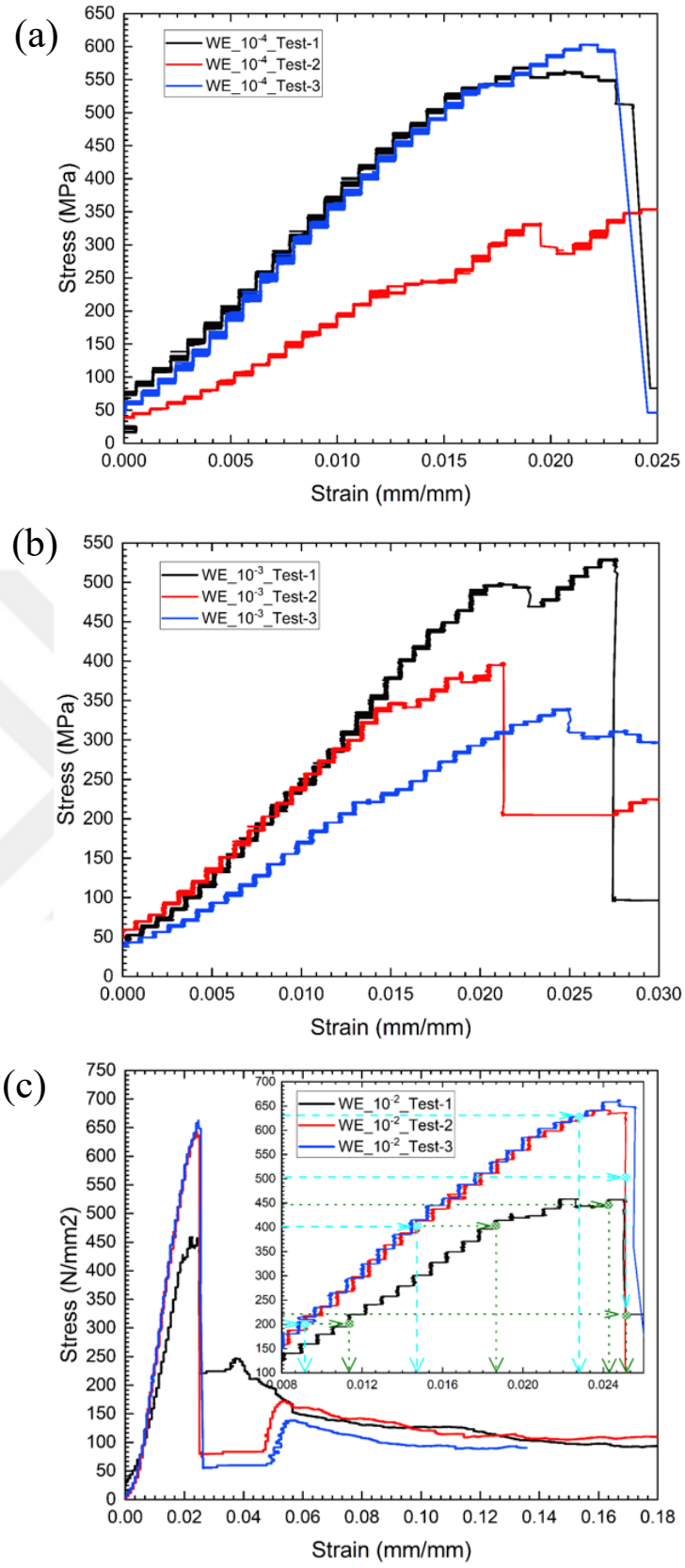

Figure 4.6. Compressive stress versus strain curves in the weft direction at (a) 10^{-4} s^{-1}, (b) 10^{-3} s^{-1} and (c) 10^{-2} s^{-1} strain rates

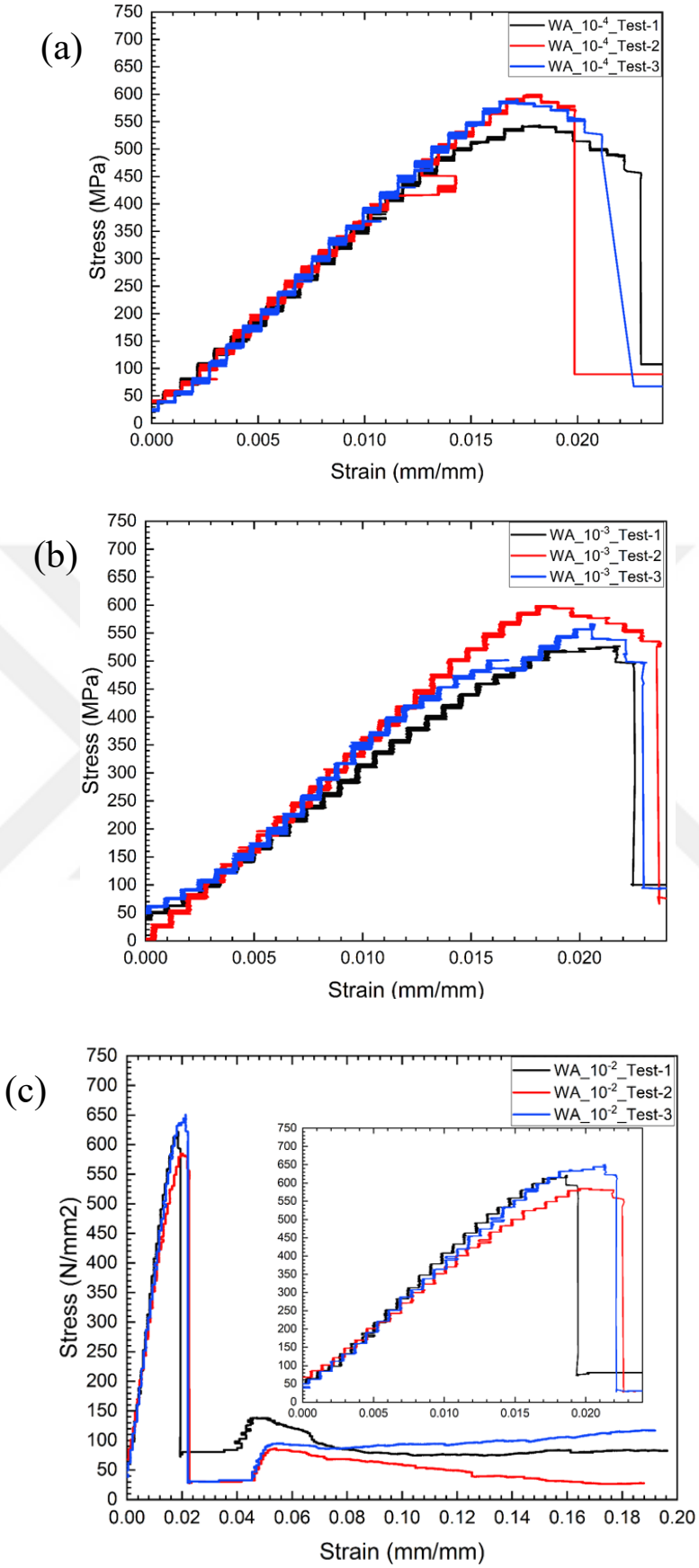

Figure 4.7. Compressive stress versus strain curves in the warp direction at (a) 10^{-4} s^{-1}, (b) 10^{-3} s^{-1} and (c) 10^{-2} s^{-1} strain rates

Table 4.10. Compression test results of the cubic samples in the through thickness direction at different quasi-static rates

	Failure Strain (mm/mm)	Elastic Modulus (GPa)	Peak Stress (MPa)
TT_10^{-4}_Test-1	0.0874	10.34	930.4
TT_10^{-4}_Test-2	0.0880	10.92	967.0
TT_10^{-4}_Test-3	0.0900	10.52	968.7
TT_10^{-4}_Test-4	0.0887	10.64	958.8
TT_10^{-3}_Test-1	0.0817	10.52	883.7
TT_10^{-3}_Test-2	0.0874	10.66	956.6
TT_10^{-3}_Test-3	0.0910	10.66	989.2
TT_10^{-2}_Test-1	0.0931	10.55	1009.9
TT_10^{-2}_Test-2	0.0859	10.82	952.8
TT_10^{-2}_Test-3	0.0794	11.20	910.8
Mean	0.0873	10.68	952.8
Std Dev	0.0041	0.24	36.7
COV (%)	4.73	2.28	3.85

Through-thickness compressive properties calculated are summarized in Table 4.10. It can be seen that peak stress, elastic modulus and failure strain do not change a lot with increasing strain rate. It can be therefore said that the effect of strain rate is negligible. The effect of strain rate on compressive properties in thickness direction was found to be the same as with those in the weft and warp directions. The average peak stress, elastic modulus and failure strain were calculated as 910.8±36.7 MPa, 10.68 GPa±0.24 and 0.0873±0.0041, respectively. In addition, the average peak stress and elastic modulus were determined as 952.8±36.7 MPa and 10.68±0.24 GPa. Stress strain curves generated can be found in Figure 4.8 whilst Figure B.4 (c) depicts tested cubic samples. The failure mode of the composite in the thickness direction was found out to be the shearing out of fiber planes followed by the fiber plane crushing. Table 4.11 presents the results of the cubic samples with end-caps in the weft and warp direction, and includes the results obtained from the compressive test of the weft samples adhered to end-caps. The average peak stress, elastic modulus and failure strain determined in the weft direction were found to be similar to those obtained in the warp direction. The average compressive properties that were calculated from both the weft and warp cubic samples with and without end-caps, and the standard test method were found out to be nearly the same except for elastic modulus and failure strain.

Table 4.11. Compression test results of the (a) weft, (b) warp samples with end-caps and (c) weft samples adhered to end-caps

(a)	Failure Strain (mm/mm)	Elastic Modulus (GPa)	Peak Stress (MPa)
WE_W(ECP)_10^{-3}_Test-1	0.0240	32.19	656.8
WE_W(ECP)_10^{-3}_Test-2	0.0297	28.99	602.3
WE_W(ECP)_10^{-3}_Test-3	0.0232	24.33	602.1
Mean	0.0256	28.50	620.4
Std Dev	0.0035	3.95	31.5
COV (%)	13.79	13.87	5.08

(b)	Failure Strain (mm/mm)	Elastic Modulus (GPa)	Peak Stress (MPa)
WA_W(ECP)_10^{-3}_Test-1	0.0296	25.39	597.7
WA_W(ECP)_10^{-3}_Test-2	0.0304	19.85	533.2
WA_W(ECP)_10^{-3}_Test-3	0.0281	22.53	593.4
Mean	0.0294	22.59	574.8
Std Dev	0.0011	2.77	36.1
COV (%)	3.86	12.25	6.28

(c)	Failure Strain (mm/mm)	Elastic Modulus (GPa)	Peak Stress (MPa)
WA_W(ECP-ADV)_10^{-3}_Test-1	0.0386	11.91	479.3
WA_W(ECP-ADV)_10^{-3}_Test-2	0.0636	12.01	613.9
WA_W(ECP-ADV)_10^{-3}_Test-3	0.0557	14.34	630.7
Mean	0.0526	12.76	574.7
Std Dev	0.0128	1.38	83.0
COV (%)	24.29	10.79	14.44

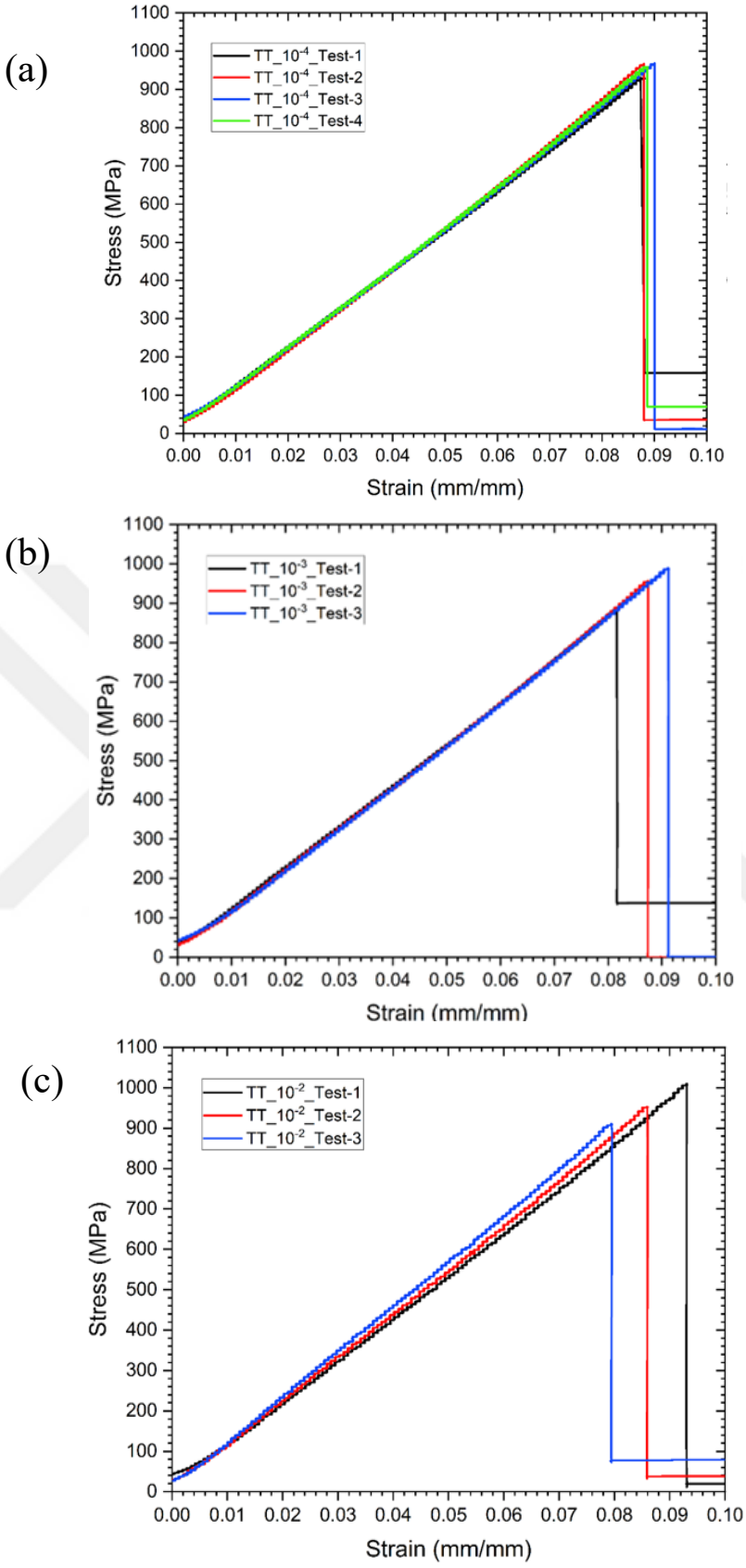

Figure 4.8. Compressive stress versus strain curves in the through-thickness direction at (a) 10^{-4} s^{-1}, (b) 10^{-3} s^{-1} and (c) 10^{-2} s^{-1} strain rates

Stress strain results of these samples with end-caps can be depicted in Figure 4.9. While, the deformed samples are illustrated in Figure B.5 (a) - Figure B.5 (c). As opposed to the samples without end-caps, the samples with end-caps deformed a complex interaction between fiber shear and delamination since brooming occurred at the ends of the samples was prevented.

4.3.3. High Strain Rate Test Results

The high strain rate results of the composites in the weft, warp and through-thickness directions are summarized in Table 4.12 (a), (b) and (c), respectively. The average strain rates are calculated as 368.5 s-1 and 826 s-1 for the weft direction, 384.5 s-1 and 1198.5 s-1 for the warp direction and 583 s-1 and 1253 s-1 for the through-thickness direction. Based on the results shown in the table, it can be said that with increasing dynamic strain rate, the average peak stresses and failure strains in these directions increase while the elastic moduli decrease. Compared to the results obtained at quasi-static strain rates, the in-plane and out-of-plane properties are found to be rate dependent, except for the failure strain showing a negative strain rate effect. A significant variation can be seen in the elastic modulus and peak stress results of the composites in the in-plane directions compared to those in the through-thickness direction. This is due to the fracturing of the in-plane composite specimens by brooming. To reduce variation in the mechanical properties in these directions, it would be good to test the standard composite test coupons at quasi-static strain rates via the standard test fixture (Figure 2.11) while a modified test fixture is employed at high strain rates since the specimen would be fixed from its ends by the test fixture. In this way, it is thought that the crack initiation and propagation to occur at the loading ends of the standard test coupon can be prevented. The effect of the quasi-static and high strain rates on the mechanical properties in the warp, weft and through-thickness direction can be seen in Figure 4.10. As shown in the figures, a pronounced strain rate effect on the peak stress and elastic modulus is observed while the rate effect is found to be negligible in the failure strain results. Based on the results available in the open literature, it can be said that the rate sensitivity in the in-plane directions is likely due to the fiber planes-matrix-dominated mechanical properties[114–117] while the rate dependent mechanical properties in the through-thickness direction are simply due to viscoelastic matrix-dominated mechanical behavior[118].

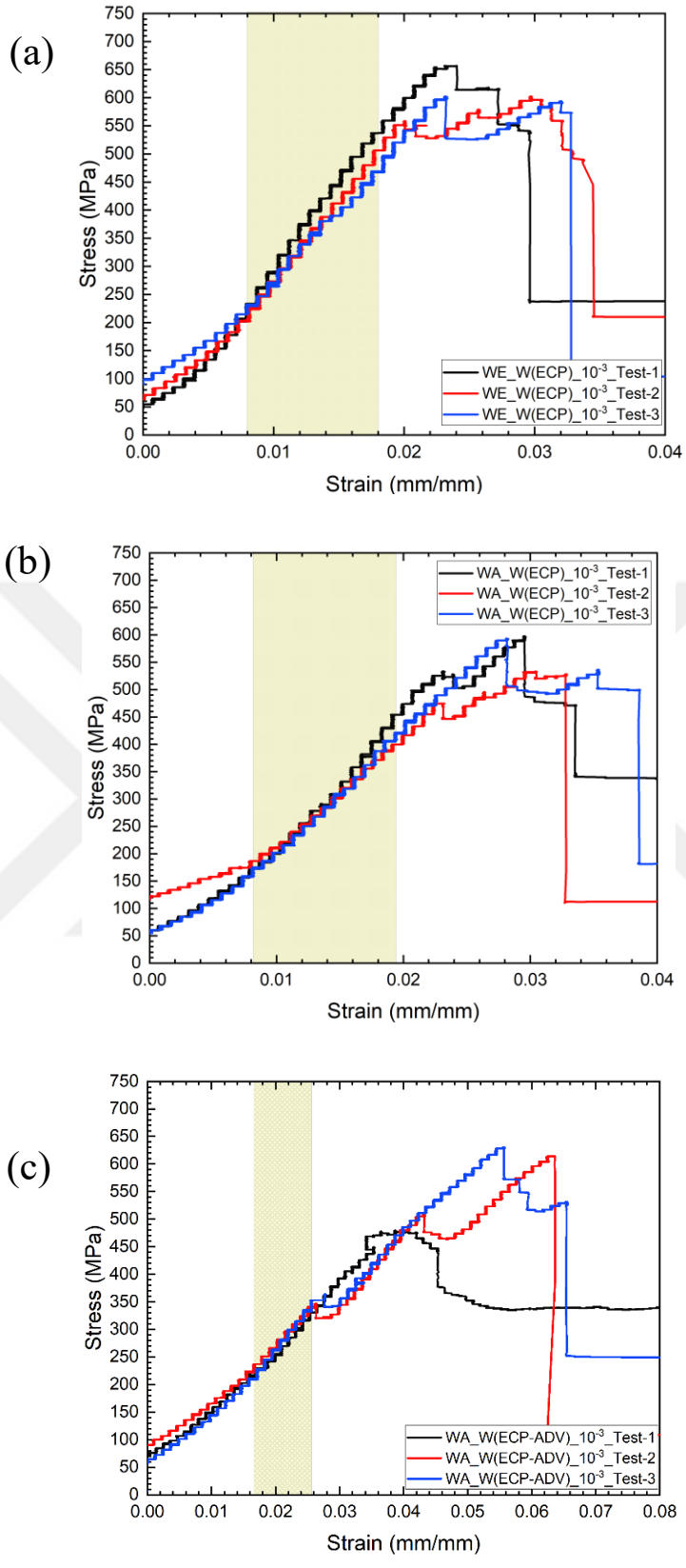

Figure 4.9. Compression test results of (a) the weft, (b) the warp samples with end-caps, and (c) the weft samples adhered to end-caps

Table 4.12. High strain rate compression test results obtained (a) in the weft direction, (b) in the warp direction and (c) in the through-thickness direction

(a)	Failure Strain (mm/mm)	Elastic Modulus (GPa)	Peak Stress (MPa)	Strain Rate (s^{-1})
Test-1	0.0177	39.23	581.34	487.00
Test-2	0.0168	54.47	762.93	356.00
Test-3	0.0160	55.27	734.20	381.00
Mean	**0.0164**	**54.87**	**748.57**	**368.50**
Std Dev	**0.0006**	**0.57**	**20.32**	**17.68**
COV (%)	**3.45**	**1.03**	**2.71**	**4.80**
	Failure Strain (mm/mm)	**Elastic Modulus (GPa)**	**Peak Stress (MPa)**	**Strain Rate (s^{-1})**
Test-1	0.0200	43.23	801.67	754.60
Test-2	0.0246	38.50	743.02	827.00
Test-3	0.0217	44.93	803.04	825.00
Mean	**0.0232**	**41.72**	**773.03**	**826.00**
Std Dev	**0.0021**	**4.55**	**42.44**	**1.41**
COV (%)	**8.86**	**10.90**	**5.49**	**0.17**

(b)	Failure Strain (mm/mm)	Elastic Modulus (GPa)	Peak Stress (MPa)	Strain Rate (s^{-1})
Test-1	0.0157	52.40	701.41	428.00
Test-2	0.0158	53.60	751.23	388.00
Test-3	0.0156	53.00	736.91	381.00
Mean	**0.0157**	**53.30**	**744.07**	**384.50**
Std Dev	**0.0001**	**0.42**	**10.13**	**4.95**
COV (%)	**0.86**	**0.80**	**1.36**	**1.29**
	Failure Strain (mm/mm)	**Elastic Modulus (GPa)**	**Peak Stress (MPa)**	**Strain Rate (s^{-1})**
Test-1	0.0170	55.45	754.86	1212.00
Test-2	0.0177	52.30	725.30	1206.00
Test-3	0.0192	52.60	781.13	1191.00
Mean	**0.0185**	**52.45**	**753.21**	**1198.50**
Std Dev	**0.0011**	**0.21**	**39.48**	**10.61**
COV (%)	**5.75**	**0.40**	**5.24**	**0.88**

(c)	Failure Strain (mm/mm)	Elastic Modulus (GPa)	Peak Stress (MPa)	Strain Rate (s^{-1})
Test-1	0.0777	13.37	1000.68	344.00
Test-2	0.0687	13.41	899.00	592.00
Test-3	0.0706	13.82	920.28	574.00
Mean	**0.0696**	**13.61**	**909.64**	**583.00**
Std Dev	**0.0013**	**0.29**	**15.05**	**12.73**
COV (%)	**1.93**	**2.12**	**1.65**	**2.18**
	Failure Strain (mm/mm)	**Elastic Modulus (GPa)**	**Peak Stress (MPa)**	**Strain Rate (s^{-1})**
Test-1	0.0774	13.31	971.12	1253.00
Test-2	0.0818	12.45	969.36	1253.00
Test-3	0.0826	12.66	998.80	1253.00
Mean	**0.0822**	**12.56**	**984.08**	**1253.00**
Std Dev	**0.0006**	**0.15**	**20.82**	**0.00**
COV (%)	**0.71**	**1.18**	**2.12**	**0.00**

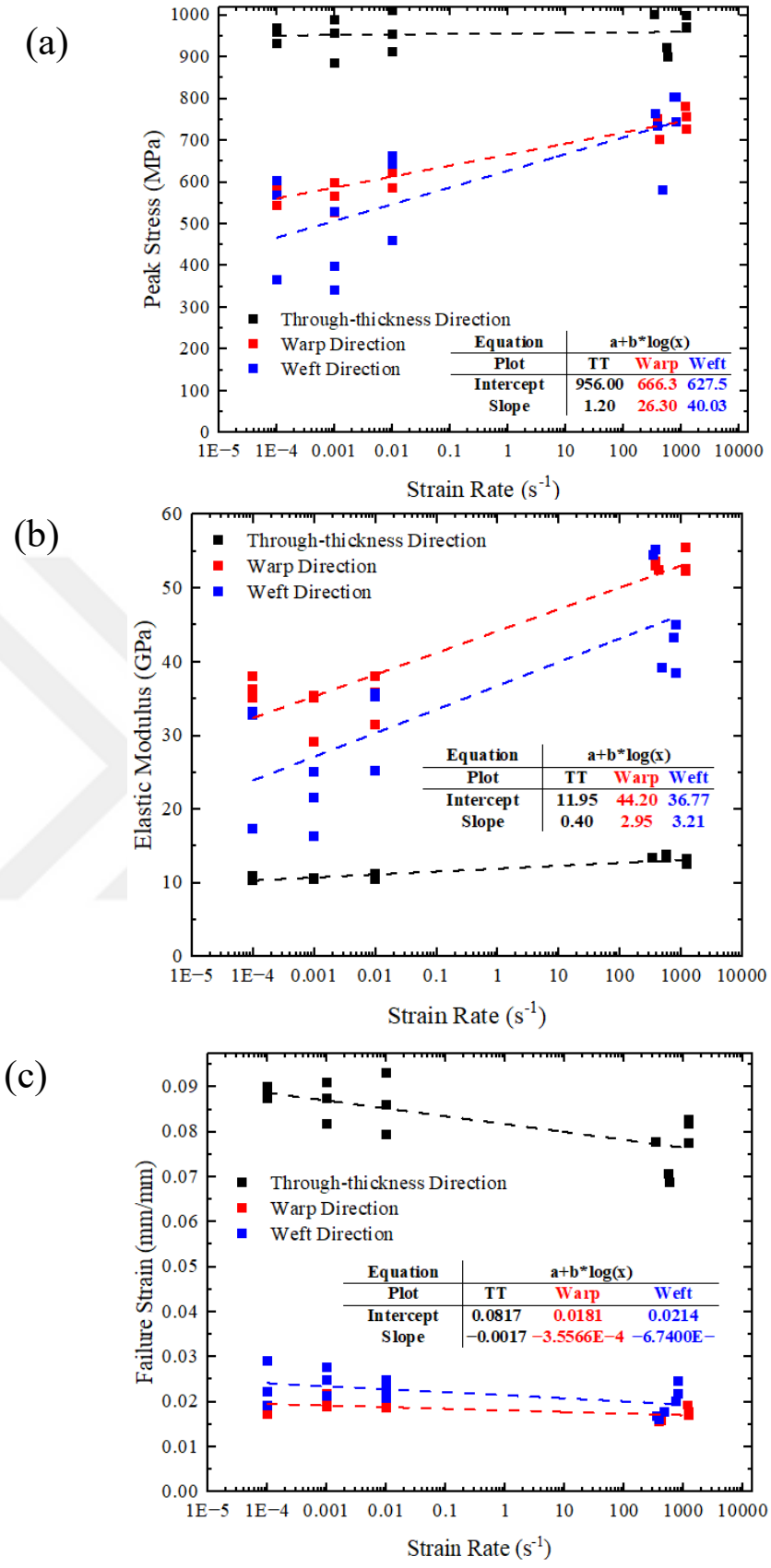

Figure 4.10. The effect of strain rate on (a) failure stress, (b) the elastic modulus and (c) the failure strain

4.4. Shear Test Results

Standard tensile test results of ±45° specimen as well as the quasi-static and dynamic test results were explained in the following sections.

4.4.1. Tensile Test Results of ±45° Carbon Fiber Composite

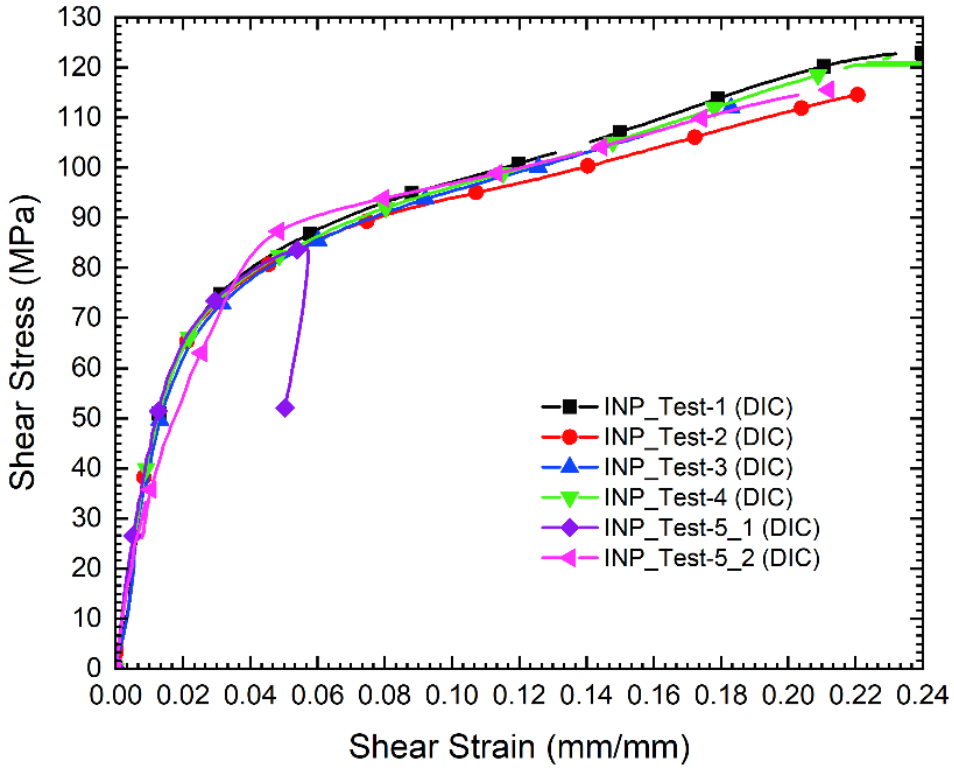

Figure 4.11. In-plane shear results

In-plane shear properties obtained from tensile tests of the test coupons with the orientation of ±45° can be seen in Table 4.13, and shear stress versus strain curves can be found in Figure 4.11. Shear stress strain curves show a bilinear behavior. The shear stress varies linearly up to a certain strain value, a hardening behavior then occurs. After reaching a specific strain value, it changes linearly with increasing strain until the fracture occurs. The slope of the first linear part is more than that of the second linear one. The average shear stress at which test coupons failed was calculated as 120.10±4.06 MPa whilst the corresponding shear strain was 0.2342±0.04689. Failed test coupons can be found in Figure B.6 (a) and (b). It was found that the shear failure occurs in a limited region of the test coupons, and the deformation begins with the fiber debonding and the

Table 4.13. In-plane shear test results: (a) Shear Strength, (b) Strain gage strain and (c) DIC strain

(a)	Shear Strength (MPa)	Shear Strain (mm/mm)
Test-1	122.98	0.2396
Test-2	114.55	0.2274
Test-3	122.50	0.1830
Test-4	123.49	0.3090
Test-5_1	X	X
Test-5_2	117.00	0.2119
Mean	**120.10**	**0.2342**
Std Dev.	**4.06**	**0.04689**
COV (%)	**3.38**	**20.02**

(b)	Strain Gage	
	Shear Modulus (GPa)	Shear Strength (MPa)
Test-1	4.464	85
Test-2	4.249	84
Test-3	4.208	84.19
Mean	**4.307**	**84.397**
Std Dev.	**0.138**	**0.531**
COV (%	**3.193**	**0.600**

(c)	DIC	
	Shear Modulus (GPa)	Shear Strength (MPa)
Test-1	4.626	83.83
Test-2	4.425	82.2
Test-3	4.302	81.97
Test-4	4.445	82.96
Test-5-1	4.626	82.96
Test-5-2	3.81	87.88
Mean	**4.485**	**82.78**
Std Dev.	**0.140**	**0.73**
COV (%)	**3.100**	**0.89**

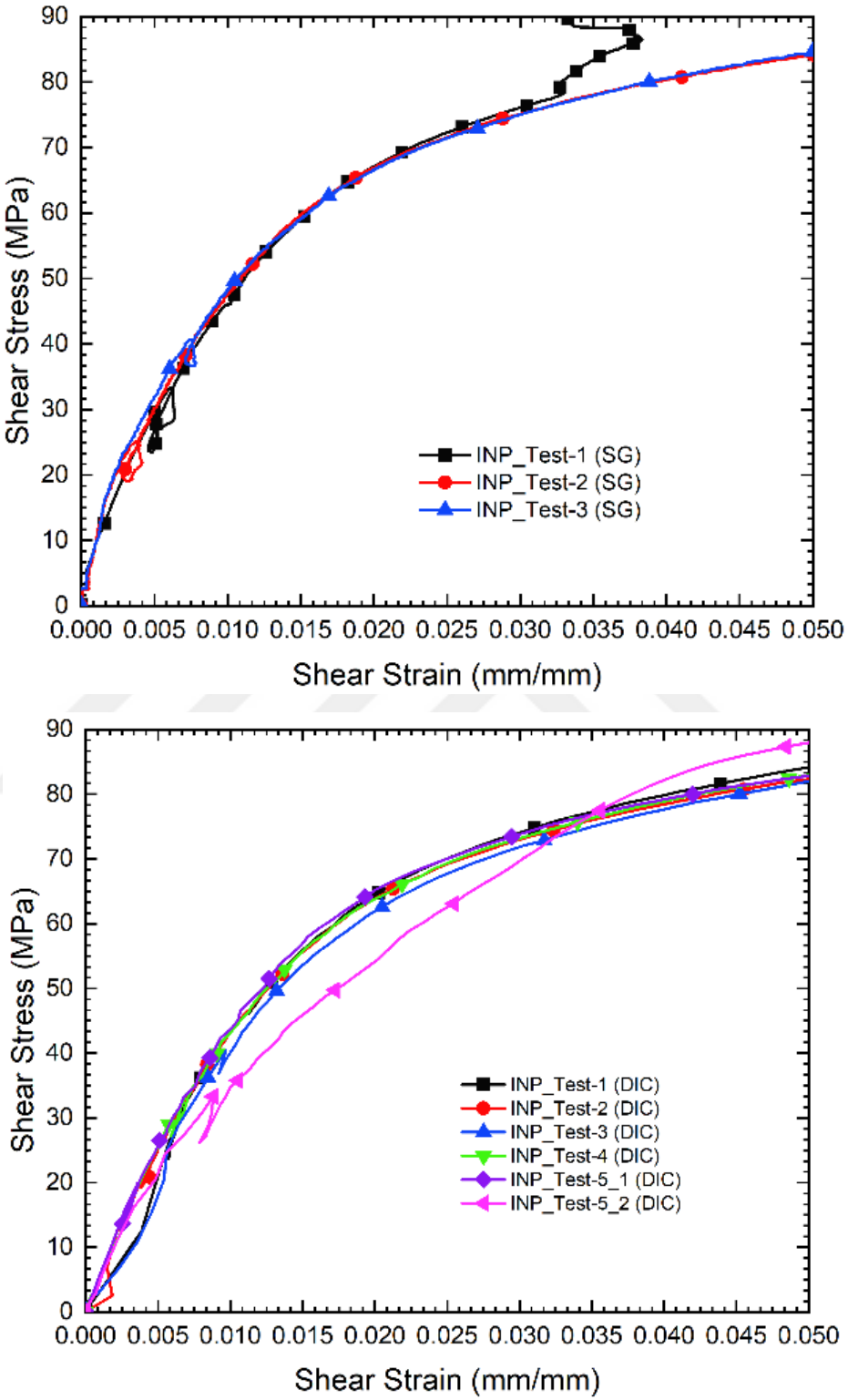

Figure 4.12. Shear test results generated from extensometer and DIC strains according to ASTM standard

rotation of fibers to the direction of the applied load and is completed when fibers are broken under tensile loading.

According to ASTM D3518[60], the maximum shear strain is assumed as 0.05 mm/mm if the failure shear strain of a composite is bigger than that value. Otherwise, the shear strain value at which the material fails is assumed as the failure shear strain since beyond a shear strain value of 0.05 excessive fiber scissoring occurs and, the results are affected by it. Although the average shear strain value of 0.2342±0.04689 was calculated in these tests, all shear stress versus shear strain curves were generated by considering a maximum shear strain value of 0.05 mm/mm. The rearranged curves are presented in Figure 4.12 and they are summarized in Table 4.13. Therefore, the average shear strength and shear modulus were calculated as 84.397±0.531 MPa and 4.307±0.138 GPa from data provided by strain gages while they were calculated as 82.78±0.73 MPa and 4.485±0.14 from strains determined from DIC measurements.

4.4.2. Quasi-static Strain Rate Test Results

Table 4.14. In-plane shear test results at different quasi-static strain rates

	Shear Modulus (GPa)	Shear Strength (MPa)
10^{-5} s^{-1}_INP1	8.03	154.2
10^{-5} s^{-1}_INP2	8.49	156.1
10^{-5} s^{-1}_INP3	8.88	155.3
Mean	**8.47**	**155.2**
Std Dev.	**0.43**	**1.0**
COV (%)	**5.02**	**0.6**
10^{-4} s^{-1}_INP2	8.51	167.3
10^{-4} s^{-1}_INP3	9.36	166.3
Mean	**8.94**	**166.8**
Std Dev.	**0.60**	**0.6**
COV (%)	**6.73**	**0.4**

Table 4.14 shows the in-plane shear properties of the carbon composite calculated at two different strain rates. These tests were first performed at a strain rate of 10^{-4} s^{-1} corresponding to the one used in ±45-degree tensile tests to investigate the effect of sample size on the shear response. A comparison of these test results can be found in Figure 4.13. The shear strength and shear modulus of the sample smaller in size were

found to be nearly two times more than that obtained from standard testing methods. The reason could be the non-standard size of samples used in quasi-static strain rates, but it can still be used to monitor the effect of strain rate on the shear strength of the composite by considering the size effect. From Table 4.14, it can be concluded that the shear strength increases with increasing strain rate while the shear modulus remains unchanged with increasing strain rates. In-plane shear properties show different behavior compared to tensile and compressive properties since epoxy matrix material is a rate-sensitive material. It means that strength and modulus change as the strain rate increases. In carbon fiber composite materials produced using epoxy as resin material, this rate effect of epoxy is prevented by carbon fibers because compared to epoxy, carbon fiber has more strength and modulus. That is why, in compression and tensile response strain rate effect cannot be seen because of the dominated material properties of carbon fiber while in shear properties, the matrix material properties are effective due to less contribution of carbon fibers to the shear properties. Shear strength was therefore found to be strain rate sensitive. Shear stress shear strain curves at different quasi-static strain rates are presented in Figure 4.14 while the images of broken test samples are depicted in Figure B.7 (a) and (b).

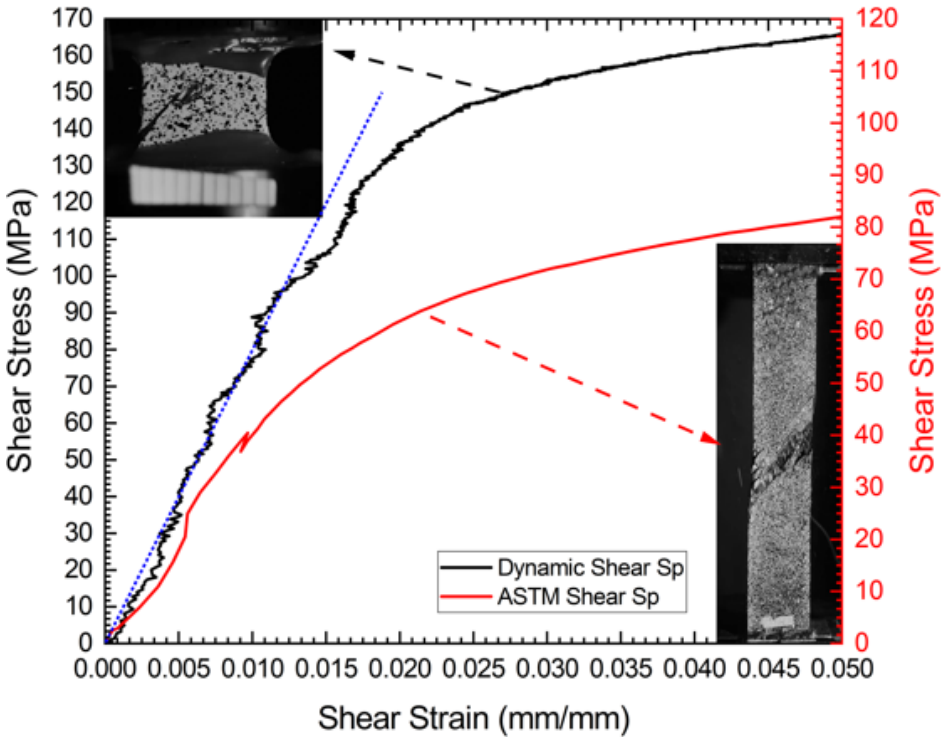

Figure 4.13. Comparison of the results obtained from the standard test method and strain rate tests

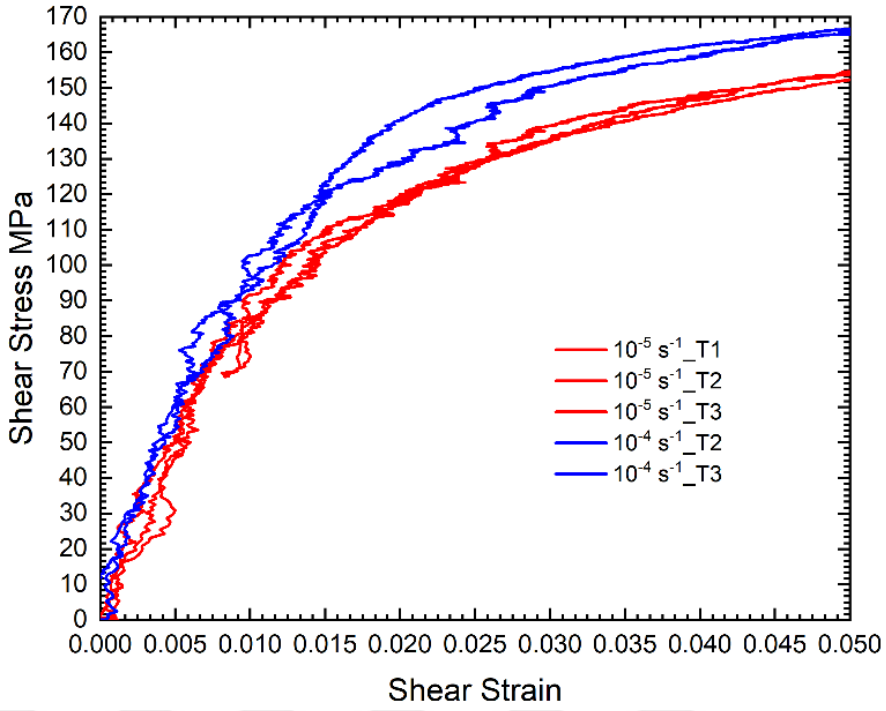

Figure 4.14. Shear stress versus shear strain curves at different quasi-static strain rates

4.4.3. High Strain Rate Test Results

The tensile test results of $[\pm 45]_n$ composite specimen at high strain rates were explained in Section 5.2.

4.4.4. V-Notched Shear Test Results

Table 4.15. Interlaminar shear properties (1-3 plane) obtained from V-notched tests

	Shear Modul (GPa)	Shear Strength (MPa)
10^{-4}_Test-1	4.24	82.45
10^{-4}_Test-2	4.73	85.15
10^{-3}_Test-1	4.42	85.49
10^{-3}_Test-2	4.05	85.86
10^{-3}_Test-3	4.29	83.38
10^{-2}_Test-1	5.12	94.66
10^{-2}_Test-2	4.80	95.01
Mean	4.25	84.91
Std. Dev.	0.19	1.34
COV %	4.44	1.58

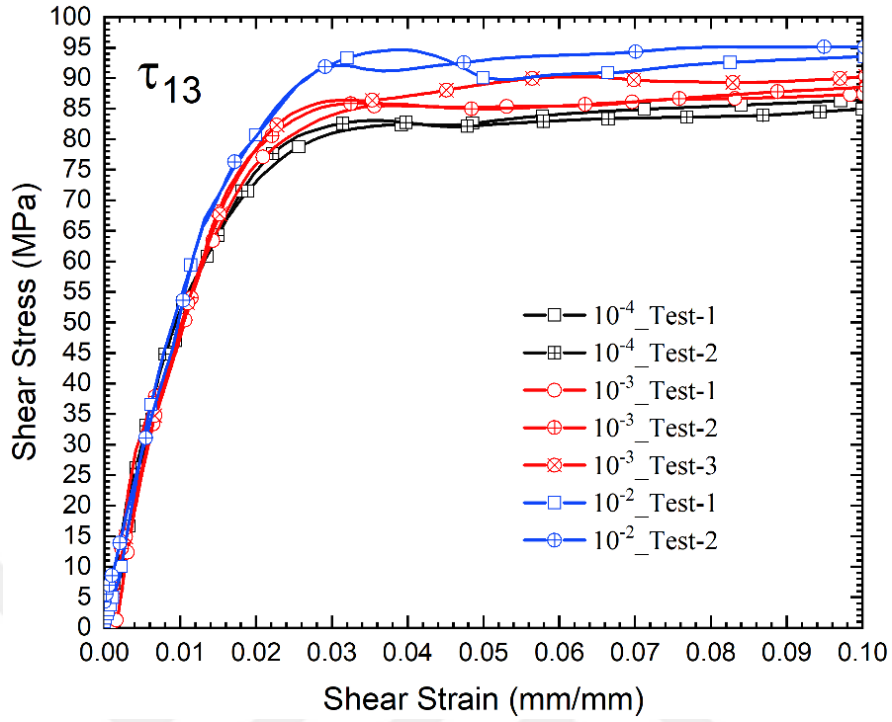

(a)

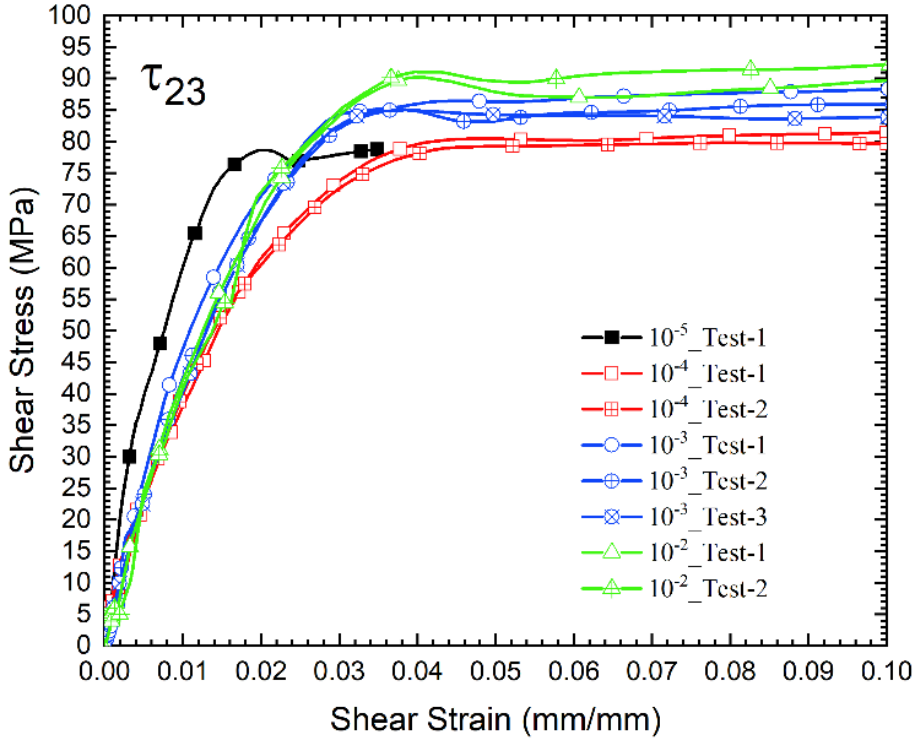

(b)

Figure 4.15. V-notched shear test results for (a) 1-3 plane and (b) 2-3 plane

Table 4.16. Interlaminar shear properties (2-3 plane) obtained from V-notched tests

	Shear Modul (GPa)	Shear Strength (MPa)
10^{-5}_Test-1	3.84	78.67
10^{-4}_Test-1	3.37	80.48
10^{-4}_Test-2	3.24	79.81
10^{-3}_Test-1	3.23	86.48
10^{-3}_Test-2	3.13	85.09
10^{-3}_Test-3	3.20	85.02
10^{-2}_Test-1	3.50	89.99
10^{-2}_Test-2	3.56	92.29
Mean	3.19	85.53
Std. Dev.	0.05	0.82
COV %	1.46	0.96

Table 4.15 shows the interlaminar shear properties of the carbon fiber laminated composite subjected to shear loading in the 1-3 plane at different strain rates. Shear stress-strain curves calculated can be seen in Figure 4.15 (a) whilst Figure B.8 (a) shows one of the tested samples and its surface in detail. Deformation occurred in the form of splitting between plies and a vertical shear zone. Based on the data in Table 4.15 it is said that the interlaminar shear strength is strain rate dependent, but shear strain does not since it does not change with increasing strain rate. Interlaminar shear strength and strain were therefore calculated for the 1-3 plane as 84.91±1.34 MPa and 4.25±0.19 GPa, respectively. According to the ASTM (Figure A.4), the failure code was defined as HGN. (H: Horizontal cracking, G: Gage section and N: between notches).

The shear stress-strain results obtained from loading V-notched test samples in the 2-3 plane at different strain rates are depicted in Table 4.16. As with interlaminar shear properties in the 1-3 plane, the shear strength increases with increasing strain rate. While, the shear modulus remains unchanged. Compared to the shear modulus in 1-3 plane, the shear modulus in 2-3 was found to be less. In these shear tests (2-3 plane), Direction 2 represents the warp direction. It means that the fibers running in the warp direction are under interlaminar shear loading. As mentioned, in the compression and tensile test results, the composite in the warp direction has lower strength values compared to that in the weft direction due to the wearing of the warp fibers during the weaving process. The reason for less shear properties in the 2-3 plane could be therefore the wearing of the warp fibers. Figure 4.15 (b) and Figure B.8 (b) shows the shear stress-

strain curves and the tested v-notched shear test coupon, respectively. Like the shear stress versus strain curves in the 1-3 plane, the shear stress changes linearly until some shear strain value, a softening region then appears in shear stress strain curves. This region is followed by a plateau region. After the plateau reaches the failure strain, shear cracking occurs between the notches. As shown in the above table, the average shear strength and shear modulus are calculated as 85.53±0.82 MPa and 3.19±0.05 GPa, respectively. The failure code was identified as HGN according to ASTM.

4.5. Elastic Constant Determination Test Results

The properties of the composite material in thickness direction determined by elastic constant determination tests at 10^{-4}, 10^{-3} and 10^{-2} s^{-1} strain rates are shown in Table 4.17, Table 4.18 and Table 4.19, respectively. All the stress-strain curves generated from this test are depicted in Figure 4.16, and Figure B.9 shows the broken pieces of the cubic samples. For each strain rate, Poisson's ratio was calculated. As shown in the above tables, the strain rate does not affect the Poisson's ratio. Therefore, the average Poisson's ratio calculated from all the available results was calculated as 0.01 for ϑ_{31} and ϑ_{32}.

Table 4.17. Through-thickness properties of the cubic sample compressed at a strain of 10^{-4} s^{-1}

	σ_3 (MPa)	E_3 (GPa)	ε_f	μ_{31}	μ_{32}
Test-1	953.93	11.01	0.0814	0.0881	0.0906
Test-2	1057.81	12.28	0.0843	0.0995	0.0890
Mean	1005.87	11.64	0.0828	0.0938	0.0898
Std. Dev.	73.45	0.89	0.0021	0.0081	0.0011
COV (%)	7.30	7.66	2.4766	8.6151	1.2285

Table 4.18. Through-thickness properties of the cubic sample compressed at a strain of 10^{-3} s^{-1}

	σ_3 (MPa)	E_3 (GPa)	ε_f	μ_{31}	μ_{32}
Test-1	1012.25	12.18	0.0813	0.0815	0.0879
Test-2	984.97	12.97	0.0731	0.0991	0.0969
Mean	998.61	12.57	0.0772	0.0903	0.0924
Std. Dev.	19.29	0.56	0.0058	0.0124	0.0064
COV (%)	1.93	4.47	7.4550	13.7122	6.8831

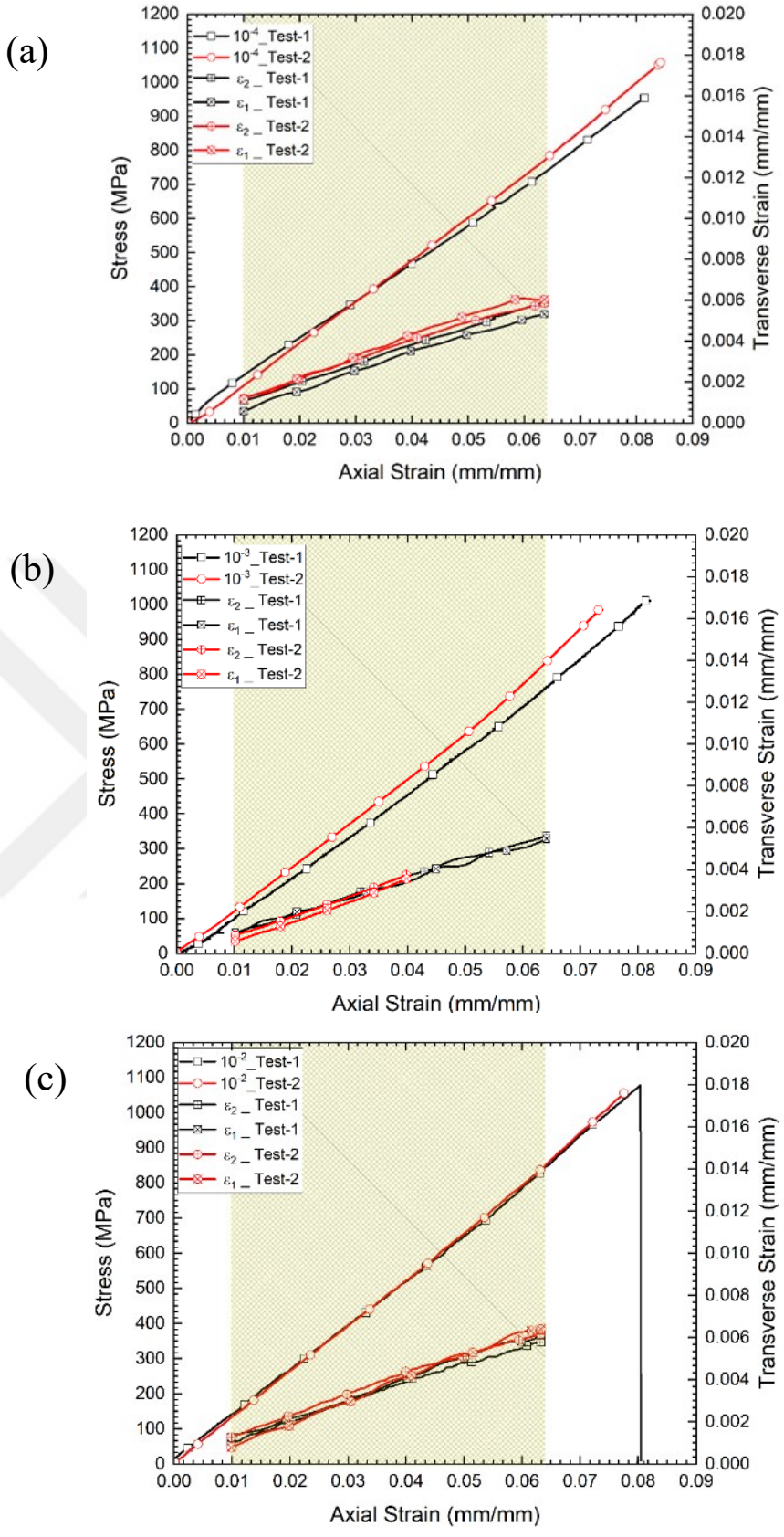

Figure 4.16. Elastic constant determination test results (a) 10^{-4} s^{-1}, (b) 10^{-3} s^{-1} and (c) 10^{-2} s^{-1} strain rate

Table 4.19. Through-thickness properties of the cubic sample compressed at a strain of 10^{-2} s^{-1}

	σ_3 (MPa)	E_3 (GPa)	ε_f	μ_{31}	μ_{32}
Test-1	1077.57	12.77	0.08038	0.09503	0.08981
Test-2	1055.42	13.16	0.07757	0.10842	0.09314
Mean	1066.49	12.97	0.07897	0.10173	0.09148
Std. Dev.	15.66	0.28	0.00199	0.00947	0.00235
COV (%)	1.47	2.13	2.52086	9.3076	2.57411

4.6. Laterally Constrained Compression Test Results

Table 4.20. Laterally constrained compression test results

	Fiber Crush Strength (MPa)	Fracture plane angle (°)	Normal Stress (MPa)	Shear Stress (MPa)	Friction angle (°)	Friction coefficient	Fiber Shear Strength (MPa)
10^{-4} Test-1	900.7	32.45	641.4	407.8	25.10	0.468	708.3
10^{-4} Test-2	795.7	30.36	592.4	347.0	29.28	0.561	679.2
10^{-3} Test-1	835.2	35.11	558.9	392.9	19.78	0.360	593.9
10^{-3} Test-2	892.0	25.77	723.4	349.3	38.46	0.794	923.9
10^{-2} Test-1	838.9	33.69	580.8	387.2	22.62	0.417	629.2
10^{-2} Test-2	875.6	34.34	597.0	407.8	21.32	0.390	640.8
Mean	**856.3**	**31.95**	**615.6**	**382.0**	**26.09**	**0.498**	**650.3**
Std. Dev.	**40.1**	**3.46**	**59.3**	**27.5**	**6.91**	**0.161**	**44.5**
COV (%)	**4.7**	**10.81**	**9.6**	**7.2**	**26.48**	**32.352**	**6.8**

By using Equations (2-14) - (2-16) with fracture angles (Figure B.10) the calculated the fiber crush strength and the fiber shear strength for each strain rate and each test can be shown in Table 4.20. The value in red is excluded from the average value and the standard deviation calculation since the angle read in that test is probably wrong. From this test results, the average fiber crush and fiber shear strength were calculated as 856.3±40.1 MPa and 650.3±44.5 MPa, respectively.

4.7. Out-of-plane Off-Axis Compression Test Results

Figure 4.17 summarize the results obtained from the out-of-plane off-axis compression tests. Interlaminar stresses and transverse stresses were determined using

Equations (2-17) - (2-19) with off-axis angles. The results are also presented in the inset of Figure 4.17. Transverse (σ_3) and interlaminar (τ_{13}) stresses in the out-of-plane directions of 0° and 90° were calculated as zero. While, the latter one was found to be zero in the 90° out-of-plane direction. As the off-axis angle increased from 0° to 90°, both transverse and interlaminar stresses were found to increase.

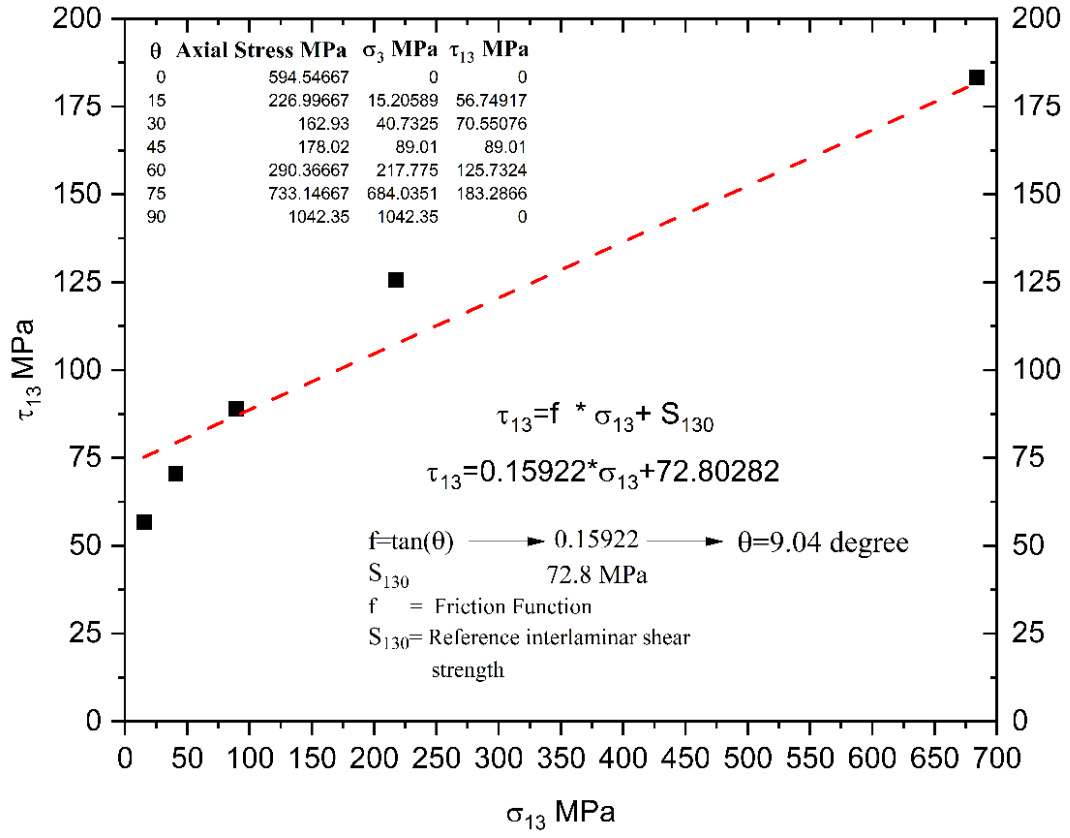

Figure 4.17. Out-of-plane off-axis compression test results

The increase in transverse stresses was more pronounced than that in interlaminar stresses. It is because the effect of the transverse stress on the fracture plane increases significantly with increasing out-of-plane angles that interlaminar stress increase. Figure B.11 and Figure B.12 depict the failed test samples. It was found out that at 0° off-axis angle the major failure mode was axial splitting, brooming and shearing whilst it was interlaminar shear failure mode for the off-axis angles between 15° and 60°. Fiber crushing and fiber shearing in addition to interlaminar shear were identified at the off-axis angle of 75°. From the linear fitting of the values of transverse and interlaminar stress, the friction angle and interlaminar shear strength were sequentially calculated as 9.04° and 72.8 MPa.

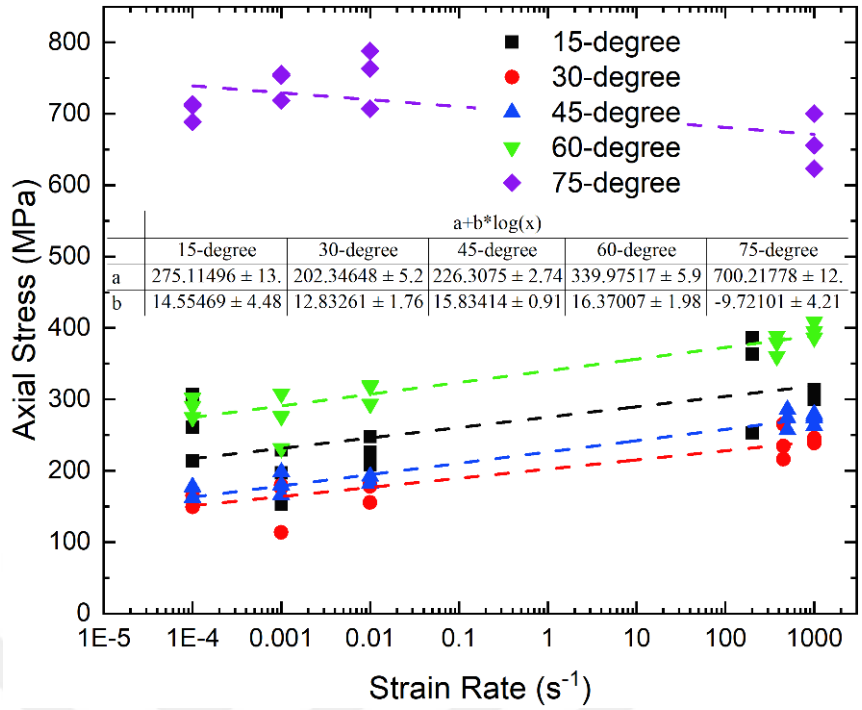

a+b*log(x)

	15-degree	30-degree	45-degree	60-degree	75-degree
a	275.11496 ± 13.	202.34648 ± 5.2	226.3075 ± 2.74	339.97517 ± 5.9	700.21778 ± 12.
b	14.55469 ± 4.48	12.83261 ± 1.76	15.83414 ± 0.91	16.37007 ± 1.98	-9.72101 ± 4.21

(a)

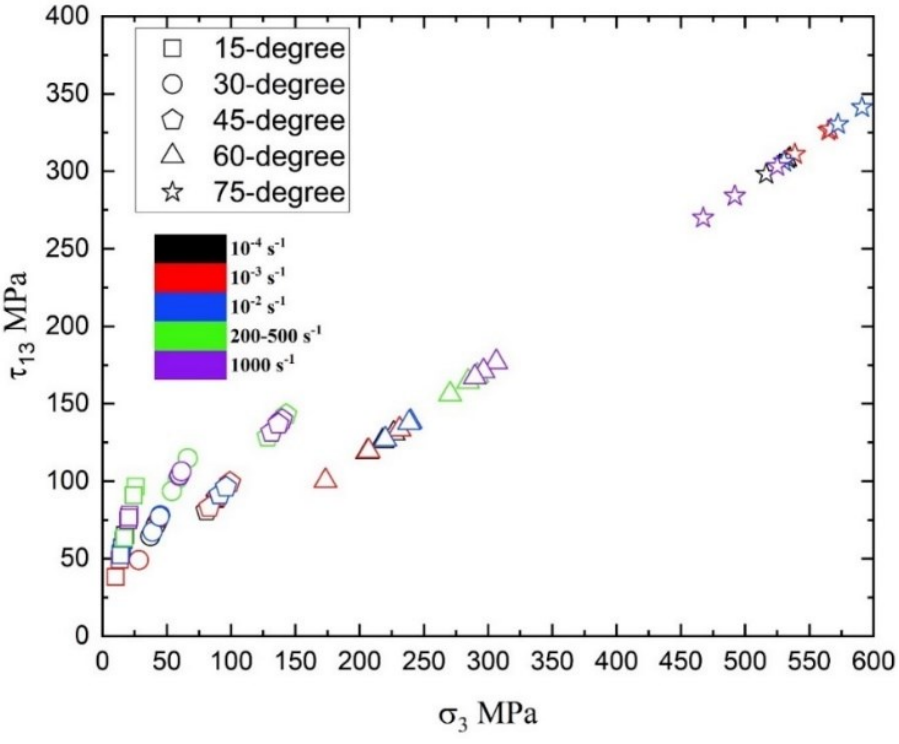

(b)

Figure 4.18. (a) Failure stress variation with log strain rate and (b) the effect of strain rate on the friction function and the interlaminar shear strength

Figure 4.18 (a) shows the effect of the quasi-static and high strain rate on the failure stresses of the off-axis specimens. It can be seen that as the strain rate increases, the failure stress increases except for that of the 75-degree specimen. 75-degree specimen fails a failure strength value obtained at the quasi-static strain rates. It can be said that this specimen shows almost strain dependent behavior at quasi-static rates, but it is rate independent as considering the failure stress at high strain rates. The slope of fit equations obtained from the other off-axis angles is almost similar as shown in the table in the inset of the figure.

When considering the interlaminar and transverse stresses at high strain rates as well as those at quasi-static strain rates (Figure 4.17), it is found that the interlaminar shear strength and friction angle remain almost constant as shown in Figure 4.18 (b).

4.8. Quasi-static Punch Shear Test Results

Table 4.21. The determination of the punch shear strength

	Specimen Thickness (mm)	Punch Circumference (mm)	Lip Thickness (mm)	Plug Thickness (mm)	Plug Area (mm^2)	Failure Load (N)	SFS (MPa)
SPR-1.1_10^{-4}_Test-1	3.86	23.8761	1.68	2.18	52.04991	23605.39	453.5
SPR-1.1_10^{-4}_Test-2	3.88	23.8761	1.78	2.1000	50.1398	23854.4	475.8
SPR-1.1_10^{-3}_Test-1	3.88	23.8761	1.90	1.9800	47.2747	23785.69	503.1
SPR-1.1_10^{-3}_Test-2	4.05	23.8761	2.00	2.0550	49.0654	23072.81	470.2
SPR-1.1_10^{-3}_Test-3	3.88	23.8761	1.81	2.0733	49.5031	22337.72	451.2
SPR-1.1_10^{-3}_Test-4	3.85	23.8761	1.70	2.15	51.33362	21643.5	421.6
SPR-1.1_10^{-2}_Test-1	3.76	23.8761	1.71	2.05333	49.0256	21922.21	447.2
SPR-1.1_10^{-2}_Test-2	3.8	23.8761	1.92	1.8825	44.9468	21659.42	481.9
Mean							463.1
Std Dev							25.0
COV (%)							5.40

The fiber shear strength of the carbon composite was calculated using Equation (2-21) for the span-to-punch ratio of 1.1. The results are presented in Table 4.21. The punched samples and load-displacement curves are sequentially illustrated in Figure B.13 and Figure 4.19 (a).

Based on the available data, it is said that for SPR=1.1 there is punch-shear fiber failure mode followed by an internal delamination region. The shear plug formed is then pushed through the thickness of the punched sample. It is completed when the main failure mode is the combination of shear and tensile fiber modes. As can be seen in the following table, the punch tests are performed at different strain rates to investigate strain

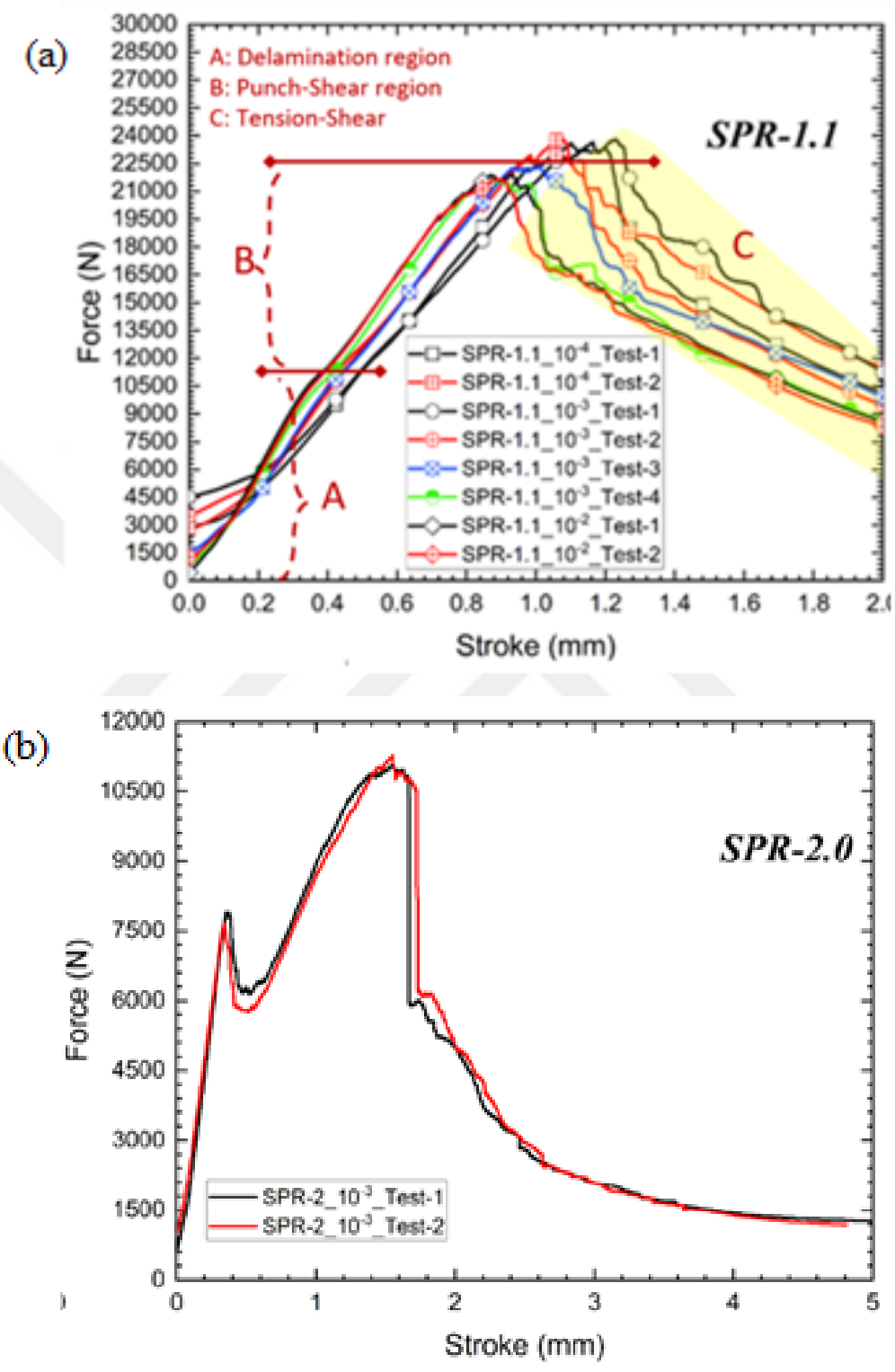

Figure 4.19. Quasi-static punch shear test results for (a) SPR=1.1 and (b) SPR=2

rate effect. The fiber shear strength was found to be strain rate independent since as the strain rate was increased from 10^{-4} to 10^{-2} s^{-1}, the fiber shear strength remained nearly the same.

The force-displacement results obtained for SPR=2 are depicted in Figure 4.18 (b). Different from the load curves of SPR=1.1, it is easy to identify failure regions from load curves of SPR=2.0 as seen in Figure 4.19 (b). The first load drop corresponds to the internal delamination. Beyond this point, with the propagation of delamination damage the sample begins to punch through the thickness until the last drop takes place. After that point the punched sample undergoing a combined tensile and punch failure is pushed through the composite. The failed test specimens can be found in Figure B.13.

4.9. Flexural Test Results

Table 4.22. Three-point bending test results

	Failure Strain (mm/mm	Bending Modulus (GPa)	Bending Strength (MPa)
WA_Test-1	0.0241	41.82	828.0
WA_Test-2	0.0239	42.56	824.4
WA_Test-3	0.0227	41.98	769.8
Mean	0.0236	42.12	807.4
Std Dev	0.0008	0.39	32.6
COV(%)	3.2130	0.93	4.0
WE_Test-1	0.0246	41.65	951.2
WE_Test-2	0.0238	43.22	855.3
WE_Test-3	0.0214	43.12	896.4
Mean	0.0233	42.66	901.0
Std Dev	0.0017	0.88	48.1
COV(%)	7.1576	2.06	5.3

3-point bending results of the test coupons in the warp and weft direction are presented in Table 4.22. The average bending strength and modulus of the warp coupons were sequentially calculated as 807.4±32.6 MPa and 42.12±0.39 GPa. While, these were calculated for the test coupons in the warp direction as 901.0±48.1 MPa and 42.66±0.88 GPa, respectively. As with the results of tensile and compression tests, the coupons in the weft direction showed more strength compared to the warp coupons. The displacement

of the test coupons at impact and back side as well as corresponding bending strain were also calculated from deformation images recorded during testing. These results can be found in Figure B.14 (a) and Figure B.15 (a) for the weft and warp samples, respectively. In addition to that, the failed weft and warp test coupons are sequentially depicted in Figure B.14 (b) and Figure B.15 (b). Failure of the all-test coupons occurred in the middle span where the coupons and the impactor were in contact. During the deformation of the samples, the bottom ply was first broken with a loud sound, the damage initiated within the samples then propagated along the in-plane directions by delamination and along the thickness by fiber breakage and shearing.

4.10. Open-Hole Test Results

Table 4.23. Open-hole compression test results

	Failure				Failure		
	Disp. (mm)	Force (N)	Stress (MPa)		Disp. (mm)	Force (N)	Stress (MPa)
OHC_WE_0.5mm/s_T1	0.250	12832.17	256.6	OHC_WA_0.5mm/s_T1	0.225	10765.36	213.2
OHC_WE_0.5mm/s_T2	0.231	11557.05	231.1	OHC_WA_0.5mm/s_T2	0.263	12311.51	243.8
OHC_WE_0.5mm/s_T3	0.265	12372.92	247.5	OHC_WA_0.5mm/s_T3	0.251	12124.78	240.1
Mean	**0.249**	**12254.05**	**245.1**	**Mean**	**0.246**	**11733.88**	**232.4**
Std Dev	**0.017**	**645.82**	**12.9**	**Std Dev**	**0.020**	**843.95**	**16.7**
COV (%)	**6.744**	**5.27**	**5.3**	**COV (%)**	**7.973**	**7.19**	**7.2**
OHC_WE_1.3mm/min_T1	0.260	11617.71	232.4	OHC_WA_1.3mm/min_T1	0.290	13409.81	265.5
OHC_WE_1.3mm/min_T2	0.245	12263.30	242.8	OHC_WA_1.3mm/min_T2	0.233	11177.92	221.3
Mean	**0.252**	**11940.51**	**237.6**	**Mean**	**0.262**	**12293.87**	**243.4**
Std Dev	**0.011**	**456.50**	**7.4**	**Std Dev**	**0.040**	**1578.18**	**31.3**
COV (%)	**4.188**	**3.82**	**3.1**	**COV (%)**	**15.486**	**12.84**	**12.8**

The results obtained from open-hole compression tests at two different displacement rates for the weft and warp direction are presented in Table 4.23. Figure B.16 (a) shows only the broken samples in the weft direction. For both the warp and weft directions, failure occurred around the hole and propagated across its center. The main failure mechanisms were found to be fiber kinking or buckling. According to the ASTM failure identification code, the failure code of the warp and weft samples was found as LGM (L: Lateral, G: Gage and M: Middle). Based on Table 4.23, the open-hole compressive strength for both the warp and weft direction changes slightly with increasing loading rates. The average open-hole compressive strength at the displacement rate of 0.5 mm/s was found to be 245.1±12.9 MPa for the weft direction and 232.4±16.7

MPa for the warp direction. Compressive strength reduction factors for the weft and warp directions were calculated as 0.358 and 0.412, respectively.

Table 4.24 shows the open-hole tensile test results of the warp and weft test coupons at two different loading rates. The average open-hole strength in the warp and weft directions was sequentially ascertained as 289±9.5 MPa and 259±10.1 MPa. Tensile strength reduction factors were calculated as 0.348 for the weft direction and 0.353 for the warp direction. Figure B.16 (b) shows the fractured samples in the weft direction. Failure identification code was ascertained as LGM for both the weft and warp directions according to the standard typical failure modes (Figure A.6).

Table 4.24. Open-hole tensile test results

	Failure				Failure		
	Disp. (mm)	Force (N)	Stress (MPa)		Disp. (mm)	Force (N)	Stress (MPa)
OHT_WE_0.5mm/min_T1	0.295	14058.35	281.9	OHT_WA_0.5mm/min_T1	0.313	13183.78	264.3
OHT_WE_0.5mm/s_T2	0.327	15144.06	303.6	OHT_WA_0.5mm/s_T2	0.286	13116.60	263.0
OHT_WE_0.5mm/s_T3	0.305	14640.28	293.5	OHT_WA_0.5mm/s_T3	0.273	12048.34	241.6
OHT_WE_0.5mm/s_T4	N.A.	14086.68	282.4	OHT_WA_0.5mm/s_T4	0.280	12961.00	259.2
OHT_WE_2mm/min_T5	0.311	14133.74	283.4	OHT_WA_0.5mm/s_T5	0.287	13307.86	266.8
Mean	**0.310**	**14412.62**	**289.0**	**Mean**	**0.288**	**12923.52**	**259.0**
Std Dev	**0.013**	**473.38**	**9.5**	**Std Dev**	**0.015**	**504.99**	**10.1**
COV (%)	**4.346**	**3.28**	**3.3**	**COV (%)**	**5.307**	**3.91**	**3.9**

4.11. Ice Impact Test Results

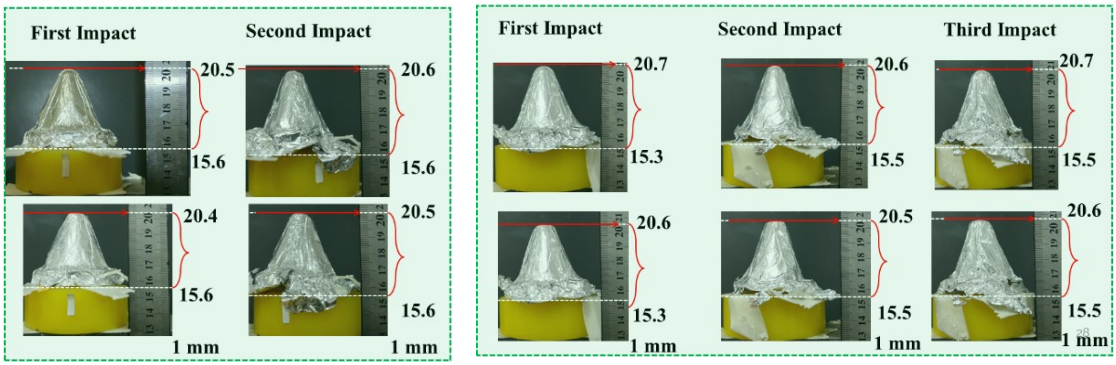

(a) (b)

Figure 4.20. The back surface displacement measurement of the carbon composite with a thickness of 0.88 mm (a) Test-1 and (b) Test-2

Figure 4.20 shows the back surface displacement results of the composite with a thickness of 0.88 mm subjected to multiple ice impacts in two different tests. The

displacement in all impact cases was measured as 1 mm, and there was no visible damage on the front and back surface of the composite after each impact.

Figure 4.21 shows the displacement values of the composite subjected to two times impacts. Like the front and back surface of the 0.88 mm thick composite plate, no visible damage on those of the 2.3 mm thick composite plate was observed, and a back surface displacement of 0.3 and 0.1 mm was obtained in the first and second impacts, respectively.

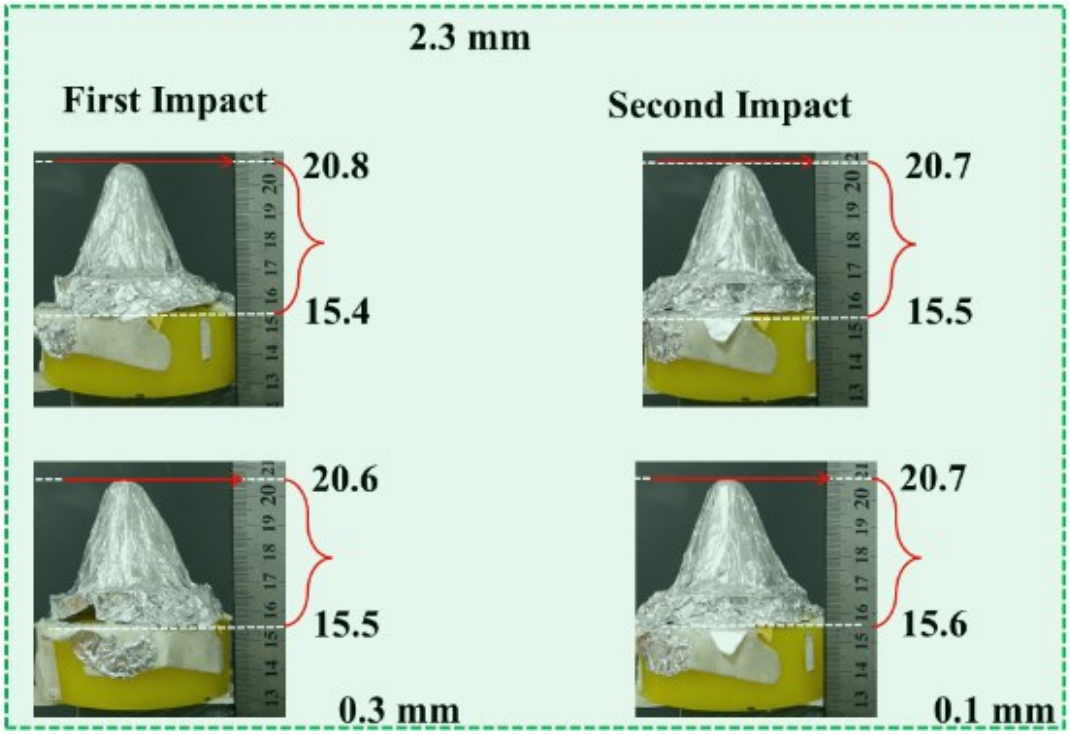

Figure 4.21. The back surface displacement measurement of the carbon composite with a thickness of 2.3 mm

4.12. Low-velocity Impact Test Results

The results obtained from the low-velocity impact tests were explained in detail in Section 5.8 by comparing with the numerical results.

4.13. Summary of The Experimental Study

The material constants obtained through the mechanical characterization tests are summarized in the following table.

Table 4.25. Material properties of the five-harness satin weave carbon composite

Density (g/cm^3)	1.57	Volume fraction (%)	57.4

TENSILE PROPERTIES

E_{xx}^T (GPa)	67.99±1.51	E_{yy}^T (GPa)	61.92±1.15
ϑ_{xy}^T	0.057±0.0018	ϑ_{yx}^T	0.0522±0.0116
S_{xx}^T (MPa)	829.5±9.8	S_{yy}^T (MPa)	732.0±42.9
ε_{xx}^T (mm/mm)	0.01175±10^{-4}	ε_{yy}^T (mm/mm)	0.01037±0.00131
S_{zz}^T (MPa)	38	E_{zz}^T (GPa)	7
ε_{zz}^T (mm/mm)	0.0046		

COMPRESSION PROPERTIES

❖ In-plane			
E_{xx}^C (GPa)	58.55±1.13	E_{yy}^C (GPa)	53.35±1.38
ϑ_{xy}^C	0.0577	ϑ_{yx}^C	0.0526
S_{xx}^C (MPa)	685.3±45.3	S_{yy}^C (MPa)	564.3±20
ε_{xx}^C (mm/mm)	0.012±10^{-3}	ε_{yy}^C (mm/mm)	0.01±0.001
❖ Out-of-plane			
E_{zz}^C (GPa)	10.68±0.24		
S_{zz}^C (MPa)	910.8±36.7		
ε_{zz}^C (mm/mm)	0.0873±0.0041		

IN-PLANE SHEAR PROPERTIES

G_{xy} (GPa)	4.485±0.14	S_{xy}^{max} (MPa)	120.10±4.06
γ_{xy}^{limit} (mm/mm)	0.05	γ_{xy}^{max} (mm/mm)	0.2342±0.04689
S_{xy}^{limit} (MPa)	84.397±0.531		

INTERLAMINAR SHEAR PROPERTIES

❖ 1-3 plane		❖ 2-3 plane	
G_{xz} (GPa)	4.25±0.19	G_{yz} (GPa)	3.19±0.05

(cont. on next page)

Table 4.25 (cont.)

γ_{xz}^{limit} (mm/mm)	0.05	γ_{yz}^{limit} (mm/mm)	0.05
S_{xz}^{limit} (MPa)	84.91±1.34	S_{yz}^{limit} (MPa)	85.53±0.82

POISSON'S RATIO

ϑ_{zx}^{C}	0.0903±0.0124	ϑ_{zy}^{C}	0.0924±0.0064

FLEXURAL PROPERTIES

❖ Weft Direction (X-Dir)		❖ Warp Direction (Y-Dir)	
Flex.Strength (MPa)	807.4±32.6	Flex. Strength (MPa)	901.0±48.1
Flex.Modulus (GPa)	42.12±0.39	Flex. Modulus (GPa)	42.66±0.88
Flex.Strain (mm/mm)	0.0236±0.0008	Flex.Strain (mm/mm)	0.0233±0.0017

OTHER MATERIAL PROPERTIES

Fiber Crush (MPa)	856.3±40.1	Laterally Constraint Compression Test
Fiber Shear (MPa)	650.3±44.5	
S_{xz} (MPa)	72.8	Out-of-Plane Off-Axis Compression Tests
Friction angle (Θ)	9.04°	
Fiber Shear (MPa)	463.1±25	Quasi-static Punch Shear Tests
Strength reduction factor (Tensile)	0.353	Open-Hole Tension and Compression Tests
Strength reduction factor (Compression)	0.382	

CHAPTER 5

NUMERICAL RESULTS

This section includes a comparison of numerical and experimental results. Also, the results obtained from the composite component subjected to foreign object impact are explained.

5.1. Numerical Tensile Test Results

The mesh sensitivity results of the standard tensile coupon using the shell elements can be seen in Figure 5.1 (a). The tensile failure stress and strain were found to increase a lot with increasing mesh size up to an element size of 2.0 mm. Beyond this element value, the failure stress and strain nearly remained unchanged, and showed an elastic-brittle failure type. Due to this fact, a mesh size of 2.5 mm was selected to model tensile tests in shell element models.

The comparison of the experimental and numerical results using both the shell elements and solid elements is illustrated in Figure 5.1 (b). As seen in the experimental results and the numerical results of both the solid and shell elements the composite behaves elastically until the failure stress, the material is then failed in a brittle manner. The difference between the experimental and numerical results is 4%. Bar stresses obtained from tests and numerical models performed at 350 s^{-1} and 1150 s^{-1} can be seen in Figure 5.2 (a) and (b), respectively. As shown in these figures, the numerical results are in tune with the experimental results at high strain rates. It was found that in the numerical models at 350 s^{-1} and 1150 s^{-1}, the strains, which were calculated from the relative displacement between the incident and transmitter bar and the nodes on the specimen surface, differed significantly from each other as shown in Figure 5.3. When the strain was determined from the former one, the numerical and experimental stress-strain curves showed good agreement (Figure 5.4 (a) and (b)) as well as the experimental results at quasi-static and dynamic strain rates (Figure 5.5). However, the strain value was found higher than that obtained from both strain gage and DIC in quasi-static tests as well as in the tensile tests of the standard test coupon. From the results in Figure 5.1 (c), it was

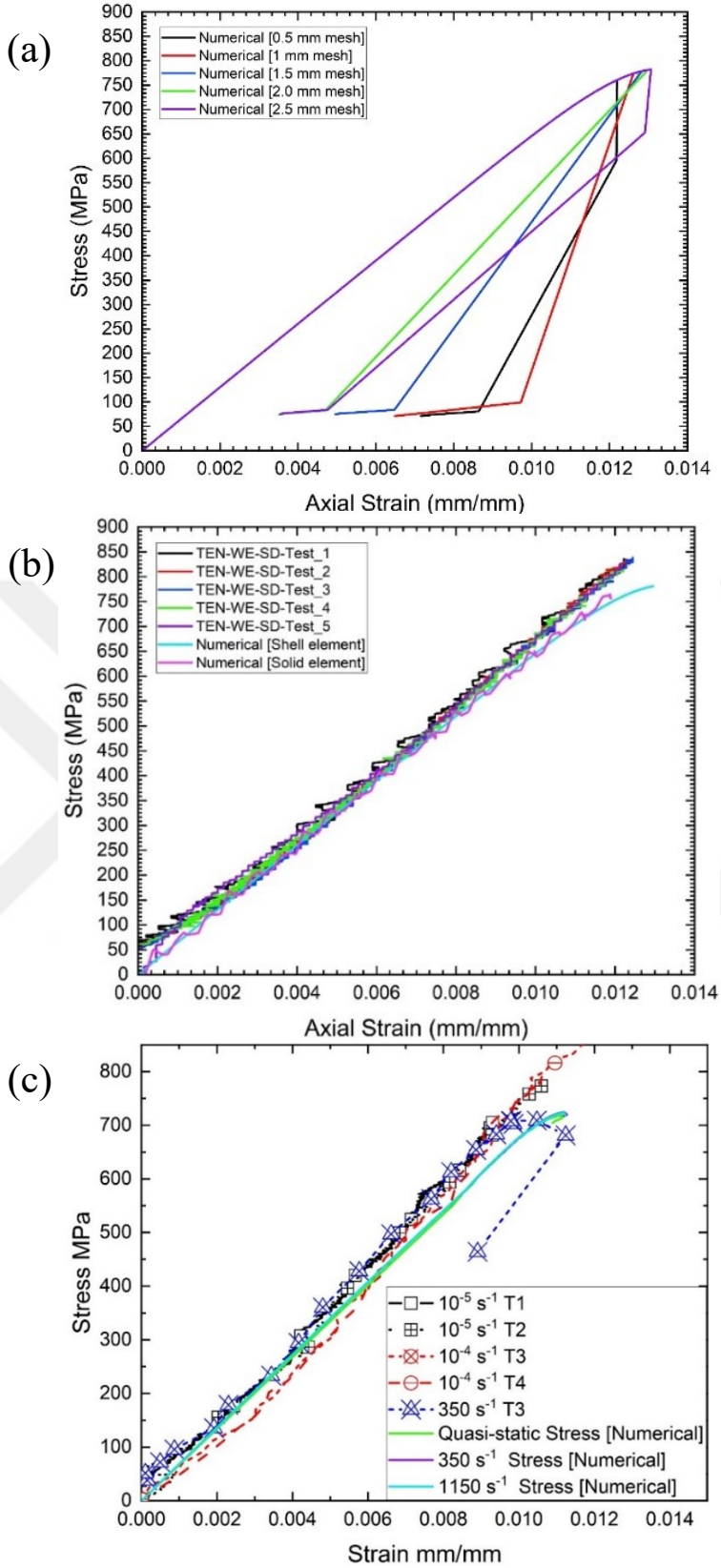

Figure 5.1. (a) The effect of mesh size, (b) comparison of the numerical and experimental results of the tensile tests and (c) experimental and numerical results at quasi-static and dynamic

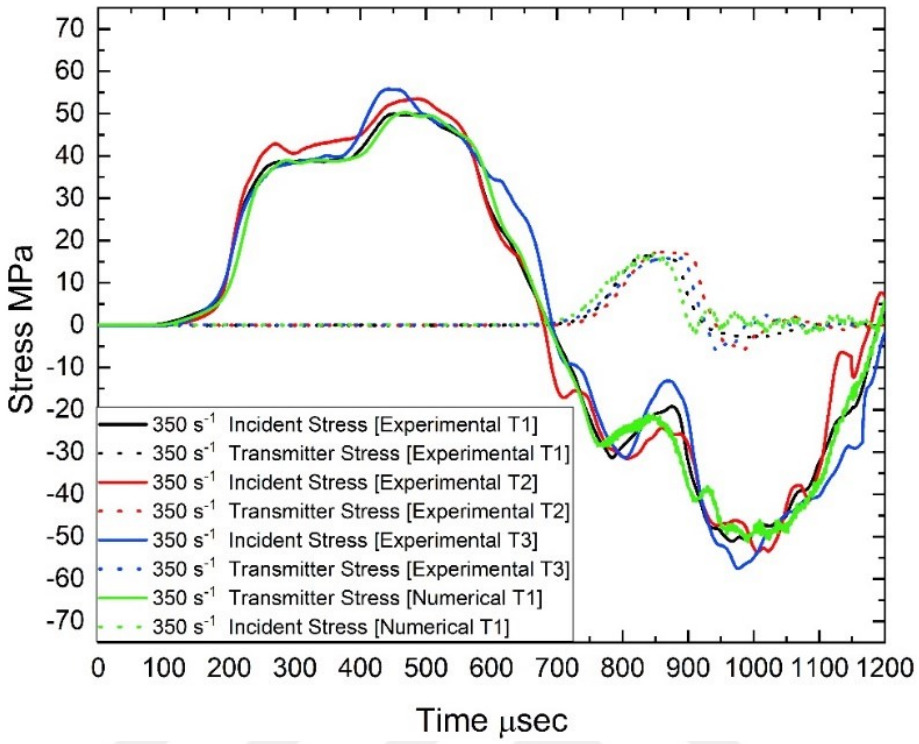

(a)

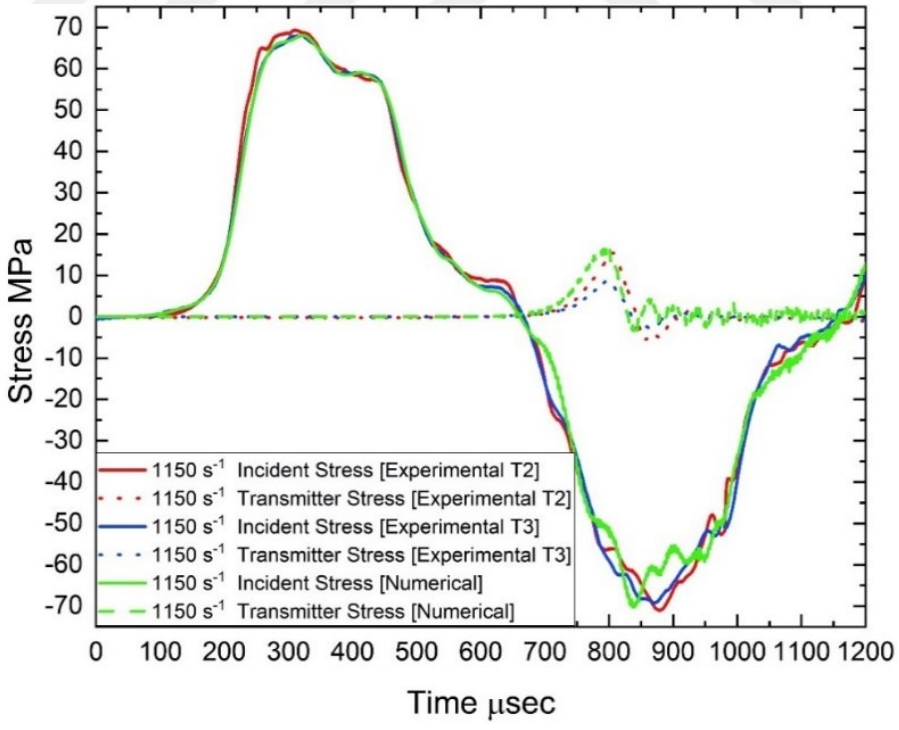

(b)

Figure 5.2. Experimental and numerical bar stress of weft specimens (a) 350 s^{-1} and (b) 1150 s^{-1}

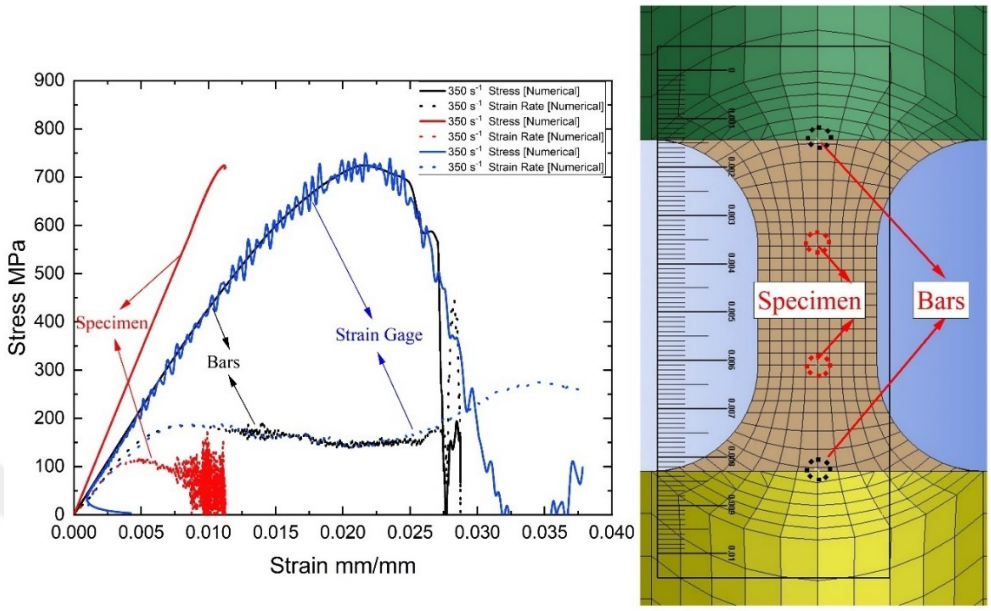

(a)

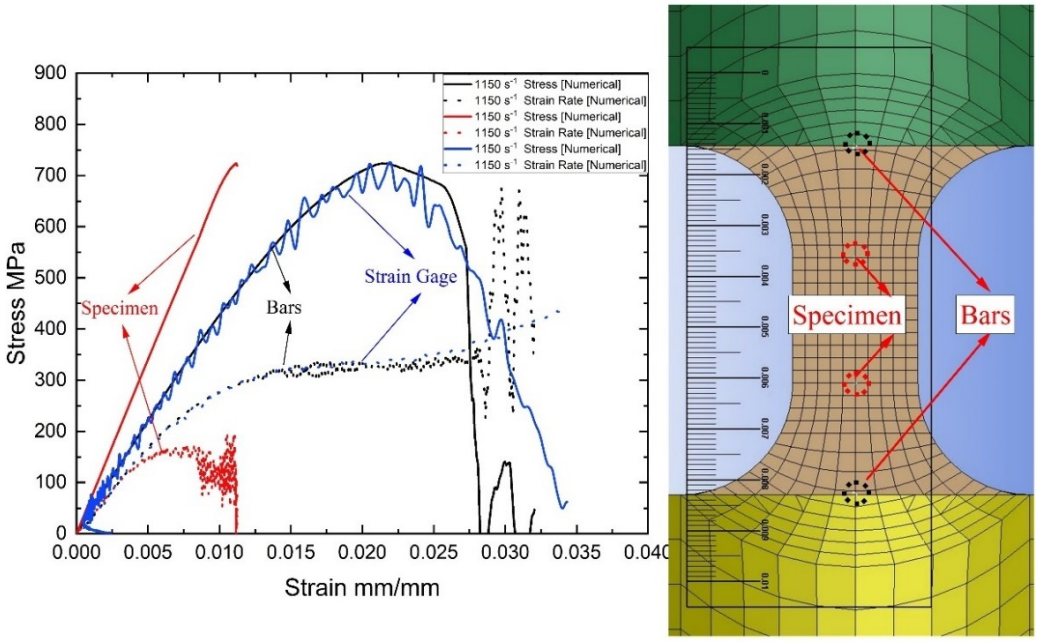

(b)

Figure 5.3. Numerical stress-strain curves of weft specimens calculated at a strain rate of (a) 350 s^{-1} and (b) 1150 s^{-1}

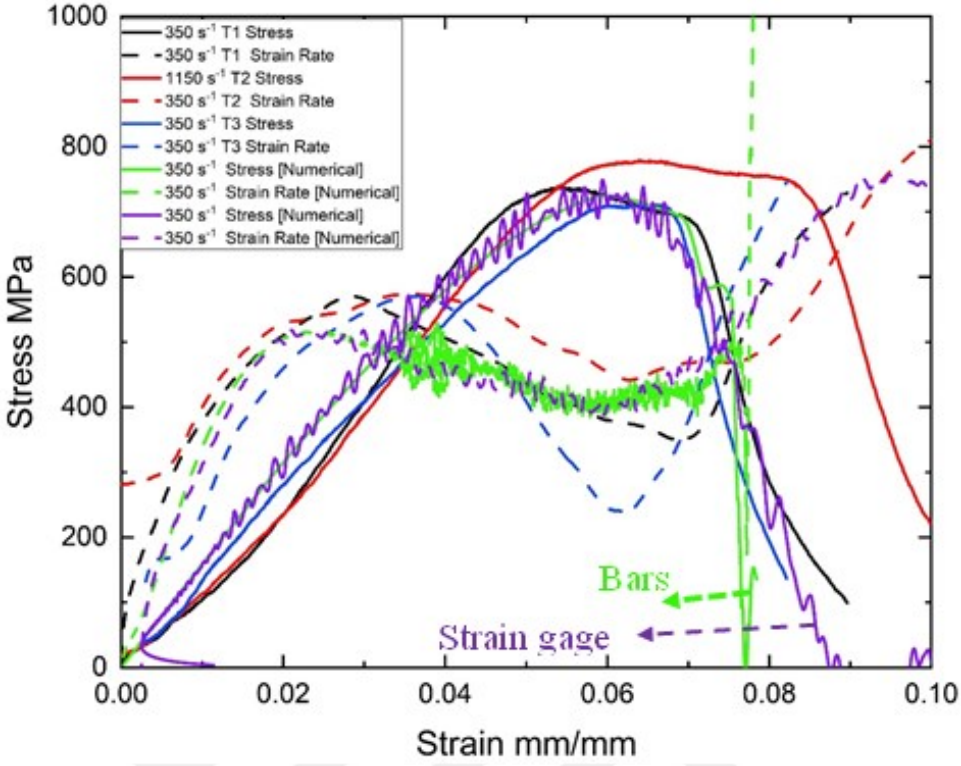

(a)

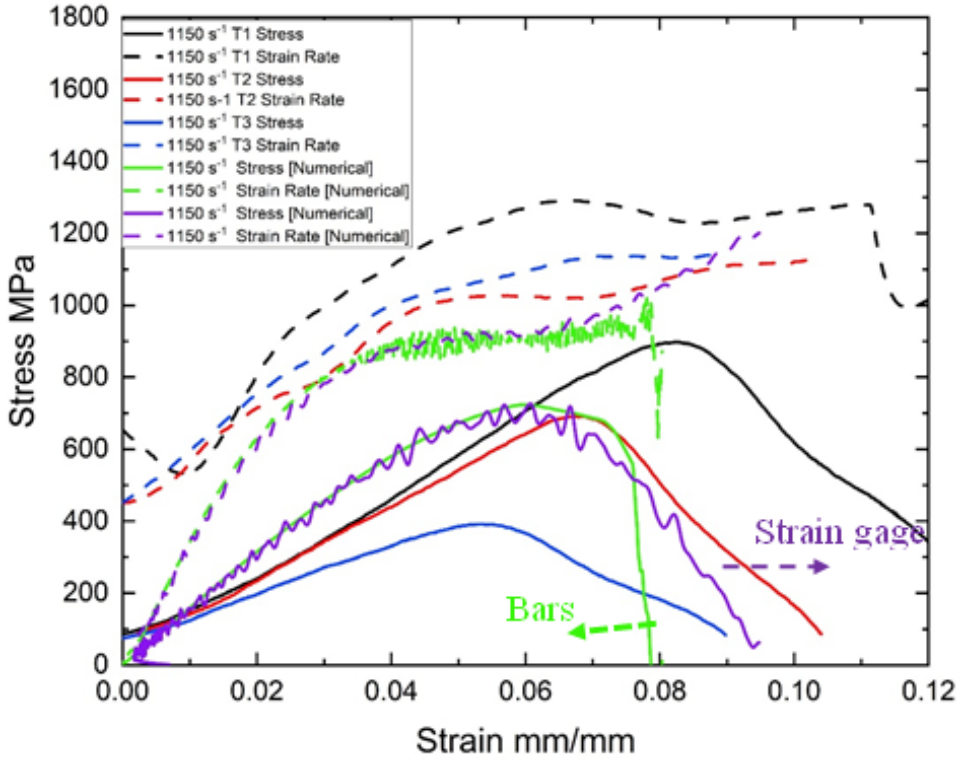

(b)

Figure 5.4. Experimental and numerical stress-strain rate-strain curves of weft specimens at (a) 350 s^{-1} and (b) 1150 s^{-1}

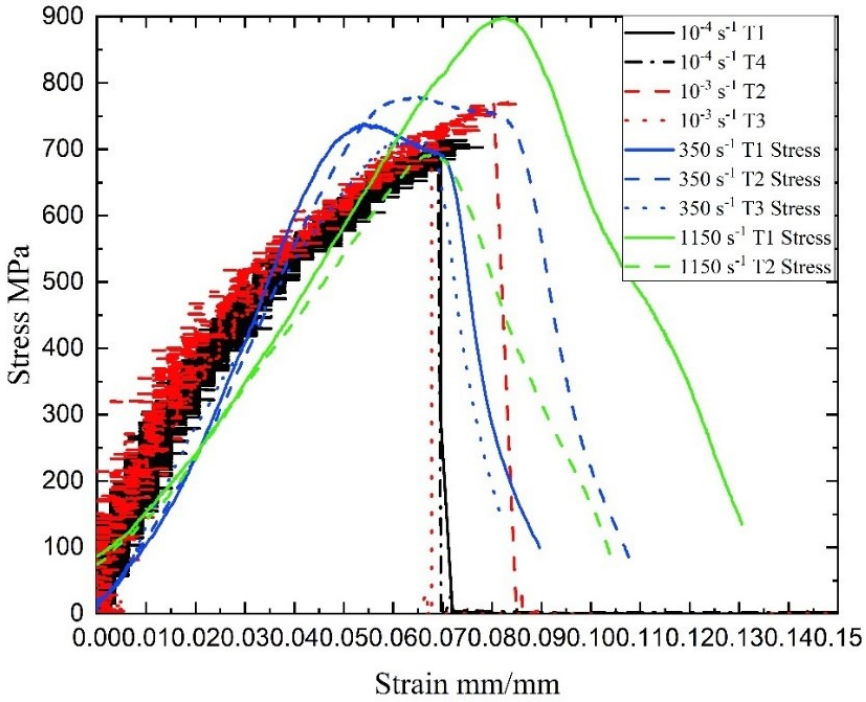

Figure 5.5. Experimental stress-strain curves obtained in the weft direction at quasi-static and dynamic strain rates

reached that the strain determined from the latter was more accurate since the strains, which were calculated by the DIC measurements (Figure 5.1 (c)) accurate since the strains, which were calculated by DIC measurements (Figure 5.1 (c)), were in tune with those determined by strain gages (Figure 5.1). Besides, the stress-strain results obtained from the standard tensile tests (Figure 5.1) were almost the same as those calculated from the tests performed at the quasi-static and dynamic strain rates (Figure 5.1) regarding the failure stress. Also, a good agreement between the experimental and numerical results is obtained: the difference is about 7%.

Figure 5.6 shows the strain distribution over the gage section of the sample tested at a strain rate of 10^{-5} s^{-1}, which is obtained from the video recorded during tests via the 2D Digital Image Correlation (DIC) method at the certain times. As can be seen in Figure 5.6, the axial strain is uniformly distributed during the entire test. On some part of the specimen corresponding to the section beginning the fillet, some local non-uniformities in strain occurs, but it is not pronounced as compared to global strain distribution. At the fracture strain (Figure 5.6 (f)), the magnitude of the strain over the gage section was found to be 0.01, which was the tensile fracture strain of the composite.

Figure 5.7, which is obtained from the 2D Digital Image Correlation (DIC) method, shows the strain distribution of the specimen tested at 350 s^{-1} strain rate for the

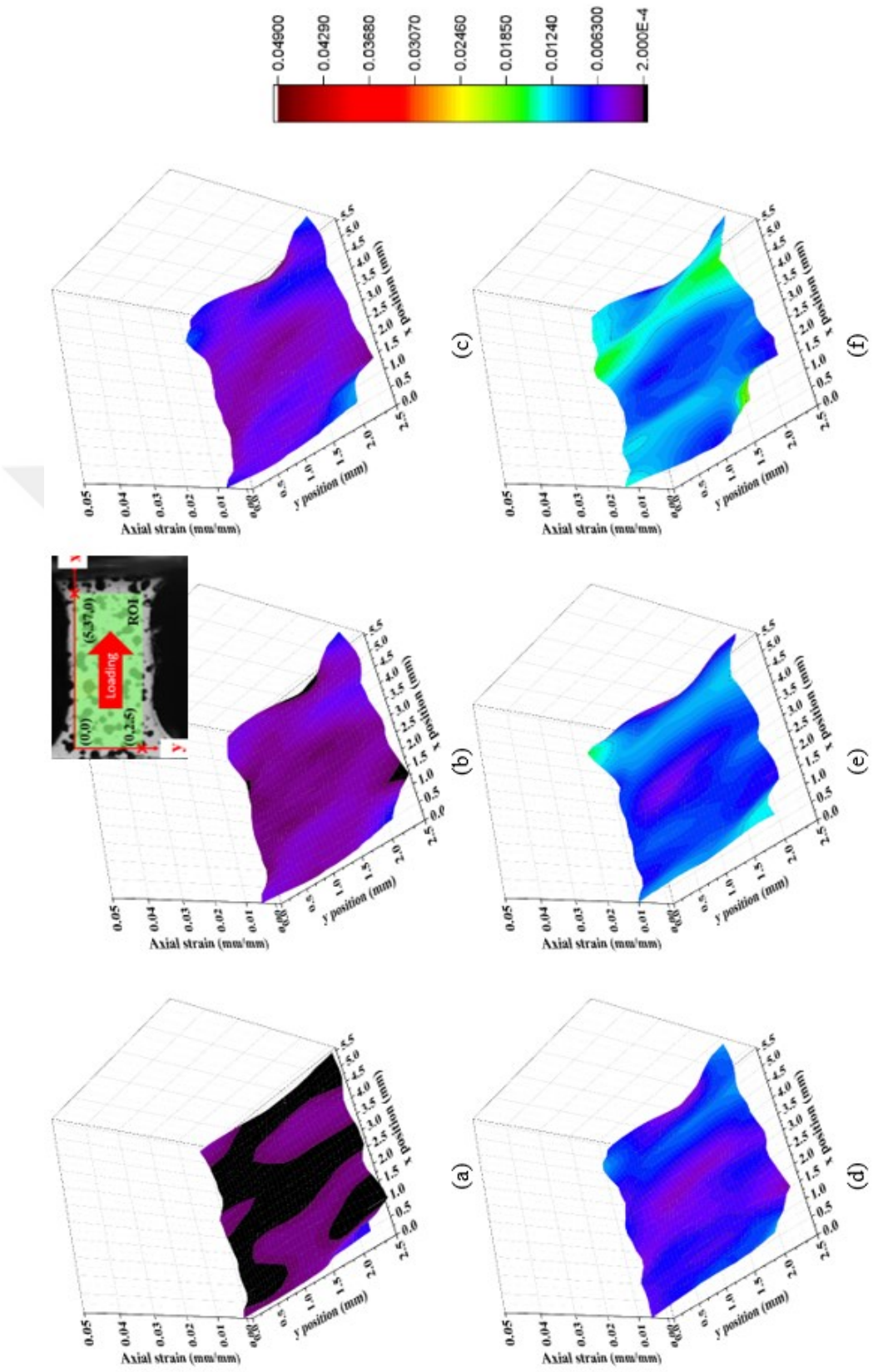

Figure 5.6. Strain distribution on the front surface at (a) 0 sec, (b) 30 sec, (c) 70 sec, (d) 115 sec, (e) 180 sec and (b) 260 sec

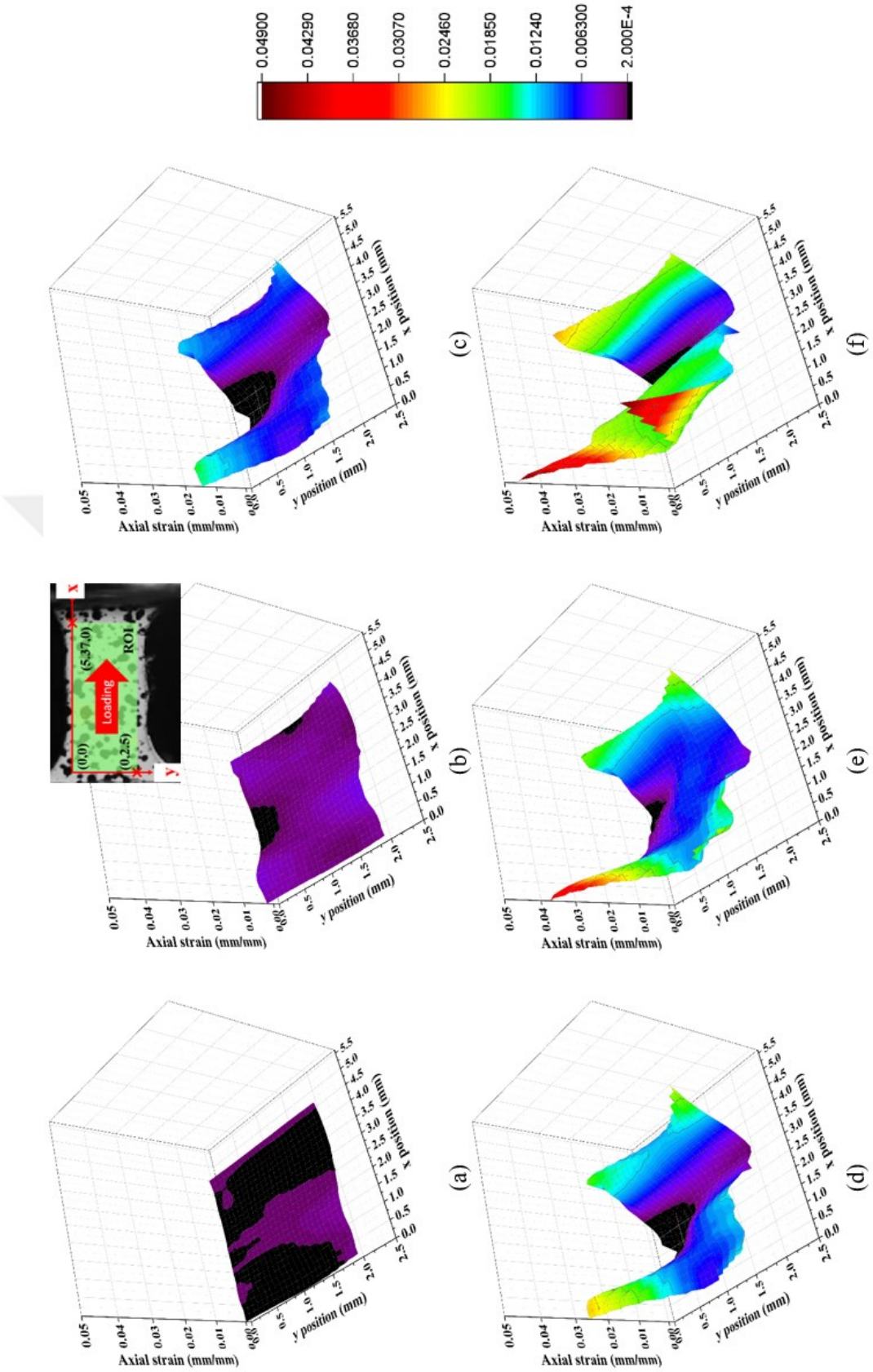

Figure 5.7. Strain distribution on the front surface at (a) 0 µsec, (b) 50 µsec, (c) 75 µsec, (d) 90 µsec, (e) 110 µsec and (b) 140 µsec

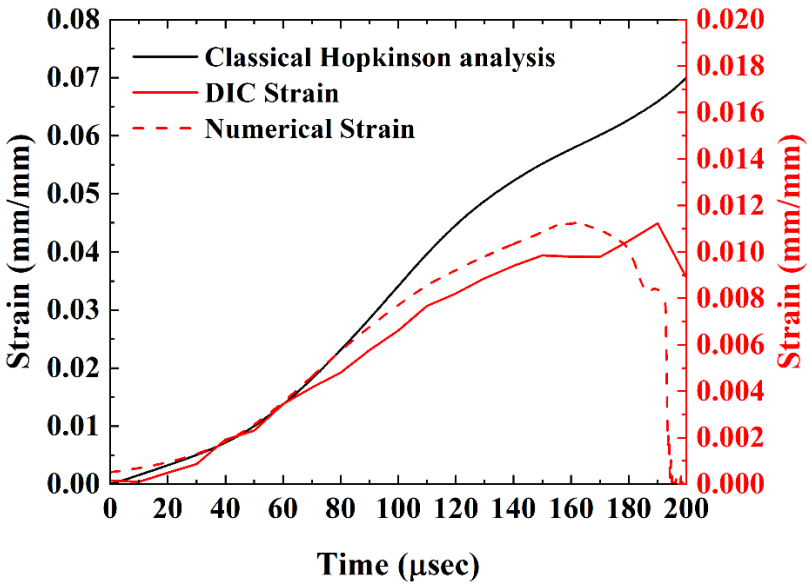

Figure 5.8. Strain-time curves calculated from Hopkinson theory, DIC method and numerical model

certain times. As shown in this figure, the nonuniform distribution of axial strain is obtained during the entire test. In all investigated times, the strain in the middle section is found to be less than the one occurring at the ends of the specimen. The cause of the nonuniformity in strain is thought to be due to the fillet parts of the specimen. Compared with the quasi-static strain distribution in Figure 5.6, a local strain distribution in the gage length at the high strain rate is observed. As getting closer to the fillet sections, the distribution was found to be non-uniform. It can be easily seen in the strain distribution at 140 μsec (Figure 5.7 (f)) that the maximum strain in the fillet section is calculated as 0.045 while it is determined in the gage section as 0.01, which is the same as the numerical strain. It is worth noting that the strain of 0.045 is nearly similar to the strain, 0.05, calculated from the Hopkinson theory (Figure 5.8). Based on this result, the reason for the difference between strain values obtained from the DIC and Hopkinson theory is the non-uniform strain distribution over the entire gage length of the tensile specimen (Figure 5.7). In dynamic tensile tests of composites in the split Hopkinson tensile test device, this effect must be eliminated by either using the strain gages directly attached on the specimen or using the DIC method to measure and calculate the strain.

Figure 5.9 shows the deformation of the numerical and experimental specimen. In this figure a, b, c, d, e, and f represent the specific time values shown in Figure 5.6 and Figure 5.7. A numerical strain plot was employed to investigate deformation in numerical models while strain distributions on the surface of the experimental specimens were ob-

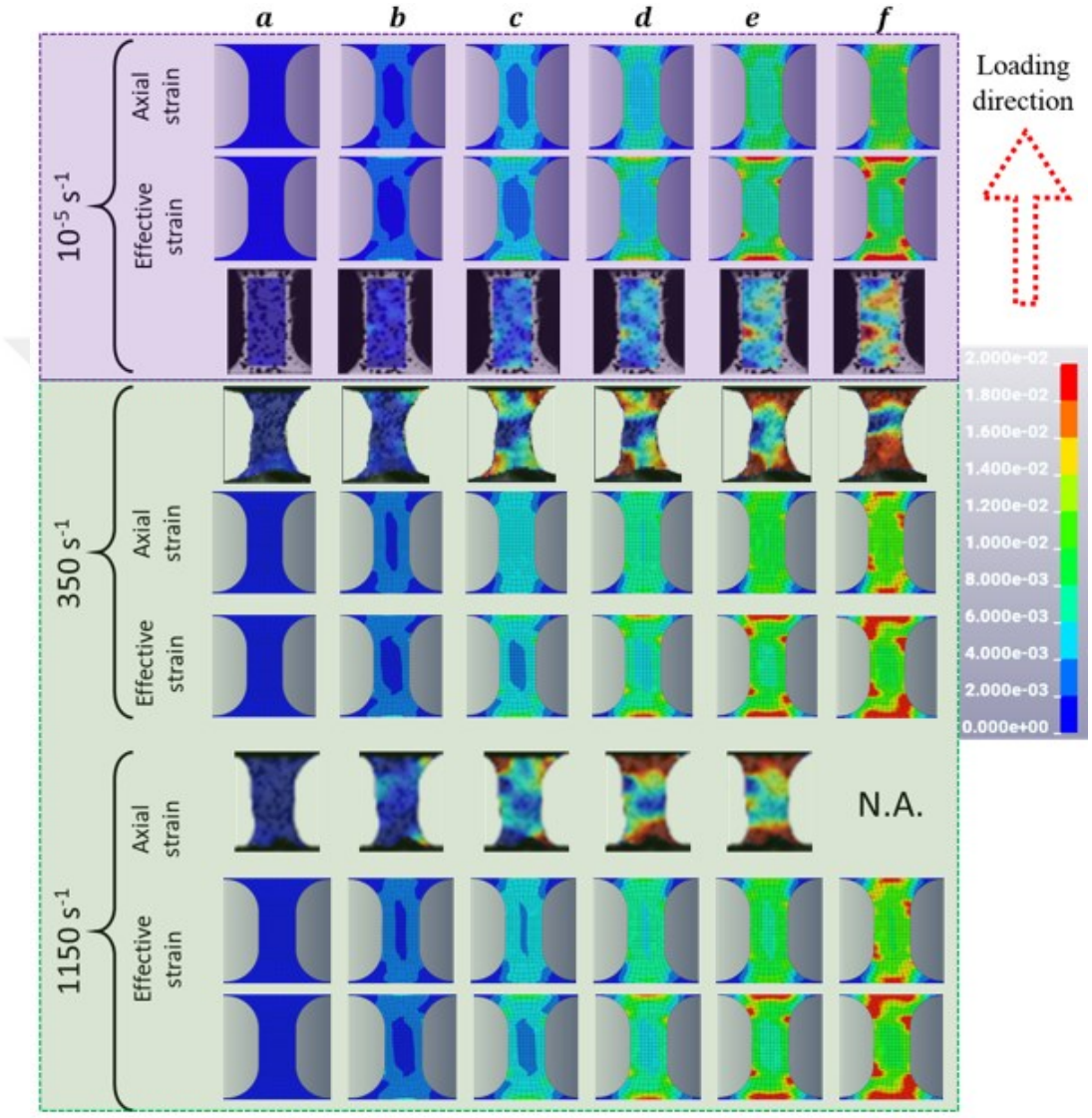

Figure 5.9. Experimental and numerical deformation on the specimen surface at the different loading stages

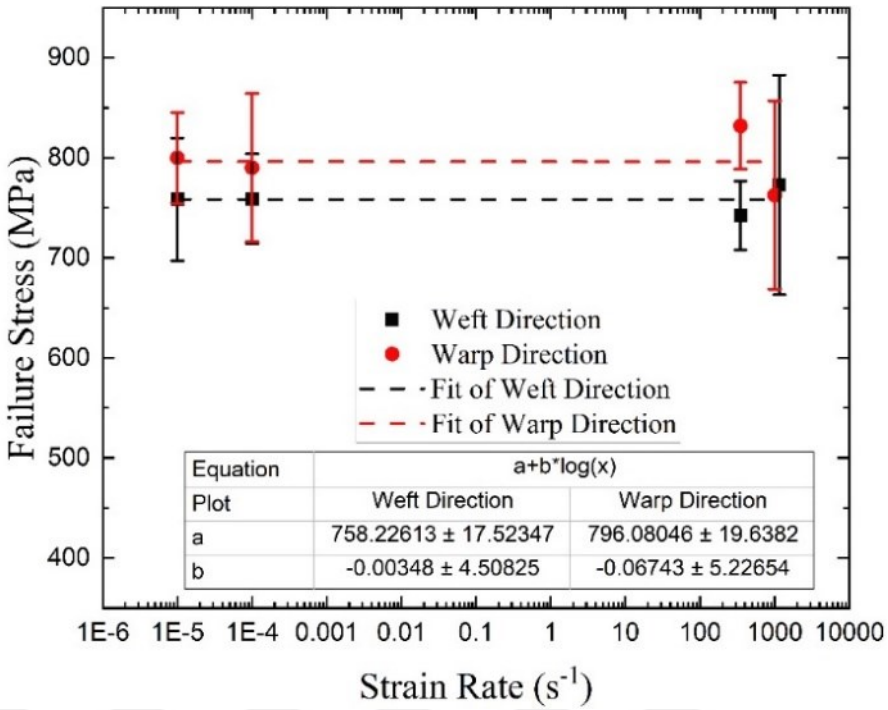

Figure 5.10. Failure stress variation with log strain rate

tained using DIC methods. As shown in the numerical and experimental quasi-static results, there is no damage occurred in the specimen up to 180 sec in the quasi-static test and 110 μsec in the dynamic test. Beyond these time values, the damage starts to accumulate at the end of the fillet sections, near the gage section, the specimen failure then occurs, about 0.01 strain, within the region where the damage accumulation takes place. Besides, the damage accumulation around the fillet section is also observed on the experimental and numerical specimens tested at high strain rates. The failure region occurring in the dynamic samples is found to be similar to that occurring in the quasi-static specimens. For both quasi-static and dynamic damage initiation and propagation results are well predicted by numerical models as shown in Figure 5.9. Moreover, the strain is distributed more uniformly throughout the gage section of the quasi-static samples compared to that of the dynamic specimens. The results obtained well agree with that seen in Figure 5.6 and Figure 5.7. As the strain rate increase, there is no time for uniform load propagation through the entire gage section of the specimen. Therefore, the damage is more accumulated in the fillet part of the dynamic specimen compared to that of the quasi-static specimen. The strain distribution in the experimental sample at the fractured time was not calculated since at that time the paint on the surface was removed.

Figure 5.10 shows the variation of failure stress with log strain rate. The fracture stress and fracture strain at the weft and warp direction as well as the elastic modulus of composite (Figure 5.1 (c)) are almost strain rate insensitive.

5.2. Numerical Compression Test Results

Standard compression test and numerical results -for both solid and shell elements- of the weft specimen can be seen in Figure 5.11. As can be seen in the figure, the experimental and numerical stress increase linearly up to the fracture stress followed by a sudden stress drop. Besides, as the shell element size decreases, the failure stress remains unchanged and the composite shows more brittle behavior. It is also seen that there is a good agreement between the numerical and experimental results. The difference between them is about 9%.

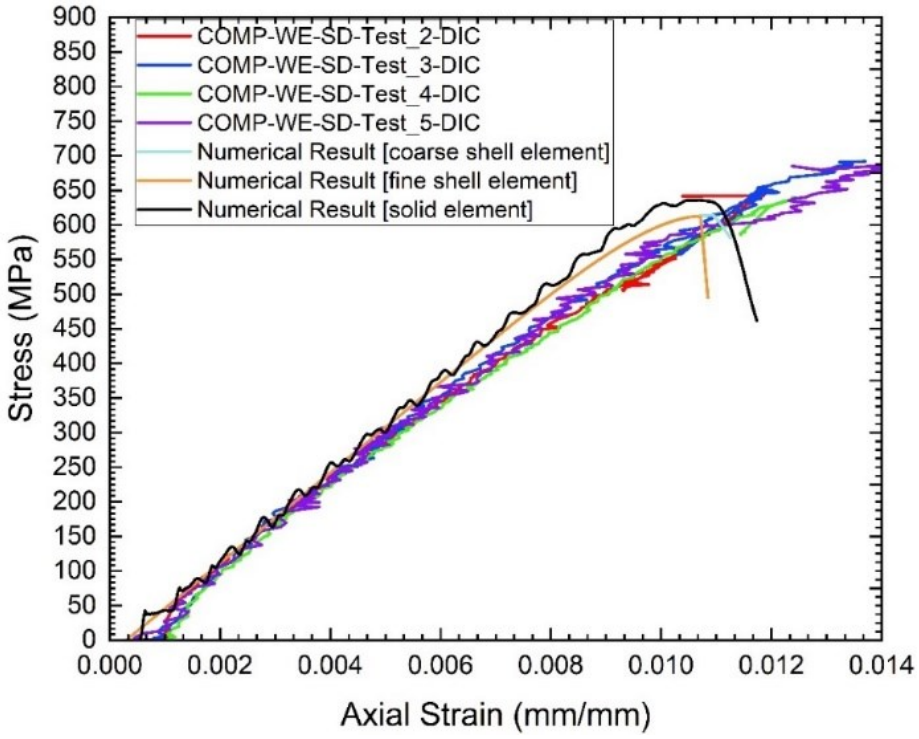

Figure 5.11. Comparison of the experimental and numerical stress-strain curves

5.3. Numerical In-plane Shear Test Results

In the shell element model of the standard in-plane shear test specimen, TAU and GAMMA parameters were first optimized by considering the linear part and the

hardening part of the shear stress versus shear strain curve. Figure 5.12 shows the optimization results of these parameters of material model 58. A reasonable agreement between the experiment (the solid black line with cross symbols) and the numerical result (the solid purple line) was obtained as the TAU and GAMMA parameters were selected as 77.8 MPa and 0.0375, respectively. In addition, experimental and numerical results can be seen in Figure 5.13 (a). In solid element models, the hardening behavior presented in the shear stress-shear strain curves was obtained by selecting the softening parameter (AM4) of the material model 162 as -0.17. As seen in the figure, the experimental result is in tune with the results of the numerical models using shell and solid elements.

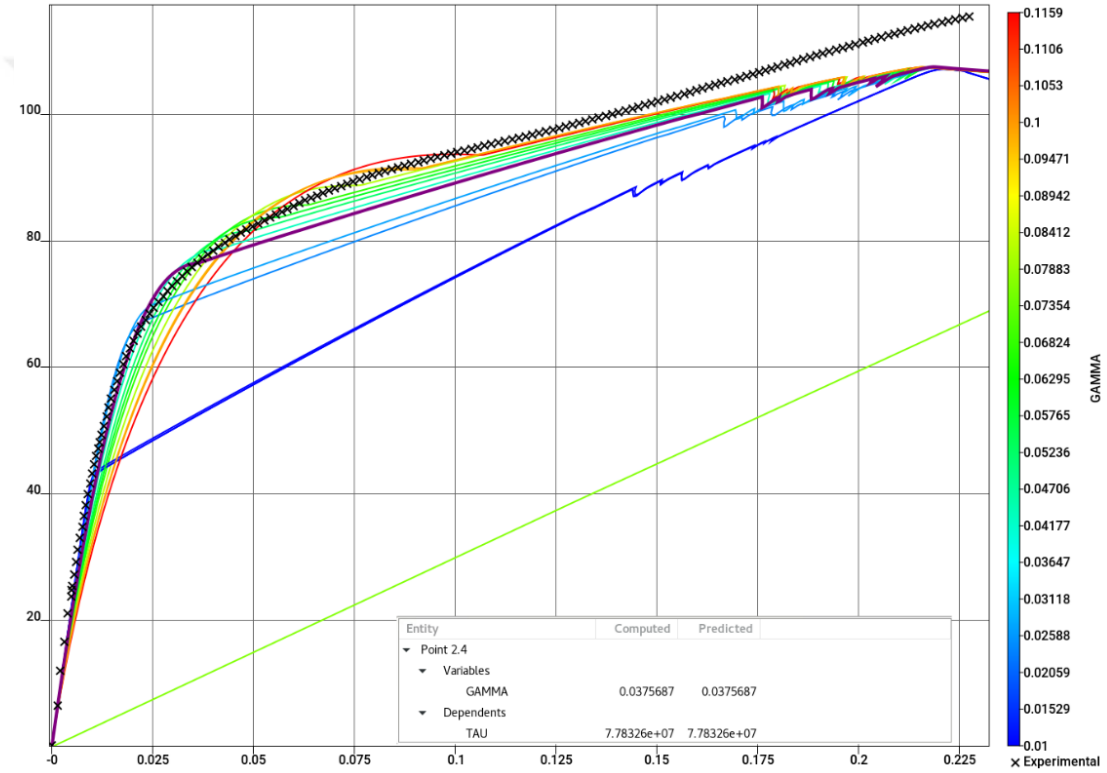

Figure 5.12. Optimization results for TAU and GAMMA parameters of MAT_58

Figure 5.13 (b) shows a comparison between shear stress-shear strain results obtained from the experimental and numerical models at quasi-static and high strain rates. Contrary to the experimental and numerical results of the standard in-plane shear tests, the numerical shear stress value reached on the hardening part of the shear stress curve was found to be higher than that obtained from the experiment. The reason could be the fiber scissoring (the rotation of fibers towards the loading direction) occurring during the deformation of in-plane specimens, which is not possible to model numerically.

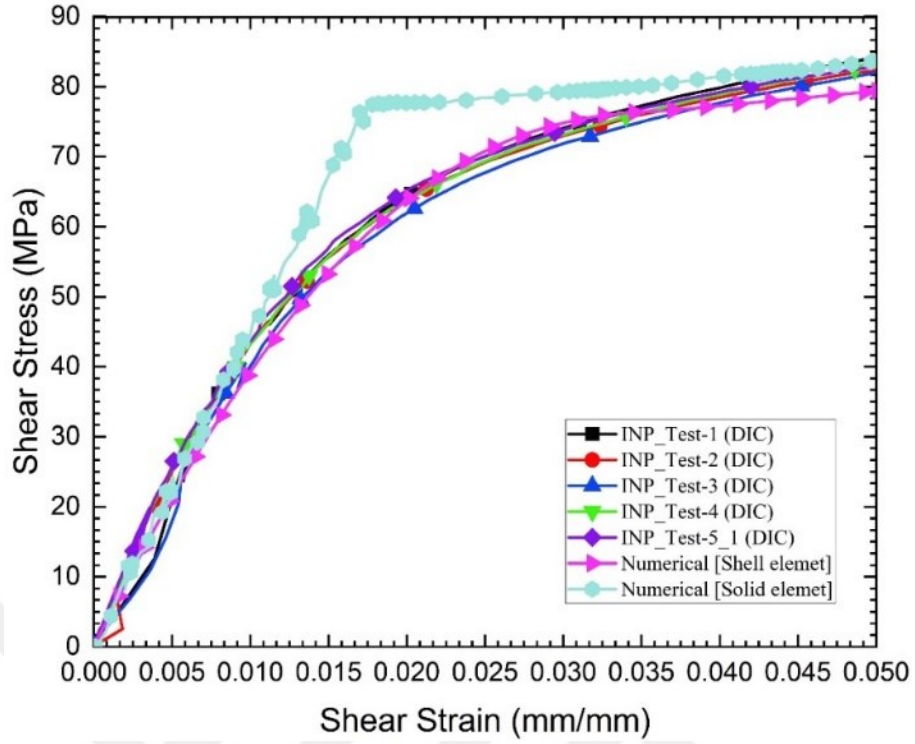

(a)

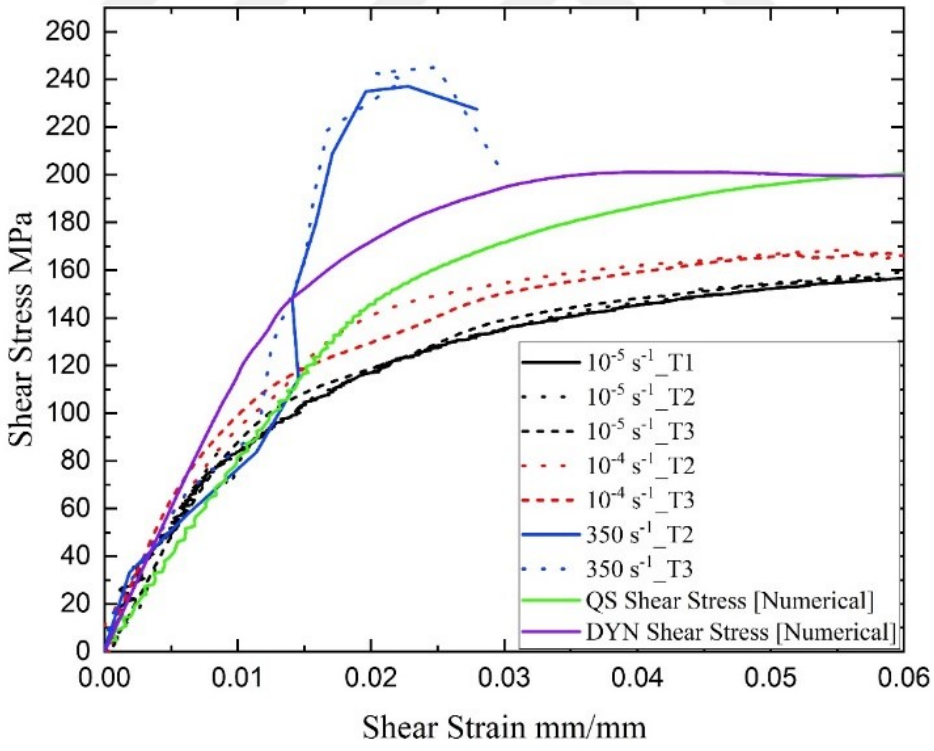

(b)

Figure 5.13. Experimental and numerical shear stress-shear strain curves obtained from (a) the standard tests and (b) quasi-static and dynamic tests

5.4. Numerical Out-of-plane Off-axis Compression Test Results

Comparison between the experimental and numerical results of 0°,15°,30°, 45°,60°,75° and 90° off-axis specimens at quasi-static and high-strain rates can be found in Figure 5.14 - Figure 5.17. A good consistency was observed in the experimental and numerical stress-strain curves of 0°,15°,30°, 75° and 90° off-axis specimens at quasi-static strain rates as well as those of 15° and 30° off-axis specimens at high strain rates in terms of the failure stress. The difference between the experimental and numerical results of the 0°,15°,30°, 75° and 90° off-axis specimens at quasi-static strain rates is 10%, 27%, 13%, 10% and 2%, respectively. While, it is calculated as 10% and 30 % for 15° and 30° dynamic off-axis specimens. However, the numerical models did not show the nonlinear behavior of the experimental curves of 45° and 60° specimens. The reason could be the meshing technique of the layers of the composite. The sharp corners of the layers include irregular solid elements, it, therefore, may have caused the composite to fail before reaching its maximum strength, i.e. irregular elements may have caused premature failure.

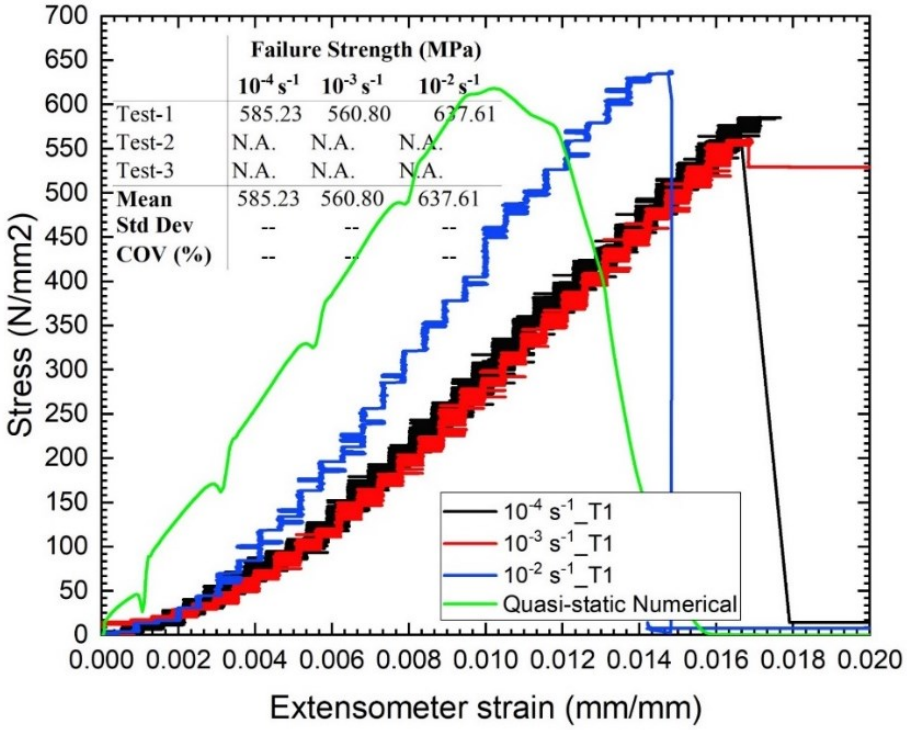

Figure 5.14. Numerical and experimental quasi-static compression test results obtained from the specimen having an off-axis angle of 0°

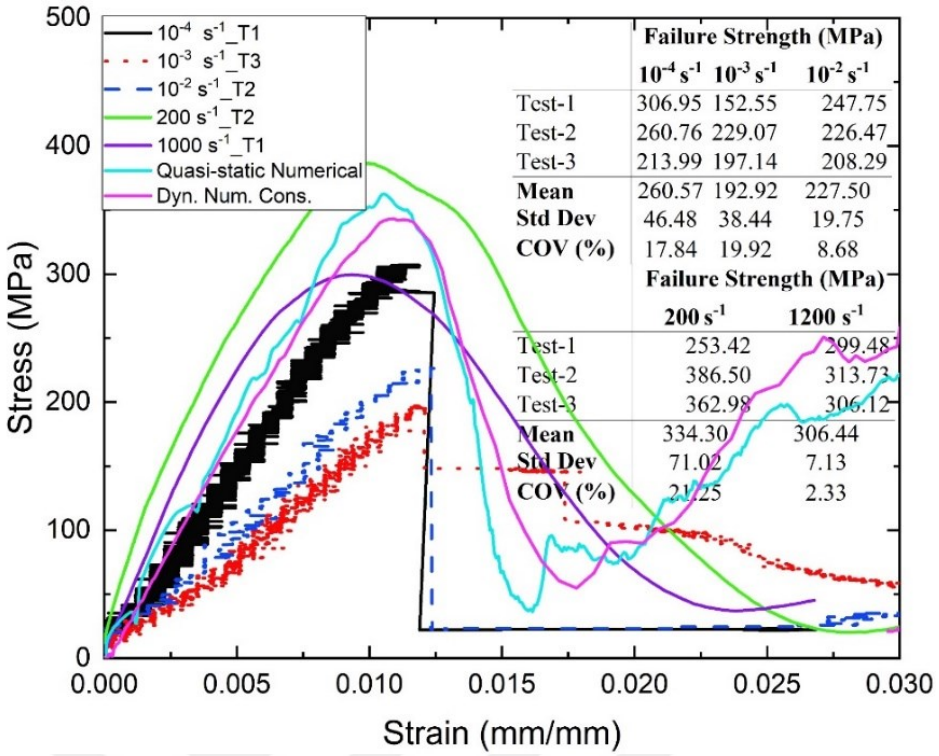

	Failure Strength (MPa)		
	10^{-4} s^{-1}	10^{-3} s^{-1}	10^{-2} s^{-1}
Test-1	306.95	152.55	247.75
Test-2	260.76	229.07	226.47
Test-3	213.99	197.14	208.29
Mean	260.57	192.92	227.50
Std Dev	46.48	38.44	19.75
COV (%)	17.84	19.92	8.68

	Failure Strength (MPa)	
	200 s^{-1}	1200 s^{-1}
Test-1	253.42	299.48
Test-2	386.50	313.73
Test-3	362.98	306.12
Mean	334.30	306.44
Std Dev	71.02	7.13
COV (%)	21.25	2.33

(a)

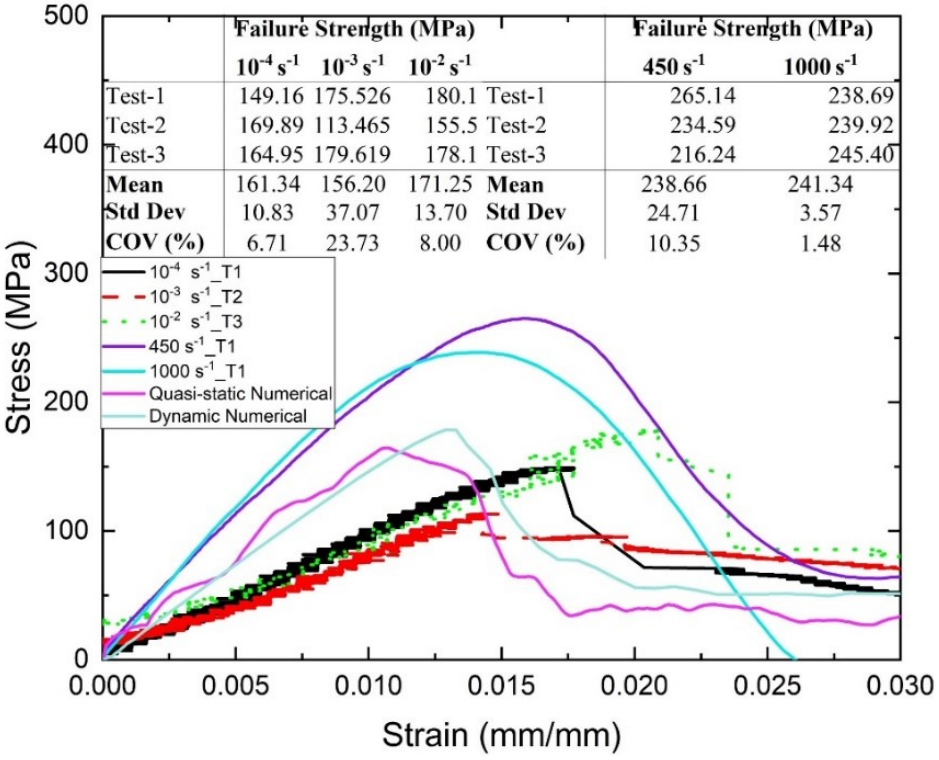

	Failure Strength (MPa)				Failure Strength (MPa)	
	10^{-4} s^{-1}	10^{-3} s^{-1}	10^{-2} s^{-1}		450 s^{-1}	1000 s^{-1}
Test-1	149.16	175.526	180.1	Test-1	265.14	238.69
Test-2	169.89	113.465	155.5	Test-2	234.59	239.92
Test-3	164.95	179.619	178.1	Test-3	216.24	245.40
Mean	161.34	156.20	171.25	**Mean**	238.66	241.34
Std Dev	10.83	37.07	13.70	**Std Dev**	24.71	3.57
COV (%)	6.71	23.73	8.00	**COV (%)**	10.35	1.48

(b)

Figure 5.15. Numerical and experimental quasi-static and dynamic compression test results obtained from the specimen having an off-axis angle of (a) 15° and (b) 30°

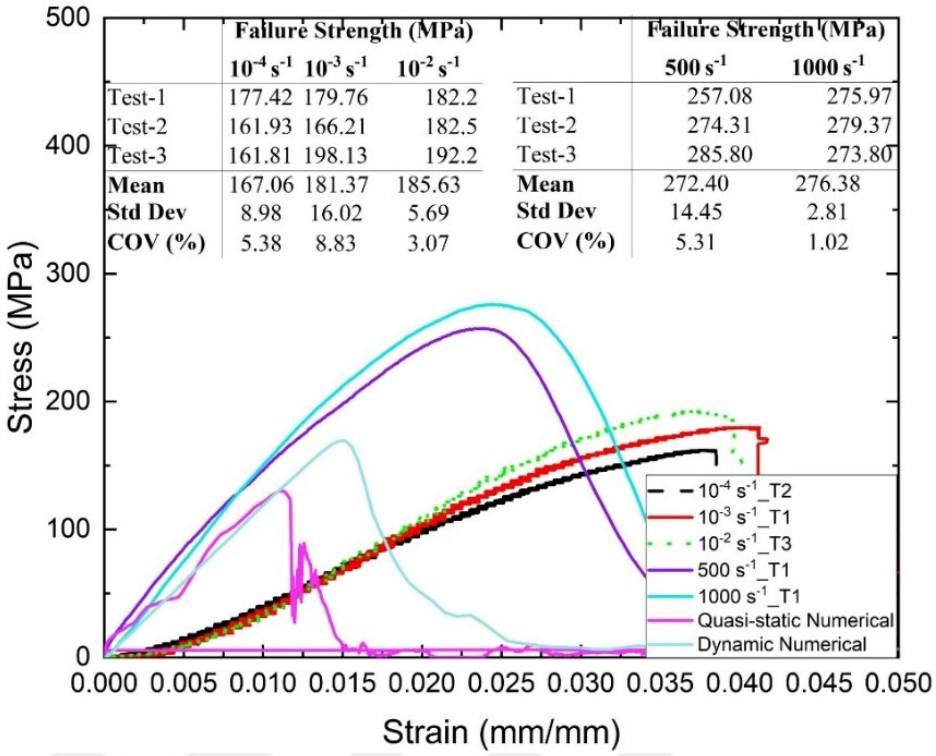

(a)

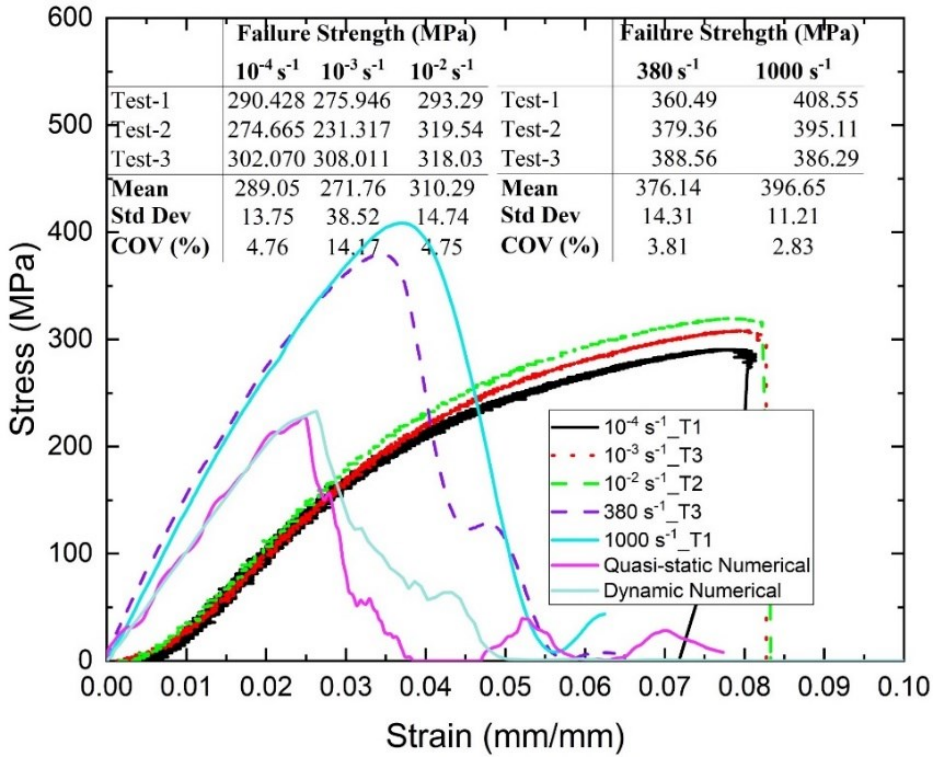

(b)

Figure 5.16. Numerical and experimental quasi-static and dynamic compression test results obtained from the specimen having an off-axis angle of (a) 45° and (b) 60°

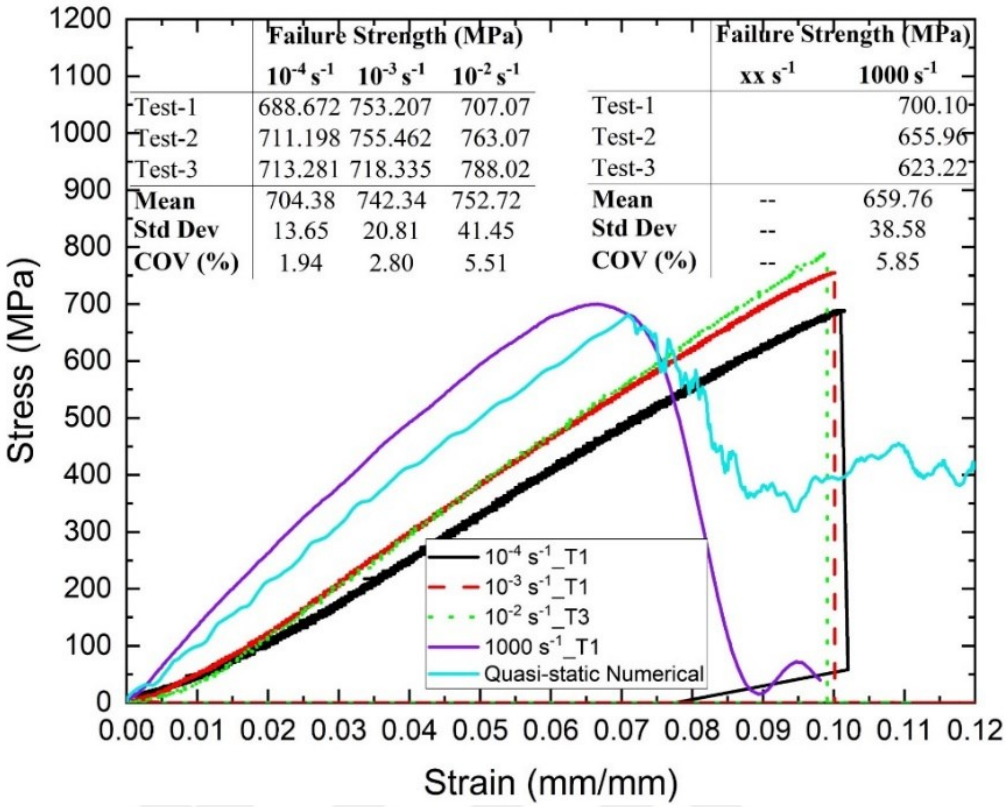

(a)

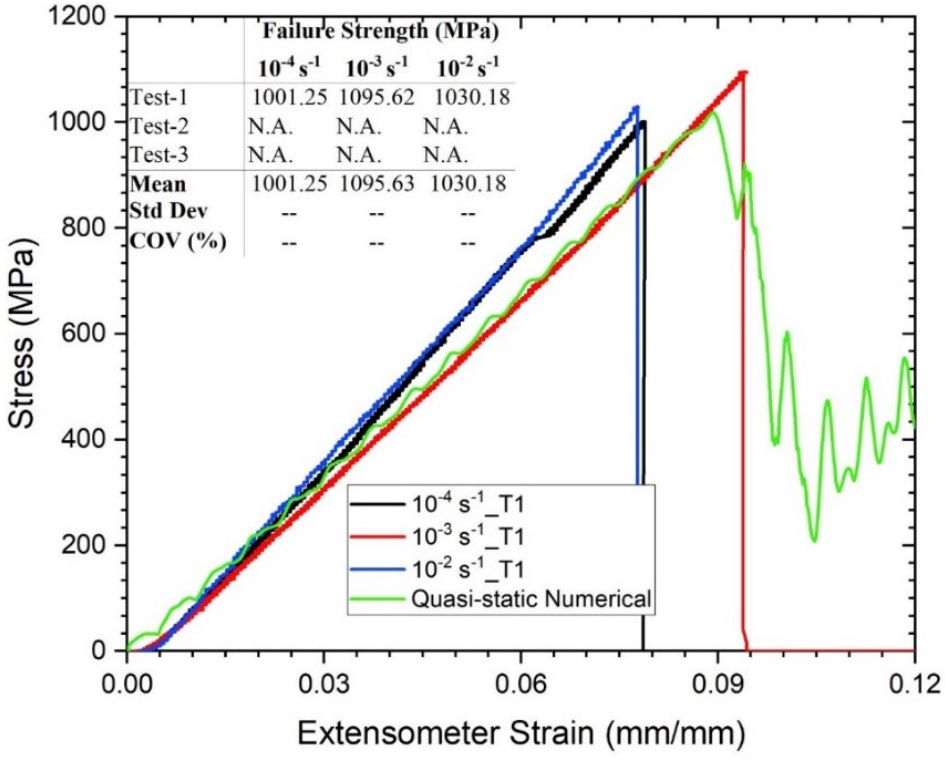

(b)

Figure 5.17. Numerical and experimental quasi-static and dynamic compression test results obtained from the specimen having an off-axis angle of 75°

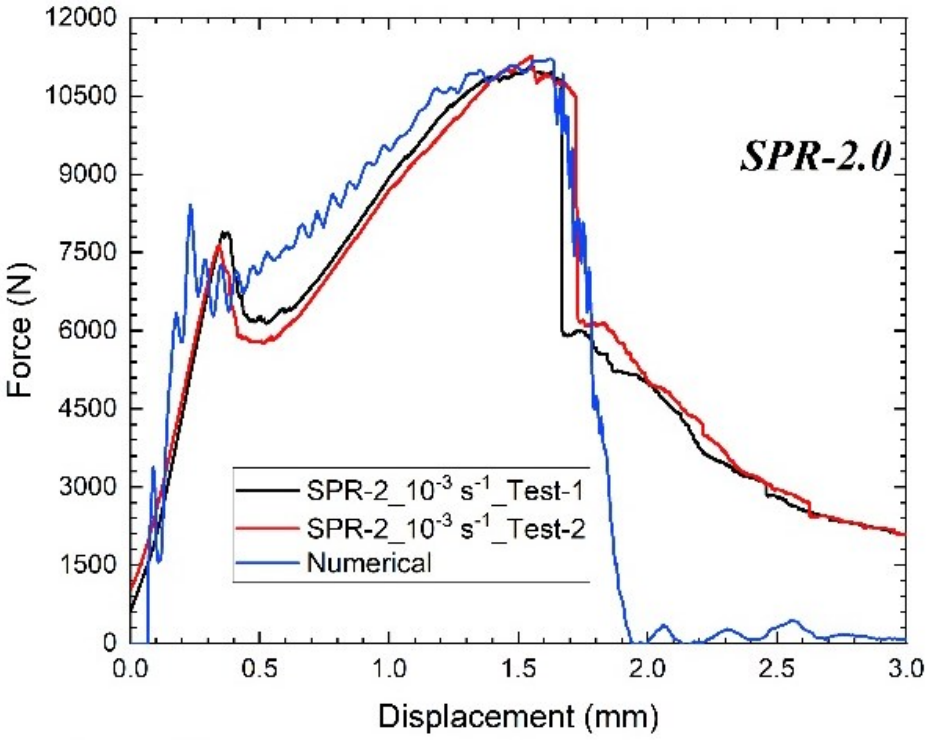

(a)

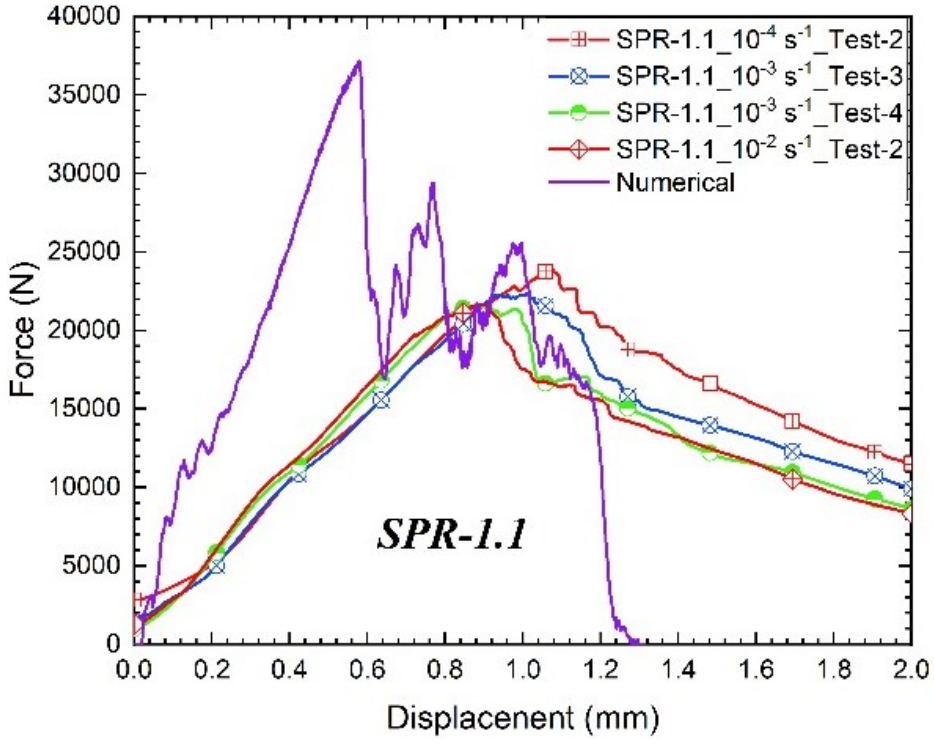

(b)

Figure 5.18. Comparison of numerical and experimental results of punch shear tests, (a) SPR 2 and (b) SPR 1.1

5.5. Numerical Quasi-static Punch Shear Test Results

Figure 5.18 (a) shows a comparison of experimental and numerical punch shear results for the support span-to-punch ratio (SPR) of 2. To obtain the numerical results shown in Figure 5.18 (a), suitable values for the softening parameters (AM1, AM2, AM3 and AM4) and erosion parameter – expansive relative volume (EEXPN)- of material model 162 were investigated by trial-and-error method. By selecting an appropriate value for the AM4 parameter, which is 0.14, the first peak (corresponds to the internal delamination) in the force-displacement curve was tuned with the experimental one. Then, the second peak (corresponding to punch failure) in the force-displacement curve was investigated for different AM3 values, and by using a value of 0.1 the second peak in the experimental curve was well predicted by the numerical model. AM1 and AM2 parameters were assumed to be equal to each other since the composite used in this study is woven composite and has almost similar mechanical properties in the weft and warp directions. Therefore, the load drop beyond the second peak was caught by a value of 0.1 for AM1 and AM2 parameters as well as the EEXPN parameter with a value of 1.3.

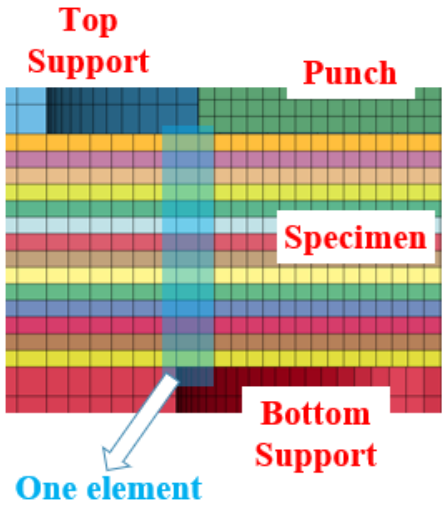

Figure 5.19. Numerical model of the punch shear test with the SPR 1.1

Experimental and numerical results obtained in the case of SPR 1.1 are illustrated in Figure 5.18 (b). Numerical results for SPR 1.1 were obtained by using the softening and erosion parameters validated or calibrated in the punch model with the SPR of 2. Experimental and numerical force-displacement curves show a bilinear behavior. The force increases linearly up to 10 kN, it then continues to increase with a lower force rate.

Compared to the displacement in the experimental result, that in the numerical model is found to be less: the difference is about 40%. The reason could be the number of the solid element of the specimen between the bottom support and the punch. As shown in Figure 5.19, the specimen includes only one element between the support and punch. In the model, the element size was 0.28 mm. Since using a smaller element size demands more computational power, the result (Figure 5.18 (b)) obtained from the numerical model was considered to be sufficient.

5.6. Numerical Flexural Test Results

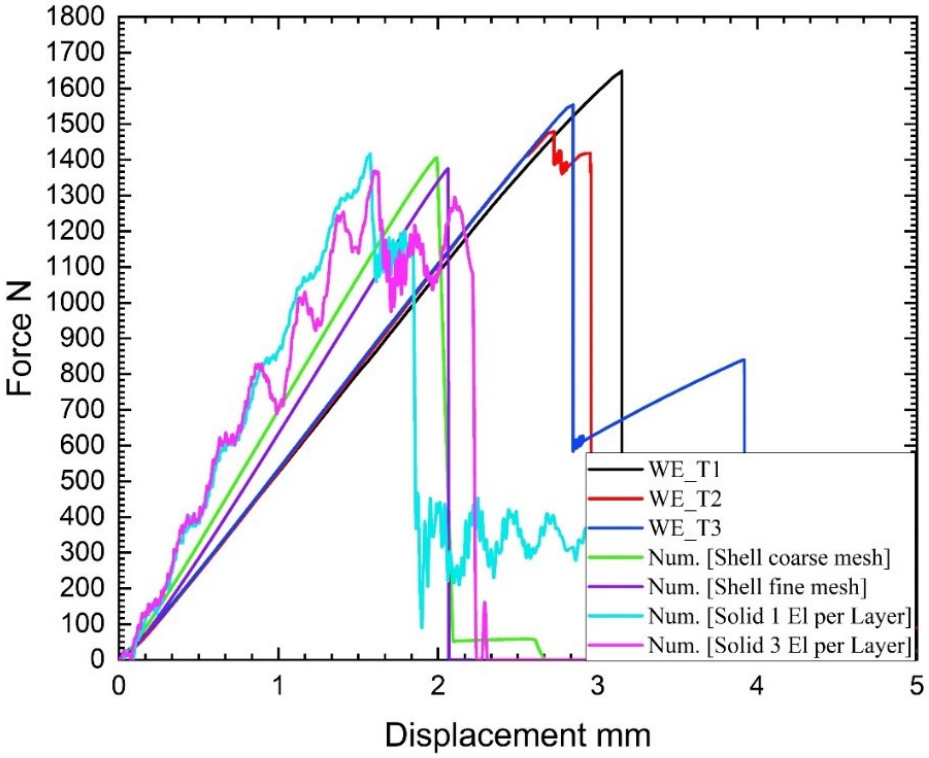

Figure 5.20. Numerical and experimental 3-point bending test results

The numerical and experimental results of the punch shear test are illustrated in Figure 5.20.In the experimental results it is seen that the specimen continues to withstand loads after the peak value is reached. By synchronizing video records of the test and its force-time curves, it was found that the load drop appearing in the results corresponded to the failure of the bottom layers of the composite. The load drop after reaching the peak is also seen in the numerical results obtained from the solid element model in which the specimen is meshed with a single element through the thickness. This behavior was not

predicted by the shell element model and the solid element model in which the specimen is meshed with three elements through the thickness since in the shell models the layers of the composite were modeled as a single layer, and three elements through the thickness in the solid model made the composite more rigid. Both shell and solid models could not accurately predict the displacement of the loading pin (the error between experimental and numerical results is 30%), but it can be seen in the shell model results that as the mesh size decreases, the predicted displacement value by the numerical model approaches the experimental one. Because it is very challenging to obtain the solution of the solid element model with much smaller element sizes, the result obtained is considered to be sufficient.

5.7. Numerical Ice Impact Test Results

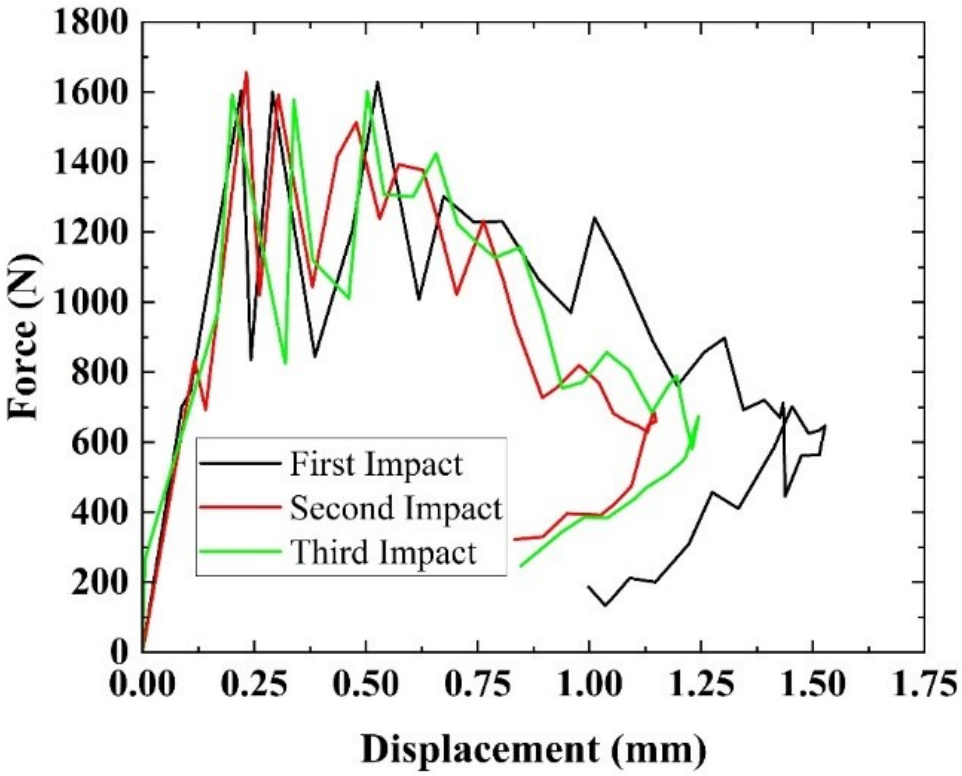

Figure 5.21. Numerical results of the multiple ice impact test

The simulation results of the 2 mm composite plate subjected to multiple ice impacts can be seen in Figure 5.21. In three impact cases, the maximum force is found to be about 1600 N while the displacement of the bottom surface is calculated as 1.5 mm for the first impact, 1.13 mm for the second impact and 1.25 mm for the third impact. The difference between the displacement values is due to the oscillation of the composite

plate. That is, the composite plate is still oscillating before it is impacted by the following ice. That's why, the constant displacement is not obtained in these impact cases. Because the impact energy is low, no damage is observed within the composite plate, meaning that the composite specimens deform elastically. Besides, the displacement of the specimen is calculated in experiments as 0.3 mm and 0.1 mm for the first and second impacts. The experimental displacements are lower than the numerical ones. The reason could be the aluminum foil that was used in the experiments to measure displacement. Probably, the foil does not measure such a small displacement value. Using the strain gage could have given a more accurate displacement result.

Figure 5.22 shows the comparison of the force displacement curves obtained from the ice impact simulation of the 0.88 mm and 2 mm composite specimens. It can be seen that the displacement of the 0.88 mm composite is found to be twice as much as that of the 2 mm specimen while a higher force is determined in the impact case of the 2 mm plate. As expected, the thinner composite plate is more elastically deformed compared to the thicker one. Thus, the thinner plate displaces more, and the ice impact causes a lower contact force.

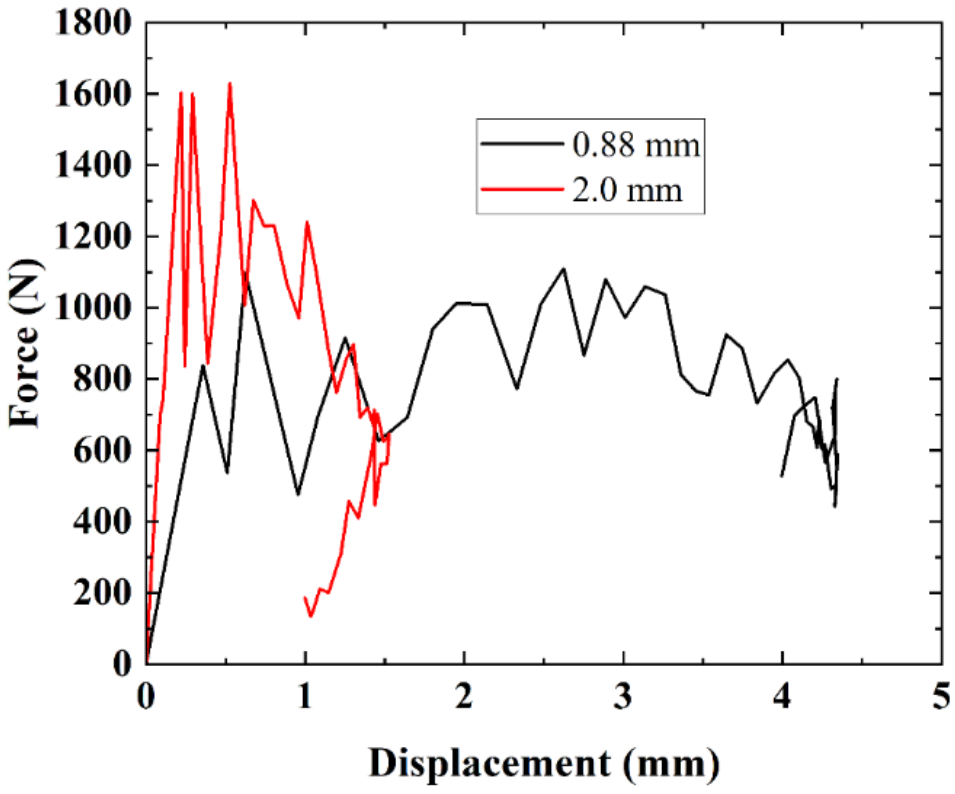

Figure 5.22. Force displacement curves of 0.88 mm and 2 mm composite plates

5.8. Numerical Low-velocity Impact Test Results

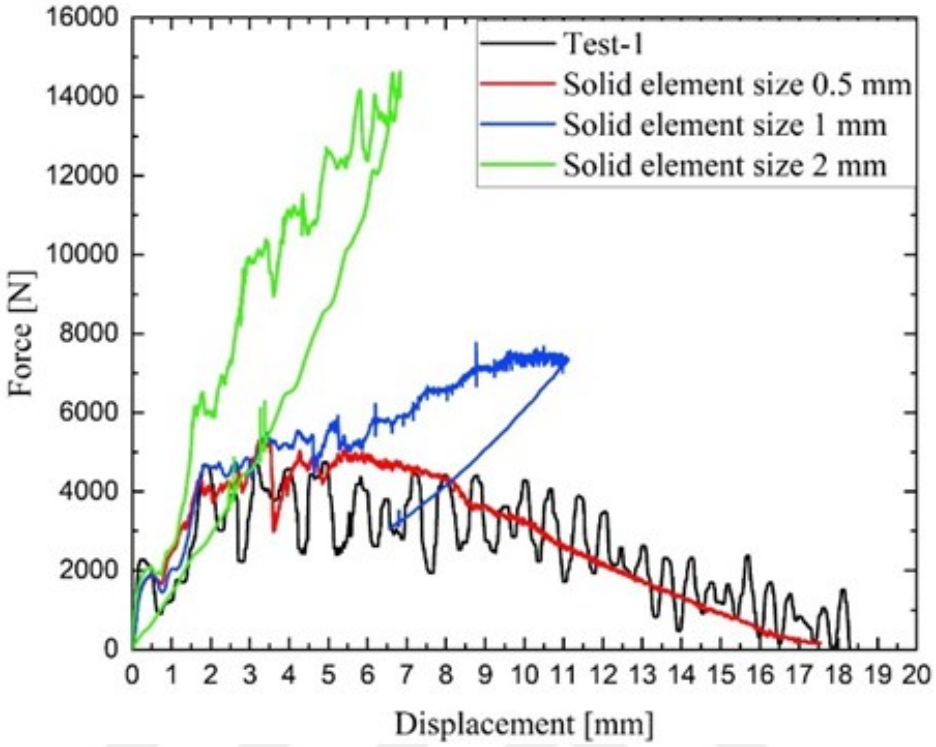

Figure 5.23. Comparison of the results obtained from the experiments and numerical models with solid element sizes of 0.5, 1 and 2 mm

Figure 5.23 shows the comparison of experimental and numerical force-displacement curves obtained in the perforation case. Different numerical models with element sizes of 0.5 mm, 1 mm and 2 mm were simulated to investigate the element size effect. It is seen in Figure 5.23 that as the element size decreases, the force-displacement curve of the numerical model shows similar behavior to that of the experimental one. Based on this result, it can be said that using an element size smaller than 0.5 mm will probably give better results in terms of force-displacement curve. However, due to the limited computing power available, an element size of 0.5 mm was selected to investigate damage occurring within the composite during the impact event.

Figure 5.24 shows the results obtained from the shell models with different element sizes of 0.28 mm, 1.25 mm and 2.5 mm together with the experimental result. From the results presented in the figure, it can be said that the model with an element size of 2.5 mm shows the closest behavior to the experimental curve among the other element sizes. Therefore, the shell model with a 2.5 mm element size was employed to model the perforation and penetration tests.

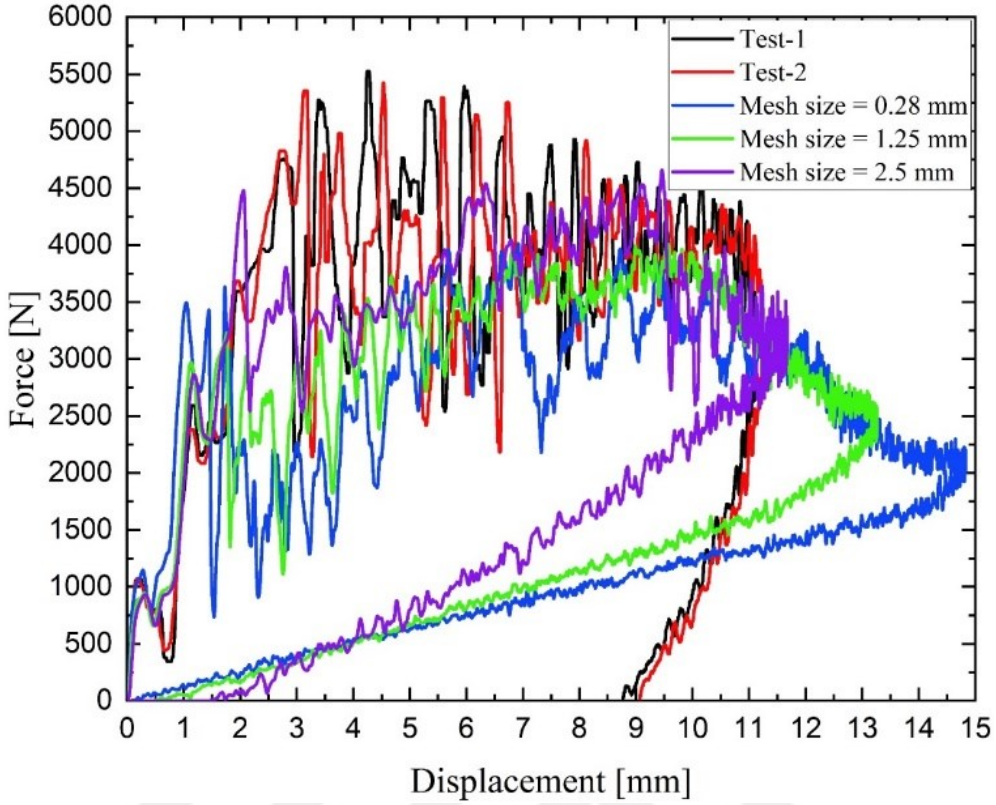

Figure 5.24. Comparison of the results obtained from the experiments and numerical models with shell element sizes of 0.28, 1.25 and 2.5 mm

Experimental and numerical force-displacement curves for the perforation case can be seen in Figure 5.25 (a). The numerical result includes the results of both shell and solid models. As seen in the figure, the initial part of the experimental force-displacement curve is well predicted by the shell and solid models. However, the sudden drop in force after the first peak and the second peak is exhibited better in the shell model. While the solid model captures the general behavior of the experimental curve. Longitudinal and transverse damage on the front and back surfaces of the composite induced after impact in the experiment and numerical models is illustrated in Figure 5.26. The damaged region measured in the experiment and solid model is almost similar while that measured in the shell model is found to be lower than those calculated in the experiment and solid model. The experimental and numerical results obtained in the penetration case can be seen in Figure 5.25 (b). In this figure, it can be seen that the solid model shows almost similar behavior to the experiments but fails to predict the rebounding of the striker. The reason could be the element size or the damage softening parameters of the MAT_162 material model. Because the rebounding of the striker is almost similar in solid and shell models

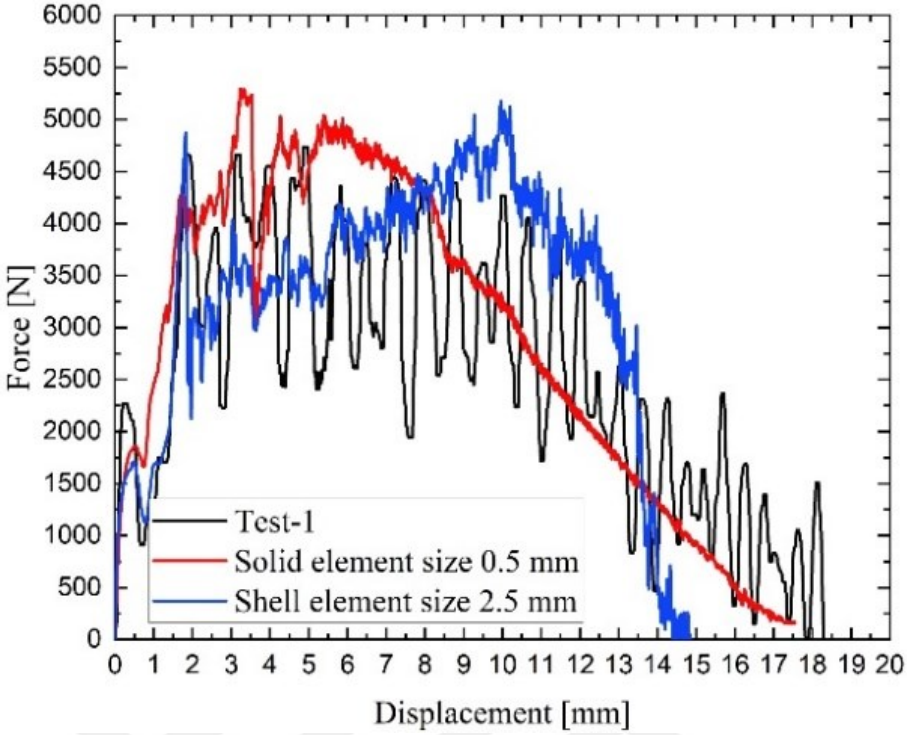

(a)

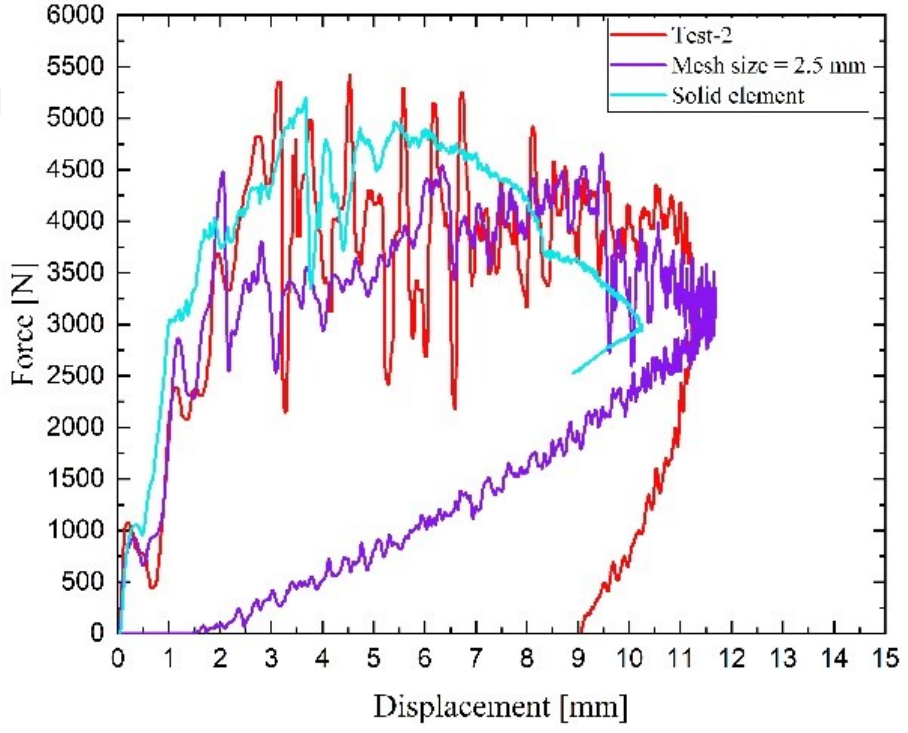

(b)

Figure 5.25. Experimental and numerical force-displacement curves for (a) perforation case and (b) penetration case

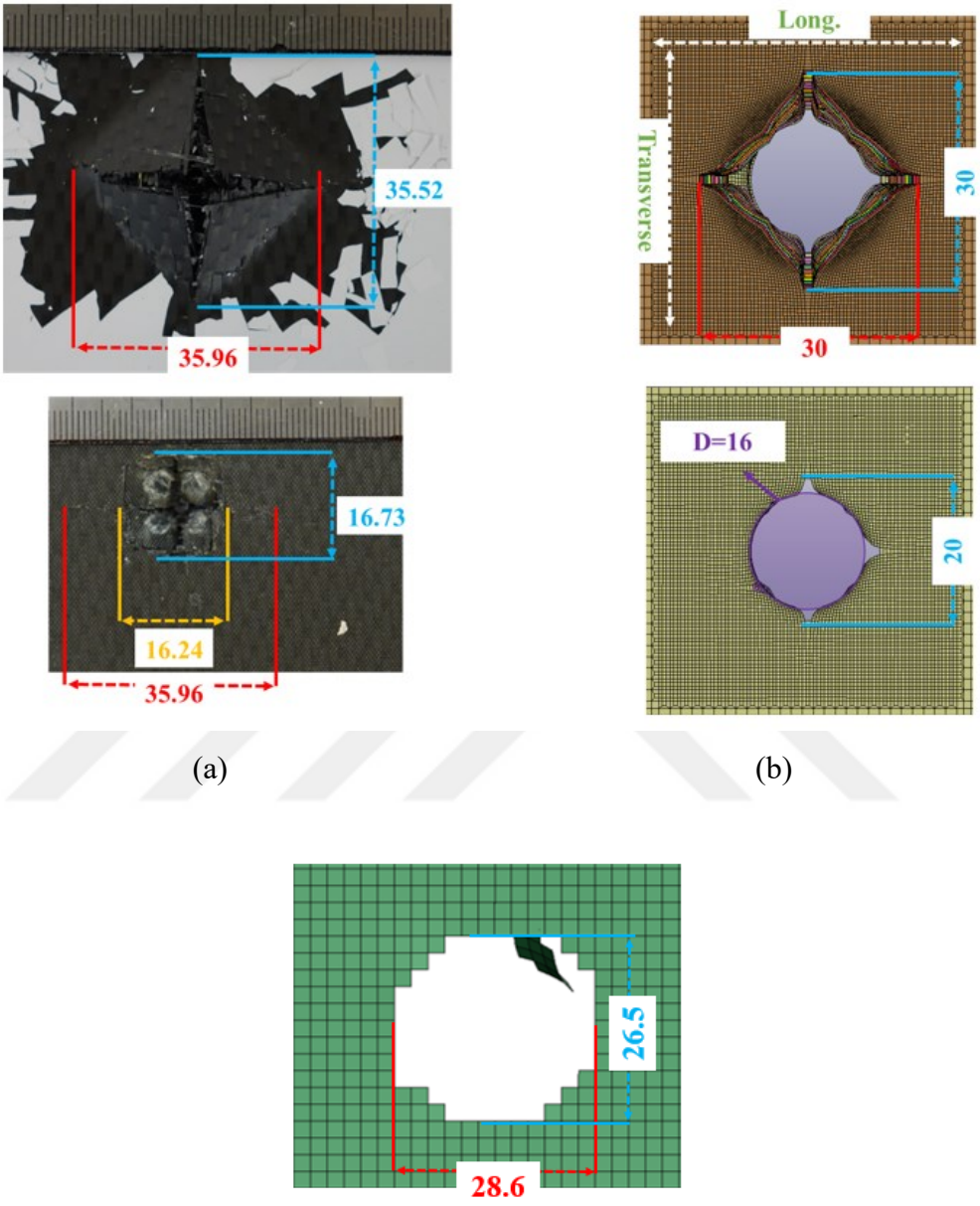

(a) (b)

(c)

Figure 5.26. Longitudinal and transverse damages on the front and back surface of the composite occurring after impacting, (a) experimental, (b) solid model and (c) shell model

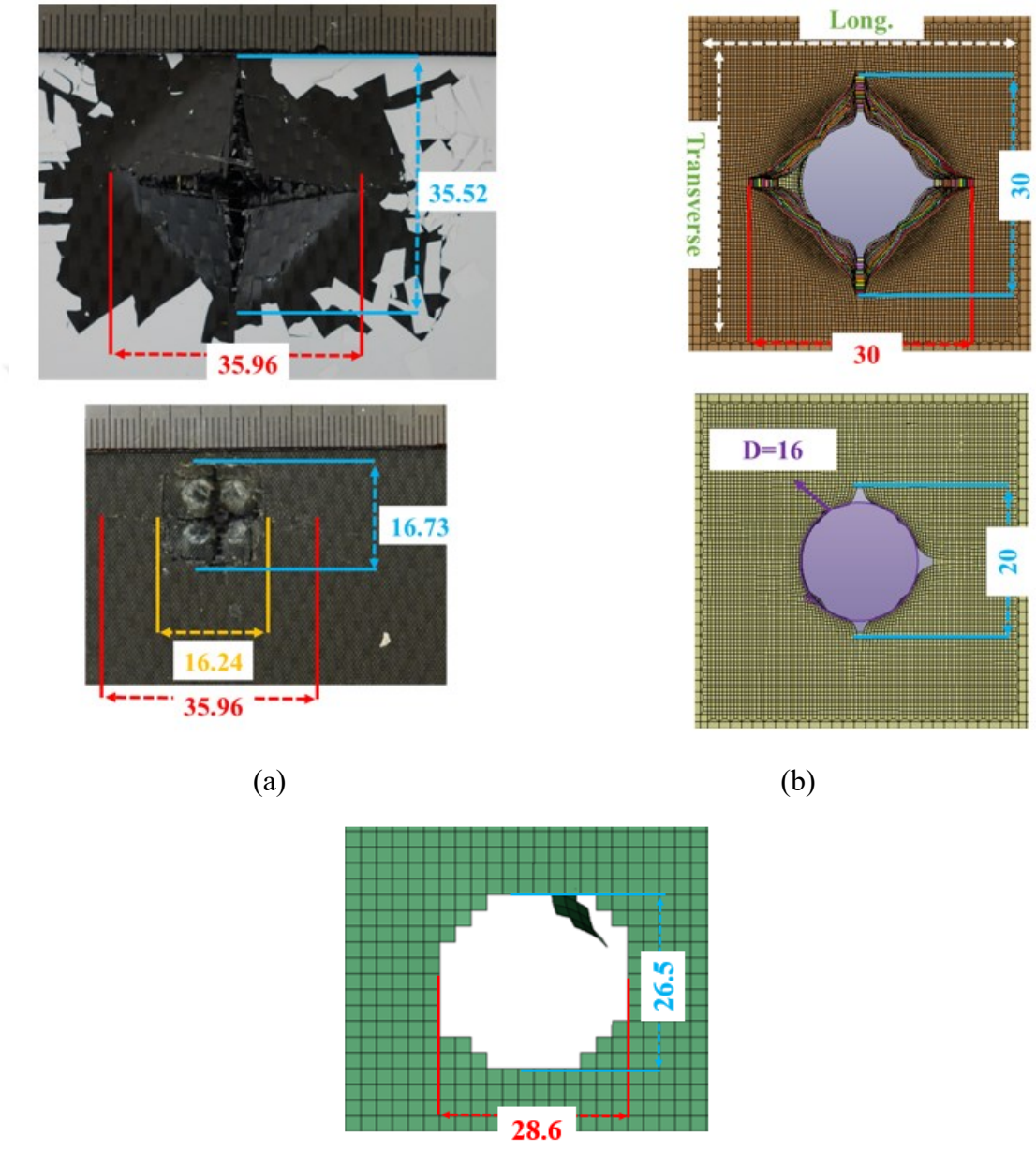

(a) (b)

(c)

Figure 5.27. Longitudinal and transverse damages on the front and back surface of the composite occurring after impacting, (a) experimental, (b) solid model and (c) shell model

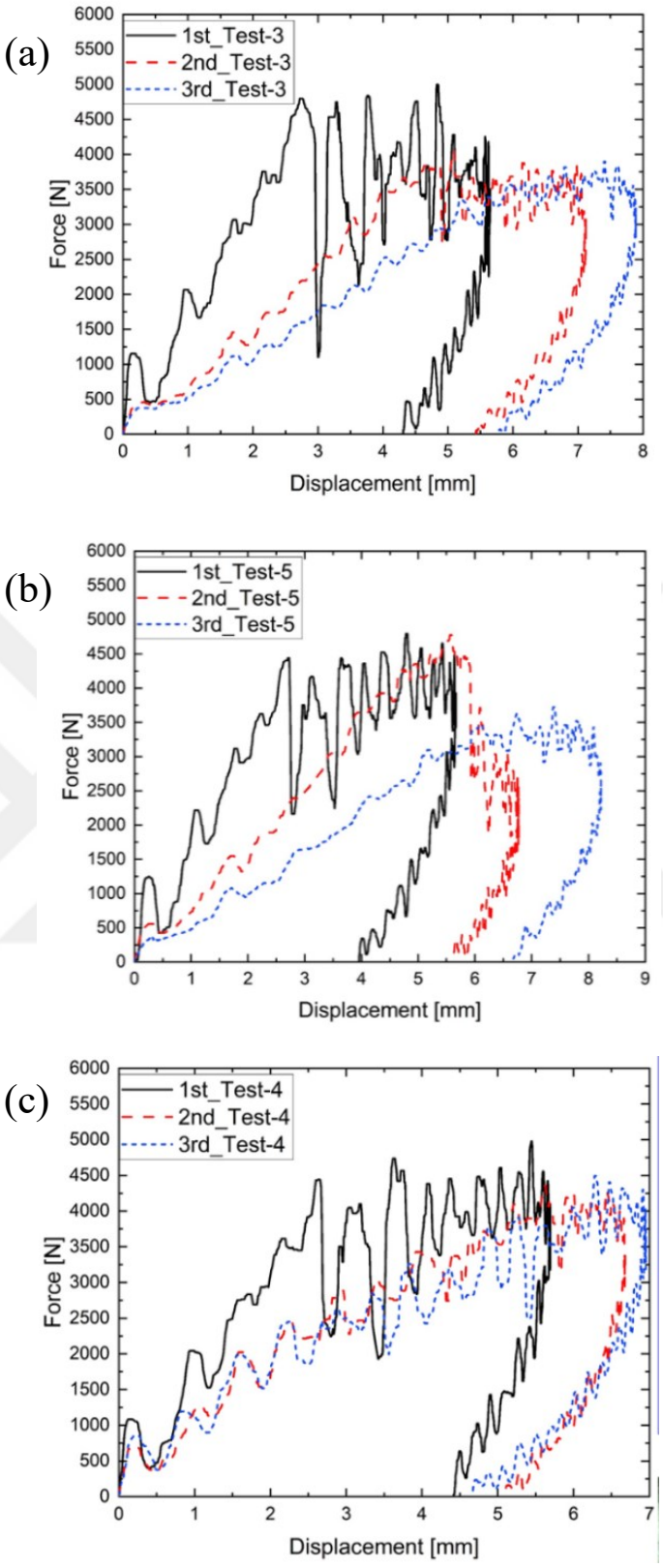

Figure 5.28. Force-displacement curves obtained from the composite subjected to (a),(b) multiple impacts at the same location and (c) impacts at the different locations

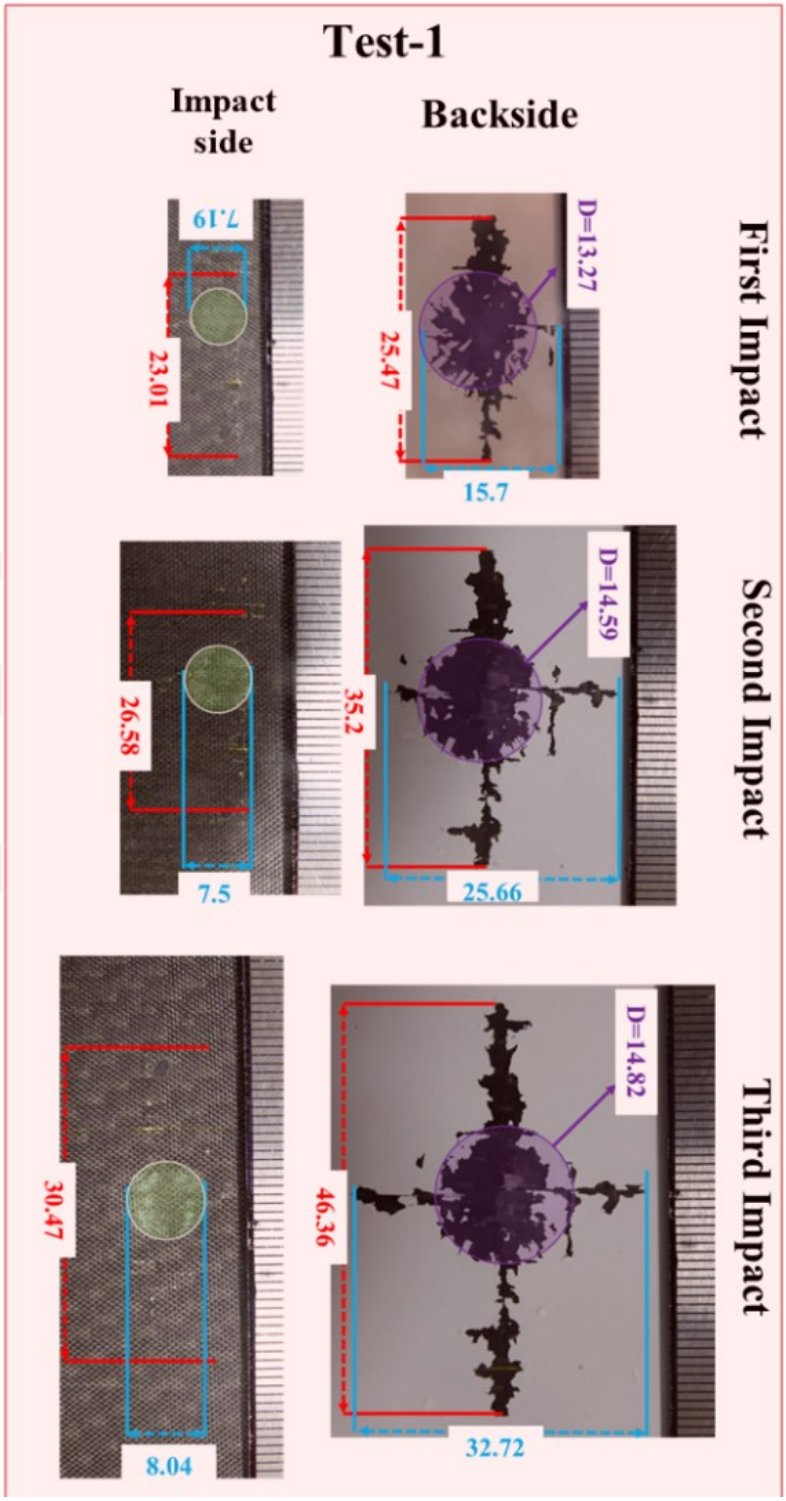

Figure 5.29. Longitudinal and transverse damages on the front and back surface of the composite occurring after the first impact, the second impact and the third impact in Test-1

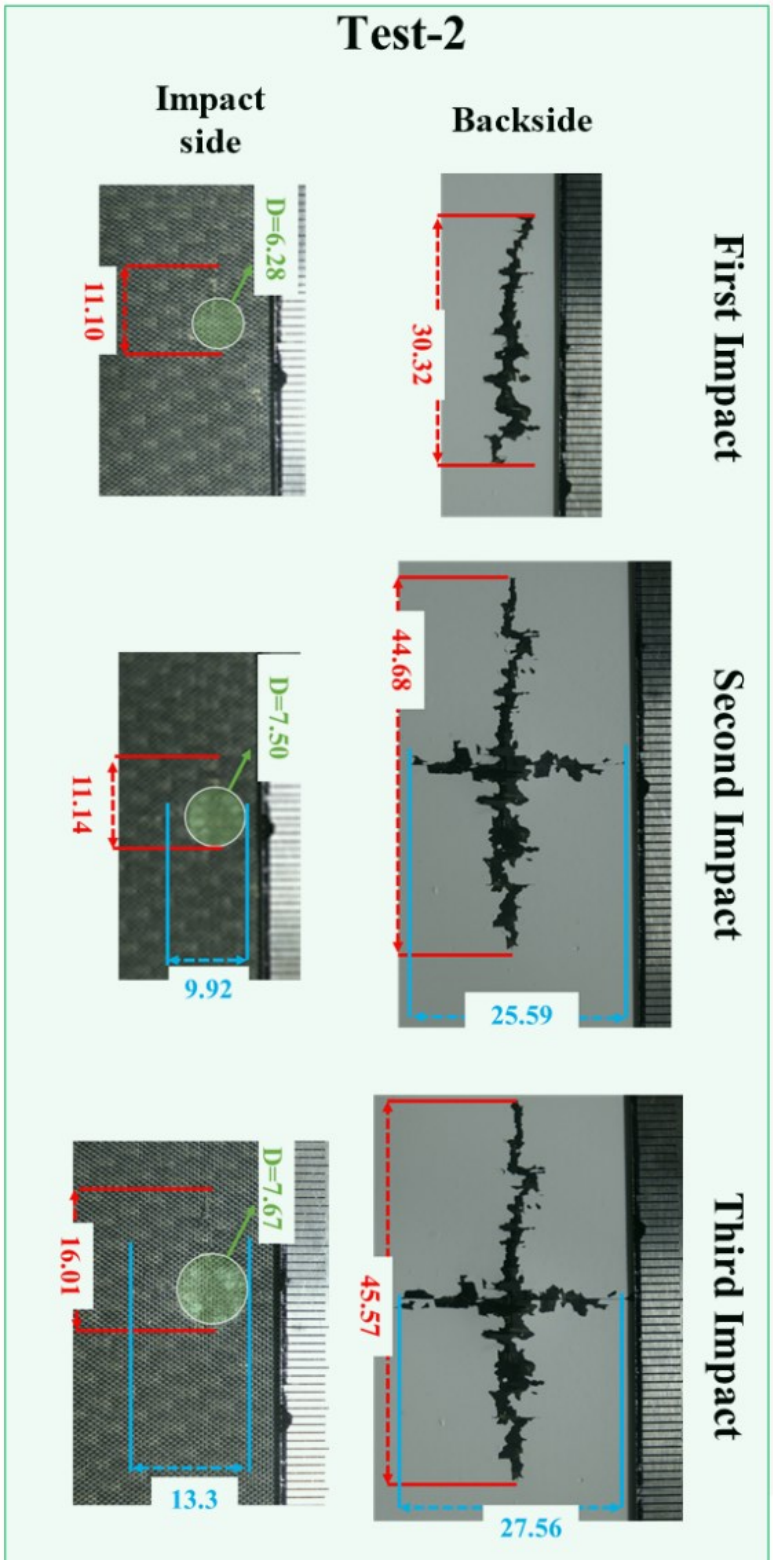

Figure 5.30. Longitudinal and transverse damages on the front and back surface of the composite occurring after the first impact, the second impact and the third impact in Test-2

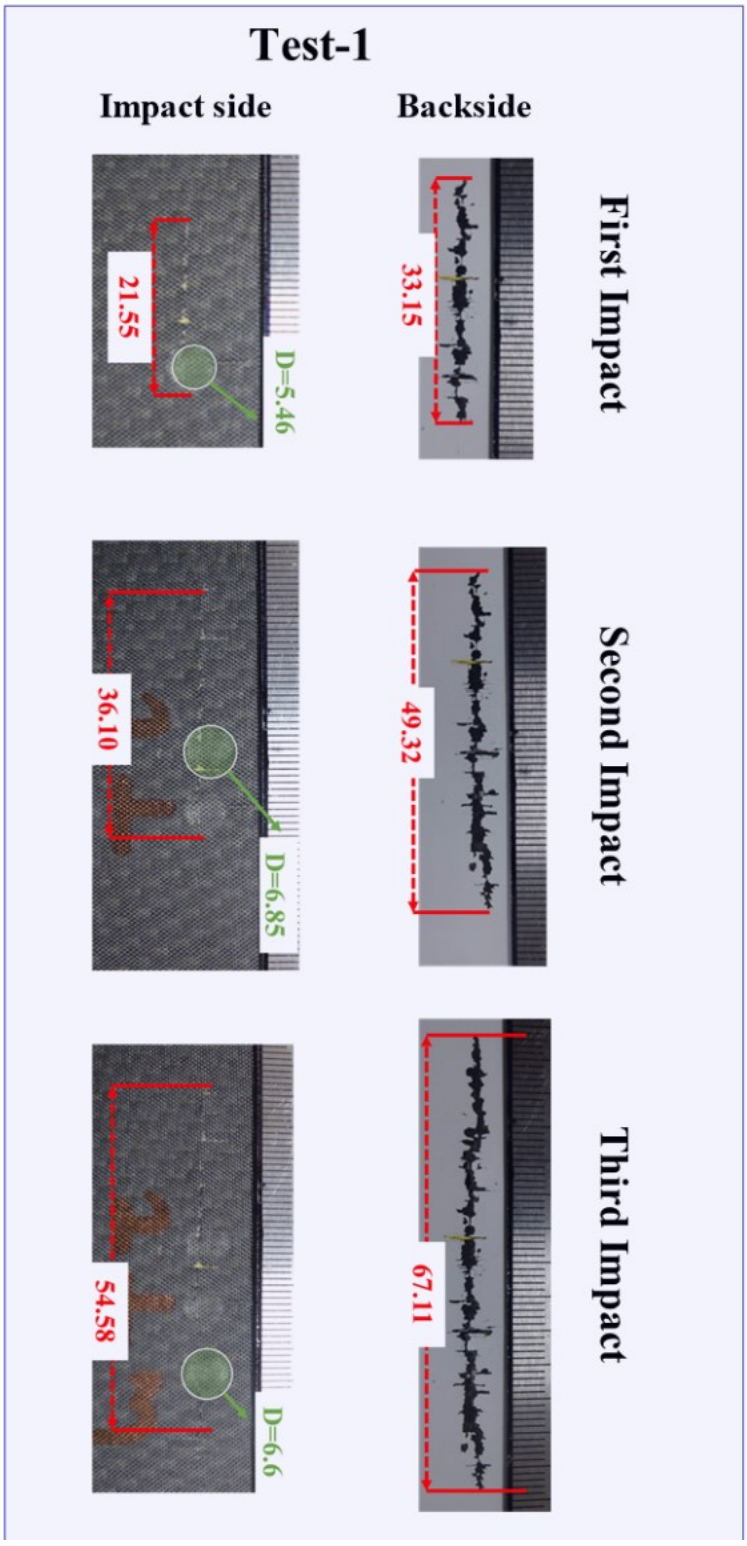

Figure 5.31. Longitudinal and transverse damages on the front and back surface of the composite occurring after the first impact, the second impact and the third impact in Test-1

in terms of the force-displacement path exhibited, the latter reason mentioned above could not be true. Besides, the force- displacement curve exhibited in the experiment up to the rebounding of the striker is well captured by the shell model compared to the solid model. Longitudinal and transverse damage on the front and back surfaces of the composite occurring in the experiment and numerical models can be seen in Figure 5.27. It is seen that both solid and shell model predict the damaged region on the front and back surface of the composite almost similar to those in the experiment.

Figure 5.28 shows force-displacement curves obtained from the composite subjected to multiple impacts at the same location and different locations while the damaged region occurring at the front and the bottom surface of the composite after each impact can be seen in Figure 5.29 - Figure 5.31. As shown in Figure 5.29 and Figure 5.30, the damage region increases with the number of impacts. For the composite impacted at different locations, the initial slope decreases in the second impact, but it remains almost unchanged in the third impact. The sudden load drop beyond the first peak is observed in all force-displacement curves. Compared to impact results performed at the same location, the force-displacement curves obtained at the second and third impact are similar to each other.

As seen in Figure 5.31, the damaged region increases with increasing the number of impacts. It is also found that the damaged regions obtained from the impacts at the same location were lower than those obtained from the different locations, i.e. impacts at different locations caused more damage to the composite. Figure 5.32 shows the experimental and numerical damage comparison on the bottom surface for three sequential impacts. It can be seen that the experimental damage for each impact case is well predicted by the numerical model in terms of fiber damage and matrix damage. Moreover, the amount of delimitation damage that occurred through the multiple impacts can be seen in Figure 5.33 (a). As shown in the figure, at the end of the first impact delamination damage takes place in almost all interfaces. Especially, more damage in Interface 4 is found to be occur than that in the other interfaces. The reason could be high bending stress occurring in the bottom plies. High bending stress may result in matrix damage, and the damage propagates between the plies as delamination damage. In all multiple impact events performed at the same location, the initial slope of the force-displacement curve decreases with increasing the number of impacts. Also, the sudden drop in force after the first peak was not seen in the force curves of the other impacts since the delamination damage had occurred at the impact region of the composite in the

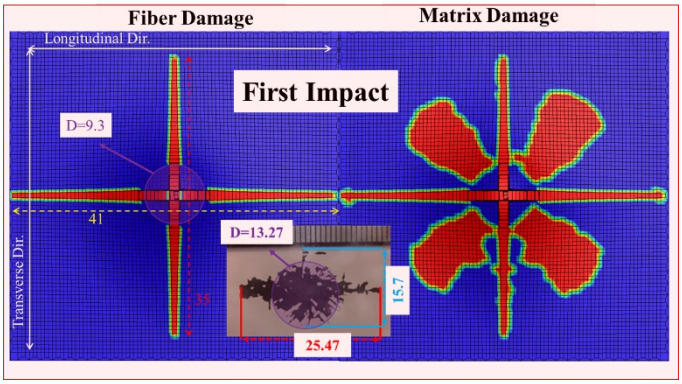

(a)

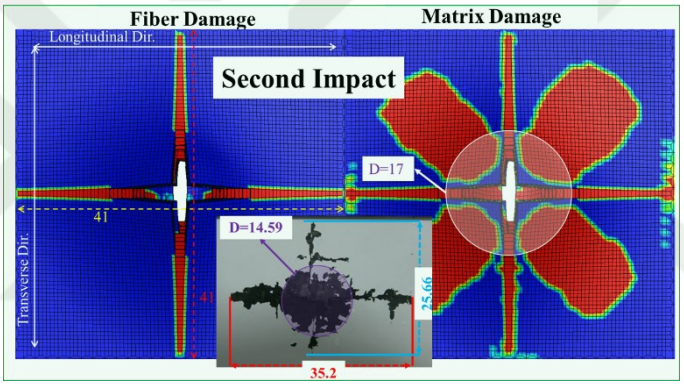

(b)

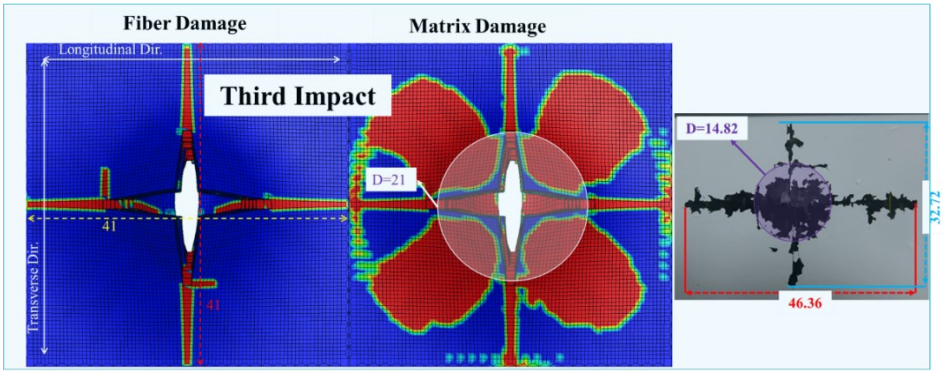

(c)

Figure 5.32. Fiber and matrix damage obtained after (a) the first impact, (b) the second impact and (c) the third impact

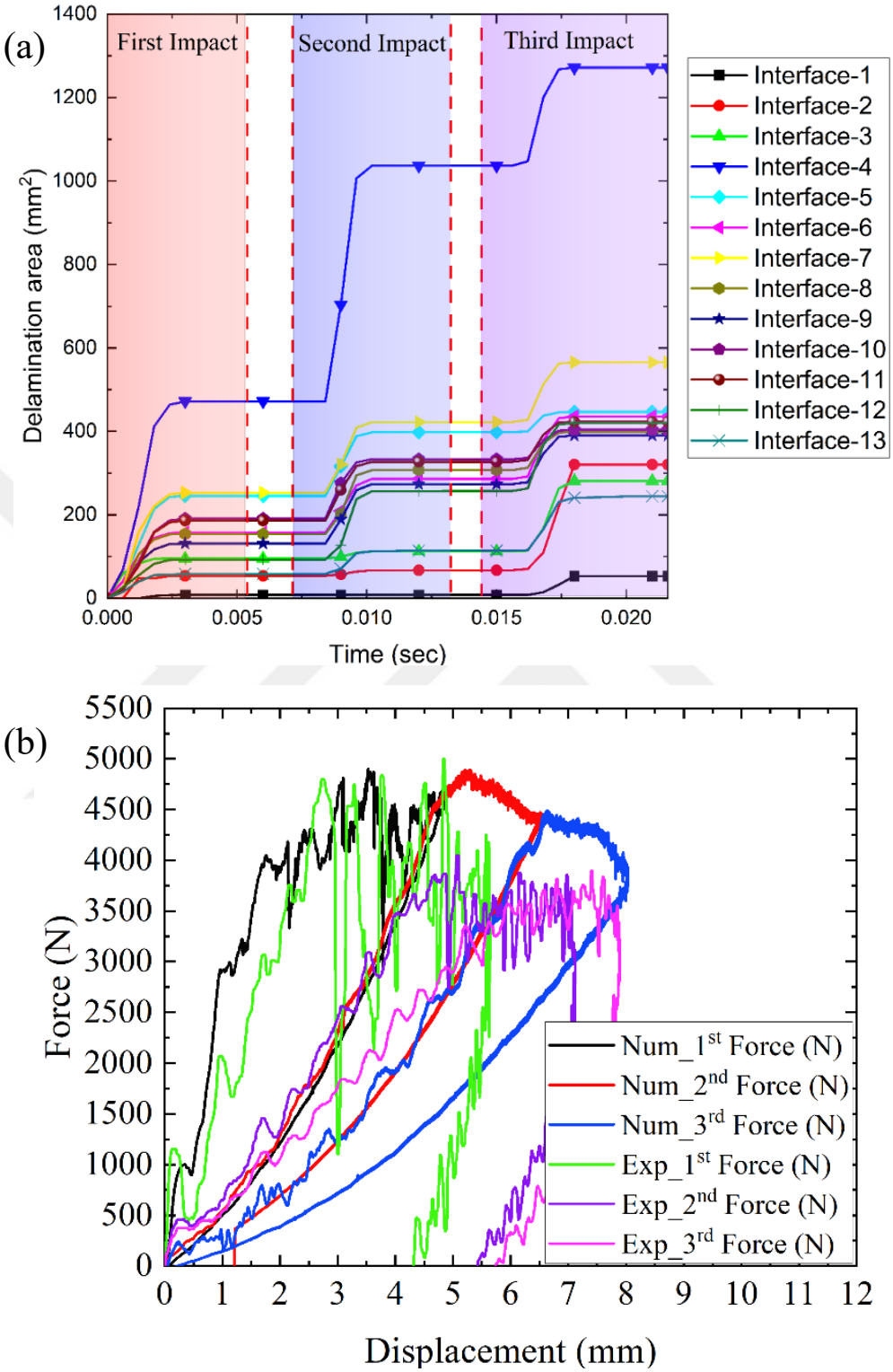

Figure 5.33. (a) The amount of the delamination damage occurred through low-velocity multiple impacts and (b) Comparison of the experimental and numerical results of the composite subjected low-velocity multiple impacts

first impact so in the following impacts this damage did not take place (Figure 5.33 (b)). Similar force curves are obtained from the experimental and numerical study for the first, second and third impacts: the difference between the experimental and numerical forces is sequentially 6%, 28% and 21%. In addition to that, a good agreement between the experimental and numerical results is obtained in terms of the deformation.

5.9. Foreign Body Impact Simulation Results

The longitudinal and transverse damages of the composite plate impacted by the bird can be seen in Figure 5.34 (a). The regions in red color are where the composite takes damage after impact. As can be seen in the figure, consistent results with the literature are obtained in terms of damage. No fracture or rupture is observed except for the parts of the composite along the boundary. Due to the fixed boundary condition used, the composite fails in these regions. The same conclusion is also reached by other studies available in the literature. Besides, because of the effect of the impact, the impact region deforms elastically, resulting in the collapse of the composite in the impact zone.
The damage results obtained from the drone impact simulation are illustrated in Figure 5.34 (b). As in the bird impact case, the composite fails through the boundary due to the fixed boundary condition, and also the collapse in the impact zone occurs. Unlike the bird strike results, fracture or rupture takes place in the impact zone since the drone includes hard components such as camera, gimbal and battery, and the impact of these Components on the composite results in the fracture. It is worth noting that although the kinetic energies of the bird and drone are the same, drone impact results in catastrophic failure of the composite due to reasons explained earlier.

Figure 5.35 shows the force-time comparison of the bird and drone impacts. Since the bird and drone have the same amount of kinetic energy, the force-time curves show similar trend. However, the force results of the drone impact include a few peak points while a smoother curve is obtained in the bird impact case. They correspond to the impact of the camera, the gimbal and the body of the drone, respectively. After reaching the last peak, the impact of the body, the force gradually decreases to 2.5 N, then it remains unchanged up to the end of the impact.

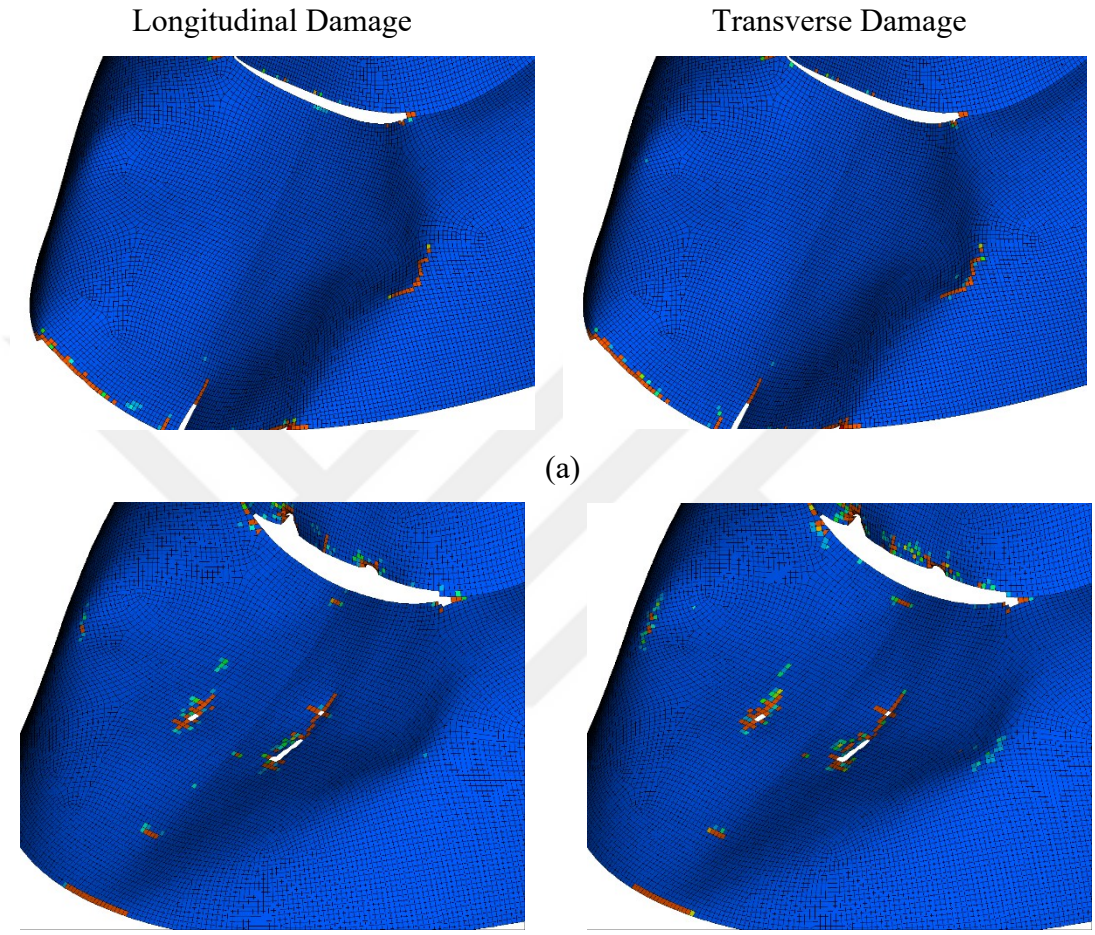

Figure 5.34. Longitudinal and Transverse damage occurred in the composite specimen after (a) the bird impact and (b) the drone impact

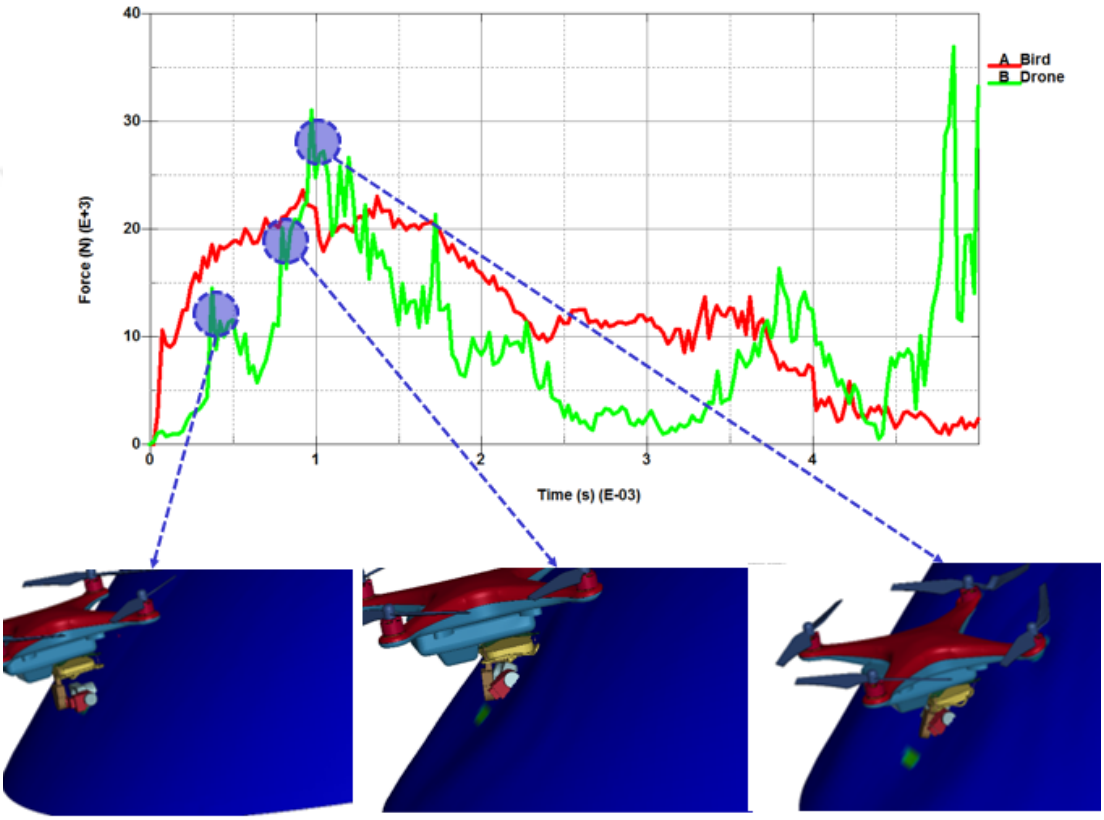

Figure 5.35. Comparison of force vs time curves of the bird and drone impact

CHAPTER 6

CONCLUSIONS

Detailed mechanical characterization tests on the five-harness satin carbon fiber composite were performed to explore its mechanical behavior under quasi-static and dynamic loading and to determine its material constants. According to the ASTM standard, the density and volume fraction of fiber was calculated as 1.570 g/cm^3 and 57.4 %, respectively. In the in-plane tensile tests, the composite was found to show brittle behavior since the fracture occurred immediately after the completion of the elastic deformation. Based on the quasi-static and dynamic in-plane tensile test results, due to the increased loading rate a non-uniform strain distribution over the gage length of the specimen was obtained in high-strain rate tests compared to in quasi-static strain rate tests. Also, the effect of the strain rate on the in-plane tensile properties was found to be negligible due to the fiber-dominated failure modes that occurred. Since tensile strength, elastic modulus and failure strain calculated in the in-plane directions were found to be almost the same at the quasi-static and dynamic strain rates, in the numerical model the material model constants regarding to strain rate sensitivity were taken as zero, especially, four different Crates parameters in the MAT_162 material model. In the compression test results, due to the fiber planes-matrix-dominated mechanical properties in the in-plane direction a significant rate sensitivity was detected while in the out-of-plane direction viscoelastic matrix-dominated behavior of the composite resulted in the rate sensitivity. In the in-plane shear test results, during loading, due to the rotation of the fibers (fiber scissoring), a softening behavior was observed, and then the shear stress increased up to fracture. Unlike the numerical models of the standard in-plane shear test, the softening behavior observed could not be predicted by the numerical models performed at the quasi-static and high strain rate due to the use of non-standard specimen type and/or geometry. It also resulted in different shear strength and shear modulus values compared to that obtained in the standard tests. Based on the test results performed at quasi-static and high strain rates, the in-plane shear properties were found to be strain rate dependent due to the matrix-dominated mechanical properties. In the shell element model, the optimum values for the TAU and GAMMA parameters of the MAT_58 material model were determined as 77.8 MPa and 0.0375 mm/mm by comparing the experimental and

numerical results of $[\pm 45]_n$ specimen subjected to tensile loading. of means of LSOPT optimization software. Moreover, Coulomb friction parameter (PHIC) of the solid material model was determined as 9.04 from the results of the out-of-plane off-axis compression tests, and the scale for the residual compressive strength (SFFC) parameter was calculated to be 0.382 via open-hole tension/compression tests. Fiber shear strength was determined to be 463 MPa from the quasi-static punch shear test. The punch shear test results were also used to determine the softening parameters (AM1, AM2, AM3 and AM4) available in the MAT_162. By comparing experimental and numerical results and using a trial-and-error method, these parameters were found to be 0.1, 0.1, 0.1 and 0.14, respectively. Besides, the numerical and experimental damages that occurred within the composite after the low-velocity impact were compared to calibrate and validate the material model parameters used for the shell and solid elements, especially the MAT_162 material model. It was found that as the element size decreased, the damage in the experiment was captured well, and the multiple impact studies showed that impacts at different locations caused more damage to the composite compared to impacts at the same location since each impact resulted in damage initiation in different regions. With the combination of the damaged regions the damage propagated quickly within the composite plate. In numerical models, because of the computational power available, using a mesh size of 0.5 mm and 2.5 mm, a good agreement between the experimental and numerical results was obtained in terms of both the amount of damage and force-time history. Finally, in the ice impact test, because the kinetic energy of the ice was low, the composite plate in 0.88 mm and 2 mm thickness deformed elastically. There was also no visible damage on the composite in the multi-hit impact events. In the experiments, the back surface displacement of the composite was not calculated accurately due to the aluminum foils used to measure displacement. However, it was predicted by the numerical models.

In addition, the numerical models of the forward cowling of a helicopter subjected to bird impact and drone impact were established to observe the damage severity. It was found that the component was severely damaged in the drone impact compared to the bird impact. Unlike the bird strike, the impact of the rigid components of the drone such as the camera, gimbal and battery resulted in the fracture or rupture of the composite component. In both impact events, due to fixed boundary conditions, the rupture was observed in these regions. A similar trend for the force time curves was obtained from both impact events. However, due to the contact of the rigid components of the drone, its force-time curve showed a few peak points, showing the fracture of the composite component.

REFERENCES

(1) Naik, N. K.; Shembekar, P. S.; Hosur, M. V. Failure Behavior of Woven Fabric Composites. *Journal of Composites Technology and Research* **1991**, *13* (1), 107–116.

(2) D 3039/D3039M ASTM. Standard Test Method for Tensile Properties of Polymer Matrix Composite Materials. *Annual Book of ASTM Standards* **2000**. https://doi.org/10.1520/D3039_D3039M-08.

(3) Hou, J. P.; Ruiz, C. Measurement of the Properties of Woven CFRP T300/914 at Different Strain Rates. *Compos Sci Technol* **2000**, *60* (15), 2829–2834. https://doi.org/10.1016/S0266-3538(00)00151-2.

(4) Kumagai, S.; Shindo, Y.; Horiguchi, K.; Takeda, T. Mechanical Characterization of CFRP Woven Laminates between Room Temperature and 4 K. *JSME International Journal, Series A: Solid Mechanics and Material Engineering*. 2003, pp 359–364. https://doi.org/10.1299/jsmea.46.359.

(5) Paiva, J. M. F. De; Mayer, S.; Rezende, M. C. Comparison of Tensile Strength of Different Carbon Fabric Reinforced Epoxy Composites. *Materials Research* **2006**, *9* (1), 83–90. https://doi.org/10.1590/s1516-14392006000100016.

(6) Vieille, B.; Taleb, L. About the Influence of Temperature and Matrix Ductility on the Behavior of Carbon Woven-Ply PPS or Epoxy Laminates: Notched and Unnotched Laminates. *Compos Sci Technol* **2011**, *71* (7), 998–1007. https://doi.org/10.1016/j.compscitech.2011.03.006.

(7) Abot, J. L.; Yasmin, A.; Jacobsen, A. J.; Daniel, I. M. In-Plane Mechanical, Thermal and Viscoelastic Properties of a Satin Fabric Carbon/Epoxy Composite. *Compos Sci Technol* **2004**, *64* (2), 263–268. https://doi.org/10.1016/s0266-3538(03)00279-3.

(8) Montesano, J.; Fawaz, Z.; Bougherara, H. Non-Destructive Assessment of the Fatigue Strength and Damage Progression of Satin Woven Fiber Reinforced Polymer Matrix Composites. *Compos B Eng* **2015**, *71*, 122–130. https://doi.org/10.1016/j.compositesb.2014.11.005.

(9) Lu, J.; Zhu, P.; Ji, Q.; Cheng, Z. Experimental Study of In-Plane Mechanical Properties of Carbon Fibre Woven Composite at Different Strain Rates. *Polymers and Polymer Composites* **2017**, *25* (4), 289–298.

(10) Barile, C.; Casavola, C.; De Cillis, F. Mechanical Comparison of New Composite Materials for Aerospace Applications. *Compos B Eng* **2019**, *162* (February 2018), 122–128. https://doi.org/10.1016/j.compositesb.2018.10.101.

(11) Zhou, G.; Sun, Q.; Meng, Z.; Li, D.; Peng, Y.; Zeng, D.; Su, X. Experimental Investigation on the Effects of Fabric Architectures on Mechanical and Damage Behaviors of Carbon/Epoxy Woven Composites. *Compos Struct* **2020**, *257* (May 2020), 113366. https://doi.org/10.1016/j.compstruct.2020.113366.

(12) Lu, J.; Zhu, P.; Ji, Q.; Cheng, Z. Experimental Study of In-Plane Mechanical Properties of Carbon Fibre Woven Composite at Different Strain Rates. *Polymers and Polymer Composites* **2017**, *25* (4), 289–298. https://doi.org/10.1177/096739111702500406.

(13) Naresh, K.; Shankar, K.; Velmurugan, R.; Gupta, N. K. Statistical Analysis of the Tensile Strength of GFRP, CFRP and Hybrid Composites. *Thin-Walled Structures* **2018**, *126* (September 2016), 150–161. https://doi.org/10.1016/j.tws.2016.12.021.

(14) Zhang, X.; Shi, Y.; Li, Z. X. Experimental Study on the Tensile Behavior of Unidirectional and Plain Weave CFRP Laminates under Different Strain Rates. *Compos B Eng* **2019**, *164* (January), 524–536. https://doi.org/10.1016/j.compositesb.2019.01.067.

(15) Al-Mosawe, A.; Al-Mahaidi, R.; Zhao, X. L. Engineering Properties of CFRP Laminate under High Strain Rates. *Compos Struct* **2017**, *180*, 9–15. https://doi.org/10.1016/j.compstruct.2017.08.005.

(16) Kawata, K.; Hashimoto, S.; Takeda, N. Mechanical Behaviours in High Velocity Tension of Composites. **1982**.

(17) Saka, K.; Harding, J. *Behaviour of Fibre-Reinforced Composites under Dynamic Tension, (Third Progress Report)*; Oxford University Engineering Laboratory Report No. OUEL 1654186, 1986.

(18) Saka, K.; Harding, J. The Deformation and Fracture of Hybrid Reinforced Composites under Tensile Impact. *Macro- and Micro-Mechanics of High Velocity Deformation and Fracture* **1987**, No. 3, 97–111. https://doi.org/10.1007/978-3-642-82767-9_8.

(19) Groves, S. E.; Sanchez, R. J.; Lyon, R. E.; Brown, A. E. High Strain Rate Effects for Composite Materials. *ASTM Special Technical Publication* **1993**, No. 1206, 162–176. https://doi.org/10.1520/stp12626s.

(20) Daniel, I. M.; Hsiao, H. M.; Cordes, R. D. Dynamic Response of Carbon/Epoxy Composites. *American Society of Mechanical Engineers, Aerospace Division (Publication) AD* **1995**, *48*, 167–177.

(21) Eskandari, H.; Nemes, J. A. Dynamic Testing of Composite Laminates with a Tensile Split Hopkinson Bar. *J Compos Mater* **2000**, *34* (4), 260–273.

(22) Todo, M.; Takahashi, K.; Béguelin, P.; Kausch, H. H. Strain-Rate Dependence of the Tensile Fracture Behaviour of Woven-Cloth Reinforced Polyamide Composites. *Compos Sci Technol* **2000**, *60* (5), 763–771. https://doi.org/10.1016/S0266-3538(99)00184-0.

(23) Gilat, A.; Goldberg, R. K.; Roberts, G. D. Experimental Study of Strain-Rate-Dependent Behavior of Carbon/Epoxy Composite. *Compos Sci Technol* **2002**, *62* (10–11), 1469–1476. https://doi.org/10.1016/S0266-3538(02)00100-8.

(24) Syed, I. H. Strain Rate Sensitivity of Graphite/Polymer Laminate Composites. **2003**, *693*, 693–696. https://doi.org/10.1063/1.1483632.

(25) Gómez-del Río, T.; Barbero, E.; Zaera, R.; Navarro, C. Dynamic Tensile Behaviour at Low Temperature of CFRP Using a Split Hopkinson Pressure Bar. *Compos Sci Technol* **2005**, *65* (1), 61–71. https://doi.org/10.1016/j.compscitech.2004.06.004.

(26) Taniguchi, N.; Nishiwaki, T.; Hirayama, N.; Nishida, H.; Kawada, H. Dynamic Tensile Properties of Carbon Fiber Composite Based on Thermoplastic Epoxy Resin Loaded in Matrix-Dominant Directions. *Compos Sci Technol* **2009**, *69* (2), 207–213. https://doi.org/10.1016/j.compscitech.2008.10.002.

(27) AL-Zubaidy, H.; Zhao, X. L.; Al-Mihaidi, R. Mechanical Behaviour of Normal Modulus Carbon Fibre Reinforced Polymer (CFRP) and Epoxy under Impact Tensile Loads. *Procedia Eng* **2011**, *10*, 2453–2458. https://doi.org/10.1016/j.proeng.2011.04.404.

(28) Foroutan, R.; Nemes, J.; Ghiasi, H.; Hubert, P. Experimental Investigation of High Strain-Rate Behaviour of Fabric Composites. *Compos Struct* **2013**, *106*, 264–269. https://doi.org/10.1016/j.compstruct.2013.06.014.

(29) Chen, X.; Li, Y.; Zhi, Z.; Guo, Y.; Ouyang, N. The Compressive and Tensile Behavior of a 0/90 C Fiber Woven Composite at High Strain Rates. *Carbon N Y* **2013**, *61*, 97–104. https://doi.org/10.1016/j.carbon.2013.04.073.

(30) Al-Zubaidy, H.; Zhao, X. L.; Al-Mahaidi, R. Mechanical Characterisation of the Dynamic Tensile Properties of CFRP Sheet and Adhesive at Medium Strain Rates. *Compos Struct* **2013**, *96*, 153–164. https://doi.org/10.1016/j.compstruct.2012.09.032.

(31) Naito, K. Effect of Strain Rate on Tensile Properties of Carbon Fiber Epoxy-Impregnated Bundle Composite. *J Mater Eng Perform* **2014**, *23* (3), 708–714. https://doi.org/10.1007/s11665-013-0823-5.

(32) Ou, Y.; Zhu, D.; Zhang, H.; Yao, Y.; Mobasher, B.; Huang, L. Mechanical Properties and Failure Characteristics of CFRP under Intermediate Strain Rates and Varying Temperatures. *Compos B Eng* **2016**, *95*, 123–136. https://doi.org/10.1016/j.compositesb.2016.03.085.

(33) Li, X.; Yan, Y.; Guo, L.; Xu, C. Effect of Strain Rate on the Mechanical Properties of Carbon/Epoxy Composites under Quasi-Static and Dynamic Loadings. *Polym Test* **2016**, *52*, 254–264. https://doi.org/10.1016/j.polymertesting.2016.05.002.

(34) Bang, H.; Cho, C. Failure Behavior / Characteristics of Fabric Reinforced Polymer Matrix Composite and Aluminum6061 on Dynamic Tensile Loading. *Journal of Mechanical Science and Technology* **2017**, *31* (8), 3661–3664. https://doi.org/10.1007/s12206-017-0705-0.

(35) Harding, J.; Li, Y. L. Analysis of Failure in Woven Carbon/Epoxy Laminates under Quasi-Static and Impact Loading. *Le Journal de Physique IV* **1991**, *1* (C3), C3-51.

(36) Daniel, I. M.; Liber, T. *Strain Rate Effects on Mechanical Properties of Fiber Composites. Part 3.*; ILLINOIS INST OF TECH CHICAGO, 1976.

(37) Daniel, I. M.; Liber, T. Testing of Fiber Composites at High Strain Rates. In *ICCM/2; Second International Conference on Composite Materials*; 1978.

(38) Daniel, I. M.; LaBedz, R. H.; Liber, T. New Method for Testing Composites at Very High Strain Rates. *Exp Mech* **1981**, *21* (2), 71–77. https://doi.org/10.1007/bf02325199.

(39) Kawata, K. Dynamic Behaviour Analysis of Composite Materials. *Composite Materials: Mechanics, Mechanical Properties and Fabrication* **1981**, 2–11.

(40) Hayes, S. V; Adams, D. F. Rate Sensitive Tensile Impact Properties of Fully and Partially Loaded Unidirectional Composites. *J Test Eval* **1982**, *10* (2), 61–68. https://doi.org/10.1520/JTE10234J.

(41) Daniel, I. M.; Hamilton, W. G.; LaBedz, R. H. Strain Rate Characterization of Unidirectional Graphite/Epoxy Composite. *ASTM Special Technical Publication* **1982**, 393–413. https://doi.org/10.1520/stp28492s.

(42) Harding, J.; Welsh, L. M. A Tensile Testing Technique for Fibre-Reinforced Composites at Impact Rates of Strain. *J Mater Sci* **1983**, *18* (6), 1810–1826. https://doi.org/10.1007/BF00542078.

(43) Adams, D. F.; Adams, L. G. Tensile Impact Tests of AS4/3501-6 and S2/3501-6 Unidirectional Composites and the 3501-6 Epoxy Matrix. *J Compos Mater* **1990**, *24* (3), 256–268.

(44) Mak, Y.-P. Strain Rate Effects on Tensile Fracture and Damage Tolerance of Composite Laminates. Massachusetts Institute of Technology 1992.

(45) Wang, W.; Makarov, G.; Shenoi, R. A. An Analytical Model for Assessing Strain Rate Sensitivity of Unidirectional Composite Laminates. *Compos Struct* **2005**, *69* (1), 45–54. https://doi.org/10.1016/j.compstruct.2004.04.017.

(46) Deshpande, A. B. Characterization of CFRP and GFRP Composite Materials at High Strain Rate Tensile Loading. 2006.

(47) Taniguchi, N.; Nishiwaki, T.; Kawada, H. Tensile Strength of Unidirectional CFRP Laminate under High Strain Rate. *Advanced Composite Materials: The Official Journal of the Japan Society of Composite Materials* **2007**, *16* (2), 167–180. https://doi.org/10.1163/156855107780918937.

(48) Orton, S. L.; Chiarito, V. P.; Rabalais, C.; Wombacher, M.; Rowell, S. P. Strain Rate Effects in CFRP Used for Blast Mitigation. *Polymers (Basel)* **2014**, *6* (4), 1026–1039. https://doi.org/10.3390/polym6041026.

(49) Kwon, J.; Choi, J.; Huh, H.; Lee, J. Evaluation of the Effect of the Strain Rate on the Tensile Properties of Carbon–Epoxy Composite Laminates. *J Compos Mater* **2017**, *51* (22), 3197–3210. https://doi.org/10.1177/0021998316683439.

(50) Welsh, L. M.; Harding, J. Effect of Strain Rate on the Tensile Failure of Woven Reinforced Polyester Resin Composites. *Journal de Physique (Paris), Colloque* **1985**, *46* (8), 405–414. https://doi.org/10.1051/jphyscol:1985551.

(51) Lodeiro, M. J.; Broughton, W. R.; Sims, G. D. Understanding Limitations of through Thickness Test Methods. *Plastics, Rubber and Composites Processing and Applications* **1999**, *28* (9), 416–424. https://doi.org/10.1179/146580199101540583.

(52) Jackson, W. C.; Ifju, G. Through-the-Thickness of Textile Composites Tensile Strength. *NASA Tech Memo* **1994**.

(53) Chen, D.; Lu, F.; Jiang, B. Tensile Properties of a Carbon Fiber 2D Woven Reinforced Polymer Matrix Composite in Through-Thickness Direction. *J Compos Mater* **2012**, *46* (26), 3297–3309. https://doi.org/10.1177/0021998312437800.

(54) Abot, J. L.; Daniel, I. M. Through-Thickness Mechanical Characterization of Woven Fabric Composites. *J Compos Mater* **2004**, *38* (7), 543–553. https://doi.org/10.1177/0021998304042394.

(55) Nakai, K.; Yokoyama, T. Dynamic Tensile Stress-Strain Characteristics of Carbon/Epoxy Laminated Composites in through-Thickness Direction. *EPJ Web Conf* **2015**, *94*. https://doi.org/10.1051/epjconf/20159401039.

(56) ASTM D6641. Standard Test Method for Compressive Properties of Polymer Matrix Composite Materials Using a Combined Loading Compression (CLC) Test Fixture. *ASTM International* **2012**.

(57) Liu, J. C.; Wang, T. J.; Zhang, W. Experimental Study on the Mechanical Properties of Satin Carbon Fabric/Epoxy Composites. *Key Eng Mater* **2005**, *297–300*, 2909–2914. https://doi.org/10.4028/www.scientific.net/kem.297-300.2909.

(58) Shi, C.; Guo, B.; Sarıkaya, M.; Çelik, M.; Chen, P.; Güden, M. Determination of the Material Model and Damage Parameters of a Carbon Fiber Reinforced Laminated Epoxy Composite for High Strain Rate Planar Compression. *Int J Impact Eng* **2021**, *149*. https://doi.org/10.1016/j.ijimpeng.2020.103771.

(59) D3410M, A. D. /. Standard Test Method for Compressive Properties of Polymer Matrix Composite Materials with Unsupported Gage Section by Shear Loading. *ASTM International* **2016**.

(60) ASTM D3518. Standard Test Method for In-Plane Shear Response of Polymer Matrix Composite Materials by Tensile Test of a ±45 ° Laminate. *Annual Book of ASTM Standards* **2007**.

(61) ASTM. Standard Test Method for Shear Properties of Composite Materials by V-Notched Rail Shear Method. *Astm D5379/D 5379M-05* **2005**, *i*, 1–14. https://doi.org/10.1520/D5379.

(62) Tehrani, M.; Boroujeni, A. Y.; Al-Haik, M. S. Modeling and Simulation of Impact and Perforation in Fiber Reinforced Composites. *Proceedings of the American Society for Composites - 29th Technical Conference, ASC 2014; 16th US-Japan Conference on Composite Materials; ASTM-D30 Meeting* **2014**, No. 505.

(63) U.S. Department of Transportation. AC 150/5210-24: Airport Foreign Object Debris (FOD) Management. *FAA, Washington, DC* **2010**.

(64) National Transportation Safety Board. *Inflight collision of UAS and helicopter*. https://data.ntsb.gov/Docket/?NTSBNumber=DCA17IA202AB (accessed 2023-03-11).

(65) Civil Aviation Safety Authority. *Potential Damage Assessment of a Mid-Air Collision with a Small UAV*; Technical Report, 2013.

(66) Song, Y.; Horton, B.; Bayandor, J. Investigation of UAS Ingestion into High-Bypass Engines, Part I: Bird vs. Drone. In *58th AIAA/ASCE/AHS/ASC Structures, Structural Dynamics, and Materials Conference, 2017*; American Institute of Aeronautics and Astronautics Inc, AIAA, **2017**. https://doi.org/10.2514/6.2017-0186.

(67) Schroeder, K.; Song, Y.; Horton, B.; Bayandor, J. Investigation of UAS Ingestion into High-Bypass Engines, Part 2: Parametric Drone Study. In *58th AIAA/ASCE/AHS/ASC Structures, Structural Dynamics, and Materials Conference*; American Institute of Aeronautics and Astronautics: Reston, Virginia, **2017**. https://doi.org/10.2514/6.2017-0187.

(68) Olivares, G.; Gomez, L.; Espinosa de los Monteros, J.; Baldridge, R. J.; Zinzuwadia, C.; Aldag, T. Volume II–UAS Airborne Collision Severity Evaluation–Quadcopter. **2017**.

(69) D'Souza, K.; Lyons, T.; Lacy, T.; Kota, K. R. Volume IV–UAS Airborne Collision Severity Evaluation–Engine Ingestion. **2017**.

(70) Meng, X.; Sun, Y.; Yu, J.; Tang, Z.; Liu, J.; Suo, T.; Li, Y. Dynamic Response of the Horizontal Stabilizer during UAS Airborne Collision. *Int J Impact Eng* **2019**, *126*, 50–61.

(71) Drumond, T.; Greco, M.; Cimini, C. Evaluation of Increase Weight in a Wing Fixed Leading Edge Design to Support UAS Impact. *Proceedings of the 10th Aerospace Technology Congress, October 8-9, 2019, Stockholm, Sweden* **2019**, *162* (October), 71–80. https://doi.org/10.3384/ecp19162008.

(72) Liu, H.; Mohd, H. C. M.; Ng, B. F.; Low, K. H. Airborne Collision Evaluation between Drone and Aircraft Engine: Effects of Position and Posture on Damage of Fan Blades. In *AIAA Aviation 2020 Forum*; **2020**; p 3214.

(73) Dadouche, A.; Greer, A.; Galeote, B.; Breithaupt, T.; Vidal, C.; Gould, R. *Drone Impact Assessment on Aircraft Structure: Windshield and Leading Edge Testing and Analysis*; CR-GTL-2020–0054, **2020**.

(74) Jonkheijm, L. Predicting Helicopter Damage Caused by a Collision with an Unmanned Aerial System Using Explicit Finite Element Analysis. **2020**.

(75) Lu, X.; Liu, X.; Li, Y.; Zhang, Y.; Zuo, H. Simulations of Airborne Collisions between Drones and an Aircraft Windshield. *Aerosp Sci Technol* **2020**, *98*, 105713.

(76) Lu, X.; Liu, X.; Zhang, Y.; Li, Y.; Zuo, H. Simulation of Airborne Collision between a Drone and an Aircraft Nose. *Aerosp Sci Technol* **2021**, *118*, 107078.

(77) Liu, H.; Hasrizam Che Man, M.; Ng, B. F.; Low, K. H. Airborne Collision Severity Study on Engine Ingestion Caused by Harmless-Categorized Drones. In *AIAA Scitech 2021 Forum*; 2021; p 1263.

(78) Sivakumar, A. K.; Man, M. H. C.; Liu, H.; Low, K. H. Collision Severity Evaluation of Generalized Unmanned Aerial Vehicles (UAVs) Impacting on Aircraft Engines. In *2021 International Conference on Unmanned Aircraft Systems (ICUAS)*; IEEE, **2021**; pp 1240–1247.

(79) Liu, H.; Man, M. H. C.; Low, K. H. UAV Airborne Collision to Manned Aircraft Engine: Damage of Fan Blades and Resultant Thrust Loss. *Aerosp Sci Technol* **2021**, *113*, 106645.

(80) Che Man, M. H.; Low, K. H. Damage Severity Prediction of Helicopter Windshields Caused by a Collision with a Small Unmanned Aerial Vehicle (SUAV). In *AIAA AVIATION 2021 FORUM*; **2021**; p 3001.

(81) Royal NLR. Multiple Unmanned Aerial Systems Collision Impact on Wing Leading Edge. **2021**.

(82) Heimbsa, S.; Hansena, J.; Woidta, M. Comparison of Drone Collision and Bird Strike on Aircraft Radome Using Experimental and Simulation Methods. **2022**.

(83) Che Man, M. H.; Liu, H.; Low, K. H. Severity Assessment of Aircraft Engine Fan Blades under Airborne Collision of Unmanned Aerial Vehicles Comparable to Bird Strike Certification Standards. *Proc Inst Mech Eng G J Aerosp Eng* **2022**, *236* (9), 1817–1835.

(84) Franke, F.; Slowik, T.; Burger, U.; Hühne, C. Numerical Investigation of Drone Strikes with Various Aircraft Targets. In *AIAA SCITECH 2022 Forum*; 2022; p 2603.

(85) HexPly. *HexPly ® 8552 Epoxy Matrix (180°C/356°F Curing Matrix)*; 2020.

(86) Blaber, J.; Adair, B.; Antoniou, A. Ncorr: Open-Source 2D Digital Image Correlation Matlab Software. *Exp Mech* **2015**. https://doi.org/10.1007/s11340-015-0009-1.

(87) Astm D729. Standard Test Methods for Density and Specific Gravity (Relative Density) of Plastics by Displacement. *American Society for Testing and Materials* **2008**, 6. https://doi.org/10.1520/D0792-20.2.

(88) ASTM D3171. *Standard Test Methods for Constituent Content of Composite Materials*; 2015.

(89) Sheet, P. D. HexPly ® 8552. **2020**, 1–6.

(90) D7291M-15, A. D. /. Standard Test Method for Through-Thickness "Flatwise" Tensile Strength and Elastic Modulus of a Fiber-Reinforced Polymer Matrix Composite Material. *ASTM International* **2015**.

(91) ASTM D5379 / D5379M. Standard Test Method for Shear Properties of Composite Materials by the V-Notched Beam Method. *ASTM International, West Conshohocken, PA* **2012**.

(92) Pankow, M.; Yen, C. F.; Justusson, B.; Waas, A. M. Through-the-Thickness Response of Hybrid 2D and 3D Woven Composites. *Collection of Technical Papers - AIAA/ASME/ASCE/AHS/ASC Structures, Structural Dynamics and Materials Conference* **2013**.

(93) Gillespie, J. W.; Gama, B. A.; Cichanowski, C. E.; Xiao, J. R. Interlaminar Shear Strength of Plain Weave S2-Glass/SC79 Composites Subjected to out-of-Plane High Strain Rate Compressive Loadings. *Compos Sci Technol* **2005**, *65* (11–12), 1891–1908. https://doi.org/10.1016/j.compscitech.2005.04.006.

(94) Haque, B. Z.; Chowdhury, S. C.; Biswas, I.; Schweiger, P. M.; Gillespie, J. W.; Hartman, D. R. Modeling the Low Velocity Impact Damage Behavior of S-Glass/Phenolic Composites. *SAMPE 2012* **2012**.

(95) ASTM D790. Standard Test Methods for Flexural Properties of Unreinforced and Reinforced Plastics and Electrical Insulating Materials. *Annual Book of ASTM Standards* **2002**.

(96) Livermore Software Technology. Ls-Dyna® Keyword User's Manual Volume II Material Models. **2021**.

(97) Hallquist, J. O. LS-DYNA Theory Manual. *Livermore software Technology corporation* **2006**, *3*, 25–31.

(98) Matzenmiller, A.; Lubliner, J.; Taylor, R. L. A Constitutive Model for Anisotropic Damage in Fiber-Composites. *Mechanics of Materials* **1995**, *20* (2), 125–152.

(99) Hashin, Z. Failure Criteria for Unidirectional Fiber Composites. *J Appl Mech* **1980**, *47* (2), 329–334.

(100) Gama, B. A.; Bogetti, T. A.; Gillespie Jr, J. W. Progressive Damage Modeling of Plain-Weave Composites Using LS-Dyna Composite Damage Model MAT162. In *7th European LS-DYNA Conference*; 2009; pp 14–15.

(101) Xiao, J. R.; Gama, B. A.; Gillespie, J. W. Progressive Damage and Delamination in Plain Weave S-2 Glass/SC-15 Composites under Quasi-Static Punch-Shear Loading. *Compos Struct* **2007**, *78* (2), 182–196. https://doi.org/10.1016/j.compstruct.2005.09.001.

(102) Jordan, J. B.; Naito, C. J.; Haque, B. Z. G. Progressive Damage Modeling of Plain Weave E-Glass/Phenolic Composites. *Compos B Eng* **2014**, *61*, 315–323.

(103) Gama, B. A.; Bogetti, T. A.; Gillespie Jr, J. W. Progressive Damage Modeling of Plain-Weave Composites Using LS-Dyna Composite Damage Model MAT162. *7th European LS-DYNA Conference* **2009**, No. January.

(104) Kona, A.; Bhasin, A.; Gomez, L.; Olivares, G.; Gomez, A.; Keshavanarayana, S.; Pang, J.; Molitor, M.; Rassaian, M. Evaluation of Ls-Dyna Mat162 for Modeling Composite Fastener Joints for High Rates of Loading. *AIAA Scitech 2019 Forum* **2019**, 1–14. https://doi.org/10.2514/6.2019-2058.

(105) Hazzard, M. K.; Trask, R. S.; Heisserer, U.; van der Kamp, M.; Hallett, S. R. Finite Element Modelling of Dyneema® Composites: From Quasi-Static Rates to Ballistic Impact. *Compos Part A Appl Sci Manuf* **2018**, *115* (September), 31–45. https://doi.org/10.1016/j.compositesa.2018.09.005.

(106) Zhang, T. G.; Satapathy, S. S.; Lionel, R.; Walsh, S. M. Modeling Ballistic Response of Ultra-High- Molecular-Weight Polyethylene (UHMWPE). **2016**.

(107) Jiang, W.; Hallett, S. R.; Green, B. G.; Wisnom, M. R. A Concise Interface Constitutive Law for Analysis of Delamination and Splitting in Composite Materials and Its Application to Scaled Notched Tensile Specimens. *Int J Numer Methods Eng* **2007**, *69* (9), 1982–1995.

(108) Ata, T. T. 2D and 3D Finite Element Analyses of Dynamic Delamination in Curved CFRP Laminates. Middle East Technical University 2019.

(109) *ANSYS LS-DYNA*. https://awg.ansys.com/Material+Parameter+Sets (accessed 2023-04-02).

(110) *Agusta Westland AW139*. https://grabcad.com/library/agusta-westland-aw139-1 (accessed 2023-04-01).

(111) *Dji Phantom 3 quadcopter*. (2019). https://grabcad.com/library/dji-phantom-3-quadcopter-1 (accessed 2023-04-01).

(112) Hedayati, R.; Sadighi, M. *Bird Strike: An Experimental, Theoretical and Numerical Investigation*; Woodhead Publishing, **2015**.

(113) *ANSYS LS-DYNA*. https://awg.ansys.com/QA+test+example+5 (accessed 2023-04-02).

(114) Naik, N. K.; Kavala, V. R. High Strain Rate Behavior of Woven Fabric Composites under Compressive Loading. *Materials Science and Engineering: A* **2008**, *474* (1–2), 301–311.

(115) Yokoyama, T.; Nakai, K. Impact Compressive Failure of a Unidirectional Carbon/Epoxy Laminated Composite in Three Principal Material Directions. In *Proceedings of DYMAT 2009 conference*; **2009**; Vol. 1, p 2.

(116) Sivashanker, S.; Osiyemi, S. O.; Asim, B. Compressive Failure of a Unidirectional Carbon-Epoxy Composite at High Strain Rates. *Metallurgical and Materials Transactions* **2003**, *34* (6), 1396–1400.

(117) Hall, I. W.; Güden, M. High Strain Rate Testing of a Unidirectionally Reinforced Graphite Epoxy Composite. *J Mater Sci Lett* **2001**.

(118) Hosur, M. V; Alexander, J.; Jeelani, S.; Vaidya, U. K.; Mayer, A. High Strain Compression Response of Affordable Woven Carbon/Epoxy Composites. *Journal of reinforced plastics and composites* **2003**, *22* (3), 271–296.

(119) ASTM D6484/D6484M. Standard Test Method for Open-Hole Compressive Strength of Polymer Matrix Composite Laminates. *ASTM Compass* **2018**.

(120) ASTM D5766. Standard Test Method for Open-Hole Tensile Strength of Polymer Matrix Composite Laminates. *ASTM Standard* **2013**.

APPENDIX A

ASTM DOCUMENTS AND FAILURE IDENTIFICATION TABLES

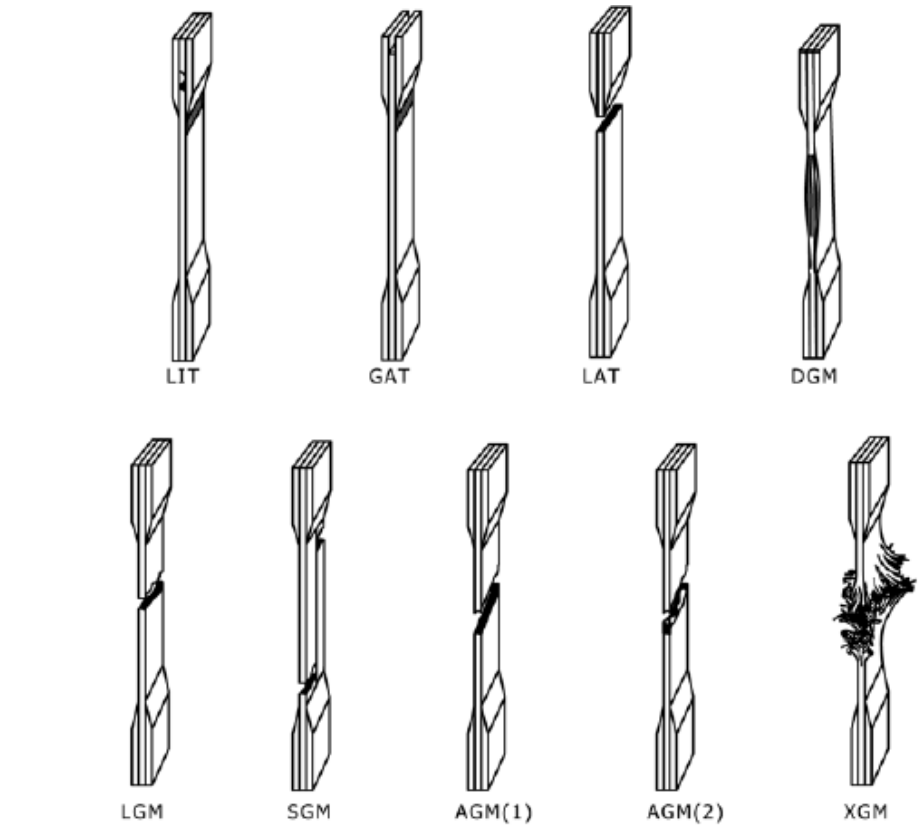

First Character

Failure Type	Code
Angled	A
edge Delamination	D
Grip/tab	G
Lateral	L
Multi-mode	M(xyz)
long. Splitting	S
eXplosive	X
Other	O

Second Character

Failure Area	Code
Inside grip/tab	I
At grip/tab	A
<1W from grip/tab	W
Gage	G
Multiple areas	M
Various	V
Unknown	U

Third Character

Failure Location	Code
Bottom	B
Top	T
Left	L
Right	R
Middle	M
Various	V
Unknown	U

Figure A.1. Tensile specimen failure identification (Source: ASTM D3039[2])

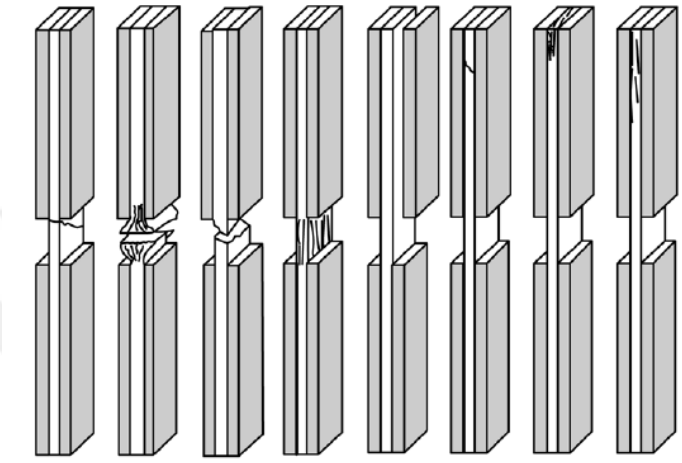

First Character

Failure Mode	Code
Angled	A
Brooming	B
end-Crushing	C
Delamination	D
Euler buckling	E
tHrough-thickness	H
Kink bands	K
Lateral	L
Multi-mode	M(xyz)
long.-Splitting	S
Transverse shear	T
eXplosive	X
Other	O

Second Character

Failure Area	Code
Inside grip/tab	I
At grip/tab	A
Gage	G
Multiple Areas	M
Tab adhesive	T
Various	V
Unknown	U

Third Character

Failure Location	Code
Bottom	B
Top	T
Left	L
Right	R
Middle	M
Various	V
Unknown	U

Figure A.2. Compression specimen failure identification (Source: ASTM D6641[56])

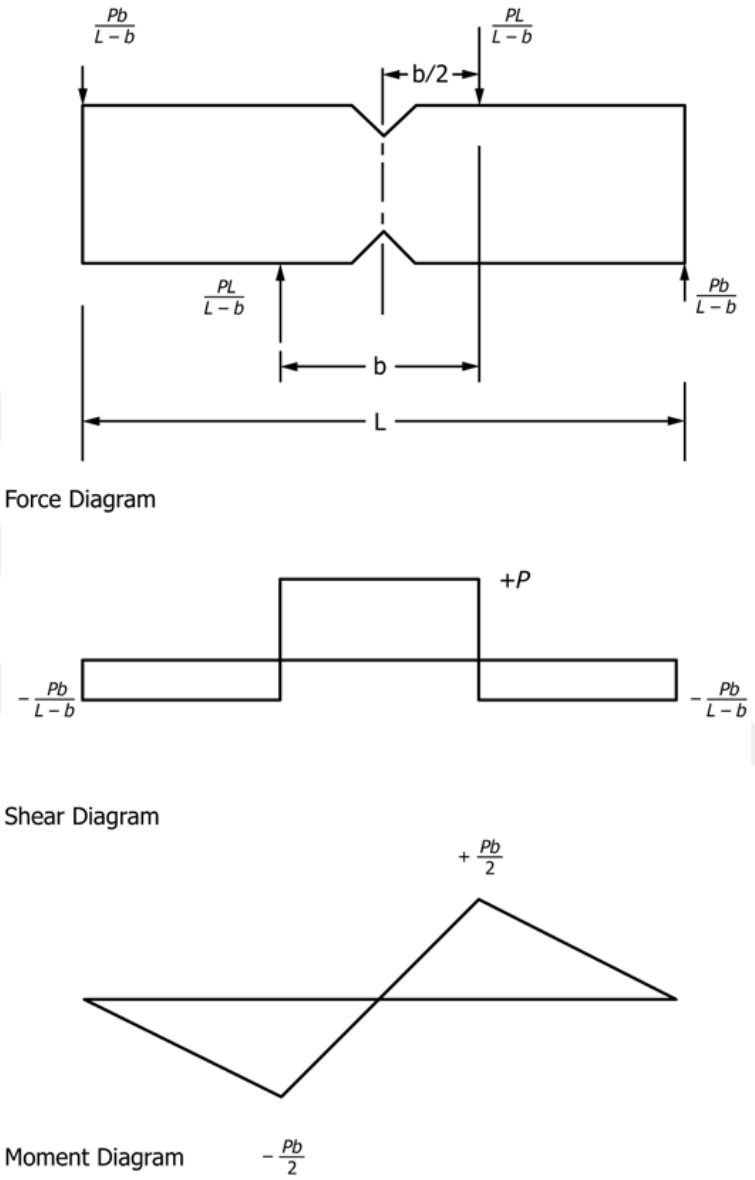

Figure A.3. Force, Shear and Moment Diagrams (Source: ASTM D5379[91])

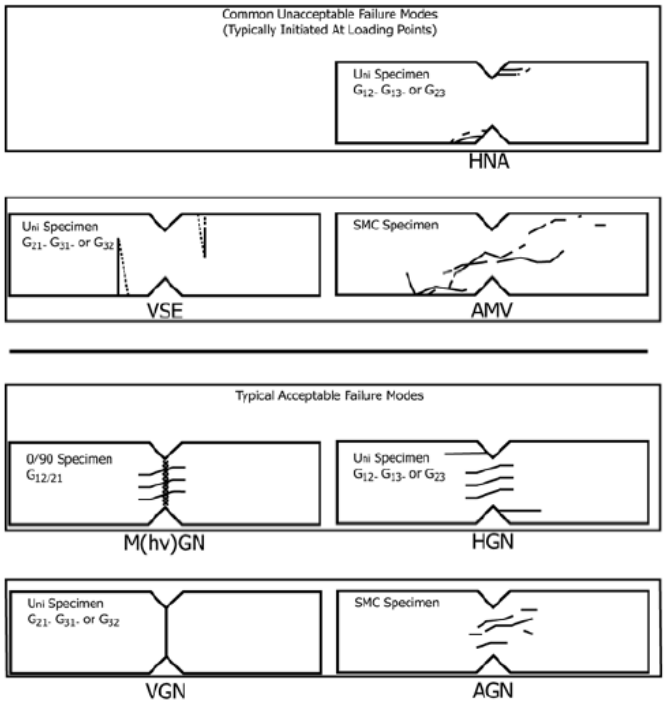

First Character

Failure Type	Code
Horizontal cracking	H
Vertical cracking	V
Angled cracking	A
Edge crushing	E
Multi-mode	M(xyz)
Other	O

Second Character

Failure Area	Code
Gage section	G
Notch region	N
Side region	S
Multiple areas	M
Various	V
Unknown	U

Third Character

Failure Location	Code
Bottom	B
Top	T
Left	L
Right	R
between Notches	N
Adjacent to notches	A
top and/or bottom Edge	E
Various	V
Unknown	U

FIG. 11 V-Notched Beam Shear Test Failure Codes/Typical Modes

Figure A.4. V-notched shear specimen failure identification (Source: ASTM D5379[91])

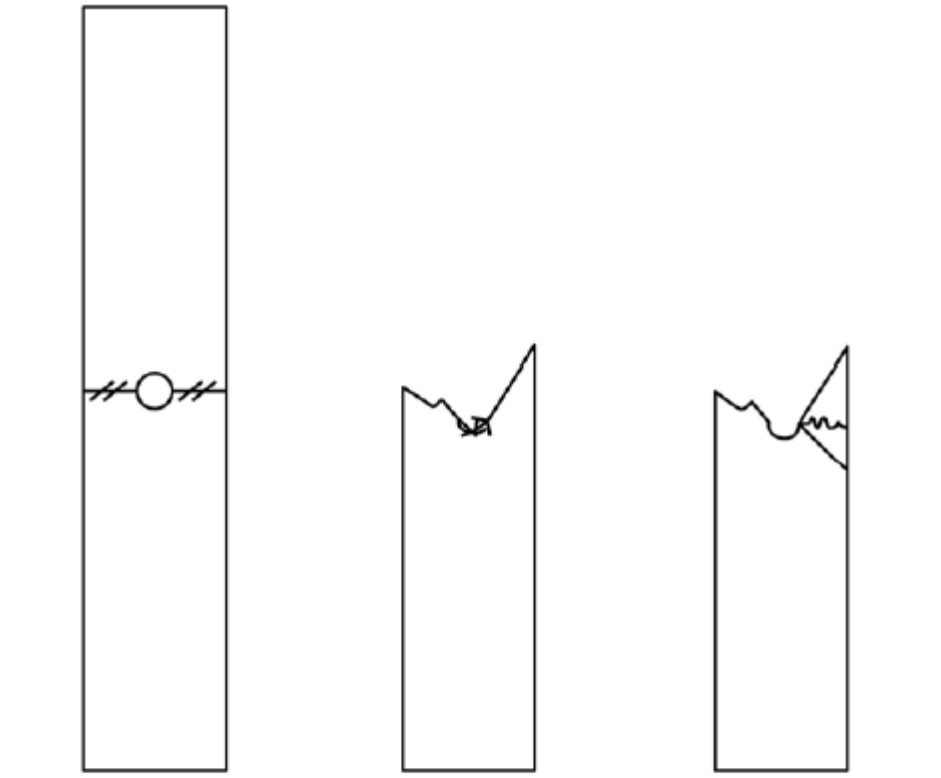

First Character		Second Character		Third Character	
Failure Type	Code	Failure Area	Code	Failure Location	Code
Angled	A	Inside grip/tab	I	Bottom	B
edge Delamination	D	At grip/tab	A	Top	T
Grip/tab	G	<1W from grip/tab	W	Left	L
Lateral	L	Gage	G	Right	R
Multimode	M(xyz)	Multiple areas	M	Middle	M
long, Splitting	S	Various	V	Various	V
eXplosive	X	Unknown	U	Unknown	U
Other	O				

Figure A.5. Failure identification codes for open-hole compression test samples (Source: ASTM D6484[119])

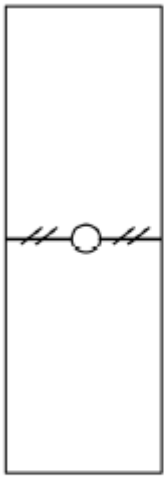

LGM

Laminate tensile failure laterally across the center of the hole. Splits and delaminations may be present.

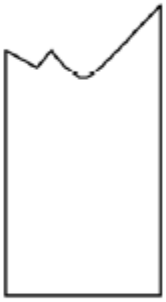

AGM

Laminate generally fails in tension at the hole, but remnants of angle plies cross the hole lateral centerline. Splits and delaminations may be present.

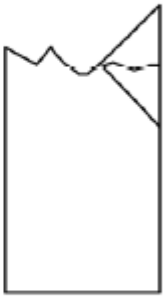

MGM

Laminate fails in tension at the hole and exhibits multiple modes of failure in various sublaminates. Extensive splitting and delamination present.

First Character		Second Character		Third Character	
Failure Type	Code	Failure Area	Code	Failure Location	Code
Angled	A	Inside grip/tab	I	Bottom	B
edge Delamination	D	At grip/tab	A	Top	T
Grip/tab	G	<1W from grip/tab	W	Left	L
Lateral	L	Gage	G	Right	R
Multi-mode	M(xyz)	Multiple areas	M	Middle	M
long. Splitting	S	Various	V	Various	V
eXplosive	X	Unknown	U	Unknown	U
Other	O				

Figure A.6. Failure identification codes for open-hole tensile test samples (Source: ASTM D5766[120])

APPENDIX B

FAILED SPECIMENS

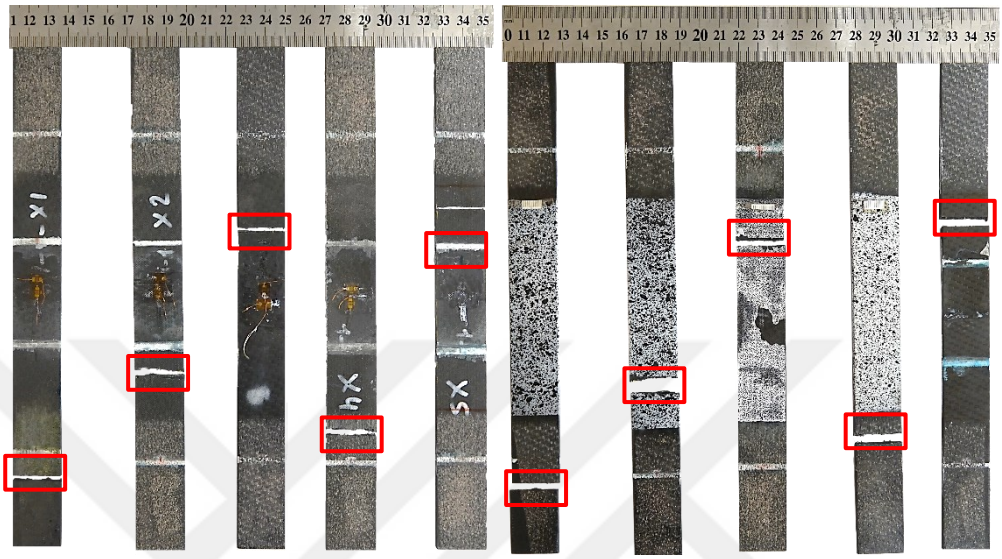

Front face Back Face

(a)

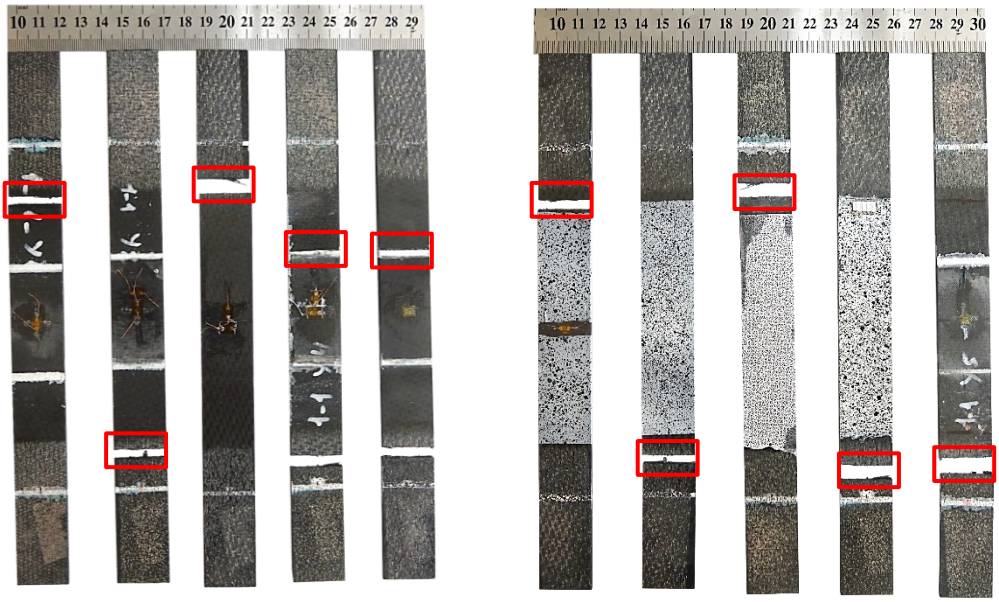

Front face Back Face

(b)

Figure B.1. Failed tensile test specimens (a) in the weft direction and (b) in the warp direction

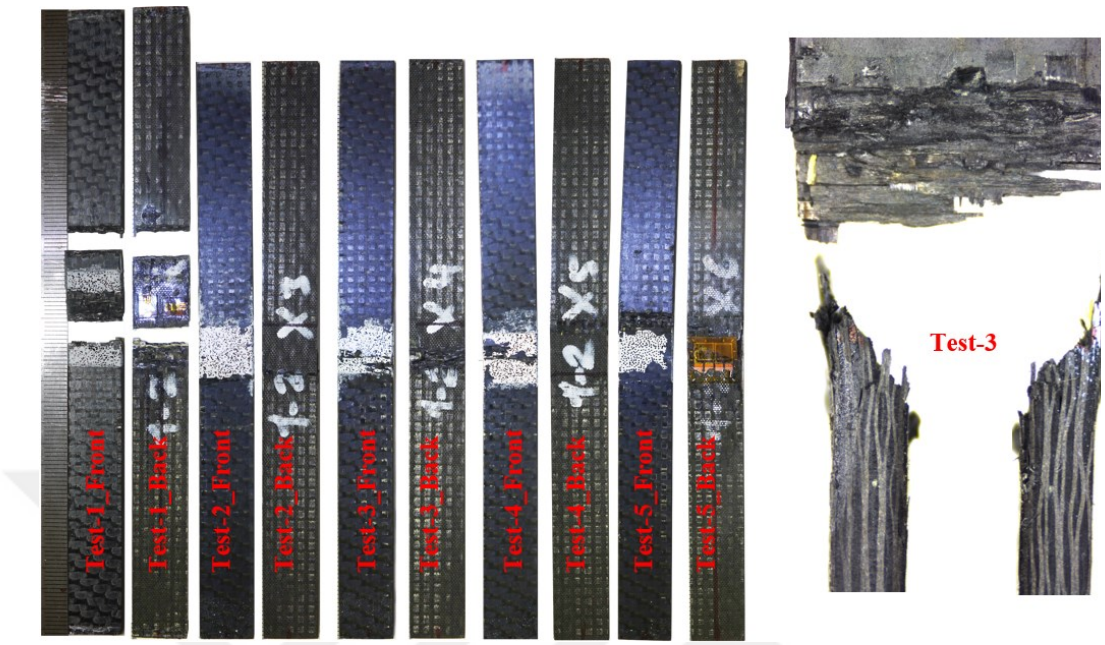

(a)

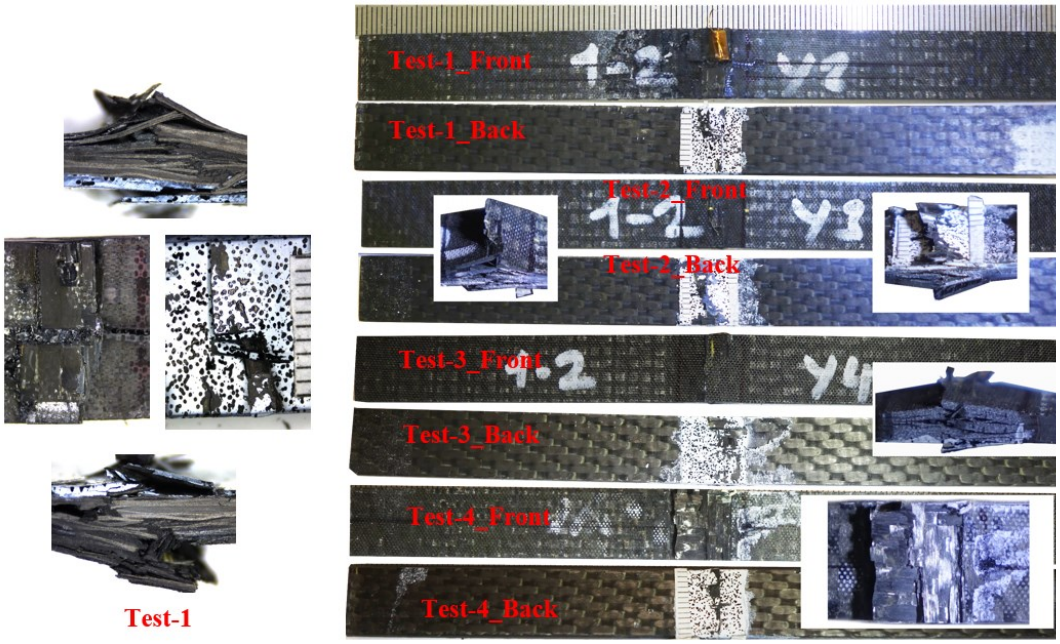

(b)

Figure B.2. Failed compression test specimens (a) in the weft direction and (b) in the warp direction

10^{-4} s^{-1}

Test-1

Time (sec)	0	287.85	425.6	532.6	576.04	580.6	596	606.72	670.86	866.28	900.86	1513.26
Strain	0	0.00458	0.011	0.01584	0.01904	0.01986	0.02066	0.03671	0.04557	0.06723	0.07077	0.13472
Stress (MPa)	0	201.6063	400.6327	537.7902	568.6622	552.7587	562.9592	83.94395	127.7104	89.17068	82.82595	41.3318

Test-3

Time (sec)	0	218.7	356.1	473.46	474	537.5	541.36	541.42	652.2	1099.66	2233.72
Strain	0	0.00558	0.01111	0.01746	0.01745	0.02221	0.02301	0.02454	0.05075	0.0967	0.21075
Stress (MP	0	201.5433	400.2813	543.1435	540.1911	602.8712	583.944	46.31608	125.9231	88.78571	84.69462

10^{-3} s^{-1}

Test-1

Time (sec)	0	25.28	48.4	49.24	54.98	55.36	55.4	62.56	93.78	153.78	272.06
Strain	0	0.00836	0.0211	0.02274	0.0275	0.02752	0.02842	0.04836	0.08205	0.14374	0.26383
Stress (MPa)	0	201.2968	498.8309	469.198	529.5053	513.9757	96.77704	161.1336	115.061	82.28293	69.08875

Test-2

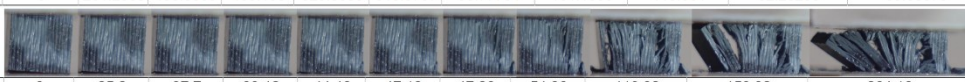

Time (sec)	0	25.2	37.7	39.12	44.46	47.18	47.26	54.36	110.92	150.92	264.16
Strain	0	0.00784	0.01491	0.01584	0.01974	0.02134	0.02285	0.03387	0.09636	0.13838	0.25139
Stress (MPa)	0	201.2994	341.3932	340.4823	373.1282	397.4257	205.1571	131.5083	92.22849	63.28146	60.13296

10^{-2} s^{-1}

Test-1

Time (sec)	0	2.6	4.14	4.8	5.04	5.08	5.52	7.08	11.84	19.84
Strain	0	0.011	0.0186	0.023	0.0249	0.0249	0.037	0.056	0.11	0.1898
Stress (MPa)	0	204	403	443.69	452.8	219.47	246.12	154.27	126.036	87

Test-2

Time (sec)	0	2.12	3.46	5.18	5.26	5.36	6.48	11.16	19.3
Strain	0	0.009	0.016	0.0235	0.0243	0.0251	0.0530	0.1025	0.1846
Stress (MPa)	0	201.36	447.4	638.33	632.96	501.49	172.20	120.79	108.84

(a)

(b)

Figure B.3. (a) The deformation results of cubic samples in the weft direction over time at different strain rates and (b) the failed cubic samples in the weft direction

10^{-4} s^{-1}

Test-1

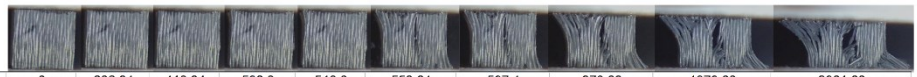

Time (sec)	0	282.94	418.34	538.3	546.6	553.64	597.4	970.68	1370.68	2061.68
Strain	0	0.00935	0.01658	0.0431	0.0439	0.04472	0.0496	0.08895	0.1299	0.19017
Stress (MPa)	0	344.09	522.6597	139.3287	135.5324	134.5927	122.5051	85.49315	78.39064	78.10128

Test-2

Time (sec)	0	213.9	345.64	494.18	506.84	574.48	760.52	1360.52	1560.52	1744.52
Strain	0	0.00705	0.0127	0.03994	0.0408	0.04798	0.06805	0.12979	0.14996	0.16362
Stress (MPa)	0	266.8486	466.673	124.7571	137.7685	140.8111	110.702	72.88031	81.35157	84.40942

10^{-3} s^{-1}

Test-1

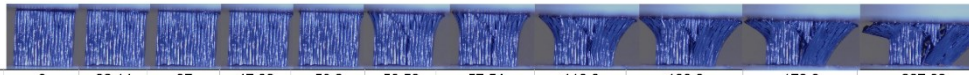

Time (sec)	0	22.14	37	47.32	50.2	50.58	57.54	118.8	138.8	178.8	227.62
Strain	0	0.00646	0.01299	0.0193	0.0217	0.0217	0.0432	0.10707	0.12778	0.16694	0.21633
Stress (MPa)	0	200.7601	399.4137	518.4365	526.408	505.0123	158.3601	79.51981	60.67839	68.08924	63.05691

Test-2

Time (sec)	0	31.48	44.68	45.86	48.36	57.96	98.68	138.68	207.2
Strain	0	0.01166	0.01804	0.0181	0.02367	0.04703	0.08958	0.12968	0.19812
Stress (MPa)	0	399.8288	585.9052	598.2215	66.3007	147.2234	106.8157	91.50043	107.9721

10^{-2} s^{-1}

Test-1

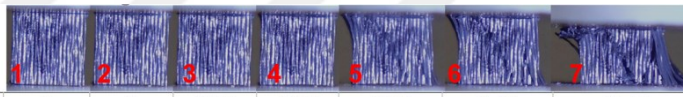

Time (sec)	0	2	3.32	5.04	5.08	5.88	20.72
Strain	0	0.00503	0.00975	0.01867	0.0194	0.0473	0.1964
Stress (MPa)	0	202.201	399.770	620.857	589.16	138.01	82.32

Test-2

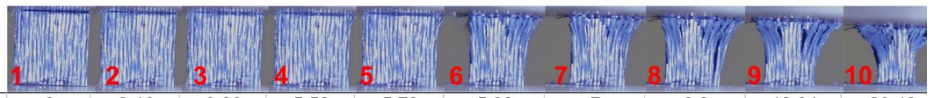

Time (sec)	0	2.46	3.88	5.52	5.78	5.82	7	8.8	12.04	20.42
Strain	0	0.00536	0.01093	0.01955	0.02193	0.02187	0.05355	0.07176	0.10417	0.18783
Stress (MPa)	0	202.1748	400.3054	584.9175	580.1599	563.8282	85.80154	72.81261	57.48543	27.67353

(a)

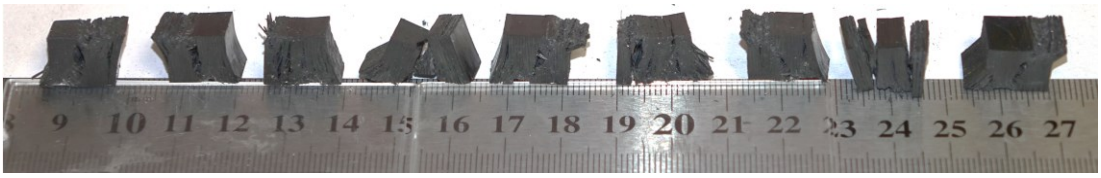

(b)

(c)

Figure B.4. (a) The deformation results of cubic samples in the warp direction over time at different strain rates, the failed cubic samples (b) in the warp and (c) in the thickness direction

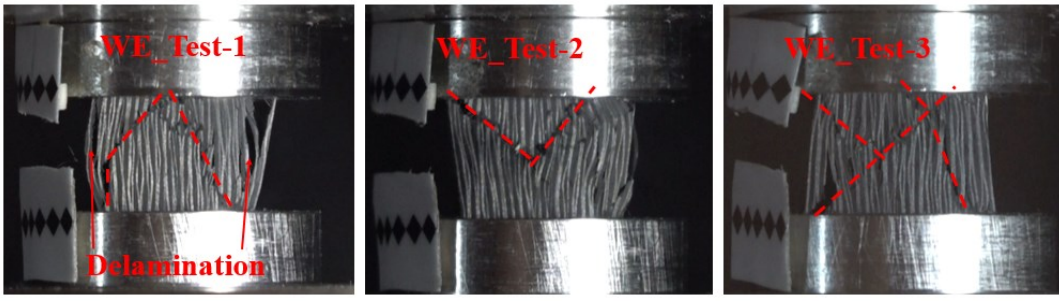

(a)

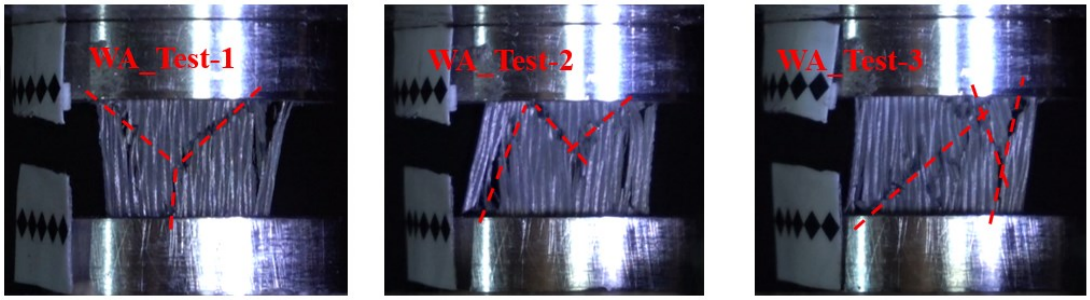

(b)

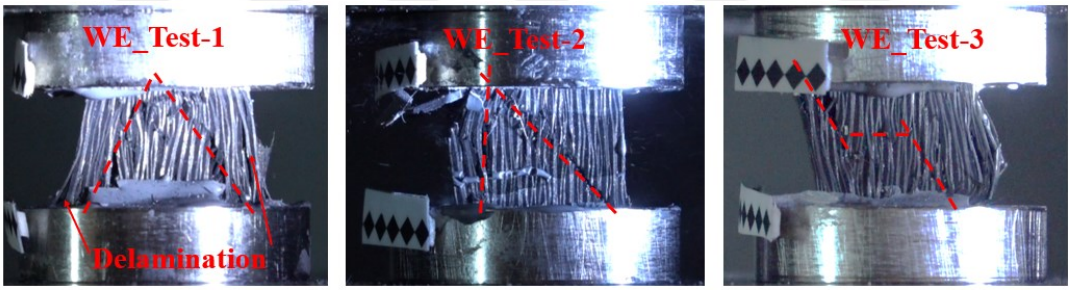

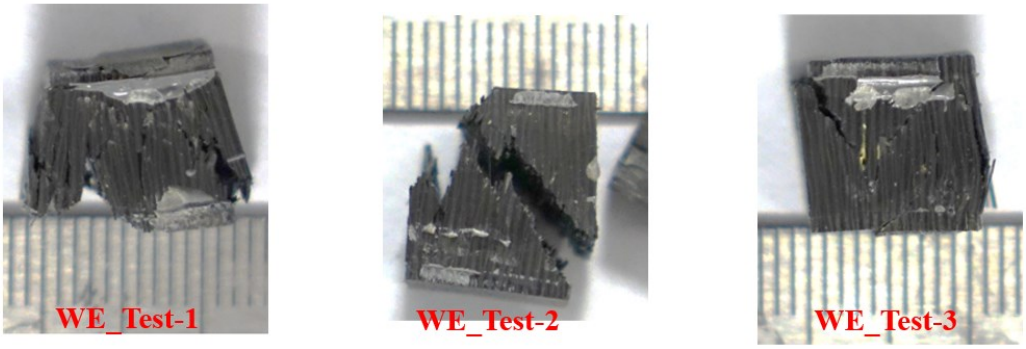

(c)

Figure B.5. (a) The tested weft samples with end-caps, (b) the tested warp samples with end-caps and (c) the tested weft samples adhered to end-caps

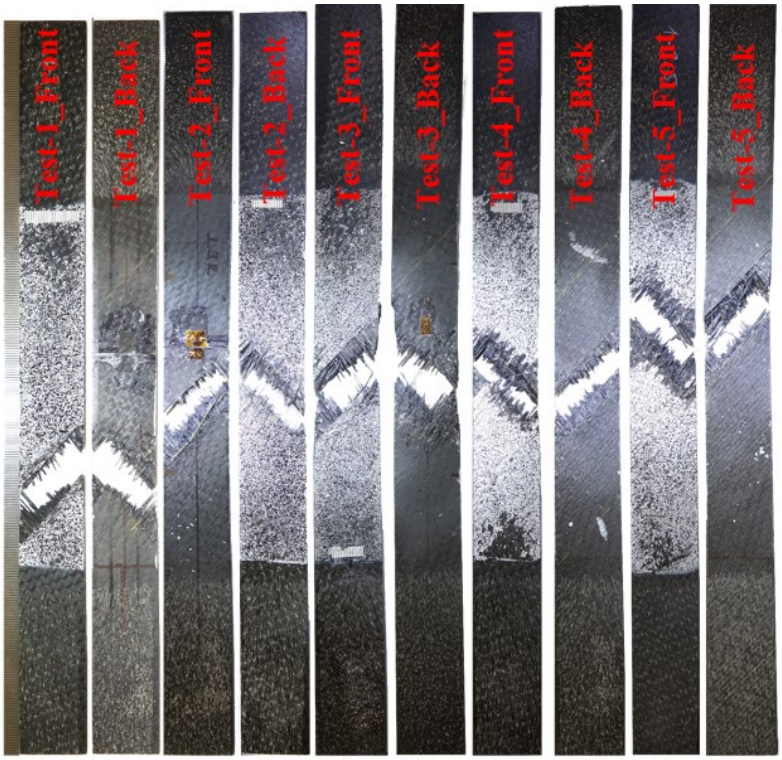

(a)

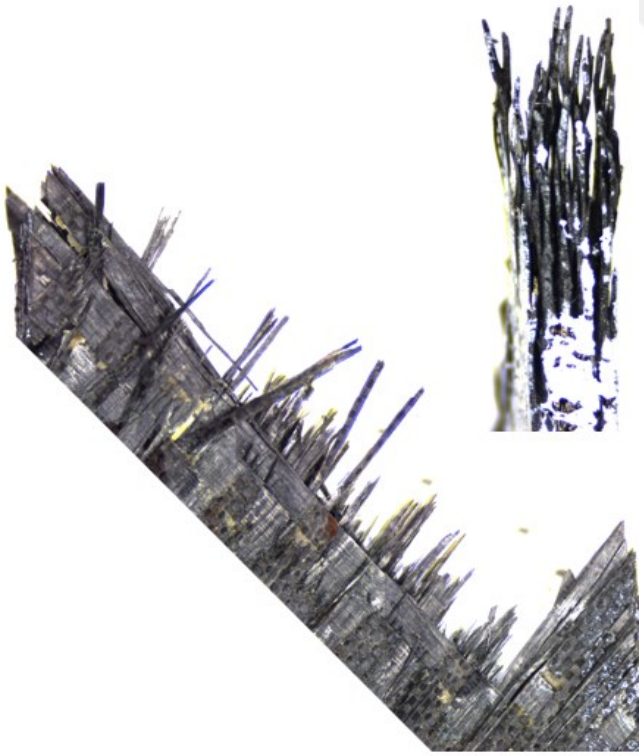

(b)

Figure B.6. Failed shear test coupons in tensile loading and (b) detailed cross-section image of the test coupon

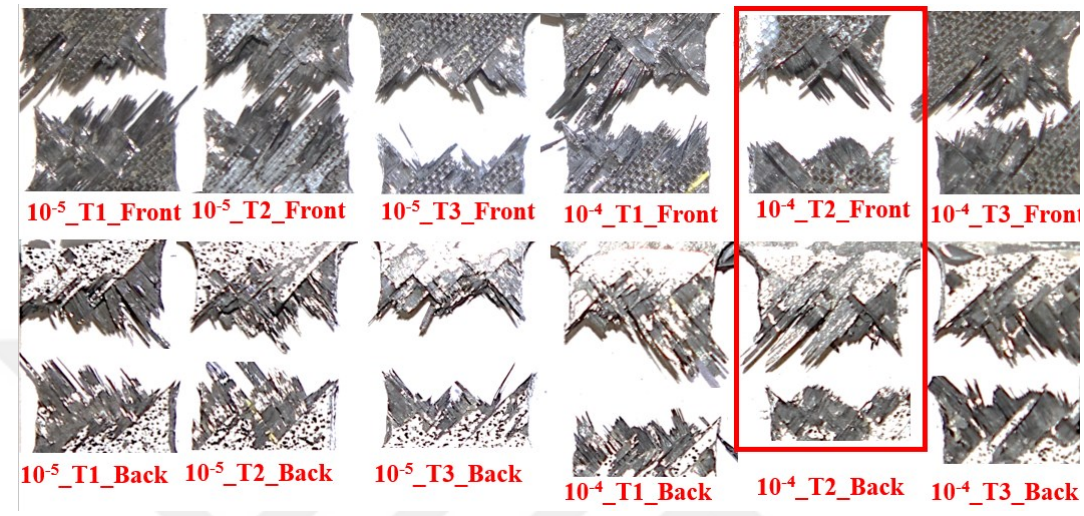

(a)

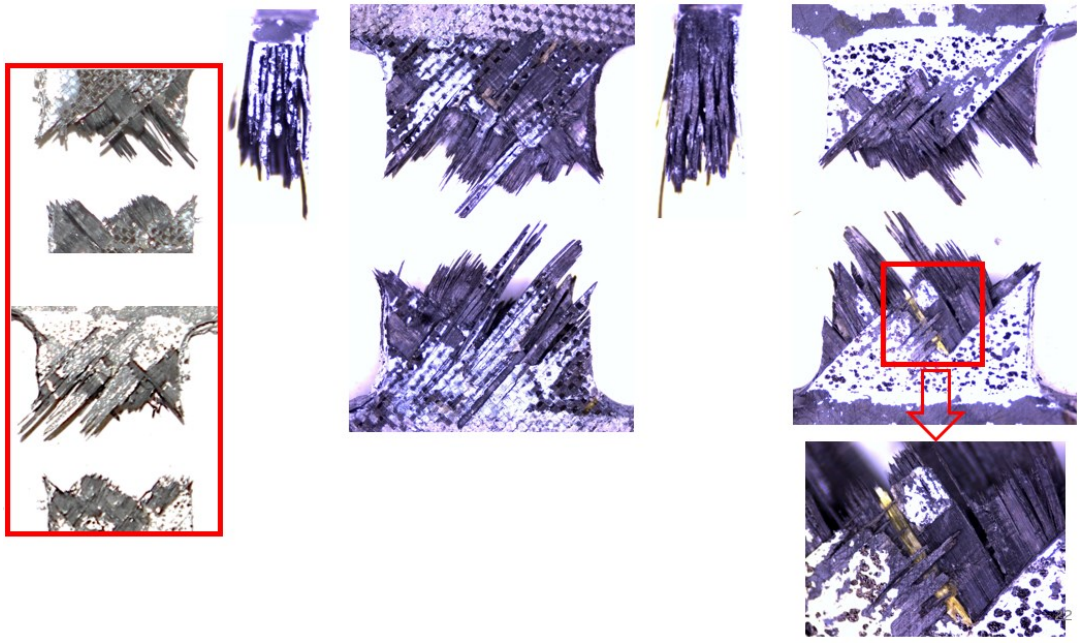

(b)

Figure B.7. (a) Failed ±45° composite samples at different quasi-static strain rates and (b) detailed failure image of one of the test coupons

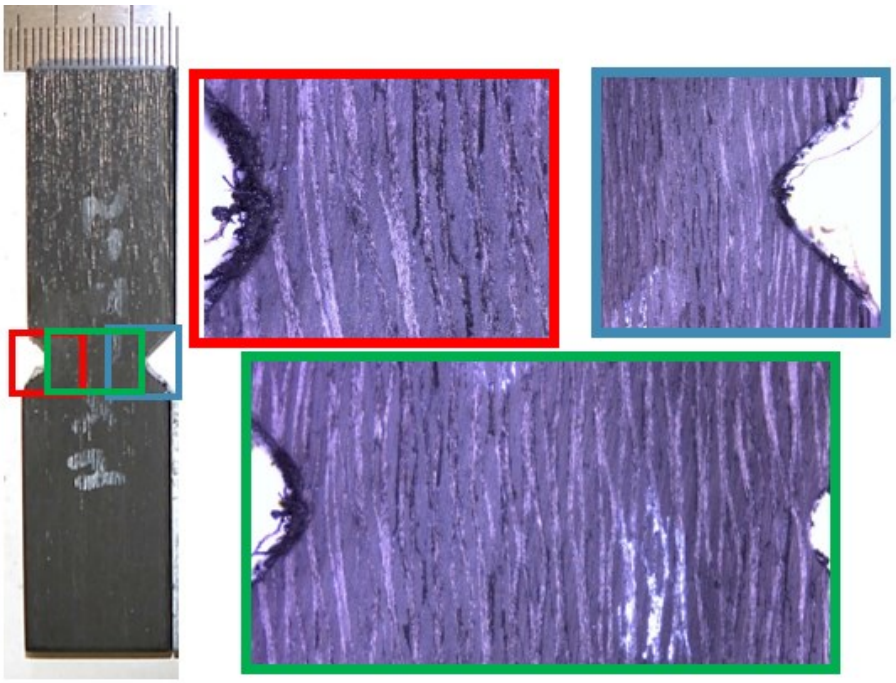

(a)

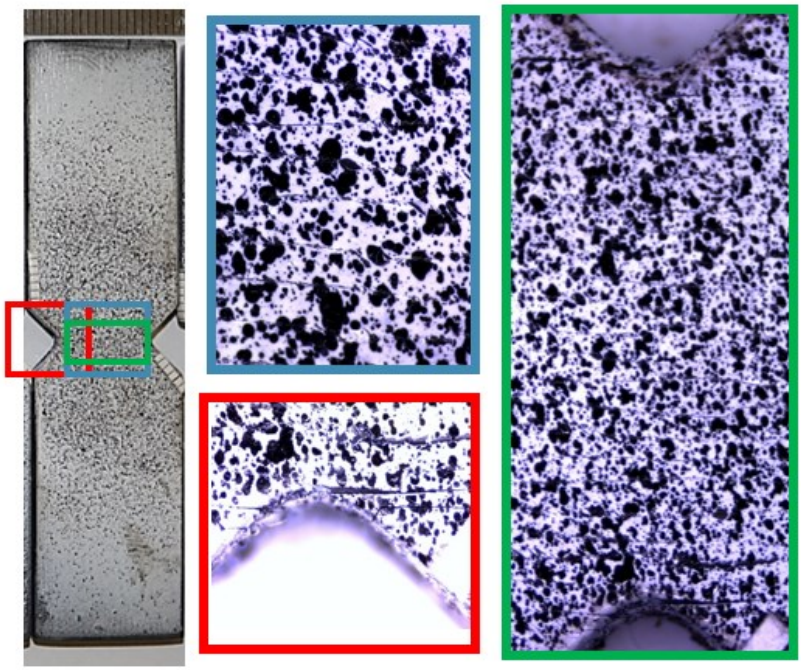

(b)

Figure B.8. Detailed fracture image of the test coupon failed in (a) 1-3 plane and (b) 2-3 plane

Figure B.9. Broken elastic constant determination test samples

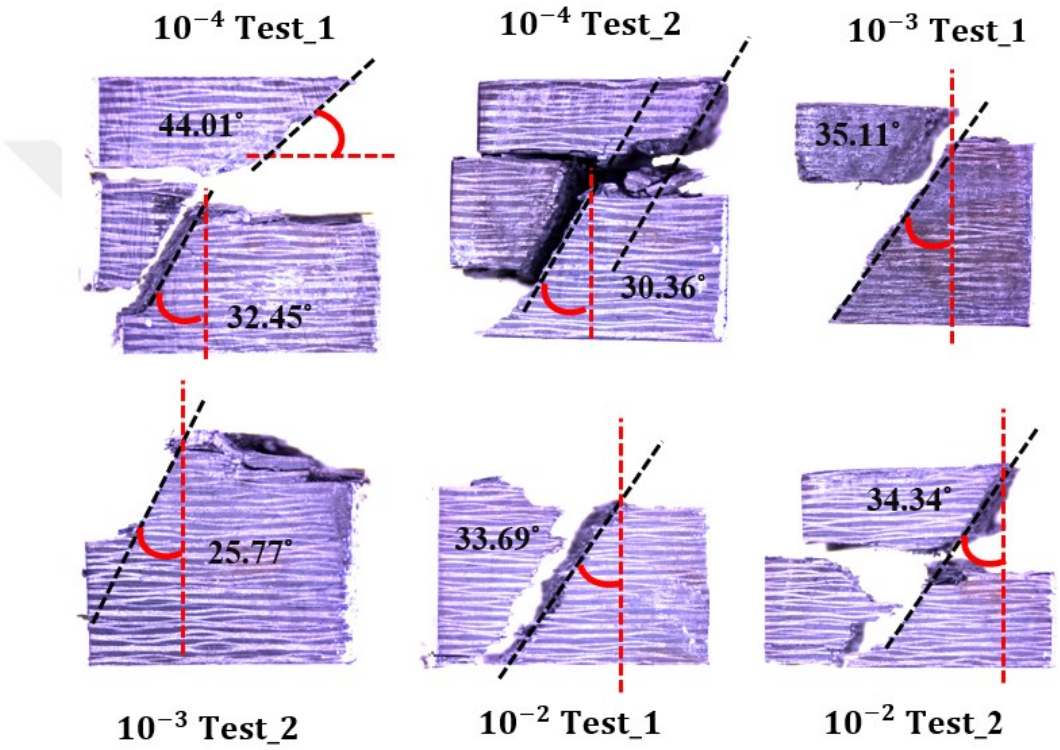

Figure B.10. Broken laterally constant compression test samples

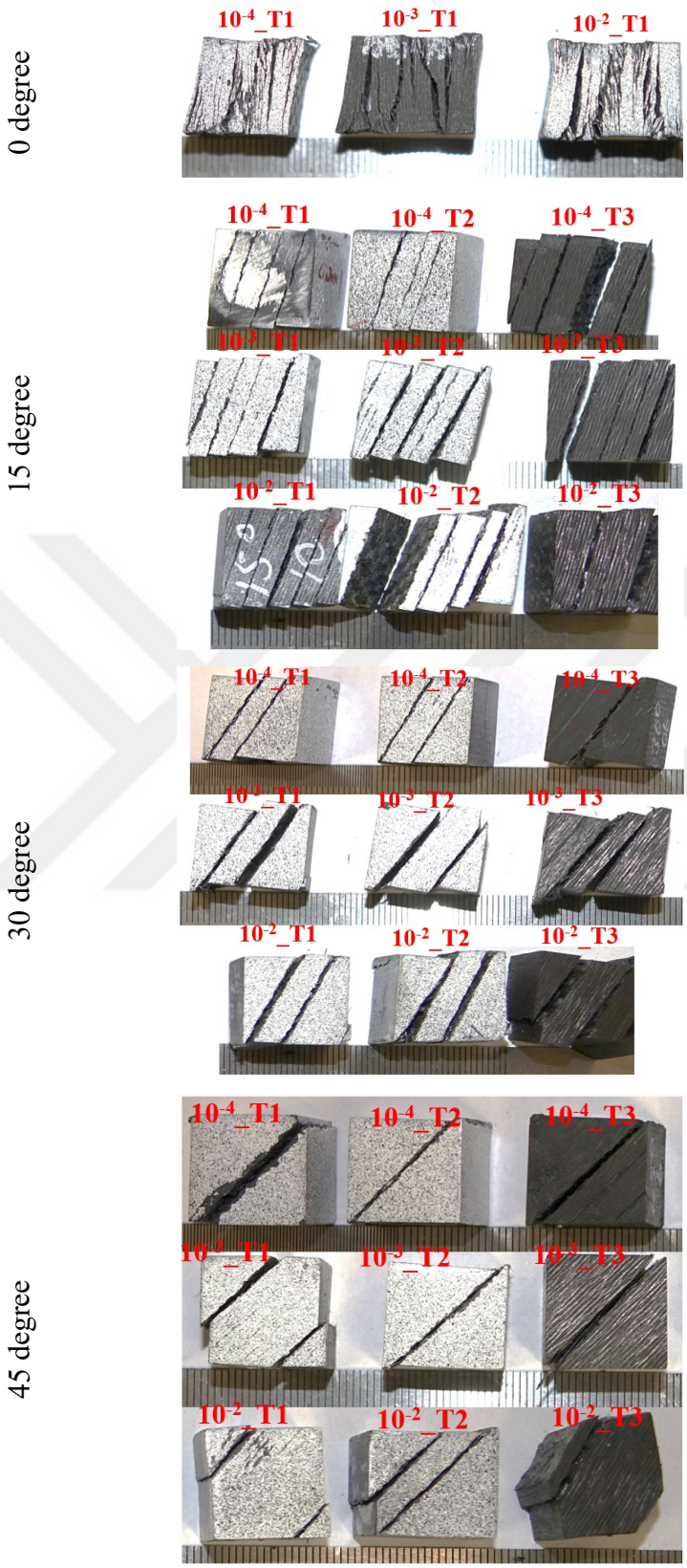

Figure B.11. Failed off-axis compression test specimens

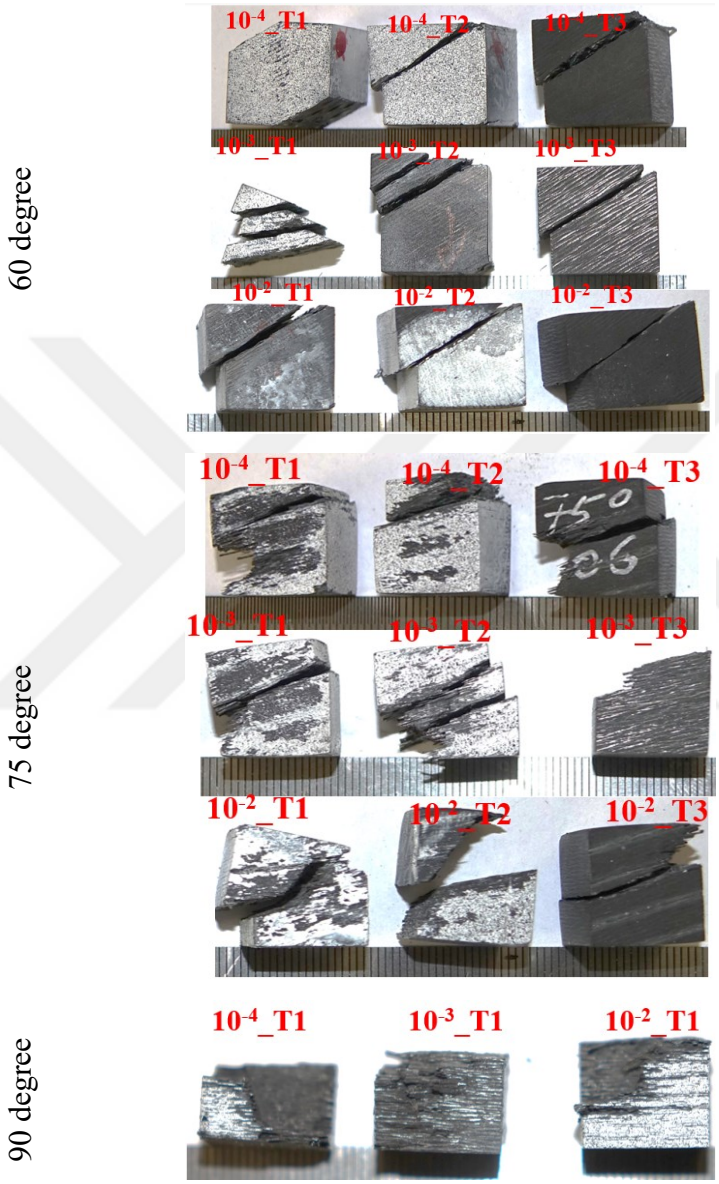

Figure B.12. Failed off-axis compression test specimens

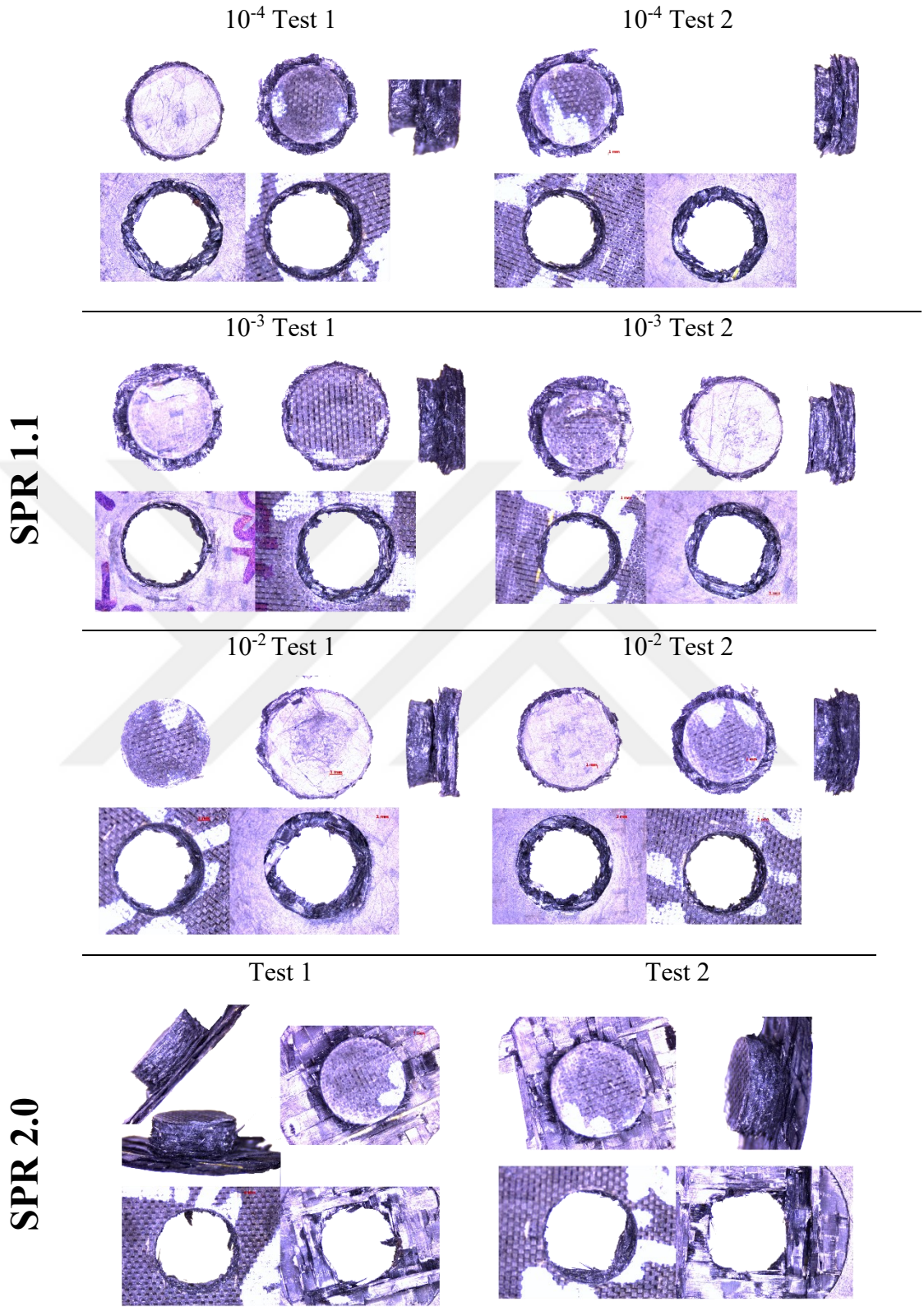

Figure B.13. Specimens failed by punch shear tests

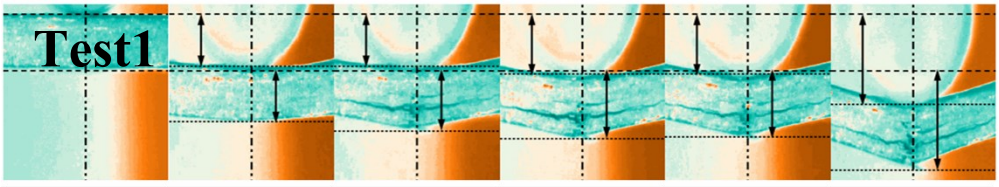

0	2.944	2.944	3.37067	3.37067	5.12	
0	0.02261	0.02261	0.02589	0.02589	0.03932	
0	2.90133	3.49867	3.88267	3.75467	5.632	
0	0.02228	0.02687	0.02982	0.02884	0.04325	

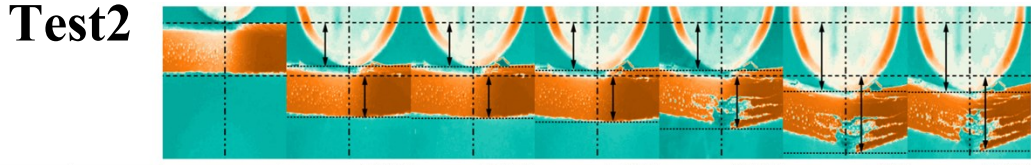

Damage Side	Disp.	0	2.62169	2.66024	2.89157	2.89157	4.1253	4.20241
	Flex. Strain	0	0.02013	0.02043	0.02221	0.02221	0.03168	0.03227
Back Side	Disp.	0	2.50602	2.54458	2.7759	3.2	4.66506	4.5494
	Flex. Strain	0	0.01925	0.01954	0.02132	0.02458	0.03583	0.03494

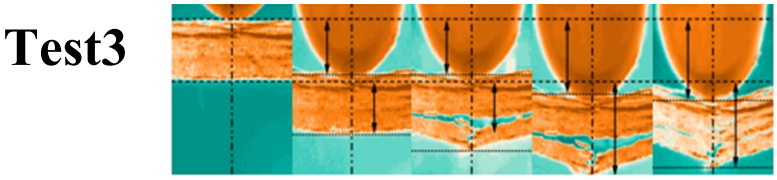

Damage Side	Disp.	0	2.85714	2.85714	3.84762	4.15238
	Flex. Strain	0	0.02194	0.02194	0.02955	0.03189
Back Side	Disp.	0	2.74286	3.54286	4.87619	4.41905
	Flex. Strain	0	0.02107	0.02721	0.03745	0.03394

(a)

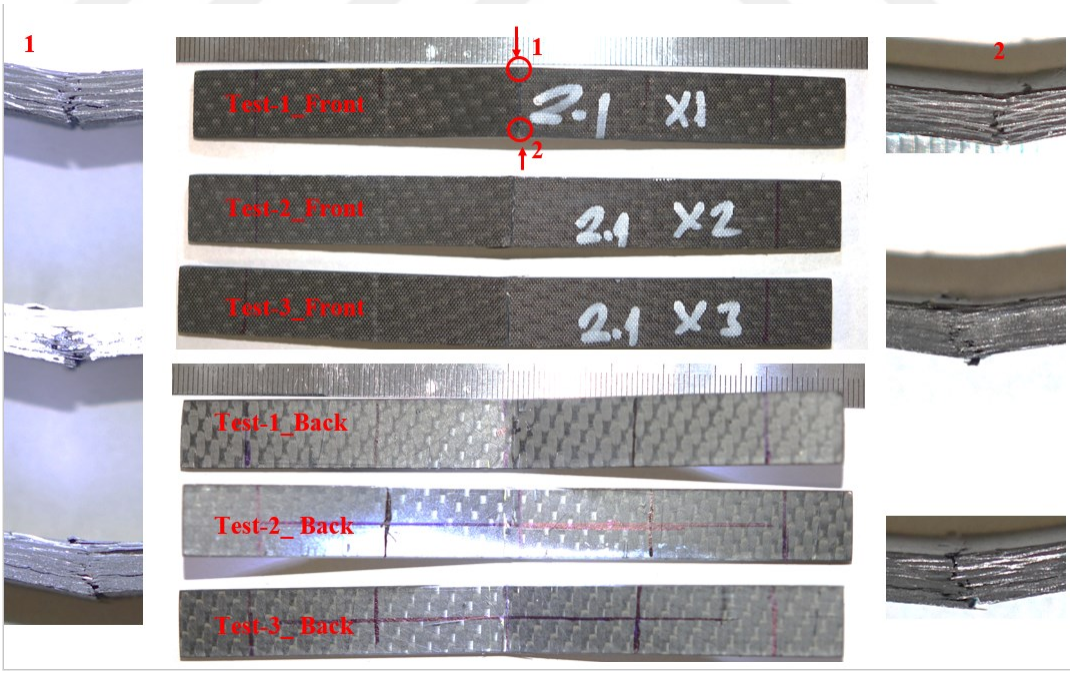

(b)

Figure B.14. (a) Flexural strain correction of the samples in the weft direction and (b) broken flexural test coupons in the warp direction

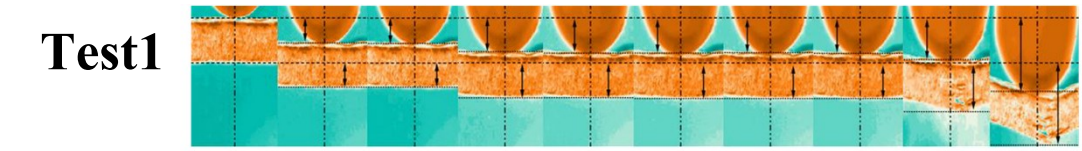

Damage Side	Disp.	0	1.77349	1.81205	2.58313	2.62169	2.66024	2.66024	2.6988	2.96867	5.20482
	Flex. Strain	0	0.01362	0.01392	0.01984	0.02013	0.02043	0.02043	0.02073	0.0228	0.03997
Back Side	Disp.	0	1.73494	1.73494	2.46747	2.46747	2.54458	2.54458	2.54458	3.46988	5.86024
	Flex. Strain	0	0.01332	0.01332	0.01895	0.01895	0.01954	0.01954	0.01954	0.02665	0.04501

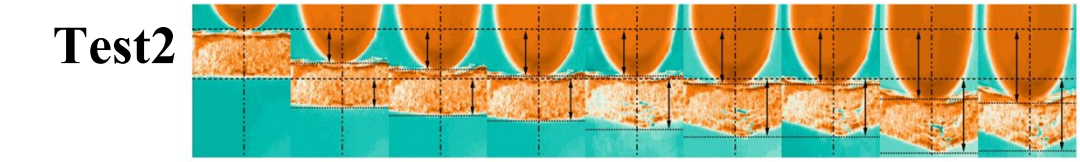

Damage Side	Disp.	0	2.71264	3.26437	3.77011	3.77011	4.41379	4.45977	5.65517	5.97701
	Flex. Strain	0	0.02083	0.02507	0.02895	0.02895	0.0339	0.03425	0.04343	0.0459
Back Side	Disp.	0	2.34483	2.94253	3.4023	4.09195	4.68966	4.68966	5.97701	5.7931
	Flex. Strain	0	0.01801	0.0226	0.02613	0.03143	0.03602	0.03602	0.0459	0.04449

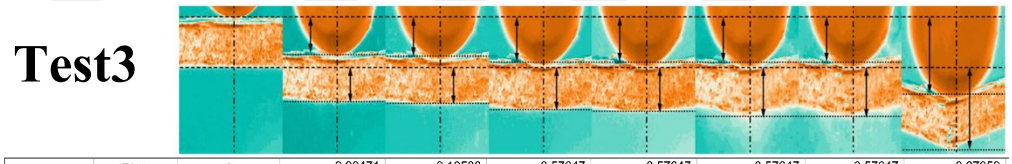

Damage Side	Disp.	0	2.96471	3.10588	3.57647	3.57647	3.57647	3.57647	6.07059
	Flex. Strain	0	0.02277	0.02385	0.02747	0.02747	0.02747	0.02747	0.04662
Back Side	Disp.	0	2.68235	2.82353	3.29412	3.43529	3.85882	3.85882	6.49412
	Flex. Strain	0	0.0206	0.02168	0.0253	0.02638	0.02964	0.02964	0.04987

(a)

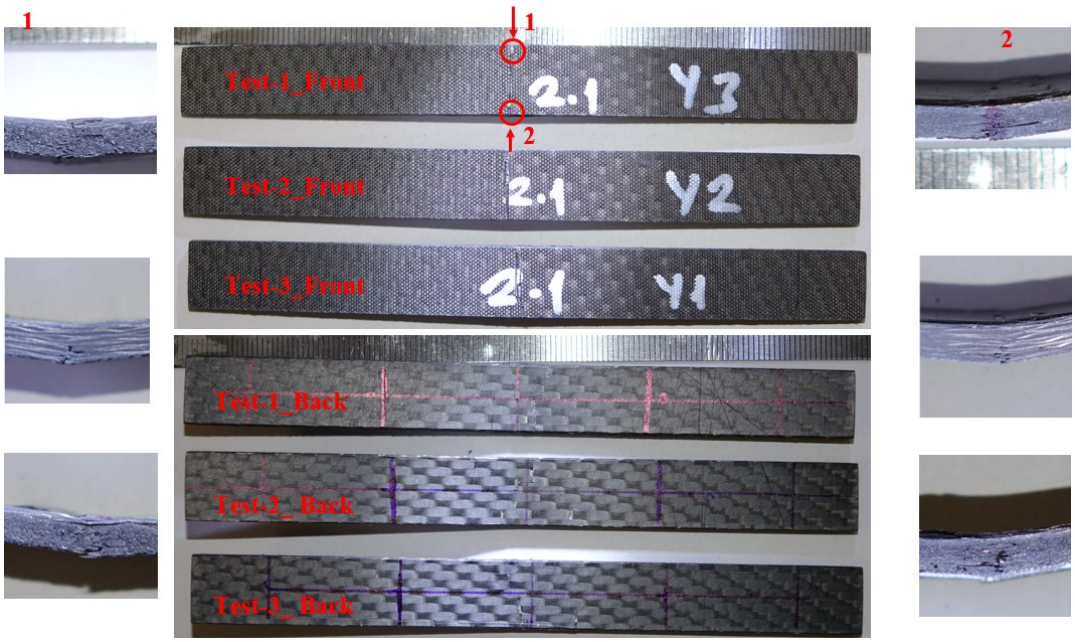

(b)

Figure B.15. (a) Flexural strain correction of the samples in the warp direction and (b) broken flexural test coupons in the warp direction

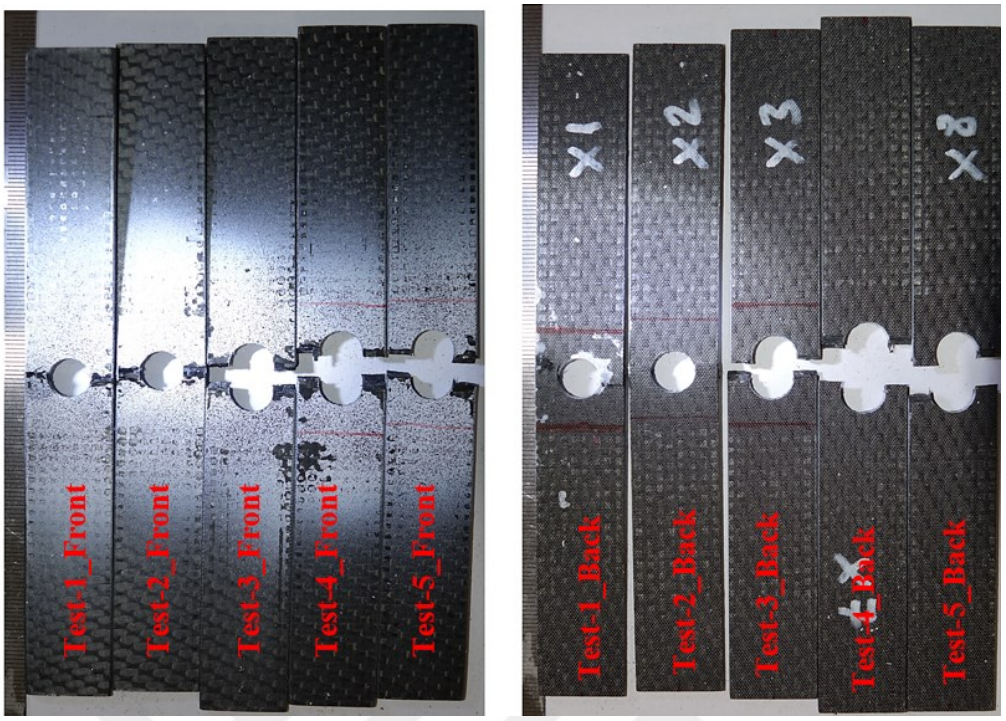

(a)

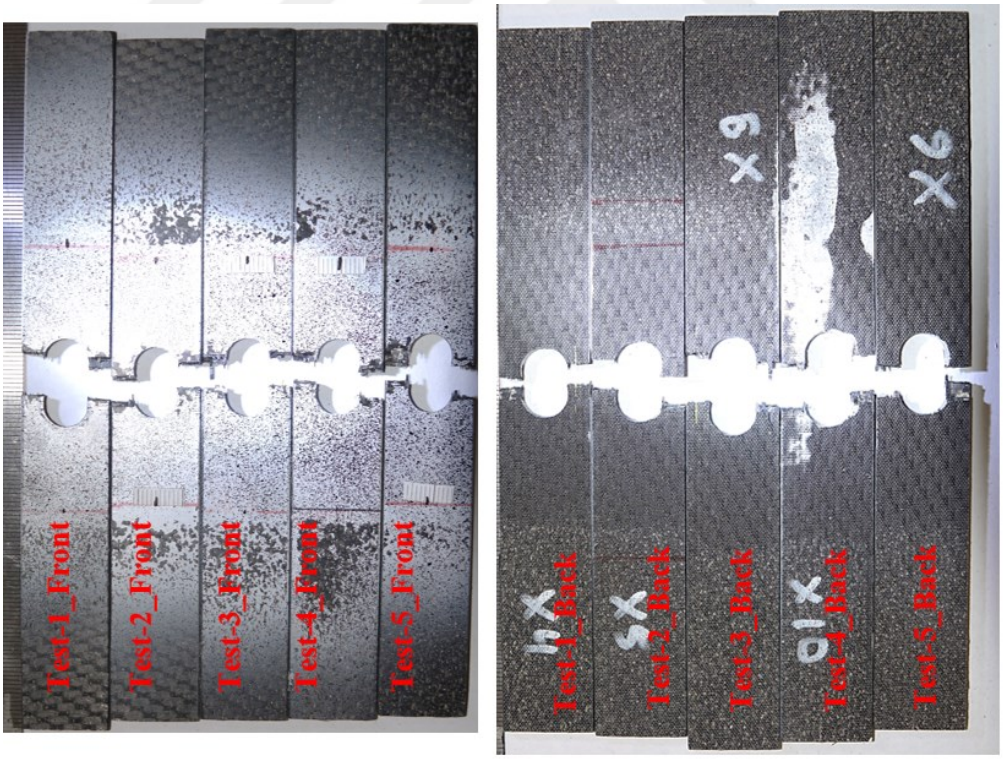

(b)

Figure B.16. (a) Open-hole compression and (b) Open-hole tension test samples test samples in the weft direction

VITA

He studied the Mechanical Engineering at Erciyes University and graduated in June 23, 2015. He continued to pursue his master degree in the same department in Izmir Institute of technology from 2016 to 2019 and received his master degree in engineering mechanics in January 21, 2019. In February 13, 2019 he attended to the same university to pursue his Doctor of Philosophy degree.

Publications

- M. Bayhan, S.B. Seven, A. Ramyar, M. Güden, A. Taşdemirci, "Damage formation of an E/Glass fiber reinforced polyester composite plate under multi-impact loadings", SAVTEK Defense Technologies Congress, 27-29/2018.
- M. Bayhan, S.B. Seven, A. Ramyar, M. Güden, A. Taşdemirci, "Experimental and numerical investigation of quasi-static and high strain rate compression behavior of a (0/90) cross-ply e-glass/polyester composite", IV. International Ege Composite Materials Symposium, 6-8/2018
- M. Güden, M. Bayhan, S.B. Seven, A. Ramyar, A. Taşdemirci, "Dynamic compressive behavior of an e-glass/polyester composite material subjected to repeated loads", Sustainable Industrial Processing Summit and Exhibition, 2018
- M. Güden, S. Enser, M. Bayhan, A. Taşdemirci, H. Yavaş, "The strain rate sensitive flow stresses and constitutive equations of a selective-laser-melt and an annealed-rolled 316L stainless steel: A comparative study", Materials Science and Engineering: A, vol. 838, 2022